Mechanical Loading Impacts Intramuscular Drug Transport:
Impact on Local Drug Delivery

by

Peter I-Kung Wu

B.S. Mechanical Engineering
University of California, Berkeley, 2000

S.M. Mechanical Engineering
Massachusetts Institute of Technology, 2007

SUBMITTED TO THE DIVISION OF HEALTH SCIENCES AND TECHNOLOGY
IN PARTIAL FULFILLMENT OF THE REQUIREMENTS FOR THE DEGREE OF

DOCTOR OF PHILOSOPHY IN MECHANICAL AND MEDICAL ENGINEERING

at the

MASSACHUSETTS INSTITUTE OF TECHNOLOGY

September 2008

Signature of Author: _____
Harvard-MIT Division of Health Sciences and Technology
August 23, 2008

Certified by: _____
Elazer R. Edelman, M.D., Ph.D.
Thomas D. and Virginia W. Cabot Professor of Health Sciences and Technology
Thesis Supervisor

Accepted by: _____
Martha L. Gray, Ph.D.
Edward Hood Taplin Professor of Medical and Electrical Engineering
Director, Harvard-MIT Division of Health Sciences and Technology

Mechanical Loading Impacts Intramuscular Drug Transport:
Impact on Local Drug Delivery

by

Peter I-Kung Wu

Submitted to the Harvard-MIT Division of Health Sciences and Technology
on August 23, 2008 in Partial Fulfillment of the
Requirements for the Degree of
Doctor of Philosophy in Mechanical and Medical Engineering

ABSTRACT

Controlled-release drug-delivery systems enable efficient and defined administration of therapeutic agents to target tissues. However, ultimate drug distribution and pharmacologic effect are determined by target tissue pharmacokinetics. In muscular tissues, complex architecture that is further augmented by dynamic motion and contraction can alter the pharmacokinetics and deposition of locally delivered macromolecules. We developed a system and applied a quantitative schema to investigate the impact of controlled mechanical loads applied to skeletal and cardiac muscle tissue on intramuscular transport of locally delivered drug. In a series of studies, we examined how the interaction between architectural configuration and functional mechanics alters the transport of drugs across both physicochemical and binding properties. We correlated these pharmacokinetic effects with characteristic parameters in the physiologic range of the tissue to derive mechanistic insight into the fundamental structural and dynamic elements that underlie these effects. While previous studies have revealed the unilateral scaling of substrate uptake with mechanical influences, we elucidated an architecturally defined pharmacokinetic setpoint whereby maximal drug penetration corresponds with optimal muscle function. Our findings elucidate basic biologic design in muscle that optimizes the interface between tissue and its physical environment. The unique insights from our investigations have broad impact on current understanding of the pharmacokinetic influences of biologic form and function, and elucidate new clinical strategies for controlled release and local delivery of a wide range of therapeutic compounds to mechanically active tissues.

Thesis Supervisor: Elazer R. Edelman
Title: Thomas D. and Virginia W. Cabot Professor of Health Sciences and Technology

TABLE OF CONTENTS

LIST OF FIGURES

LIST OF TABLES

1. INTRODUCTION

1.1 Motivations and Significance

1.1.1 Clinical Problem

Coronary heart disease (CHD) and peripheral arterial disease (PAD), the ischemic consequences of atherosclerosis, are increasingly dominant causes of chronic disability and death around the world. In the U.S. alone, CHD currently affects an estimated 16 million people and stands as the single leading cause of death, accounting for over 600,000 deaths – 20% of all deaths – every year [1]. Moreover, the risk of having either a fatal or nonfatal cardiovascular ischemic event is significantly increased for those who have PAD. Peripheral vascular disease serves as an independent risk factor for CHD [2], increasing the risk of mortality from CHD by 6.6 times [3]. However, large-vessel PAD is frequently asymptomatic and remains both under-diagnosed and underestimated. Nonetheless, it affects up to 8.5 million Americans [4] and is, in turn, 2 to 3 times as likely to occur in patients with cardiovascular disease [5]. Ultimately, PAD leads to progressive disability and risk of limb loss. As a result of their increasing prevalence and incidence with the increasing mean age of the population, both CHD and PAD present major scientific and medical challenges for developing advanced therapies that both successfully treat ischemic damage to tissues, and restore the supply of blood to these tissues.

1.1.2 Current Treatments

Presently, over 3.3 million interventional procedures are performed each year for attempted relief of the complications of CHD [1]. Current invasive interventions for treating cardiac or skeletal muscle ischemia are designed to mechanically restore blood flow to the compromised tissues. These therapies consist of traditional surgical revascularization methods like coronary artery bypass grafting (CABG) and the commonly applied catheter-based intervention of percutaneous transluminal coronary angioplasty (PTCA) combined with stent placement. However, despite advances in these therapies, there still remains a significant and apparently increasing number of patients who are either ineligible for such treatments, or for whom such treatments are ineffective in salvaging ischemic yet viable tissues. Up to 12% of patients with symptomatic CHD have diffuse vessel disease, small distal vessels, or other comorbidities that render this subset of patients poor candidates for revascularization by PTCA or CABG [6]. Similarly, the use of these mechanical interventions for patients with PAD is limited by the same complications [7]. Unfortunately because of the aging population, the proportion of CAD and PAD patients who are not amenable to these standard therapies is estimated to increase. Yet, despite their severe ischemia, such patients may still have a relatively large enough amount of viable cardiac or skeletal muscle that can be salvaged. Therefore, it appears warranted to incorporate alternative strategies, either as independent therapies or as adjuncts to conventional revascularization, for improving blood flow and mechanical performance to the heart or skeletal muscle.

As a result, research efforts have been directed towards investigating therapeutic angiogenesis as an alternative treatment for ischemic vascular disease. This promising

therapy uses the local administration of pro-angiogenic growth factors to pharmacologically promote endogenous blood vessel formation and growth. By augmenting blood flow to ischemic tissues in this way, therapeutic angiogenesis has the potential to salvage ischemic myocardium or skeletal muscle, and reduce infarct size. Such treatment can thus compensate for the apparently inadequate angiogenic response in patients with advanced vascular disease [8] and may provide them with symptomatic relief, improvement in quality of life, and perhaps improvement in overall survival.

1.1.3 Therapeutic Angiogenesis

Therapeutic angiogenesis has been proposed since the 1970s [9] to "biologically bypass" obstructed arteries in order to prevent, compensate for, and treat ischemic disease. The most extensively studied pro-angiogenic factors have been vascular endothelial growth factor (VEGF) and fibroblast growth factor 2 (FGF2), both of which are key endothelial and vascular mitogens [10-12]. The ability of these polypeptides to promote blood vessel formation and maturation, as well as their synergistic contribution to regulating vessel growth, have been well studied *in vitro* [12-17]. As a result, numerous experimental animal studies and clinical trials have investigated the potential for promoting therapeutic neovascularization in myocardial ischemia or PAD using either protein or gene delivery of VEGF or FGF.

Results from initial studies of VEGF and FGF protein administration to animal models of hindlimb and myocardial ischemia have raised hopes for the therapeutic effectiveness of pro-angiogenic growth factor delivery. For example, animal studies by various groups revealed that VEGF is effective in increasing tissue perfusion and

improving muscle function [18-21], and that bFGF produces dose-dependent increases in collateral vessel formation and blood flow [22-29]. However, despite encouraging findings from many animal studies, the results from nearly a decade of human clinical trials using growth factor delivery have shown mixed success and have raised major concerns about the potential side-effects of delivering angiogenic growth factors. These inconsistent findings include, on the one hand, mildly encouraging results from mostly small and uncontrolled clinical studies. These small studies showed that intramyocardial, perivascular, or intracoronary administration of FGF2 or VEGF in patients with end-stage myocardial ischemia can lead to improvements in exercise tolerance and angiographic scores of collateral growth [30-38]. On the other hand, less successful results have come from larger multi-center, randomized controlled trials. For example, the 2002 FGF Initiating RevaScularization Trial (FIRST) [39] showed no significant increase in treadmill exercise tolerance or myocardial perfusion after intracoronary FGF2 treatment. Similarly, a comparable pattern of mixed results also emerged from multi-center, randomized controlled trials for PAD, such as the TRAFFIC study [40] and RAVE trial [41].

These larger trials for CAD and PAD also revealed the various side-effects that can result from systemic exposure to growth factors, or when growth factors deposit in non-target tissues. Gene transfer of VEGF caused transient lower extremity edema [42-44], intracoronary delivery of FGF2 caused hypotension [39], and systemic intravenous delivery of FGF2 resulted in severe proteinuria and renal toxicity [45]. These findings suggested that perhaps optimizing the local delivery of growth factors to target tissues

may potentially bridge the discrepancy between their therapeutic potential and clinical effectiveness.

1.1.4 Local Delivery

With the idea that proximity of the administration site to the target-tissue can increase therapeutic effectiveness, many efforts to improve angiogenic therapy have centered on designing strategies for effective local delivery of growth factors, especially since ischemic lesions are typically spatially focal in nature. Local delivery offers the advantage of being able to present growth factor protein directly and efficiently to desired target tissues at *physiologic* rather than *pharmacologic* doses, thus minimizing systemic losses to non-target tissues [46]. Furthermore, local delivery can potentially achieve a desired spatial distribution for a temporal duration long enough to accommodate the typically long time course of new collateral vessel development. With this notion, various strategies have been employed for local delivery of growth factors. Such delivery strategies have used intrapericardial, perivascular, and intramuscular routes via various administration modalities including osmotic pumps, gene therapy, or sustained delivery polymers [47-52] to yield various degrees of improved results. For example, myocardial uptake of FGF2 from pericardial administration was shown to be approximately 5 times that from intracoronary administration [46]. However, even as these local delivery methods ascend in interest and importance, many still remain unproven in terms of clinical effectiveness, safety, and superiority. This is because many issues regarding the local pharmacokinetics of growth factors within their target tissues remain to be elucidated before an optimal local delivery method can be designed. For example, an

incomplete understanding of intramyocardial transport after intrapericardial delivery may limit growth factor deposition to only the epicardial layers and result in poor transmyocardial diffusion and endocardial distribution [53] or lead to local toxicity that may precipitate plaque growth or destabilization [54, 55]. Thus, elucidating the forces involved in growth factor handling by target tissues will facilitate a more rational approach to the design of local delivery strategies.

1.1.5 Local Pharmacokinetics

Controlled released and local delivery strategies provide a means for efficient administration of therapeutic agents to target tissue with minimal systemic losses; however, ultimate drug distribution and pharmacologic effect are dictated by target tissue pharmacokinetics. Local delivery systems must consider that space- and time-dependent drug distribution, not simply proximity of delivery, also dictate tissue response. The spatial and temporal distribution of drug in the tissue can be influenced by general transport effects such as diffusion or convection, as well as charged partitioning, steric hindrance, or specific binding, which reflect the interaction between tissue and drug physicochemical and binding properties.

The kinetics of specific binding interaction between the delivered growth factor and its target tissue environment significantly impacts this drug distribution. Once released, exogenously delivered heparin-binding growth factors, such as FGF and VEGF, can interact with several receptors expressed in the extracellular environment. They bind with high affinity to specific cell-surface tyrosine kinase receptors, and with lower affinity to the more abundantly found cell-surface, basement-, and extracellular-

membrane co-receptors such as heparan sulfate proteoglycans (HSPG), $\alpha_V\beta_3$ integrins, and collagen types I and IV [56-61]. Studies of *in vivo* organ deposition after intravascular administration of exogenous growth factor have found the proteins to be localized to zones of these organs that are rich in HSPGs, such as the extracellular matrix and vascular endothelium in the heart [46, 62]. Binding of FGFs to these co-receptors has been found to protect FGFs from proteolytic degradation and denaturation, thereby stabilizing their local levels and increasing their half-life in tissues [63, 64]. This binding can also create a spatially distributed storage reservoir, which allows growth factor to reach higher local amounts and concentration gradients, and from which they can be released over time to sustain long-term stimulation of surface receptors on endothelial cells [65-67]. Thus, the interaction with HSPGs, depending on their location and concentration, may serve to increase both the duration of the biological activity of the growth factors and their radius of diffusion and action. Or, this interaction may serve to limit growth factor diffusibility by immobilizing them to the ECM and restricting their subsequent availability to bind to downstream tyrosine kinase receptors [62, 68].

Furthermore, as dynamic and mutable biological components, these binding sites can be affected by the physical state of the tissue. In particular, the pathologic changes during ischemia can result in a significantly different transport environment, with consequence on growth factor availability and biological activity [59]. One prime example is the increased expression of cell-surface receptors (FGFR1, VEGR1, VEGR2) as well as extracellular and basement membrane HSPGs in acutely and chronically hypoxic or collateral-dependent ischemic border zones [69-73]. But more than this, studies in both ischemic myocardium and skeletal muscle have shown that changes in

cell-surface receptor expression after an ischemic event follow a characteristic spatial and temporal kinetic. There is rapid but short-lived receptor upregulation in the non-ischemic zones, and a slower but steadier upregulation of receptors in the injured area [74, 75]. Therefore, the increase in the number of binding sites during myocardial ischemia may enhance myocardial deposition and retention of growth factor [53]. However, the early increase of receptors in non-ischemic tissue may actually limit therapeutic efficacy by sequestering available drug before it transports to the ischemic border zone. This insight into binding site mutability during ischemia underscores the need to have a better understanding of the predominant pharmacokinetic influences exerted by the target tissue on a drug in order to improve its therapeutic effectiveness.

1.1.6 Influence of Mechanical Loading

Of critical importance especially for local delivery strategies like therapeutic angiogenesis to mechanically active tissues is the matter of achieving adequate drug penetration to intramuscular targets. With a fundamental understanding of the influences of binding and specific interactions on growth factor pharmacokinetics, there is still an incomplete knowledge of the prevalent transport forces in muscle tissues. Local pharmacokinetic effects can be pronouncedly compounded by complex architecture and mechanical function. Interactions between drug and the physical structure of the tissue can sterically hinder interstitial transport of the higher molecular weight drugs that local strategies deliver. Muscle tissue presents an exclusive transport environment in which dynamic mechanical motion and loading can significantly influence the pharmacokinetics of delivered agents. These loads and motions, which are shaped by both structure and

function of the muscle, can present major, dynamic physical influences on drug transport by modulating interstitial space permeability, fluid volume distribution, and tissue deformation. In addition, the influence of such transport effects can be dramatically altered in pathologic states such as ischemia, hypertension, or hypertrophic cardiomyopathy, in which muscle tissue undergoes architectural remodeling and mechanical dysfunction. Thus, a quantitative investigation of the roles of architecture and loading dynamics in muscle tissue is necessary not only to optimize local drug delivery, but also to establish a more comprehensive understanding of intramuscular pharmacokinetics.

A diverse body of work has investigated the transport of agents in mechanically loaded tissues. Only a subset of this work has focused on the impact of mechanical loading dynamics. These studies have examined the impact of pressure-induced aortic distension on transmural transport of low-density lipoprotein and albumin [76]; the impact of static tensile loading on diffusion of water in Achilles tendon [77]; the effects of static or cyclic compression on transport of dextran [78, 79], H_2O, sodium, lithium [80], insulin-like growth factor I, proline, and sulfate [81] in articular cartilage; the effects of skeletal muscle fiber contraction on sarcoplasmic protein diffusion [82]; the role of contraction on glucose uptake in skeletal muscle [83, 84]; the influence of atrial workload on translocation of secreted atrial natriuretic peptide and extracellular fluid [85]; the influence of atrial distension on permeability of large macromolecules such as horseradish peroxidase [86]; the effects of contraction on inulin uptake and washout in papillary muscle [87]; the role of calcium in regulating glucose uptake in isolated working rat heart [88]; and the impact of cardiac contractility on interstitial washout of

raffinose [89]. Each study has revealed the influence of mechanical loading on the transport and uptake of various agents. Diminished transendocardial translocation of atrial natriuretic peptide (ANP) arises when high atrial workloads reduce the extracellular space [85]. Increases in apparent diffusion of water in statically tensile-loaded Achilles tendon are attributed to extrusion of tendon water into a bulk phase along the outside surface of the tendon during loading rather than to load-related changes in fiber spacing [77]. And, compression reduces dextran diffusivity in cartilage [78].

Findings from these studies have consistently shown mechanical loading such as tension, compression, or contraction effects transport. However, a majority of the studies in skeletal and cardiac muscle have focused on the specific role of metabolic activity-dependent transport and intracellular import of small metabolic substrates. Aslesen et al. have shown differential glucose uptake with increasing frequency of contraction in rat skeletal muscles with different metabolic demand [90]. Gissel et al. reported that skeletal muscle contraction increases sodium and calcium uptake [91], while Abraham et al. found that skeletal muscle uptake of potassium decreases with increasing rate of contraction [92]. Many groups have documented that contraction and mechanical activity in both skeletal and cardiac muscle increase glucose uptake [93-96]. Yet, no studies of this nature have investigated the pharmacokinetic influence of solely tissue architecture and mechanics. None have compared the influence of mechanical loading on transport in different muscle types, skeletal and cardiac, which differ in structural design and loading paradigm. Thus, there is a need for quantitative studies in skeletal and cardiac muscle to examine the role of mechanical loading in shaping the uptake and local retention of locally delivered drug. We sought to isolate the distinct transport and steric effects

presented by muscle architecture and mechanical dynamics on locally delivered drug and to derive the physiologic significance of these effects by correlation to functional parameters of the tissue.

1.2 Fundamental Thesis and Aims

The fundamental thesis of this work is that the functional architecture of muscular tissues impacts drug transport. The structure and mechanical function of muscle tissues may alter the pharmacokinetics and deposition of locally delivered agents independently of physicochemical and binding properties.

This work sought to elucidate a quantitative understanding of how the mechanical loading conditions, which depend on tissue architecture and function, present in skeletal and cardiac muscle affect the penetration and distribution of locally delivered drug. This work uses a systematic approach – starting with component events and building up to complicated phenomena – to study the unique pharmacokinetic and steric effects of intramuscular architectural configuration and mechanical loading, exclusive of specific binding interactions. Prior to quantifying the transport of proteins or specifically binding drugs, it is necessary to analyze the pharmacokinetics of an inert tracer such as dextran.

Both skeletal and cardiac muscles support dynamic mechanical loading conditions and are susceptible to pathologies such as ischemia that produce structural and mechanical dysfunction. However, each muscle type presents a distinct architectural environment and mechanical loading paradigm, which prompts the questions of:

1) "What is the role of uniaxial stretch and contraction on drug transport in linearly structured muscle tissue composed of longitudinally aligned fibers?"

2) "What is the role of multidimensional mechanical loading on drug transport in muscle whose structure is 3-dimensionally complex?"

A rigorous, quantitative schema was applied to address these questions experimentally in a rat animal model by investigating:

1) the transport effects of static and cyclic tensile loading, and contraction in soleus skeletal muscle, and then mathematically modeling these effects.

2) the transport effects of multidimensional ventricular distension and *in vivo* cardiac contraction, which are analogous to the static and contractile loading conditions in skeletal muscle.

Ultimately, a conceptual paradigm was formulated to elucidate the mechanistic underpinnings and physiologic significance of the impact of architectural configuration and its interaction with mechanical loading on drug transport in skeletal and cardiac muscle.

1.3 Background

1.3.1 Pharmacokinetics in Skeletal Muscle: Uniaxial Mechanical Loading

Drug transport after intramuscular delivery is thought to be affected by many physiological variables whose quantitative contributions to total absorption and therapeutic efficacy are not well understood [97]. Interstitial diffusivity, for example, is dictated by tissue architecture as well as binding site density, capillary permeability, and local blood flow. In dynamic tissues like skeletal muscle, intramuscular pharmacokinetics of growth factors can also be greatly influenced by mechanical loading, whose characteristics are largely dictated by muscle structure. As a result, both the

structure and mechanical function of muscle interact coordinately to influence drug transport.

The elongated muscle fibers in a skeletal muscle such as the slender fusiform soleus muscle are organized and bound together in a simple, uni-pinnated, parallel alignment (Figure 1.1), by a continuous network of supportive connective fibers containing both collagen and elastic fibers [98]. These intramuscular connective tissues provide lateral connection and support between parallel muscle fibers that extend throughout the entire length of the muscle. Their framework is structured into three discrete but interconnected sheaths that compartmentalize the muscle. The tough outer collagenous epimysium, composed mostly of collagen type I and a thin layer of type III, surrounds and enfolds the whole muscle as a functional unit. The epimysium extends smaller bundles of coarse collagen fibers inward to form a tough, thick perimysium. The perimysium, which is ubiquitously composed of both collagens type I and III, forms a network of septa that binds groupings of individual muscle fibers into functional bundles, or fascicles. As a result, the whole muscle is made up of many fascicles, with polygonal cross-sections (Figure 1.2). From the perimysium, thin partitions of delicate connective tissue extend into each fascicle to establish an endomysium that invests individual muscle fibers.

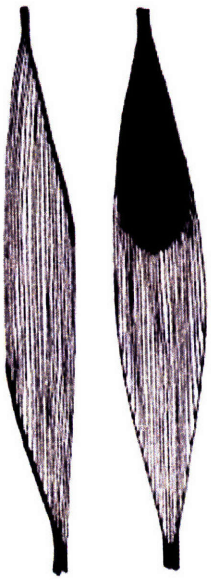

Figure 1.1. Uniaxial structure of soleus skeletal muscle.

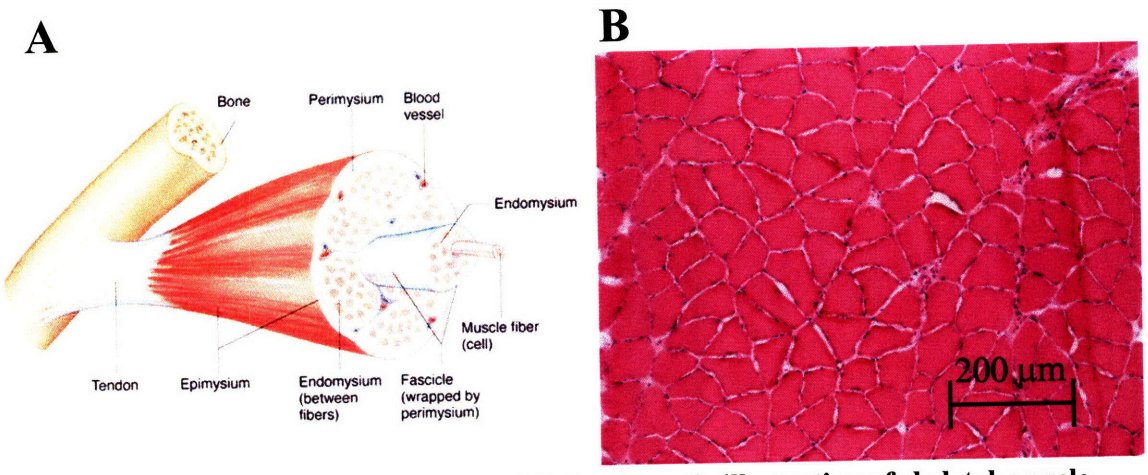

Figure 1.2. Skeletal muscle architecture. (*A*) A schematic illustration of skeletal muscle shows how it is compartmentalized by its connective tissue network. (*B*) A cross-section of rat soleus skeletal muscle, stained with Hematoxylin and Eosin, shows muscle compartments.

The endomysial connective tissue is composed mainly of collagen type III, with small random traces of type I and other types of collagen. Finally, the inner most layer of the endomysium, the basement membrane, lies immediately adjacent to the plasma membrane, or sarcolemma, of the muscle fiber. It consists of collagen type I, type III, type IV, and heparan sulfate proteoglycans [99]. Both the endomysium and perimysium

exhibit dense networks of collagen fibers that run in various directions, with no clear main orientation, during a relaxed muscle state. Endomysial fibrils run both longitudinally along the surface of muscle fibers and perpendicularly to them, forming connections between adjacent muscle fibers. Perimysial fibrils further wrap around muscle fiber fascicles to bind them to each other [100]. Thus, as a structural element, these connective tissue septa not only define the extracellular space and establish channels for transport, but also introduce barriers that hinder free passage of drug through this space. This general network of connective tissue also presents a spatially complex scaffolding of potential collagen binding sites that can localize delivered growth factors that are penetrating into the muscle. For example, intramuscular FGF has been found to be associated with the endomysial layer, likely bound to heparan sulfate proteoglycans and collagen [101].

This connective tissue network also serves to sustain the integrity of the muscle, and in turn can be affected by mechanical loading. The endomysium has been considered to be involved in both stress resistance and transmission of the active force of contraction. And, the perimysium is considered to distribute force associated with passive stretch along the muscle fiber. It also mediates lateral force transmission between fibers via shear while maintaining the relative position of the fibers [100, 102]. As a consequence of their mechanical role, the collagen fibrils in both the endomysium (Figure 1.3) and perimysium (Figure 1.4) are pulled from a normally non-specific orientation during muscle relaxation toward the circumferential direction during muscle

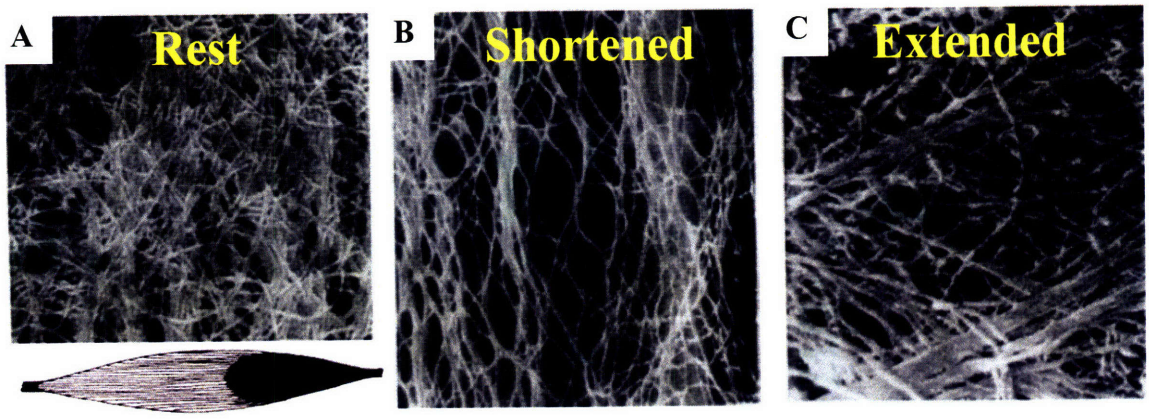

Figure 1.3. Distribution of collagen fibril orientations in the endomysium of skeletal muscle while (*A*) at rest length, (*B*) in a shortened state, and (*C*) in an extended state. SEM view (12,200×) in which the muscle fiber axis runs in the horizontal direction.

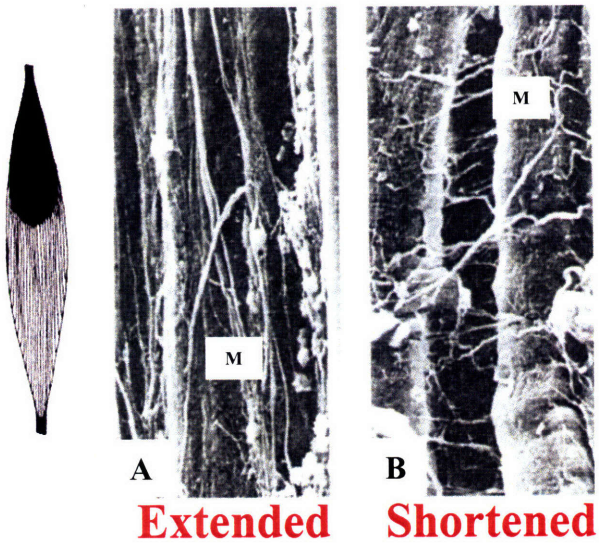

Figure 1.4. Collagen fibril orientations in the perimysium of skeletal muscle while (*A*) in an extended position and (*B*) in a shortened position. SEM view (1300×) in which muscle fiber, M, runs in the vertical direction.

shortening, or toward the longitudinal direction of the muscle axis during muscle lengthening [103-105]. As a result, such changes to connective tissue architecture brought about by mechanical loading may influence the permeability of the intramuscular interstitial space for the transport of drug.

Further mechanical loading effects such as intramuscular pressure and convective forces generated during muscle function and deformation can have an even greater influence on drug transport. Much of the deformation that occurs during either fiber shortening or lengthening results from fiber incompressibility, which keeps fiber volume constant and plays an important role in volume displacement. Consequently, lengthening results in flattening of the muscle and decrease in interstitial volume. Oppositely, contraction in a parallel-fibered muscle causes cytoplasmic volume displacement from the smaller end-regions of a fiber towards the middle region. This results in fiber angle changes at their attachment ends, forces and strains with significant perpendicular components, and a buildup of intramuscular pressure concomitant with cross-sectional bulging of the fiber and muscle [106]. Ultimately, the changes in muscle fiber cross-sectional area and internal pressure during either contraction or lengthening may be associated with water redistribution within the muscle and changes in interstitial space [107]. These changes can lead to convective forces that influence drug transport during muscle function.

Given the structure, constitution, and mechanical activity of skeletal muscle, it is reasonable to suspect drug transport is a function of not only physicochemical properties of the drug, but also tissue properties of the muscle. In particular, the complex material composition of connective tissue may lead to differential local retention of drug. This may induce large variations in drug concentration that can potentially be incompatible with achieving clinical efficacy. Ultimately, a major impact on drug distribution may come from mechanical loads that are intrinsic to the function of the muscle. Structural deformations associated with loading, such as those during passive stretch or contraction,

can alter the available interstitial space for drug uptake, intramuscular transport, and subsequent distribution. The dynamic forces, interstitial convective effects, and pressures generated by mechanical function can modulate the spatial and temporal characteristics of such drug distribution. This then raised the fundamental question of: "What is the role of uniaxial stretch and contraction on drug transport in linearly structured muscle tissue with longitudinally aligned fibers?" We sought to investigate the intramuscular penetration of locally delivered drug in skeletal muscles undergoing different mechanical loading conditions. Findings from this study may provide a quantitative scheme to tailor local delivery to skeletal muscle tissue and optimize drug deposition.

1.3.1.1 Static Tensile Strain

A quantitative evaluation of drug transport was conducted by examining the intramuscular distribution of drug that was applied from a delivery source at the muscle surface. Drug uptake was assessed from this distribution by quantifying the depth of drug penetration into the muscle from the surface. Intramuscular diffusion under these conditions is influenced by strain-dependent, structurally mediated, steric hindrance. Ultimately, this study determined how uptake, as quantified by penetration depth, was affected by the amplitude of **statically imposed tensile strain** on *ex vivo* soleus muscle preparations.

1.3.1.2 Cyclic Tensile Loading

A quantitative evaluation of drug transport in *ex vivo* soleus muscle undergoing cyclic mechanical loading determined how penetration depth and effective drug transport

were affected by the amplitude and frequency of **cyclic stretch**. In this case, the effective interstitial transport associated with dynamic loading is influenced by not only architecturally mediated steric hindrance, but also dynamic forces resulting from cyclic mechanical and structural loading. The contribution of these dynamic forces to effective transport were evaluated along with the effective diffusivity under static loading conditions to determine the impact of cyclic forces and dynamic structural deformations relative to mere structural resistance on interstitial drug transport.

1.3.1.3 Electrically Paced Contraction

Significant transport forces may be introduced during muscle contraction. Cyclic fiber shortening and relaxation can affect interstitial space and dynamic forces differently than cyclic elongation and release. Thus, this study determined how penetration depth and effective transport of drug in *ex vivo* soleus skeletal muscle was affected by electrically paced **contraction**. A comparison of transport associated with muscle shortening and contractile function to transport associated with stretch of passive muscle determined the significance of contractile compared to tensile loads on interstitial drug transport.

1.3.2 Pharmacokinetics in the Heart: Multidimensional Mechanical Loading

The practical realization of angiogenic therapy is bounded by concerns over limiting delivered growth factor concentrations in order to avoid both local and systemic side effect profiles. Since angiogenic growth factors can induce a destabilizing mitogenic response when exposed to neighboring atherosclerotic plaques, a primary concern when

delivering to the heart is to limit the local distribution of delivered proteins to the ischemic regions of the myocardium. Another concern when delivering to the heart is to avoid spillover into the systemic circulation upon exposure to coronary arteries or the intraventricular chamber. Moreover, as angiogenesis requires a tightly controlled exposure to physiologic levels of growth factors, an intimate understanding of the local pharmacokinetics in the myocardium is necessary. However, unlike the 2-dimensionally arrayed, linear architecture of skeletal muscle, heart muscle forms an elliptical chamber that is 3-dimensionally complex and has multiaxial mechanics. Thus, macromolecular transport in the heart is likely to be influenced by more complex loading conditions than those in the uniaxially loaded skeletal muscle, and remains very poorly understood.

Unlike the longitudinally aligned fibers in skeletal musculature, the myocardium is composed largely of tightly knit bundles of elongated muscle fibers, each composed of several cardiac muscle cells joined end-to-end or end-to-side in an interdigitating step-like manner by junctional complexes called intercalated disks (Figure 1.5). This manner of construct results in fibers that bifurcate longitudinally and connect with ends of adjacent fibers to form a complex, three-dimensional, branching network. Moreover, these knit cardiac bundles of fibers are wrapped together to form three major concentric layers in the cardiac wall, with each layer of fibers directed in a different orientation. The innermost layer forms the central portion of the left ventricle, and the outer two, which

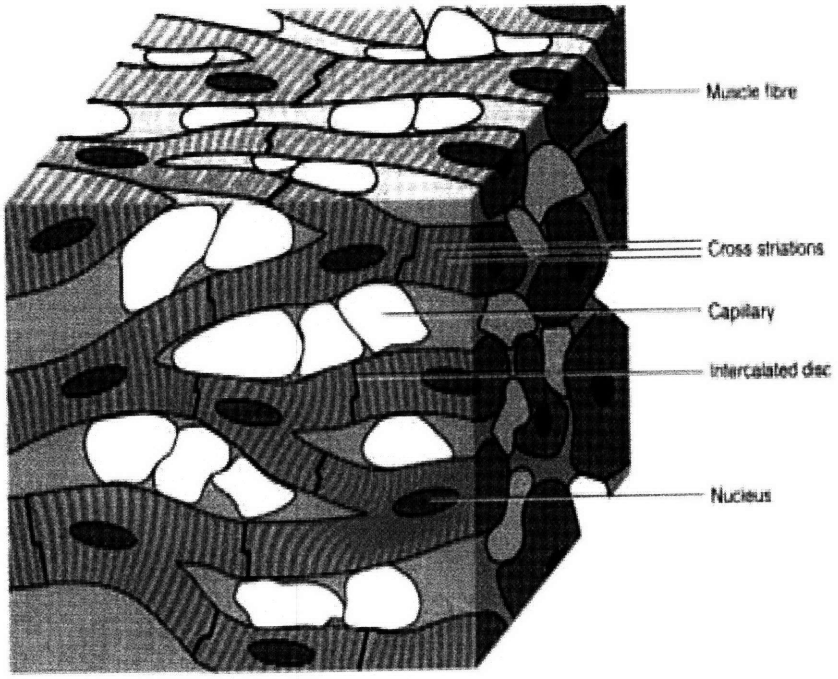

Figure 1.5. The branched myofiber network of the myocardium.

are oriented obliquely, wrap around to form the left and right ventricles. Yet, far from being discrete from each other, these layers are actually part of a contiguous strip that forms a left-handed helix in the subepicardium that progresses smoothly inward into a right-handed helix in the subendocardium. This orients the muscle fibers along figure-of-eight pathways. In the left ventricle for instance, the pattern is characterized by a train of muscle cells adjacent to the epicardium that spirals both apically and into the wall, past midwall to the endocardial side, and then spirals upon the inside past the equator, and past midwall to return back to the epicardial side. This completes the figure-of-eight by starting another figure-of-eight without actually joining it [108] (Figure 1.6) [109]. As a result of the winding circuit that these fibers take, a transmural section through the central region of a ventricular wall would show that the orientation of the muscle fibers tends to change. It would show an oblique muscle fiber orientation in the subepicardial region,

transverse orientation in the midwall, and a near vertical orientation in the subendocardial region. For an epicardially applied drug that is penetrating transmurally into the ventricular wall, such transitions in fiber orientation in these intramural sheets can introduce a local shift in mechanical loading and transport paradigm as the drug encounters each successive layer.

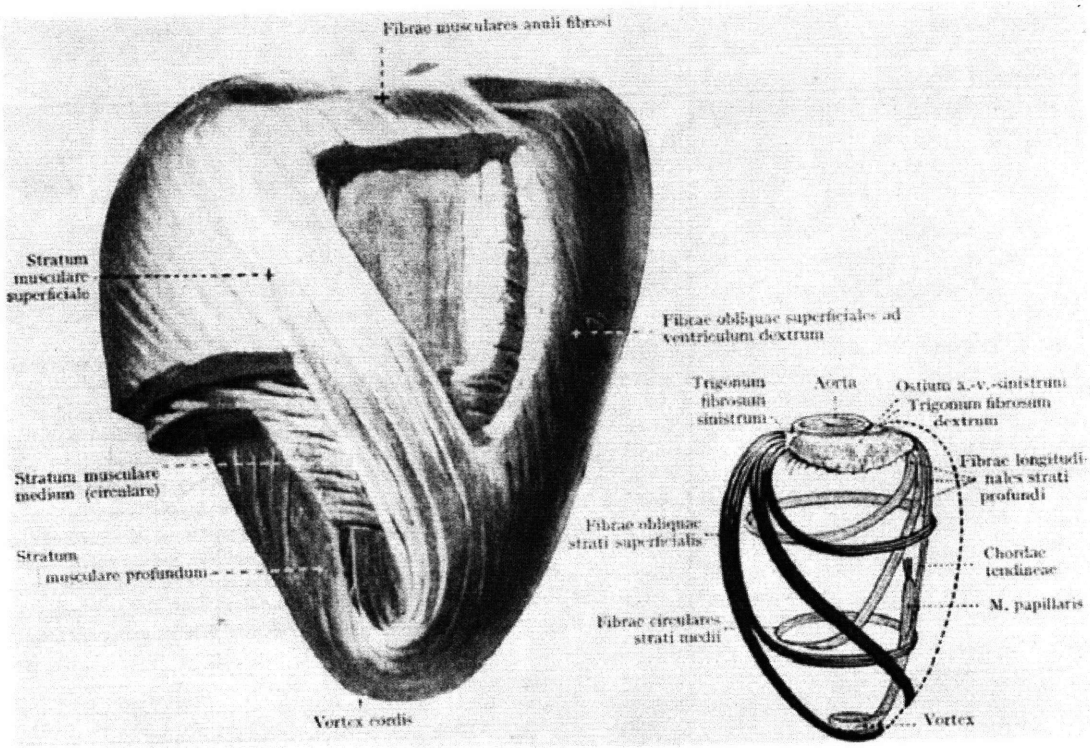

Figure 1.6. The course of left ventricular muscle fibers shown in a preparation of the human heart and as a schematic viewed from the dorsal aspect. The internal and external muscle investments of the ventricular chambers are composed of the same fiber bundles, which are strongly twisted at the apex and spiral in opposite directions towards the base. A transmural section through the ventricular wall shows that the twisting course of muscle bundles results in three major wall layers with different fiber orientations.

For another reason, penetration of drug past these myocardial fiber layers may not be as predictable as it would be if it were transporting simply past skeletal muscle bundles. This lies in the fact that the characteristically layered structural motif of myocardial tissue is comprised of multiple layers, each consisting of parenchymal and

supportive tissue bounded by mechanically protective and biologically functional "membranes." In particular, this refers not only to the fact that cardiac muscles fibers are bundled together by extracellular matrix, as with fibers in the soleus skeletal muscle, but also by the fact that cardiac muscle fibers tend to be organized transmurally into distinct layers, or laminae, of fibers separated by thin sheets of collagen. As there are relatively sparse muscle bridges between adjacent lamina, the demarcation between the layers of "collagen-muscle fiber-collagen" units is referred to as cleavage planes (Figure 1.7), which tend to open naturally upon dissection of the cardiac muscle [110].

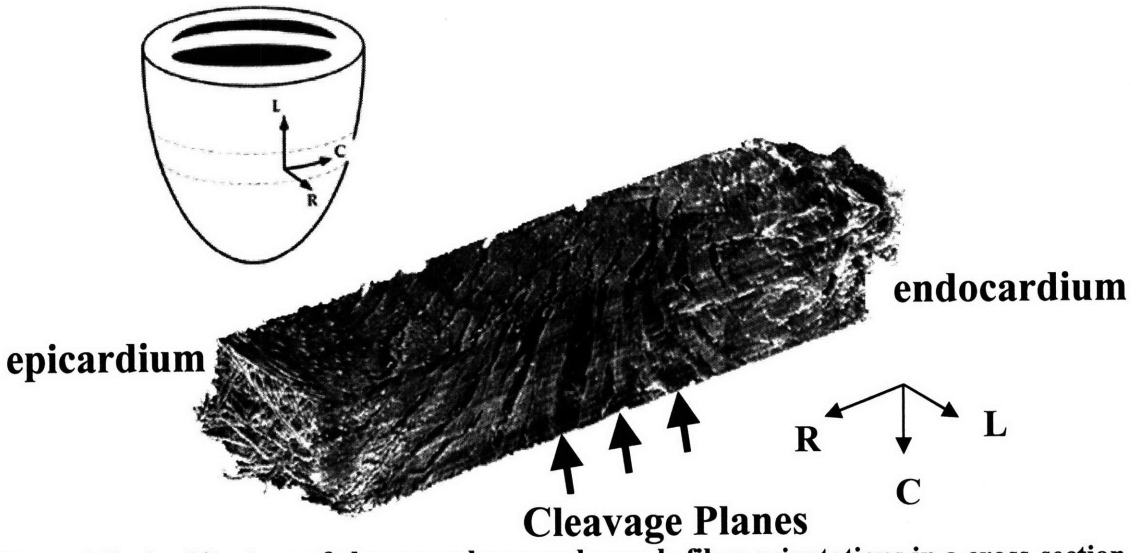

Figure 1.7. Architecture of cleavage planes and muscle fiber orientations in a cross-section through the ventricular wall.

Defined by these cleavage planes, the laminar organization of myocytes has approximately a radial (R) orientation when viewed from a longitudinal-radial cross-section. It becomes more longitudinal (L) in the subendocardial and subepicardial regions, with a pinnation pattern in the circumferential (C)-radial aspect. But regardless of orientation pattern, the myocyte axis in the subepicardium is always nearly tangential

to the epicardial surface [111]. Ultimately, these cleavage planes may serve to interrupt the transport of drug to downstream target sites, create local regions of drug accumulation, or channel the drug away along the extent of the cleavage space, thus preventing therapeutic agents from reaching ischemic targets.

In addition to architecture, the constitution of the heart may impact drug penetration into the tissue. In particular, the connective tissue network in the myocardium, as in skeletal muscle, exhibits sites that may potentially bind growth factor, localizing them and complicating their transport. The fibrous network of the heart is composed of collagen types I and III. And, the basement membrane of the cardiomyocytes contains collagen type IV, laminin, fibronectin, and heparan sulfate proteoglycans. The connective tissue serves to anchor the origin and insertion of muscle fibers, support vascular tissues, and absorb the effects of stretch before they are transmitted to myocytes. The convoluted collagen cords of the connective tissue network increase in density near the epicardial and endocardial surface, where they join a delicate sub-layer of collagenous tissue, and lie on top of a more robust fibro-elastic layer. The perimysial connective tissue in the ventricle consists of large and small spring-like, helically-coiled fibers that are arrayed parallel to the long axis of myocytes in the interstitial space. These fibers serve to interconnect fascicles of myocytes as well as whole mural layers between their extensive cleavage planes. The connective tissues forming the endomysial network, which also consists of elastin and fibronectin, connect adjacent muscle cells, wrapping them in complex pericellular weaves [112]. Thus, as in skeletal muscle, the connective tissue network may serve to bind drug and lead to local concentration gradients. For example, the collagenous and robust fibro-elastic layer

beneath the epicardial surface may localize drug while limiting its initial mural penetration.

Ultimately, the connective tissue network may act under the influence of mechanical loading to modulate drug transport. The interplay of these structures with waves of space-dependent strain during ventricular dilation presents a formidable challenge to studying drug uptake in the myocardium. The coiled fibrous networks, which are anchored at both the fibrous annulus and the apex, undergo progressive straightening of the tightly coiled configuration as the ventricular wall is stretched during filling with increasing ventricular cavity pressures. However, there is a spatial variation to this because they undergo straightening in only focal regions at low pressures, and generalized straightening and disruption at the highest pressures, while exhibiting the most pronounced changes in the mid-ventricle. This suggests that the mid-ventricle is the most susceptible to bulging associated with increased cavity pressure. And, collagen fibers in epicardial regions undergo more straightening than collagen fibers in endocardial regions, as expected from the curved shape of the heart [113]. Furthermore, the layered motif of the ventricular wall plays an integral part in its mechanics. With increasing intraventricular pressure, connective tissue struts and strut-like fibers between ventricular laminae are stretched from a perpendicular orientation to a co-alignment with muscle fibers. However, the contiguous struts within an individual lamina that join individual myocytes are often slackened during ventricular filling. This stretching and disruption of connective tissue fibers between layers of the ventricular wall permit slippage of mural layers relative to each other, accounting for a major portion of the mural thinning that occurs during ventricular filling [114].

Moreover, spatially distributed effects of contraction may have a profound effect on drug transport. During systolic contraction, in which simultaneous contraction of adjacent muscle fibers is mediated by their intercalated disk junctions, significant transmural gradients in wall strain occur in order to produce a contraction of the ventricular chamber that favors longitudinal over circumferential chamber shortening. The direction of the helically oriented left ventricular myofibers, which is maintained by the extensive collagenous network supporting the myocytes, is also affected to some degree by contraction – changing about 20 degrees in the transition from diastole to systole at any transmural position. In particular, because of the transmurally rotational splay of muscle fibers, the coordination of global contraction elicits a great deformation. This deformation occurs in a direction of shortening that is not aligned with the axes of local myofibers to result in an overall torsional effect on the ventricular chamber. And, although fiber direction and shortening direction are not substantially different in the epicardial half, they are virtually orthogonal to each other in the endocardial half of the ventricular wall. Therefore, the structural changes that occur during contraction are the result of various processes. These involve not only volume-conserving axial shortening of individual muscle fibers that cause cross-sectional shape changes of both myofibers and the interstitium, but also reorientation of the helically oriented myofibers that is accompanied by shear and extension of the transmural laminar sheets. These processes ultimately result in planar circumferential compression, especially in the inner half of the ventricular wall. This compression contributes to the unidirectional radial lengthening deformation, or mural thickening, of the ventricular wall that provides the powerful mechanism for ejection during contraction [115-121].

The multi-oriented branching fiber arrangement, the transmural variation in fiber orientation, and the laminar myofiber architecture in the heart all contribute to create the dimensionally complex deformations that occur during cyclic myocardial function. The characteristic results of torsion during chamber wall contraction followed by torsional recoil during relaxation generate a heterogeneous distribution of strains in the ventricular wall and non-axial strains across muscle fibers with every heartbeat. And ultimately, the significant mural thickening and thinning during the contractile cycle introduces a distinct dimension of transport forces oriented along the direction of transmural penetration. As this complex mechanical loading paradigm presents a dramatic contrast to the uniaxial effects found in skeletal muscle, drug delivery in the heart faces a uniquely different transport environment. This then raised the question of: "What is the role of multidimensional mechanical loading on drug uptake and transport in muscle, and how does this compare to transport in muscle of uniaxial loading pattern?" Another question was whether transport of drug in a multiaxially loaded environment could be extrapolated from a summation of the transport behavior in a uniaxially loaded environment. Using a simplified model to answer this question, we elucidated to a first approximation how ventricular dilation, contractility, and heart rate affected the penetration depth and transport of epicardially delivered drug. Findings from this study may provide a better understanding of how pharmacokinetics in the heart differs from that in skeletal muscle.

1.3.2.1 Ventricular Distension

Multidimensional strains presented by the rotationally splayed laminar architecture of myofibers in the heart during systolic ejection and diastolic filling of the

ventricular chamber may complicate intramuscular drug transport. Such transport may differ from that influenced by only uniaxial loads. Thus, this study determined how penetration and effective transmural diffusivity of both inert and specifically binding drug in the myocardium were affected by the amplitude of statically imposed **ventricular distension**. A comparison between drug penetration in uniaxially stretched skeletal muscle and volumetrically loaded ventricular myocardium elucidated the unique pharmacokinetic effects and physiologic significance of tensile strains applied to different structural paradigms.

1.3.2.2 *In Vivo* Cardiac Contraction

As in skeletal muscle, cyclic mechanical loading can introduce cyclic architectural deformations that result in dynamic forces and interstitial space variations. However, in ventricular myocardium, loading patterns are multidimensionally complex and often directed non-axially along muscle fibers. Mural thickening presents a further dimension of mechanical loads in the direction of drug penetration. These effects may transform the ventricular mural muscle into a significantly complex transport environment. This study determined how drug penetration and effective transport were affected by **heart rate and contractility**. Findings from this study may provide an understanding of how multidimensional contraction impacts transport.

2. STRUCTURAL BIOMECHANICS MODULATE INTRAMUSCULAR DRUG DISTRIBUTION: A BIOMECHANICAL LOADING SYSTEM

2.1 Abstract

Introduction: As local drug delivery continues to emerge as a clinical force, so does understanding of its potentially narrow therapeutic window. Classic molecular transport studies are of value but do not typically account for the local nature of drug transport or the regional dynamic function in target tissues like muscle that may undergo cyclical and variable mechanical motion and loading. We examine the impact of dynamic architecture on intramuscular drug distribution.

Methods and Results: We designed a tissue mounting technique and mechanical loading system that uniquely enables pharmacokinetics investigations in association with control of muscle biomechanics while preserving physiologic tissue architecture. The system was validated and used to elucidate the influence of architecture and controlled cyclic strain on intramuscular drug distribution. Rat soleus muscles underwent controlled deformations within a drug delivery chamber that preserved *in vivo* physiology. Penetration of 1 mM 20 kDa fluorescein isothiocyanate (FITC)-dextran at planar surfaces of the soleus increased significantly from 0.52 ± 0.09 mm under 80 min of static (0%) strain to 0.81 ± 0.09 mm under cyclic (3 Hz, 0-20% peak-to-peak) strain, demonstrating the driving effect of cyclic loading on transport. Penetration at curved margins was 1.57- and 2.53-fold greater than at planar surfaces under static and cyclic strain, respectively, and was enhanced 1.6-fold more by cyclic strain, revealing architecturally dictated spatial heterogeneity in transport and modulation of motion dynamics.

Discussion: Architectural geometry and dynamics modulate the impact of mechanical loading on local drug penetration and intramuscular distribution. Future work will use the biomechanical test system to investigate mechanisms underlying transport effects of specific loading regimens. It is hoped that this work will initiate a broader understanding of intramuscular pharmacokinetics and guide local drug delivery strategies.

Keywords: Mechanical; Strain; Muscle; Delivery; Transport

2.2 Introduction

Muscle tissue presents an exclusive drug transport environment in which dynamic mechanical motion and loading may be a predominant influence on the pharmacokinetics of locally delivered agents. These motions and loads, which are shaped by both structure and function of the muscle, can present significant and variable physical influences on aqueous drug transport by means of their effect on modulating extracellular space or fluid distribution [122].

The effects of mechanical loading on transport of local agents have been investigated in a variety of load-bearing tissues. Studies have examined the effects of tension-compression on solute and dextran transport in cartilage [78, 123], static tensile loading on diffusion of water in Achilles tendon [77, 124], and stretch on transmural transport of albumin, LDL, and Evans Blue in the arterial wall [76, 125]. Similar studies in skeletal muscle have investigated the impact of contraction on total uptake of glucose [94, 96]. However, no studies have investigated the interrelated effects of architecture and mechanical loading on the regional distribution – not just volumetric uptake – of

local agents in skeletal muscle. With the advent of local drug delivery to contractile tissues, and the present clinically motivated need for effective strategies to locally deliver therapeutic angiogenic growth factors to ischemic muscles [126], a quantitative knowledge of the pharmacokinetics in muscle is critically important. Thus, the goal of this study is to elucidate the combined influences of architecture and dynamic mechanical loading on the regional distribution of aqueous drug in skeletal muscle.

A tissue mounting technique and biomechanical loading system were designed to investigate intramuscular distribution of locally delivered drugs in association with control of muscle biomechanics. The preparation uniquely enables muscles to be secured in a natural, physiologic configuration and undergo *in vitro* mechanical testing while incubated in drug under functionally viable conditions to preserve accurate drug transport.

2.3 Tissue Handling and Mechanical Loading System

2.3.1 Surgical Isolation Protocol

Experiments were conducted within the animal welfare regulations and guidelines of Massachusetts. Male Sprague-Dawley rats (450-470 g) were administered 1000 U of Heparin via intraperitoneal injection 5 min prior to euthanasia with inhaled CO_2. Thoracotomy was performed immediately after euthanasia, and 60 ml of Krebs-Henseleit-Butanedione Monoxime (KH-BDM) (118.1 mM NaCl, 4.7 mM KCl, 2.5 mM $CaCl_2$, 1.2 mM $MgSO_4$, 1.2 mM KH_2PO_4, 25 mM $NaHCO_3$, 11.1 mM Glucose, supplemented with 1 mM Sodium Pyruvate, 1 mM Isoleucine, 1 mM Leucine, 1 mM

Valine, and 5 mM BDM, pH 7.4) oxygenated with 95% O_2-5% CO_2 was infused down the aorta to relax and preserve the lower extremities.

The soleus was surgically exposed in one of the distal hindlimbs. The tendons of overlying muscles at the tuber calcanei and fibular head were dissociated from the tendons of the soleus. The *in situ* length of the soleus was measured using a Mitutoyo Digimatic caliper with ± 0.01 mm precision between the proximal and distal myotendinous junctions while flexing the knee and ankle at 90°. This *in situ* length is referred to as *nominal* length. Because rats were selected in a narrow weight range, all soleus muscles were of uniform size and measured 28 mm in nominal length. The soleus was isolated from surrounding fascial connections and tissues, and resected with its tendons and segments of the calcaneus and fibula still intact.

During isolation, the soleus was regularly superfused with KH-BDM to prevent drying. Surgical isolation was repeated for the contralateral soleus while the excised soleus was held at nominal length in KH without BDM that was oxygenated and chilled on ice. After excision, soleus samples equilibrated in KH for at least 15 min before mechanical loading.

2.3.2 Mounting Configuration

A mounting technique and associated mechanical loading system were invented to investigate accurate intramuscular drug transport under mechanical loading. The excised whole muscle is secured onto specially-designed mounting blocks by inserting its intact bone segments into angled slots in the blocks (Figure 2.1). The slots secure the bone segments by mechanical fit and leverage to hold them at an acute angle to the muscle axis

without using additional fastening mechanisms that physically disrupt the soft tissues and could result in drug transport artifacts. The innovation of the blocks and mounting configuration is that they hold a muscle sample in an *in situ* configuration via its own

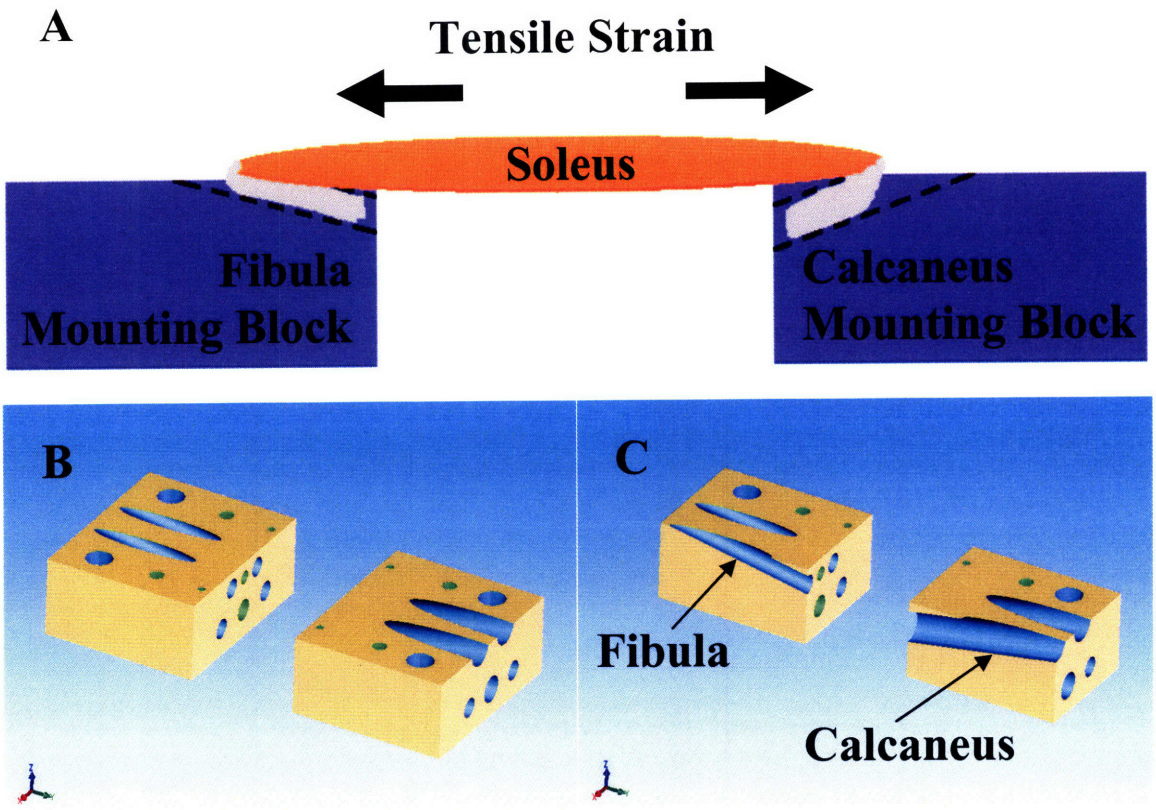

Figure 2.1. Mounting configuration and blocks. (*A*) Mounting configuration of an isolated soleus muscle and its natural bone attachments in the mounting blocks. The angled slots are sized specifically for either the calcaneus or fibula to secure the respective bone segments without using traditional mounting techniques such as sutures, hooks, clamps, pins, or other fixtures, which lead to tissue distortion, disruption of anatomic integrity and natural force transmission, and development of non-physiologic mechanical properties that could result in drug transport artifacts. (*B*) Solidworks design and rendering of the mounting blocks. (*C*) Cross-sectional view of the mounting blocks showing the internal course of the angled slots through the blocks (*arrows*). The two Lexan blocks of equal size each have two primary through-holes that run at a 10° angle from the top surface of the block to serve as mounting holes for bone segments.

physiologic attachments, and allow forces to be transmitted from the bones through the muscle in a physiologic manner to preserve the natural physical dimensions of the

muscle. The mechanical loading system consists of two major components: mounting blocks and a dynamic loading system.

2.3.3 Mounting Blocks

The conjugate mounting blocks can be secured in a static mounting assembly as a standalone device to impose static tensile strain on a pair of mounted muscle samples (Figure 2.2).

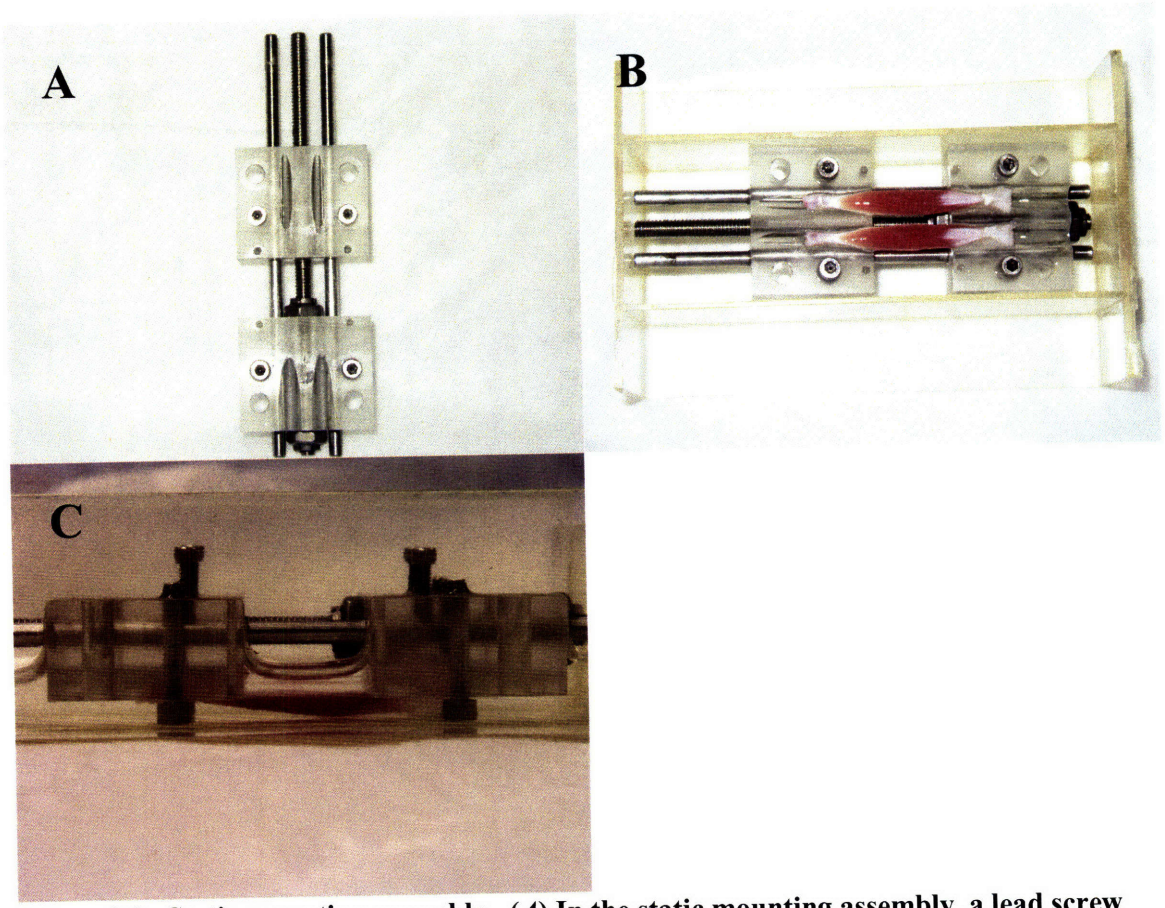

Figure 2.2. Static mounting assembly. (*A*) In the static mounting assembly, a lead screw adjusts the separation distance between the conjugate blocks. Set screws lock each block at a user-defined fixed position along the guide-rails. (*B*) Static tensile strain can be applied to a pair of mounted soleus muscles while they incubate in oxygenated drug source. (*C*) The simple mounting method allows muscles to incubate in a minimal volume of solution to conserve drug source and avoid the use of excessive, suprapharmacologic doses in transport studies.

The assembly enables samples to be stretched while incubated in drug solution. The blocks can be disengaged from the static assembly and individually attached onto the dynamic loading system to serve as mounting fixtures that hold samples in a physiologic configuration for dynamic tensile loading (Appendix A & B).

2.3.4 Dynamic Loading System

The dynamic loading system enables automated, oscillatory, linear strains to be imposed on mounted samples while they incubate in drug solution (Figure 2.3) (Appendix A & B). Mechanical loading is driven directly by a *LinMot®* *P01-37x240/60x260* linear servo motor that can achieve a peak force, velocity, and acceleration of 72 N, 0.45 m/s, and 8.5 m/s^2, respectively (Appendix C). Motor position is tracked by an internal sensor with 20 μm resolution and controlled by proportional-integral-derivative (PID) logic that enables execution of a 0.7 mm peak-to-peak displacement with ± 60 μm positional error (Appendix D). Total mechanical compliance of the series combination of motor, rack and pinion assembly, and mounting blocks is less than 0.0057 ± 0.002 mm/N and linear over a 75 N force range. This enables more precise force transmission than other systems developed to apply high frequency vibrations concurrent with larger amplitude elongations, which have 2.5- to 116-fold greater compliance [127-130]. All static and dynamic strains in our experiments were applied using the static and dynamic loading assembly, respectively.

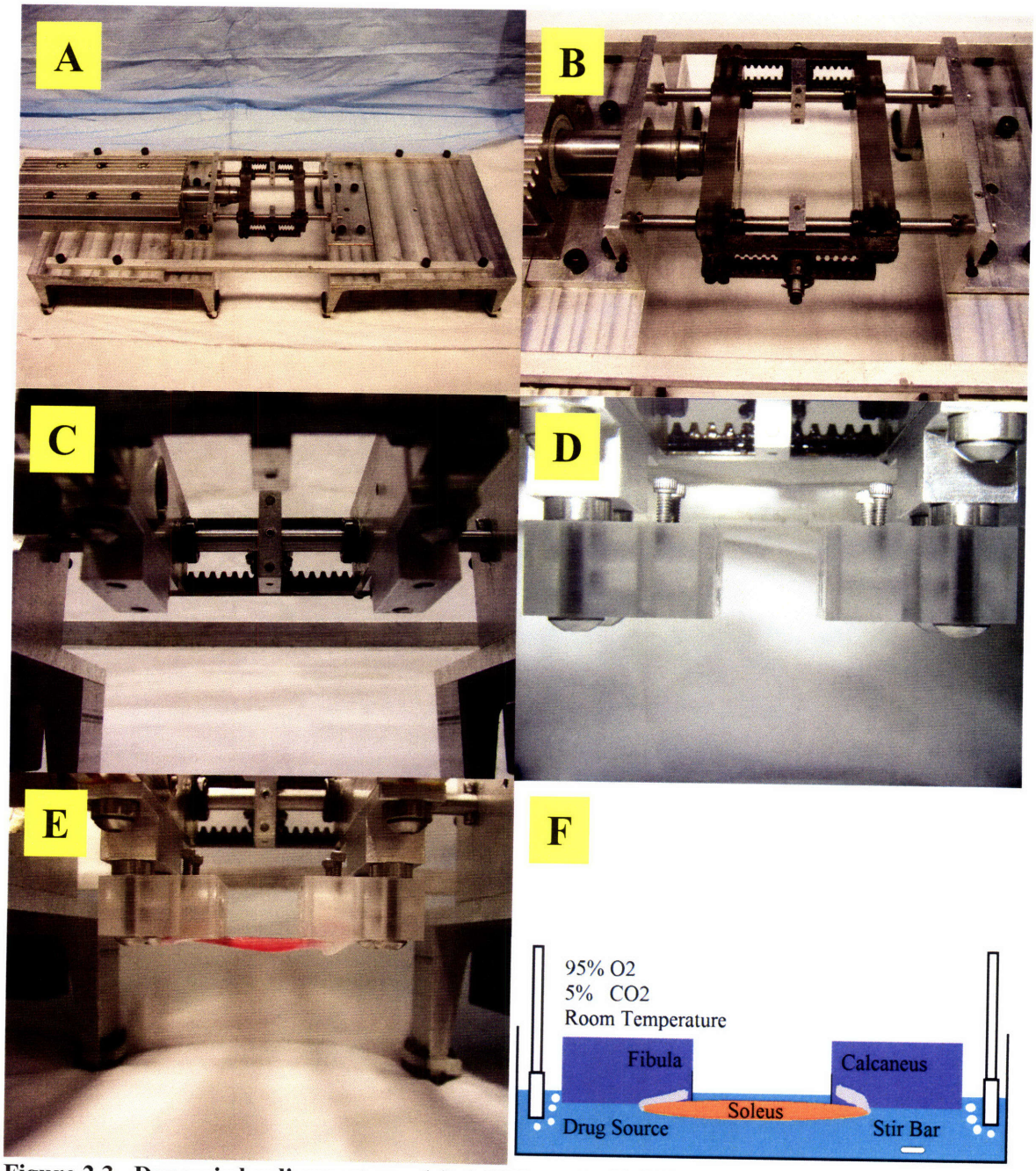

Figure 2.3. Dynamic loading system. (*A*) A PID-controlled linear servo motor actuates dynamic loading. (*B*) The dynamic mounting assembly incorporates a rack and pinion arrangement that enables the symmetric and simultaneous displacement of the ends of mounted tissue samples to impose strain. (*C*) A connecting block offsets the mounting block from the dynamic assembly to enable mounted samples to be submerged in solution during cyclic mechanical loading. (*D*) The dynamic mounting assembly with mounting blocks attached. (*E*) Mounted soleus muscles. (*F*) In the experimental setup, mounted samples are stretched either statically or dynamically while incubated in well-mixed and oxygenated drug solution at room temperature under architecturally physiologic and functionally viable conditions.

2.4 Methods

2.4.1 Force-Length Relationships

Using a reconfigured static assembly (Figure 2.4), individual muscles ($n = 7$) were pre-strained to 0%, 5%, 10%, 15%, and 20%, and stimulated to produce isometric twitch contractions using a biphasic stimulus (15 V, 50 ms pulse) applied to opposite tendons using stainless steel electrodes. Passive and total tensions were measured. Active twitch force was calculated by subtracting passive from total tension. Between recordings, samples incubated in oxygenated KH. Assessment of *in vitro* viability demonstrated samples maintained a minimum isometric twitch force of 0.19 N for at least 2 h and contractile activity at 3 Hz for at least 1 h, thereby validating our choice of the soleus as our experimental muscle model for its fatigue resistance characteristics.

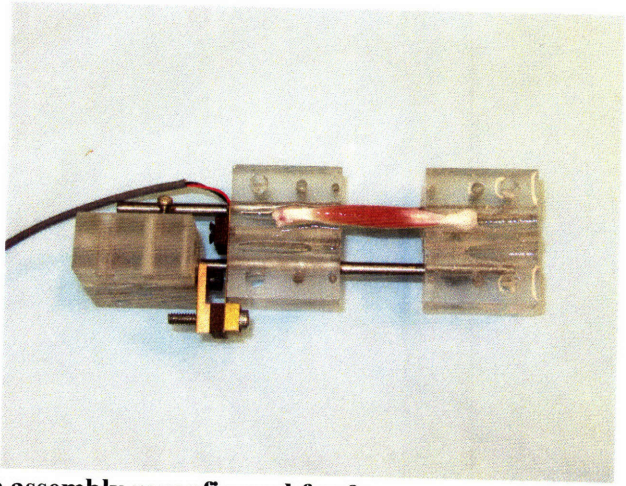

Figure 2.4. The static assembly reconfigured for force measurement. A thin-beam load cell (Omega Engineering, Inc., LCL-227G, 0-227 g) secured to one of the guide-rails was attached to the fibula mounting block, which was allowed to slide freely on the rails. The calcaneus block was fixed to the guide-rails. Electric stimulus was generated and force measurements were recorded using a National Instruments DAQPAD-6062E data acquisition board controlled by LabView 7.0.

2.4.2 Drug Transport

Soleus muscles ($n = 5$) were continuously, cyclically stretched between 0% and 20% strains at 3 Hz. Controls ($n = 5$) were held fixed at 0%. Samples were loaded for 80 min while incubated in 16 ml of 1 mM 20 kDa neutrally charged fluorescein isothiocyanate (FITC)-dextran (Sigma-Aldrich) in KH. Drug source was kept well-mixed by magnetic stir bar and oxygenated at room temperature, which is optimal for maintaining physiologic stability and functional performance of muscles *in vitro* [131-133] without inhibition of drug binding or transport properties. Fluorescence intensity of the bulk source, sampled before and after an 80-min incubation using fluorometry, remained constant. Therefore, drug source concentration remained constant throughout incubations.

Preliminary histologic assessment of tissue porosity (ratio of extracellular space area to total tissue area) demonstrated that permanent tissue degradation and injury was only a function of time and independent of mechanical loading conditions. Thus baseline architecture was consistent among all samples incubated for the same duration, and differences in extracellular transport [134, 135] of soluble dextran can be attributed to the dynamic influences of mechanical loading on architecture.

Preliminary transport studies validated the bulk uptake [136] and non-binding properties [135] of FITC-dextran in soleus tissue. Fractional volume of distribution, which defines an effective transport space reflecting the effects of both steric interaction and charged partitioning on soluble (not bound) drug distribution, was determined by the slope of the empiric relationship between equilibrium drug concentration in tissue versus the corresponding bulk source concentration. The fractional volume of distribution (ε),

defined as the ratio of the equilibrium tissue concentration of soluble drug (c_s) per unit total tissue volume (V_T) to bulk phase concentration (c_{bulk}): $\varepsilon = c_s / c_{bulk}$, reflects the partition coefficient, $\kappa_{tissue/bulk} = c_{tot} / c_{bulk}$ (where c_{tot} is the tissue concentration of soluble and bound drug in the accessible tissue volume), scaled by the ratio of the tissue volume accessible for drug distribution (V_a) to V_T (which represents sterical effects): $\varepsilon = \kappa_{tissue/bulk} \cdot V_a / V_T$ [137]. Equilibrium incubation studies demonstrated a fractional volume relationship that was linear over 0.1 μM–1 mM bulk concentrations with a slope of 84%, indicating bulk uptake of dextran. A fractional volume approximating 100% suggests minimal reduction of source concentration by charged partitioning or steric hindrance of dextran to freely diffuse throughout the muscle. Using an equilibrium distribution analysis [137] of the fractional volume relationship, bound fraction of dextran was calculated by subtracting c_s from the empiric tissue concentration. This demonstrated a spread about zero across the range of source concentrations, indicating that binding site density for dextran in the soleus was lower than the scatter in the data, and therefore insignificant. These transport characteristics and the *in vitro* stability of FITC-dextran [138, 139] enable investigation of transport that is unaffected by drug-tissue interactions and accurate demonstration of the isolated transport effects of tissue structure and mechanical loading.

2.4.3 Tissue Processing and Drug Measurement

After loading, samples were rinsed twice in 15 ml of fresh KH and snap-frozen at nominal length in -145°C Isopentane. 8 μm axial cross-sections from the midpoint of the samples were cut using a Leica CM1850 cryotome. FITC-dextran was imaged using

epifluorescence microscopy (Leica DMRA2, 50× magnification, Hamamatsu ORCA 286, Metamorph 6.3, ex: 450-490 nm bandpass/ em: 515 nm longpass). An exposure rate was chosen that eliminated tissue autofluorescence and avoided intensity saturation of the system by the drug source. Images were analyzed using Matlab. A preliminary calibration confirmed the linear relationship between image fluorescence intensities and tissue drug concentrations for 0.01 mM–1 mM bulk source concentrations of 20 kDa FITC-dextran. This is in accordance with Beer's Law for very low source concentrations, $I=\varepsilon CQ$, in which I is fluorescence intensity, ε is the molar absorption coefficient, C the molar concentration, and Q the quantum yield [140]. Drug distribution and unidirectional penetration were quantified in the muscle cross-section. Intramuscular penetration depth was defined as the perpendicular distance from the muscle surface at which fluorescence intensity decreased to 5% of the surface intensity (Appendix H).

2.4.4 Statistical Analysis

Results are presented as mean ± SD. Student's t-Test and Two-Factor Analysis of Variance (ANOVA) with Replication were applied to assess significance in force-length relationship and drug penetration data, respectively.

2.5 Results

2.5.1 Force-Length Relationships

The classic exponential curve characterizing the passive extensibility of skeletal muscle was observed (Figure 2.5). Active twitch tension demonstrated a classic parabolic increase, by 1.5-fold, to a maximum at 10% strain and fell off thereafter.

Nominal length corresponds to *initial* length and 10% strain the *optimal* length of the soleus. Peak twitch tension (0.35 ± 0.06 N) agrees with values measured by previous *in*

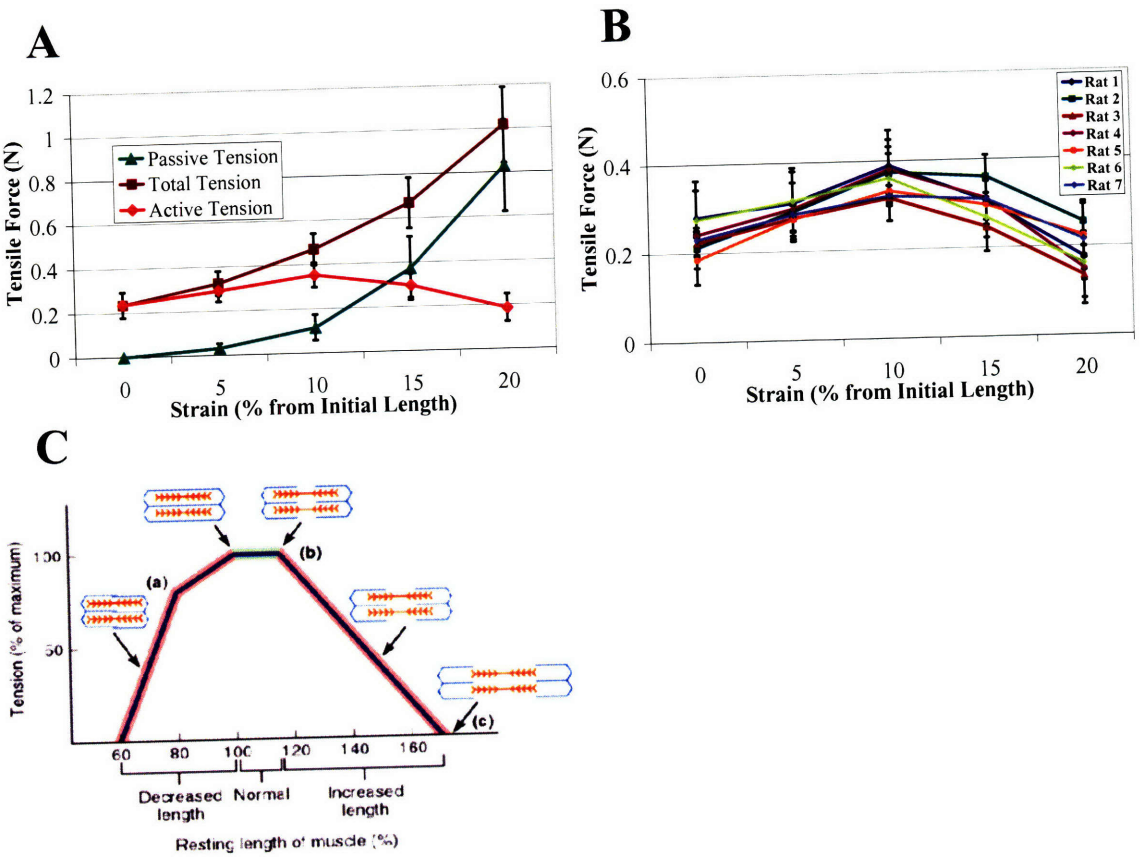

Figure 2.5. Force-length relationships of the soleus. (*A*) Total, active, and passive tensions of a single soleus muscle (n = 7). 0% strain is the nominal length, 5% strain is elongation to 105% of the nominal length, etc. Active twitch tension increases from 0.24 ± 0.06 N at 0% strain, to a maximum of 0.35 ± 0.06 N at 10%, and decreases to 0.19 ± 0.06 N at 20%. Twitch tensions measured at each strain in both the increasing and decreasing halves of the parabolic force-length relationship are statistically significantly different (T-test, $p<0.05$). Because the nominal *in situ* length, or 0% strain, is the length at which the first passive resistance to stretch occurs, it is equivalent to the *initial length* of the muscle. Maximal active force is developed at 10% strain, defining it as the *optimal* or *resting length*, L_o, of the muscle. Optimal length is the physiologically defined muscle length at which maximal active force is produced and reflects the optimal overlap of myosin and actin contractile myofilaments in the muscle. (*B*) Isometric twitch tension of 7 different single soleus samples, showing reproducibility of force measurements and consistency of muscle preservation in our drug delivery preparation. (*C*) Strain-dependent overlap of myosin (*orange*) and actin (*blue*) contractile myofilaments. Optimal overlap of myosin and actin at L_o, at which maximal muscle tension is produced, is depicted within the physiologic range of muscle lengths.

vitro (0.35 ± 0.02 N) and *in situ* (0.30 ± 0.10 N) studies using rats of similar size [141, 142]. Passive force (0.12 ± 0.06 N) at *optimal* length (10%) also agrees with previous findings (0.15 N) [142].

2.5.2 Drug Transport Under Mechanical Loading

Drug distribution and penetration was quantified at the planar and curved surfaces of the muscle cross-section (Figure 2.6). Two-Factor ANOVA revealed that while penetration (Figure 2.7) was equivalent at opposing surfaces with similar geometry ($p>0.05$), it was significantly impacted by differences in regional tissue geometry and architecture (penetration was 1.57- to 2.53-fold greater at curved than planar surfaces, $p<0.05$, under static and cyclic strain, respectively), as well as enhanced by cyclic strain ($p<0.05$). Dynamic loading interacted with regional architecture to enhance penetration at curved margins by 1.6-fold more than at planar surfaces ($p<0.05$).

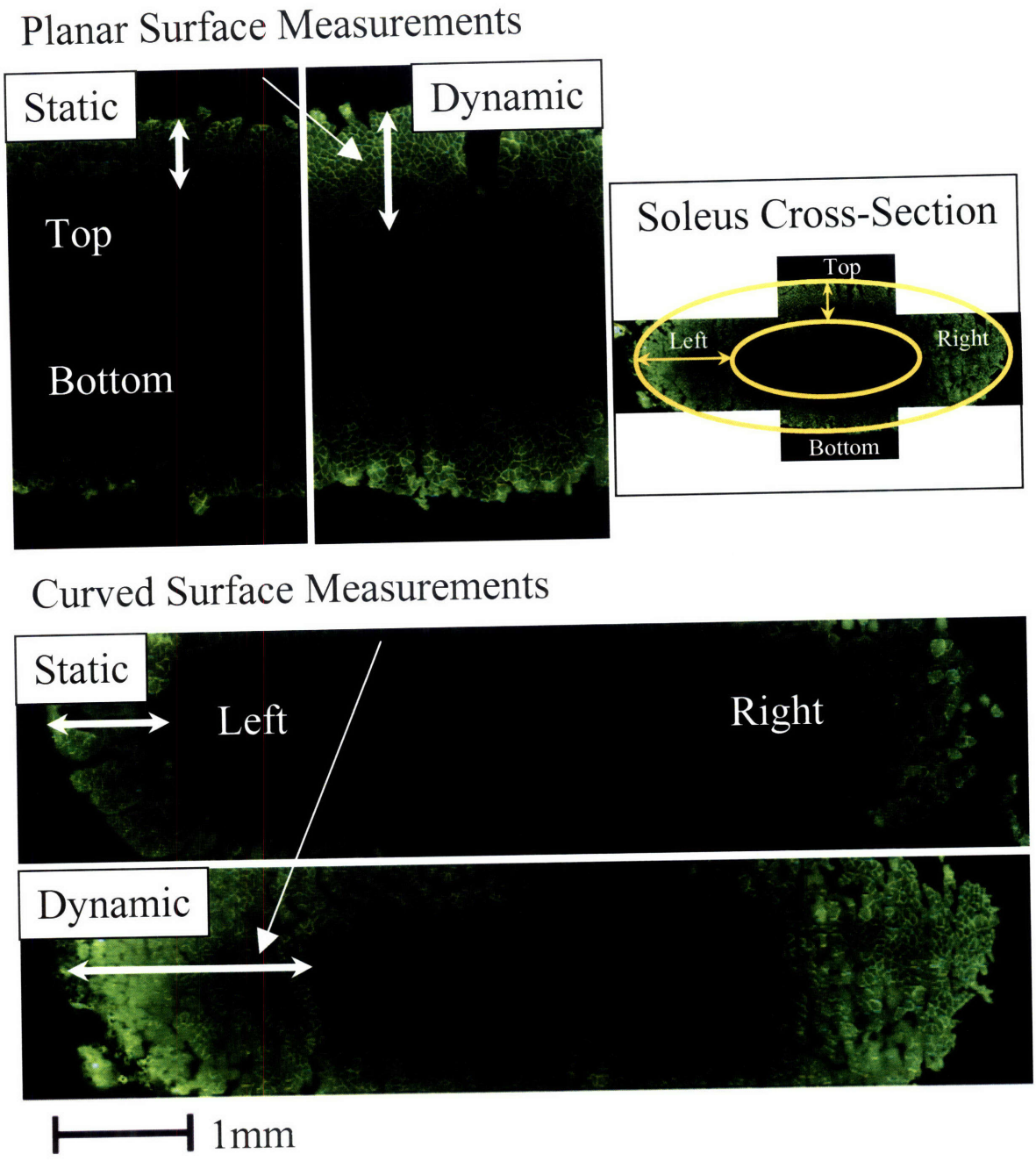

Figure 2.6. Quantification of fluorescent drug transport in statically and dynamically strained soleus. Fluorescence intensity values in images of the elliptical soleus cross-section were quantified using Matlab. Drug distribution was visualized and penetration depth was measured at the planar (*Top, Bottom*) and curved (*Left, Right*) surfaces. Planar surfaces are the dorsal and ventral surfaces, and curved surfaces are the medial and lateral margins of the muscle. Surfaces are referred to as top, bottom, left, and right based on their location in the images. Drug distribution is influenced by the regional geometry of the muscle surface. The impact of dynamic strain on drug distribution is modulated by local tissue geometry and architecture.

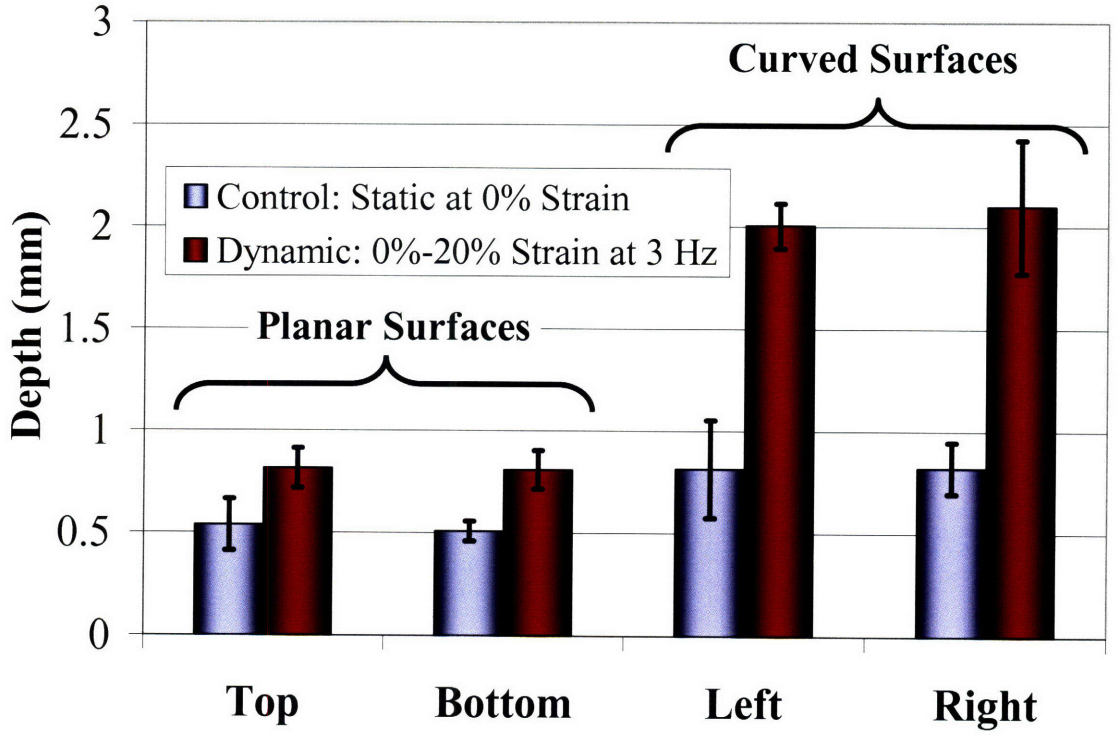

Figure 2.7. Impact of regional architecture and mechanical loading on drug transport. Penetration was equivalent at opposing planar surfaces for each loading condition, averaging 0.52 ± 0.09 mm under static strain and 0.81 ± 0.09 mm under dynamic strain. Similarly, penetration was equivalent at opposing curved surfaces, averaging 0.82 ± 0.19 mm under static strain and 2.1 ± 0.24 mm under dynamic strain. Penetration was significantly greater at curved than planar surfaces by 1.57- and 2.53-fold under static and dynamic strain, respectively. Penetration at both groups of surfaces was significantly enhanced by dynamic strain. Dynamic strain enhanced penetration at curved surfaces more than at planar surfaces by a factor of 1.6 – penetration increased by 1.56- and 2.51-fold at planar and curved surfaces, respectively.

2.6 Discussion

A quantitative knowledge of the impact of architecture and structural dynamics on local drug transport is critical to a complete understanding of intramuscular pharmacokinetics and pharmacodynamics. To date much work on intramuscular transport has focused on measuring volumetric changes in interstitial space or total tissue volume induced by strain or contraction using tritiated water [143]; molecular markers like inulin [143, 144]; albumin [145, 146]; or solutes like EDTA [145], sodium, and

potassium [122, 147]. Studies have measured contraction-induced diffusion of water [107] or myoglobin [82], but only intracellularly in single myofibers. While studies have investigated how strain or contraction in whole muscles affects total uptake of glucose [83, 84, 90, 94-96], lactate [148], phosphate [92], calcium [149, 150], and sodium [91], they focused only on the pharmacokinetic influence of activity-dependent metabolism on substrate uptake. Using and validating a robust mechanical loading preparation designed for local drug delivery in association with accurate biomechanical testing *in vitro*, this investigation visually quantified structural and mechanical loading effects on regional intramuscular drug distribution. The mounting preparation uniquely eliminated disruptive tissue handling artifacts and preserved physiologic architecture and force transmission to enable accurate drug transport while muscle samples underwent mechanical loading *in vitro*.

2.6.1 Transport Environment

As tendons exhibit minimal length extensibility within a physiologic strain range [151], the length range from 0% to 20% strain reflects the physiologic range of muscle function and viscoelastic extensibility. Drug transport within this range reflects the pharmacokinetic environment dictated by physiologic architectural configurations.

2.6.2 Intramuscular Pharmacokinetics

2.6.2.1 Regional Drug Distribution

Equivalent penetration at both sets of opposing surfaces suggests homogeneity of morphology for transport with respect to both the dorsal-ventral and medial-lateral

orientation. Assuming an isotropic transport environment based on histology, greater penetration at curved margins than at planar surfaces may result from both geometry of the curved surface and the edge effect on drug distribution occurring at the margins of a nearly flat muscle cross-section. Curvature of the margin results in a semi-circumferential exposure to drug, which increases the surface area and directionality for drug entry into a fixed tissue space. Furthermore, drug transporting from the margins readily encounters drug penetrating at planar surfaces due to the elliptical geometry of the cross-section. Thus, penetration at planar surfaces can contribute significantly to drug distribution at the margins, especially when penetration is enhanced at all surfaces by dynamic loading.

2.6.2.2 Impact of Dynamic Loading

In the absence of an external convective force driving bulk fluid flow into the muscle, and particularly as drug penetration proceeds against an increasing intramuscular pressure gradient [152] and decreased muscle volume [153] during stretch, enhancement of drug penetration by oscillatory loading is unlikely due to bulk convection. Cyclic strain may modify intramuscular accessible space, interstitial permeability, and transport kinetics. Dynamic loading between 0% and 20% strain may cyclically expose drug to strain-dependent architectural configurations with larger accessible volumes than that at nominal length. This may result from myofiber deformation, displacement, and thinning due to conservation of volume during elongation that increase tissue porosity. Cyclic increase in accessible space may create spatially and temporally heterogeneous concentration gradients that increase diffusional driving force. Interstitial permeability

may increase due to alignment of collagen fibers in their dense interstitial networks that form the endomysium and perimysium during stretch [103, 104], which reduces their screening effect on soluble drug [154]. Such changes may result in a greater time-averaged porosity and permeability that increases penetration.

The dynamics of oscillatory loading may impact transport kinetics by creating dispersive influences on soluble drug that increase transport beyond molecular diffusion alone [155]. Cyclic displacement and deformation of myofibers compress and expand extracellular space and impose normal and shear forces on interstitial fluid, resulting in pulsatile agitation of soluble drug in the absence of bulk convective fluid flow. Such pulsatile agitation can disperse or spread drug in a rate-dependent manner over a greater extracellular volume and thereby drive greater penetration.

2.6.2.3 Interaction Between Loading and Architecture

Greater enhancement of penetration at curved margins than at planar surfaces by dynamic loading may be attributed to spatially heterogeneous strain dynamics and heterogeneous extracellular space changes during stretch that are likely shaped by muscle structure and local geometry.

The uni-pinnated, parallel-fibered soleus has an elliptical cross-section that flattens and widens during muscle stretch. Studies of uni-pinnated muscle have revealed that they experience geometry changes during isometric contractions at various initial muscle lengths that consist of spatially heterogeneous changes in aponeurosis length, angle of pinnation of myofibers, and fiber length [156]. One study observed transverse (perpendicular to muscle surface) strains in superficial myofibers during isometric

contraction and aponeurosis surface area decreases with increasing initial muscle length [157]. It can be extrapolated from these studies, which assessed strains and geometry changes only from the muscle surface, that flattening and widening of the soleus resulting from conservation of muscle volume during elongation translate into heterogeneous internal fiber rearrangements and intramuscular forces that can alter local drug distribution space and dynamic dispersion effects. While superficial myofibers at planar surfaces tighten with muscle flattening, those at the curved margins of the soleus may experience increased outward transverse strains with widening. Furthermore, because superficial fibers at the margins occur more peripheral to the center of the muscle, they have more obtuse angles of insertion relative to the muscle axis compared to fibers at planar surfaces, which are located towards the midline. These differences in local muscle geometry, fiber arrangement, and angle of insertion likely dictate heterogeneous local strain dynamics and changes in extracellular space during stretch or contraction. These architectural and dynamic heterogeneities may result in greater porosity or dispersive effects at curved margins that significantly impact the heterogeneous drug distribution observed under dynamic stretch.

2.6.3 Conclusions

Dynamic loading increases drug penetration and impacts drug distribution based on the dictates of muscle structure and geometry. These findings yield broad implications for pharmacokinetics investigations and clinical drug delivery strategies to mechanically active target tissues, which should now consider the intimate interplay between tissue architecture and functional dynamics that underlies tissue

pharmacokinetics. Modulation of mechanical activity in muscle tissues may possibly serve as a physiological means for controlled drug delivery. A robust biomechanical testing preparation designed for drug transport studies was validated. Further pharmacokinetics studies using this system intend to investigate the mechanisms underlying transport effects of different mechanical loading regimens.

3. PHARMACOKINETICS IN SKELETAL MUSCLE: UNIAXIAL TISSUE ARCHITECTURE AND MECHANICAL LOADING

3.1 Abstract

Introduction: Dynamic tissue architecture and motion in mechanically active target tissues can influence the pharmacokinetics of locally delivered agents. We investigated drug transport in skeletal muscle under controlled mechanical loads.

Methods and Results: Static (0%-20%) and cyclic (± 2.5% amplitude, 0%-20% mean strains, 1 Hz-3 Hz) strains, and electrically paced isometric contractions (0.1 Hz-3 Hz, 0% strain) were applied to rat soleus while incubated in 1 mM 20 kDa FITC-dextran. Dextran penetration, tissue porosity, and active force-length relationship over 0%-20% strain correlated ($r = 0.9$-1.0), and all increased 1.5-fold from baseline at 0% to a maximum at 10% (L_o), demonstrating biologic significance of L_o, and impact of fiber size and distribution on function and pharmacokinetics. Overall penetration decreased but relative enhancement of penetration at L_o increased with drug size (4 kDa, 20 kDa, 150 kDa). Penetration increased linearly dependently (0.084 mm/Hz) with cyclic stretch, demonstrating dispersion. Penetration increased with contraction rate by 1.5-fold from baseline to a maximum at 0.5 Hz, revealing architectural modulation of dispersion. Impact of architecture and dispersion on intramuscular transport was computationally modeled.

Conclusions: Mechanical architecture and function underlie intramuscular pharmacokinetics and act in concert to effect biological resonance between optimal performance and drug uptake. Therapeutic management of characteristic function in all

tissue targets may enable a physiologic mechanism for controlled drug transport and efficacy.

Keywords: Muscle; Strain; Contraction; Porosity; Diffusion; Pharmacokinetics

3.2 Introduction

Mechanically active tissues such as skeletal muscle present a unique pharmacokinetic environment in which transport of locally delivered drug can be influenced by not only physicochemical interactions, but also dynamic architectural configurations and mechanical function. The continuous network of force-transmitting and connective perimysial and endomysial collagen fibers [99, 100, 102] between myofibers can hinder interstitial diffusion in a strain-dependent manner. Dynamic physical effects such as intramuscular pressure, fluid redistribution, and structural deformations [106, 107] during mechanical function can alter transport kinetics. Whereas local delivery strategies minimize systemic losses and enable efficient administration of therapeutic agents to target tissues [51, 158-160], ultimate drug distribution and pharmacologic effect are determined by target tissue pharmacokinetics.

Controlled release technologies must consider the transport effects of functional architecture and mechanical activity to optimize defined release kinetics [48, 161-163] for therapeutic effect. A quantitative understanding is critical for strategies like therapeutic angiogenesis to ischemic muscle, in which lesions are spatially focal [164], therapeutic windows are narrow [165-167], therapeutic response is complex [168-170], biologic half-lives of delivered proteins are short [50, 171-173], and systemic side-effects of therapies are detrimental [39, 44, 45, 54, 174].

Whereas studies have investigated how strain or contraction in whole skeletal muscles affects total uptake of glucose [83, 84, 90, 94-96], lactate [148], phosphate [92], calcium [149, 150], and sodium [91], they have predominantly elucidated the pharmacokinetic influence of activity-dependent metabolism on substrate uptake. We apply a rigorous, quantitative framework to investigate the characteristic and synergistic impact of architecture and mechanical forces on intramuscular transport of locally delivered soluble macromolecules. Having previously demonstrated that cyclic mechanical loading influences drug distribution based on the dictates of muscle geometry, we systematically investigate the transport effects of static and cyclic strain and isometric contraction, and their unique correlation with structure and function. We validate the mechanisms at hand through computational models.

3.3 Methods

3.3.1 Surgical Protocol

Experiments were conducted within the animal welfare regulations and guidelines of Massachusetts. Male Sprague-Dawley rats (450-470 g) were administered 1000 U of Heparin via intraperitoneal injection 5 min before euthanasia with inhaled CO_2. Thoracotomy was performed immediately after euthanasia, and 60 ml of Krebs-Henseleit-Butanedione Monoxime (KH-BDM) (118.1 mM NaCl, 4.7 mM KCl, 2.5 mM $CaCl_2$, 1.2 mM $MgSO_4$, 1.2 mM KH_2PO_4, 25 mM $NaHCO_3$, 11.1 mM Glucose, supplemented with 1 mM Sodium Pyruvate, 1 mM Isoleucine, 1 mM Leucine, 1 mM Valine, and 5 mM BDM at pH 7.4) oxygenated with 95% O_2-5% CO_2 was infused down the aorta to relax and preserve tissues of the lower extremities during surgery.

The soleus was surgically exposed in one of the distal hindlimbs. The tendons of overlying muscles at the tuber calcanei and fibular head were dissociated from the tendons of the soleus. The *in situ* length of the soleus was measured using a Mitutoyo Digimatic caliper with ± 0.01 mm precision between the proximal and distal myotendinous junctions while flexing the knee and ankle at 90°. This *in situ* length is referred to as the nominal length in our study, and was found to correspond to the *initial* length, the length at which the first passive resistance to stretch occurs. Because rats were selected in a narrow weight range, all soleus muscles were of uniform size and measured 28 mm in nominal length. The soleus was isolated from surrounding fascial connections and tissues and resected with its tendons and segments of the calcaneus and fibula still intact.

During isolation, the soleus was regularly superfused with KH-BDM to prevent drying. Surgical isolation was repeated for the contralateral soleus while the first excised soleus was held at nominal length in KH without BDM that was oxygenated and chilled on ice. After excision, soleus samples equilibrated in KH for at least 15 min before mechanical loading. For electrically paced groups, regular KH instead of KH-BDM was used in all parts of the protocol above.

3.3.2 Mechanical Loading and Drug Delivery

All static and cyclic strains were applied on pairs of whole soleus muscles using a mounting technique and mechanical loading system developed by our group, which enable static (fixed strain) or dynamic (cyclic) linear loading to be performed without artifactual injury or distortion of the soft tissues while samples are incubated in a drug

bath. For all loading conditions described below, soleus muscles were stretched according to their respective protocol for 1 h while incubated in 16 ml of 1 mM 20 kDa neutrally charged FITC-dextran (Sigma-Aldrich) in KH. Drug source was oxygenated with 95% O_2-5% CO_2, maintained at room temperature, and kept well-mixed by magnetic stir bar.

3.3.2.1 Static Strain

Soleus samples (n = 6) were held stretched to 0%, 5%, 10%, 15%, or 20% strain. In all loading conditions, 0% strain corresponds to nominal length, 5% strain corresponds to 105% of the nominal length, etc., (Figure 3.1*A*). 10% strain was found previously to correspond to the *optimal* length, L_o, the length at which maximal active force is generated. Samples (n = 6) were similarly stretched to 0%, 10%, or 20% strain and incubated in 1 mM 4 kDa or 1 mM 150 kDa neutrally charged FITC-dextran.

3.3.2.2 Cyclic Stretching

Soleus samples (n = 6) were cyclically loaded to sinusoidal strains with a fixed amplitude of 2.5% of the nominal length oscillating about mean strains of 0%, 5%, 10%, or 20%, at 1 Hz, 2 Hz, or 3 Hz frequencies (Figure 3.1*B*). Samples (n = 6) were also loaded at 1 Hz for 1 h, 2 Hz for 30 min, and 3 Hz for 20 min at both 0% and 5% strain.

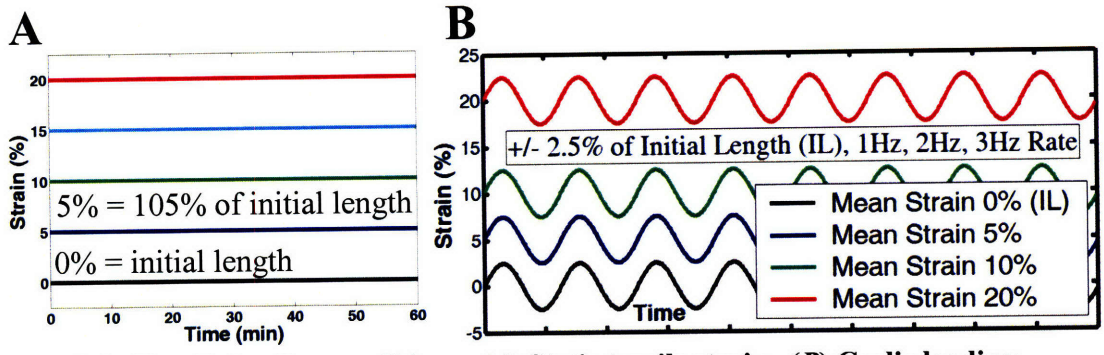

Figure 3.1. Tensile loading conditions. (*A*) Static tensile strain. (*B*) Cyclic loading.

3.3.2.3 Contractions

Soleus samples ($n = 6$) were continuously paced by electric field stimulation to produce isometric twitch contractions at nominal length at a rate of 0.1, 0.5, 1, 2, or 3 Hz. Biphasic electric stimulus (15 V, 50 ms pulse) was applied by 2 stainless steel foil plates situated in the drug bath at either end of the static loading assembly, spanning a separation distance of 10 cm. Stimulus was generated using a National Instruments DAQPAD-6062E data acquisition board controlled by the Arbitrary Waveform Generator virtual instrument in LabView 7.0 (Figure 3.2). A preliminary experiment investigated the transport effects of 1 Hz twitch contractions at nominal length after 2 h. Incubated samples produced a minimum isometric twitch force of 0.19 N for at least 2 h and maintained contractile activity at 3 Hz for at least 1 h, thereby validating our choice of the soleus as our experimental muscle model for its fatigue resistance characteristics.

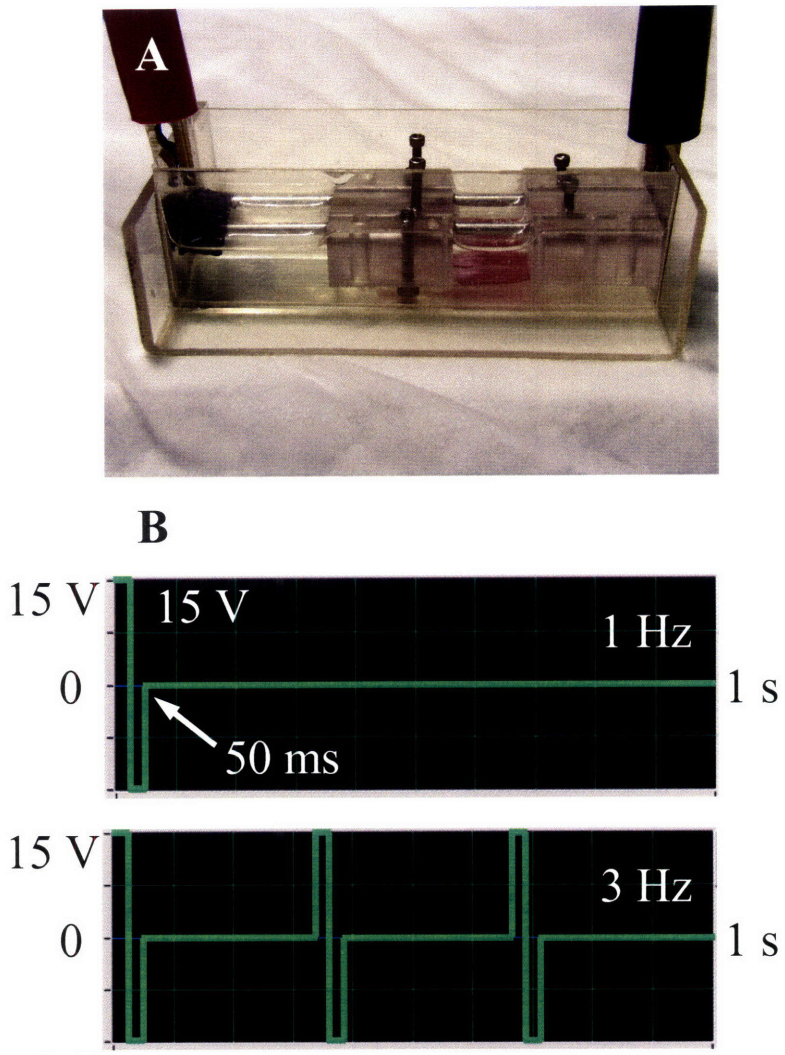

Figure 3.2. Electrically paced isometric contractions. (*A*) Soleus samples were rhythmically paced to elicit isometric twitch contractions by electric field stimulation. (*B*) Electric stimulus profile, showing pacing at 1 Hz and 3Hz, generated in LabView.

3.3.3 Tissue Processing and Measurement of Drug Transport

After loading, samples were rinsed twice in 15 ml of fresh KH and snap-frozen at nominal length in -145°C Isopentane. 8 μm axial cross-sections from the midpoint of the samples were cut using a Leica CM1850 cryotome. FITC-dextran was imaged using epifluorescence microscopy (Leica DMRA2, 50× magnification, Hamamatsu ORCA 286, Metamorph 6.3, ex: 450-490 nm bandpass/ em: 515 nm longpass). An exposure rate was chosen that eliminated tissue autofluorescence and avoided intensity saturation of the

system by the drug source. Images were analyzed using Matlab. A preliminary calibration confirmed the linear relationship between image fluorescence intensities and tissue drug concentrations for 0.01-1 mM bulk source concentrations of 20 kDa FITC-dextran. This is in accordance with Beer's Law for very low source concentrations: $I=\varepsilon CQ$, in which I is fluorescence intensity, ε is the molar absorption coefficient, C the molar concentration, and Q the quantum yield [140]. Unidirectional drug penetration at the planar surface of the muscle cross-section was quantified and analyzed. Intramuscular penetration depth was defined as the perpendicular distance from the surface at which fluorescence intensity decreased to 5% of the surface intensity. Effective diffusivity, D, associated with measured penetration depth was calculated based on the equation for diffusion in a semi-infinite solid, $D = \frac{x^2}{4 \cdot t \cdot (\mathrm{erf}^{-1}(0.95)^2)}$, where x is penetration depth, and t is the 3600 s duration of incubation. Effective diffusivity is used to describe the observed transport, which encompasses the impact of steric forces, potential specific and non-specific binding interactions within the tissue interstitium, and cellular internalization, in addition to the diffusive random thermal motion of solutes down concentration gradients.

3.3.4 Histology and Tissue Architecture

Soleus muscles ($n = 6$) were excised and immediately snap-frozen while held fixed at 0%, 5%, 10%, 15%, or 20% strain. 8 μm thickness axial cross-sections from the midpoint of the samples were cut and stained with Hematoxylin and Eosin (HE). Light microscopy images (100× magnification) were processed using CellProfiler [175], an image analysis program written in Matlab. Myofiber arrangement and distribution were

qualitatively assessed. Tissue porosity (φ, the ratio of interstitial space area between myofibers to total area), average myofiber cross-sectional area, and myofiber density (total number of myofibers per image) were quantified at each strain. Tissue degradation and injury were found to be only a function of time, thus baseline architecture was consistent among all samples incubated for the same duration, and differences in drug transport can be attributed to the distinct influences of mechanical loading.

3.3.5 Statistical Analysis

Results are presented as mean ± SD. Student's t-Test, Single Factor Analysis of Variance (ANOVA), and Two-Factor ANOVA with Replication were applied to derive significance in empirical transport results. Propagation of uncertainty in normalized data was calculated using the formula, $\frac{\Delta_z}{z} = \sqrt{(\frac{\Delta_x}{x})^2 + (\frac{\Delta_y}{y})^2}$, where Δ_x, Δ_y, and Δ_z is the standard deviation of the numerator (x), denominator (y), and normalized value ($z = x/y$), respectively.

3.3.6 Mathematical Model

3.3.6.1 Static Case

Intramuscular diffusion of soluble drug in the tortuous interstitial space between myofibers can be characterized as diffusion in a porous medium composed of an impermeable solid phase and a permeable fluid phase [176, 177]. A mathematical model used to evaluate effective diffusion in tumor cells [178] and brain tissue [179-181] was modified to derive the relationship between effective diffusivity and strain-dependent tissue porosity.

Diffusion of inert, soluble macromolecules like dextran in the interstitium is dictated by tissue porosity, φ, and interstitial fluid characteristics [178, 182]. Intramuscular effective diffusivity, D_{eff}, of drug was defined as:

$$D_{eff} = (D_1 \cdot D_2) \cdot D_w \quad (1)$$

where D_w is the free diffusivity of drug in water, and reducing factors $D_1 \cdot D_2 <= 1$. D_1 accounts for φ, fiber geometry, and arrangement and is independent of drug molecular weight. D_2 accounts for interstitial fluid characteristics and is independent of φ when drug size is considerably smaller than the interspacing between myofibers. Because the 3.2 nm hydrodynamic radius of 20 kDa dextran [183] used in our transport experiments is two orders of magnitude less than the 0.43 μm minimum interstitial spacing measured histologically in the soleus, and because interstitial fluid is assumed to be water *in vitro*, $D_2 = 1$. Thus, the dependence of D_{eff} on tissue porosity and fiber arrangement as they change with static muscle strain was investigated by modeling D_1.

Because the uniaxial soleus was exposed to constant drug source equally along its length during loading, drug transport in the radial, or cross-fiber, direction was investigated. D_1 was determined using a homogenization procedure on the diffusion equation within the tissue (Appendix E). Homogenization averages diffusion on the micro length scale of cellular structures to compute effective diffusion on the macro length scale of the entire tissue. This technique characterizes macroscopic behaviors in a composite material by averaging microscopic details in a representative periodic control volume [184]. The macroscopic domain describing the axial cross-section of the soleus was a porous medium represented by a two-dimensional, regularly repeating pattern of staggered diamond-shaped elements that define myofibers (Figure 3.3*B*) [182, 184]. The

direction of macroscopic drug diffusion, defined by a vector $\underline{e}$, runs in the negative y-direction and reproduces radial drug penetration across fibers. Diffusion in the direction of $\underline{e}$ was determined by solving the Laplacian equation in the reduced domain, Ω, formed by a single lattice arrangement of staggered diamonds (Figure 3.3*B*, *inset*):

$$\nabla^2 \chi = 0 \tag{2}$$

where the function χ represents the small periodic component of the macroscopic drug concentration field under boundary conditions determined by $\underline{e}$. The boundaries of Ω consisted of two parts, Γ_1 and Γ_2 (Figure 3.3*C*). Γ_1 corresponds to the interstitial space between lattice domains where symmetric and periodic boundary conditions are imposed. Γ_2 corresponds to the interface between the fiber and interstitial space where the following non-homogeneous Neumann condition is prescribed:

$$\underline{n} \cdot \nabla \chi = \underline{n} \cdot \underline{e} \tag{3}$$

where $\underline{n}$ is the outward unit normal vector on the fiber surface. D_1 in the direction of $\underline{e}$ was computed by:

$$D_1 = \frac{D_{eff}}{D_w} = \frac{1}{A} \int_{\Omega} \left(1 - \underline{e} \cdot \nabla \chi\right) d\Omega \tag{4}$$

where A is the area of the single lattice arrangement.

Equation 2 was solved using COMSOL Multiphysics®, a finite element numerical solver. Porosity changes were modeled by changing diamond size while maintaining their lattice positions fixed and the total area of the lattice constant. Values used for φ at each static strain were taken from empirical measurements of porosity in histologic images.

A regular lattice domain was used to model the homogeneous myofiber and interstitial architecture produced by 0% and 20% strains (Figure 3.3*A*). However, 5%, 10%, and 15% strains produced an inhomogeneous fiber arrangement with wide interstitial spaces separating groups of myofibers (Figure 3.3*D*). Thus, a widened interstitial channel aligned with the direction of transport was added to the regular lattice domain to model this architecture (Figure 3.3*E*). The regular lattice portion in this

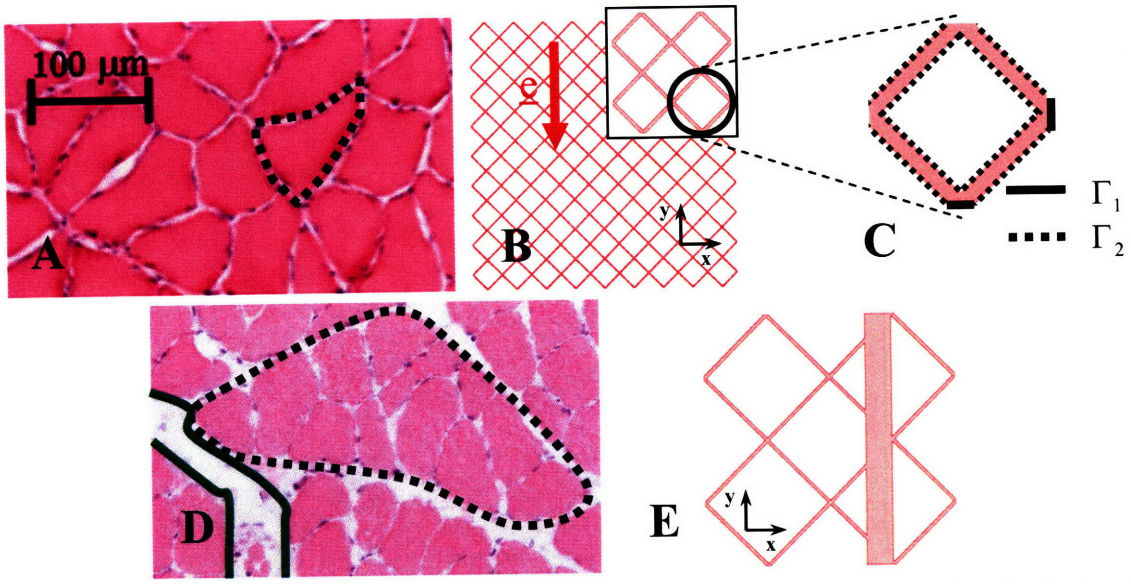

Figure 3.3. Static model. (*A*) HE image of a soleus axial cross-section showing the isotropic and homogeneous porous architecture and uniform interstitial spacing under 0% and 20% muscle strains. A single myofiber is outlined. (*B*) Two dimensional depiction on dimensionless Cartesian axes of the homogeneous muscle axial cross-section. Myofibers are idealized by a regularly repeating lattice of staggered diamonds (*white*) interspaced with interstitial channels (*pink*) of consistent width. The direction of macroscopic drug diffusion, $\underline{e}$ (*red arrow*), is in the negative y-direction. Symmetry of the mathematical problem enables the computation to be carried out on a reduced domain, Ω, formed by a single lattice arrangement of diamonds (*inset*). (*C*) Schematic of a single diamond element depicting boundary conditions. A symmetric or periodic condition is imposed on components of Γ_1 that are respectively parallel or perpendicular to $\underline{e}$. The non-homogeneous Neumann condition is imposed at Γ_2. (*D*) HE image of the inhomogeneous fiber arrangement with wide interstitial channels (*green*) separating fascicles (*black*) of myofibers that occur under 5%, 10%, and 15% strains. (*E*) Depiction of the muscle axial cross-section composed of an inhomogeneous arrangement of myofiber elements. A wide interstitial channel running in the direction of transport was added to the regular lattice domain to model wide interstitial spaces. Location of the channel with respect to the diamonds did not significantly influence transport.

domain was modeled with a porosity that equaled the local porosity measured in a single fascicle. The width of the channel was calculated so that average porosity of the entire domain equaled the average porosity measured in the entire histologic cross-sectional image.

3.3.6.2 Dynamic Case

Many studies have experimentally investigated [185] and theoretically modeled [155, 186, 187] the dispersive effects of pulsatile mechanical loading on the movement of soluble agents (Figure 3.4).

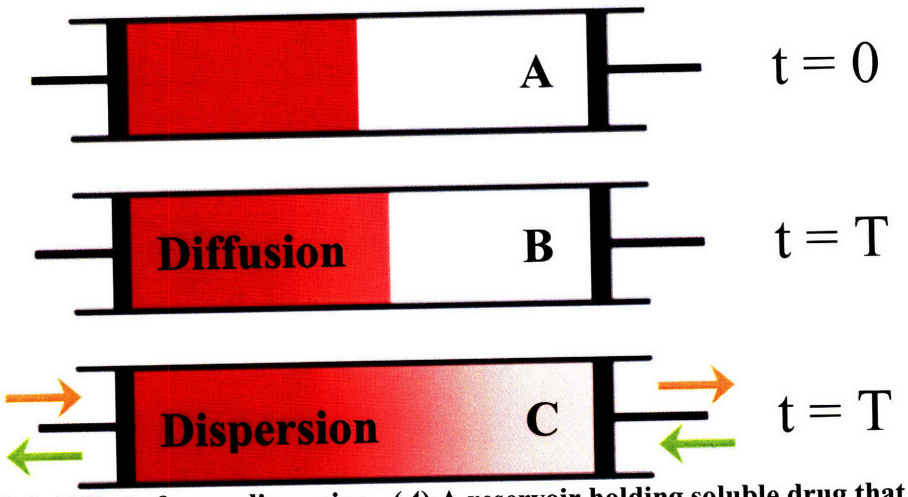

Figure 3.4. Effect of mass dispersion. (*A*) A reservoir holding soluble drug that is isolated to the left half at time t = 0. (*B*) After a time T, soluble drug diffuses towards the right half of the reservoir. (*C*) Pistons at each end of the reservoir oscillating in phase produce no net convection but cause molecular agitation or perturbation of drug so that it spreads farther across the reservoir within the same time T. Mass dispersion increases transport beyond molecular diffusion alone.

Our experiments demonstrate a linear relationship between increase in drug penetration and frequency of cyclic stretch, suggesting cyclic deformation of muscle architecture potentially results in dispersive agitation of soluble drug. The uniaxial

soleus muscle was modeled as a cylinder with a circular cross-section. A two-dimensional mathematical model was used to investigate the dispersive effects of radial deformations on radial drug penetration.

Drug transport was described by the diffusion equation on a continuous domain characterizing the entire axial cross-section of the muscle:

$$\frac{\partial c}{\partial t} - D_{static,\,Rn}\nabla^2 c = 0 \qquad \text{in } \Omega_D(t) \tag{5}$$

where c is the drug concentration field, $D_{static,\,Rn}$ is the empirical effective diffusivity associated with static stretch to the mean strain with mean radius Rn, and $\Omega_D(t)$ is the moving, continuous axial cross-sectional domain of the muscle. Equation 5 was solved on the moving domain, $\Omega_D(t)$, which is defined as:

$$\Omega_D(t) = \pi r(t)^2 = \pi(Rn)^2(1+\alpha\sin(\omega t))^2 \tag{6}$$

where r(t) is the radius of the cross-section, α is the radial strain amplitude centered about the mean radius Rn (with n = 0, 5, 10, 20), and ω is the radial frequency of pulsation or deformation (where $\omega = 2\pi, 4\pi, 6\pi$ rad/sec). Theoretical values of the radius and radial deformations resulting from axial stretch were calculated from tensile strains applied experimentally based on conservation of volume and tissue incompressibility (Poisson ratio=0.5) [188] (Appendix F).

The Arbitrary Lagrangian Eulerian (ALE) formulation [189], based on the simultaneous solutions of motion and material behavior, was used to express Equation 5:

$$\frac{\partial c}{\partial t} - D_{static,\,Rn}\nabla^2 c - \underline{w}\cdot\nabla c = 0 \qquad \text{in } \Omega_D(t) \tag{7}$$

where $\underline{w}$ is the velocity of $\Omega_D(t)$ (Appendix G). Equation 7 was solved using COMSOL to obtain the drug concentration profile in the muscle cross-section after 1 h of transport.

Drug source concentration at the boundary of $\Omega_D(t)$ was a constant value fixed at 1 and penetration depth was taken as the distance from the boundary at which concentration decreased to 0.05.

3.4 Results

3.4.1 Static Strain, Cyclic Stretching, and Contractions

Tensile strain increased intramuscular drug penetration and effective diffusivity (Figure 3.5*A*). Penetration increased by 1.45-fold to a maximum at 10% strain and fell off thereafter. This drug penetration profile correlates with the isometric twitch force-length relationship of the muscle ($r = 0.87$, Figure 3.5*B*), suggesting that architectural configuration, which is the physiologic correlate of mechanical function, simultaneously mediates a transport environment with characteristics reflecting contractile efficiency. Maximal drug penetration thus correlates with optimal length L_o, the physiologically defined length at which maximal active force is produced and reflects the optimal overlap of myosin and actin contractile myofilaments in the muscle. Dextran penetration decreased with increasing molecular weight and polymer size at baseline and with strain (Figure 3.5, *C* and *D*). Whereas 10% strain enhanced penetration past that at 0% by an increasingly greater distance for smaller molecules that are less sterically hindered (Figure 3.5, *E* and *F*), this relative enhancement effect was most evident for larger molecular sizes that encounter greater steric hindrance (Figure 3.5*F*).

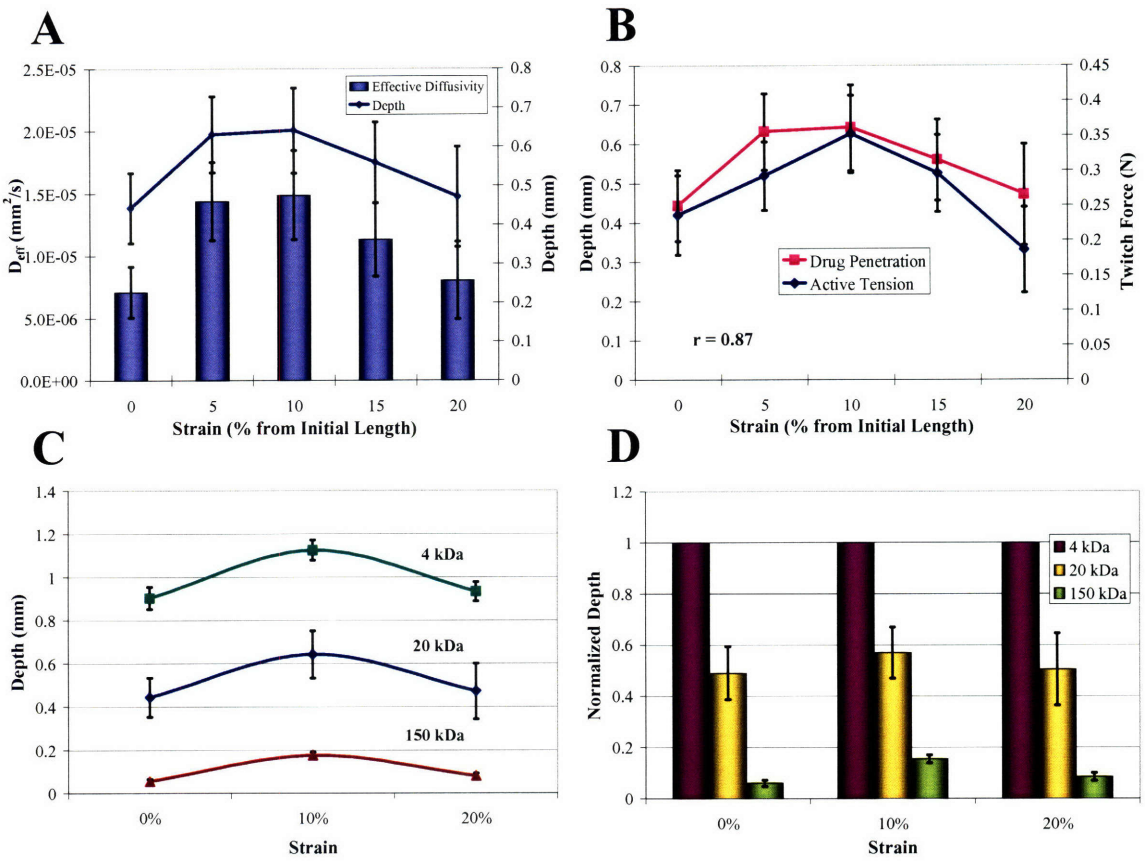

Figure 3.5 (*A-D*). Drug transport under static strain. (*A*) Penetration depth and effective diffusivity of 20 kDa FITC-dextran in soleus muscle over 0%-20% elongating strains from nominal length. Penetration increases with strain from 0.44 ± 0.09 mm ($D = 7.1x10^{-6} \pm 2.0x10^{-6}$ mm^2/s) at 0% strain to a maximum of 0.64 ± 0.11 mm ($D = 1.5x10^{-5} \pm 3.6x10^{-6}$ mm^2/s) at 10%, and decreases to 0.47 ± 0.13 mm ($D = 8.0x10^{-6} \pm 3.1x10^{-6}$ mm^2/s) by 20%. Depths at each strain in the increasing and decreasing halves of the profile, except 5% and 10%, are statistically significantly different (T-test, $p<0.05$). (*B*) Drug penetration profile correlates positively with isometric twitch force over 0%-20% strains (r = 0.87). Maximal drug penetration occurs at 10% strain, or optimal length L_o, as defined by peak twitch force. (*C*) Penetration depth decreases with increasing molecular weight at 0%, 10%, and 20% strains (Two-Factor ANOVA, $p<0.05$ between penetration depths, $p<0.05$ between molecular weights). (*D*) Penetration of 4 kDa, 20 kDa, and 150 kDa dextrans normalized to 4 kDa penetration. 4 kDa dextrans penetrate approximately 2-fold and 10-fold farther than 20 kDa and 150 kDa dextrans, respectively, at each strain.

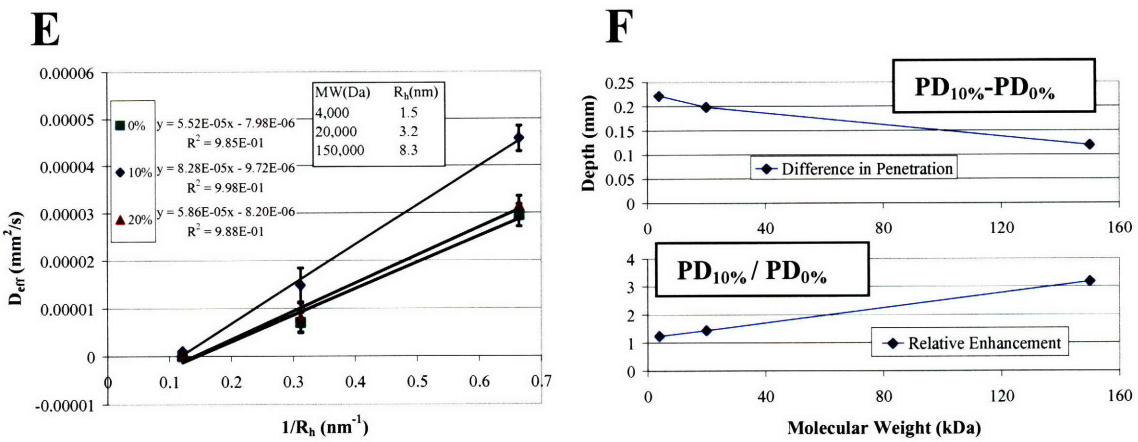

Figure 3.5 (*E-F*). Drug transport under static strain. (*E*) The rate of increase (slope) of diffusivity with decreasing molecular size (increasing $1/R_h$) at 10% strain is 1.4-fold greater than the rate at 0% and 20% strain. Hydrodynamic radius (R_h) of dextrans was computed from molecular weight (MW) using the relationship $R_h = 0.305*(MW)^{0.47}$ [190]. Effective diffusivities of dextrans vary inversely with hydrodynamic radius, as expected for the mobility of inert macromolecules in a simple fluid based on the Stokes-Einstein equation [191]. (*F*) The difference between penetration depths at 10% and 0% strain decreases with increasing molecular weight, demonstrating a difference of 0.22 mm for 4 kDa, 0.20 mm for 20 kDa, and 0.12 mm for 150 kDa dextran. The relative enhancement of penetration at 10%, or the ratio of penetration at 10% to 0%, increases with increasing molecular weight from 1.25-fold for 4 kDa, to 1.45-fold for 20 kDa, to 3.18-fold for 150 kDa. The difference in penetration and relative enhancement change oppositely (r = -1) with molecular weight.

The effects of dynamic loading were isolated from that of architecturally modulated steric hindrance observed under static strain by loading samples to the same cyclic profile at each of the static strain conditions. Cyclic loading enhanced the drug penetration produced by static strain (Figure 3.6*A*). At each mean strain, cyclic loading consistently increased penetration by an average of 0.084 mm for every 1 Hz increase in cycling rate (Figure 3.6*B*). As a result, the penetration profile across mean strains for each cycling rate shares the same shape as the static strain profile (Figure 3.6*C*). As penetration was linearly dependent on cycling rate, it was directly dependent on the number of cycles of loading. Drug penetration was identical over a range of frequencies when the product of loading duration and frequency was held constant such that all tissues were subjected to 3600 cycles of loading (Figure 3.6*D*).

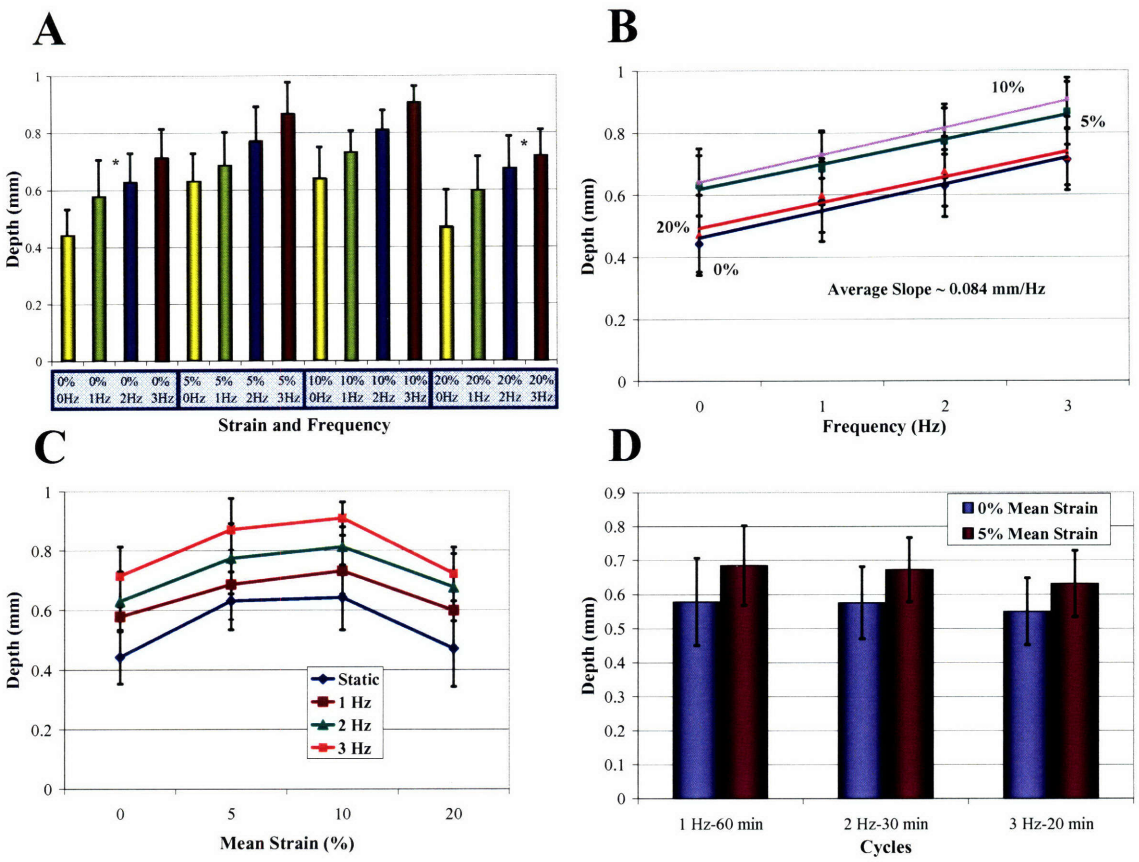

Figure 3.6. Impact of cyclic strain on drug penetration. (*A*) Cyclic tensile loading at 1 Hz-3 Hz increases drug penetration at each mean strain linearly proportionally to the frequency of loading. 0 Hz groups received no cyclic loading and are the same statically stretched cases shown in Figure 3.5*A*. Penetration depths produced by each loading frequency applied at each mean strain are statistically significantly different (T-test, $p<0.05$) except for groups with an * between them. (*B*) The slopes of the linear relationship between penetration and loading frequency at each mean strain are statistically the same, averaging 0.084 mm/Hz (Single-Factor ANOVA, $p>0.05$). (*C*) Penetration at each frequency of loading follows the same trend dictated by static stretch. (*D*) Penetration is directly dependent on the number of cycles of strain. Penetration is statistically the same at each mean strain over a range of loading frequencies when the imposed number of loading cycles is held fixed at 3600 cycles (Two-Factor ANOVA, $p<0.05$ between 0% and 5%, $p>0.05$ among loading groups). The 1 Hz, 60 min group for 0% and 5% strain are the same cases shown in Figure 3.6*A*.

Isometric twitch contractions increased drug penetration above that occurring without contraction. Preliminary findings demonstrated the pharmacokinetic impact of the presence of contraction (Figure 3.7). Quantitative studies of contraction rates from

0.1-3 Hz showed that penetration increased with contraction rate by 1.52-fold to a maximum at 0.5 Hz and fell off thereafter (Figure 3.8).

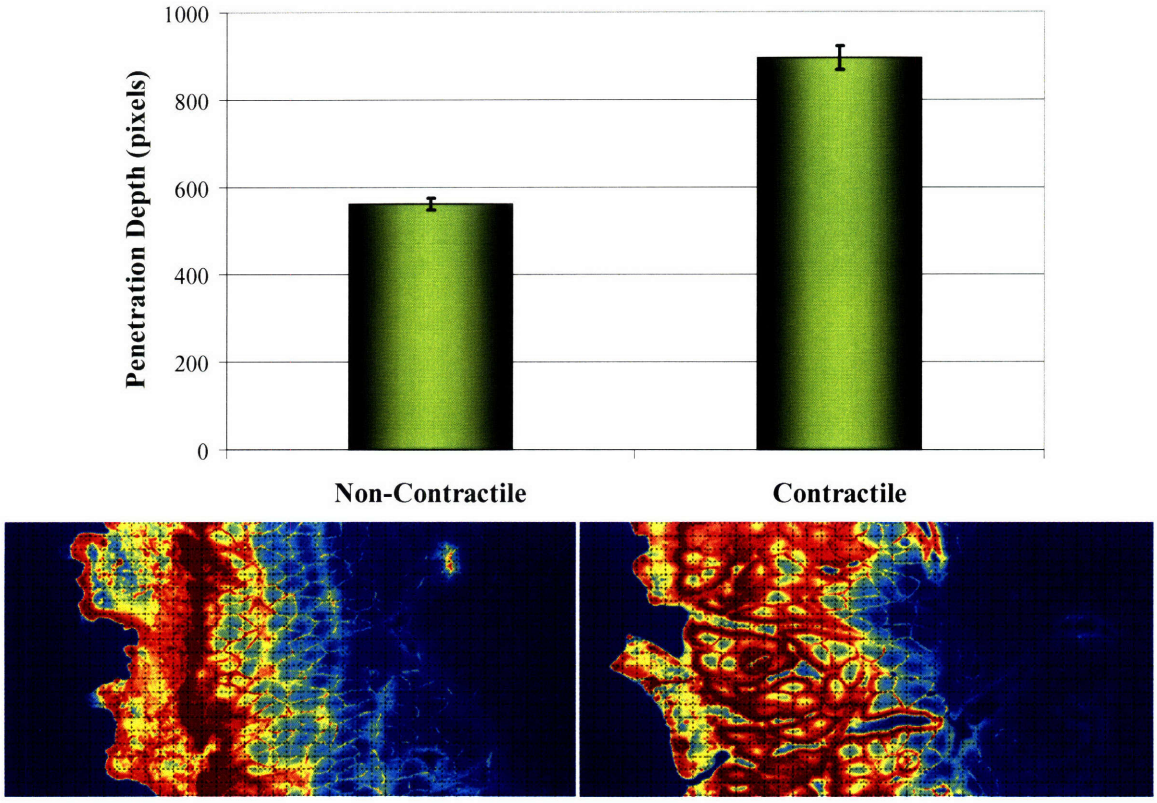

Figure 3.7. Impact of contraction on drug transport. Rhythmic contraction increases intramuscular penetration of 20 kDa FITC-dextran, suggesting dynamic forces created by contraction increase interstitial drug transport. Fluorescence intensity images of axial cross-sections of the soleus show drug distribution under non-contractile and contractile loading conditions.

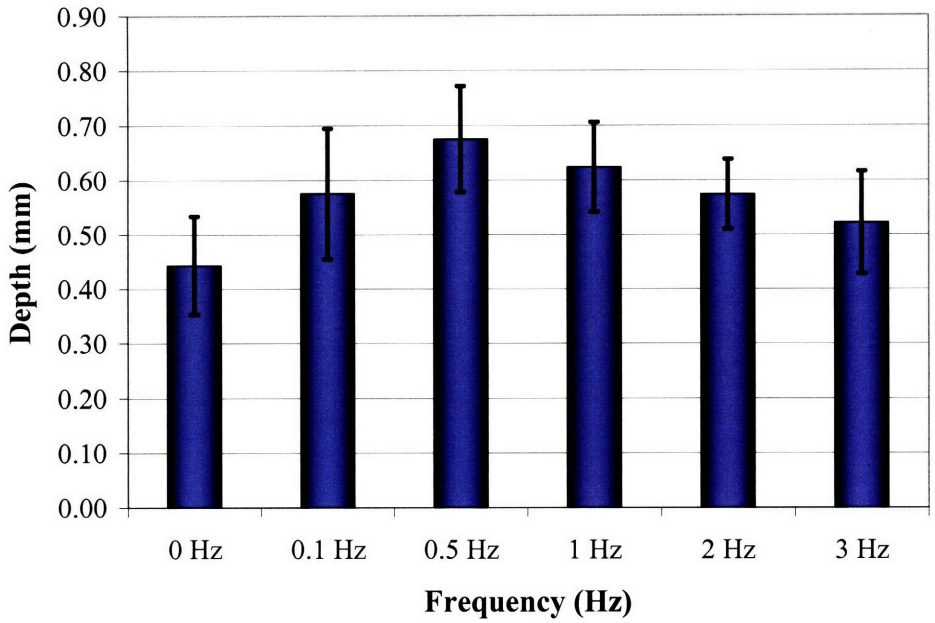

Figure 3.8. Impact of contraction frequency on drug penetration. Isometric twitch contractions of 0.1 Hz-3 Hz at nominal length increase penetration above that occurring with static strain, 0 Hz. The 0 Hz group received no electric pacing and is the same 0% group shown in Figure 3.5*A*. Penetration increases with contraction rate from 0.44 ± 0.09 mm at 0 Hz to a maximum of 0.67 ± 0.10 mm at 0.5 Hz and decreases to 0.52 ± 0.09 mm by 3 Hz. Penetration depths measured at each frequency in both the increasing and decreasing halves of the profile are statistically significantly different (T-test, $p<0.05$).

3.4.2 Tissue Architecture

3.4.2.1 Myofiber Arrangement

Minimum interstitial spacing between myofibers in histologic images was 0.43 μm, which is comparable to experimental values (~ 0.1 μm) found previously [192]. Myofiber arrangement was isotropic at 0% and 20% strains (Figure 3.9*A*). This homogeneous distribution was interrupted by enlarged intercellular channels, of 11.1 μm-34.7 μm width, at 5%, 10%, and 15% strains. Fiber rearrangement by channels, which cleave muscle bundles in orientations that correlate with fascicular borders, not only increases porosity, but is also an independent parameter that significantly impacts drug transport, as shown in our computational model.

3.4.2.2 Tissue Porosity

Tissue porosity was 0.12 ± 0.01 at 0% strain (Figure 3.9*B*). This is in agreement with inulin distribution space, which characterizes the volume of extracellular space, found previously in rat soleus (0.14 ± 0.01, 0.12 ± 0.01, and 0.13 ± 0.01) [143, 193, 194]. Porosity increased with tensile strain by 1.5-fold to a maximum at 10% strain, or optimal length L_o, and fell off thereafter. That this porosity profile correlates with the isometric twitch force-length relationship of the muscle (r = 0.87) and exactly with the drug penetration profile with static strain (r = 1) suggests that tissue porosity, which is the architectural correlate of functional state, is a direct determinant of drug transport in contractile tissues (Figure 3.9*C*).

3.4.2.3 Average Fiber Cross-Sectional Area and Fiber Density

Whereas average cross-sectional area of myofibers decreased to an asymptotic value, fiber density increased from an asymptotic value with increasing strain (Figure 3.9*D*). Both profiles inflected symmetrically at L_o, indicating the significant correspondence of architectural state with muscle function and pharmacokinetics. The product of average area and density represents the fractional space occupied by myofibers (Figure 3.9*E*) and demonstrated a profile that was the mathematical complement of porosity (r = -0.99). Fiber density plotted against fiber area was a nonlinear curve (Figure 3.9*F*), demonstrating the presence of porosity changes with strain, as constant porosity would have produced a linear relationship between fiber density and average area. These findings suggest porosity, fiber area, and fiber density are distinct parameters that change interrelatedly to affect the transport environment.

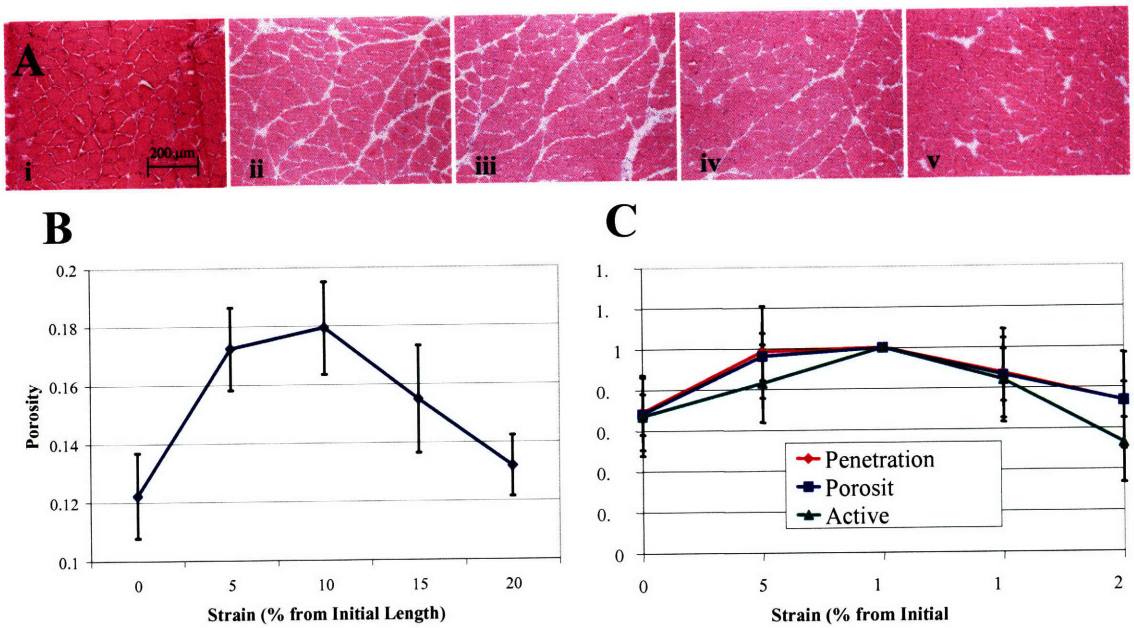

Figure 3.9 (*A-C*). Architectural parameters over 0%-20% strains. (*A*) Axial cross-sections of HE stained soleus muscles undergoing (*i*) 0%, (*ii*) 5%, (*iii*) 10%, (*iv*) 15%, and (*v*) 20% static strain. Myofibers are pink and interstitial space is white. (*B*) Porosity increases with strain from 0.12 ± 0.01 at 0% strain to a maximum of 0.18 ± 0.02 at 10% and decreases to 0.13 ± 0.01 by 20%. (*C*) The porosity profile correlates with the isometric twitch force-length relationship (r = 0.87) and exactly with the drug penetration profile over static strain (r = 1). Profiles are normalized to their respective peak values at L_o.

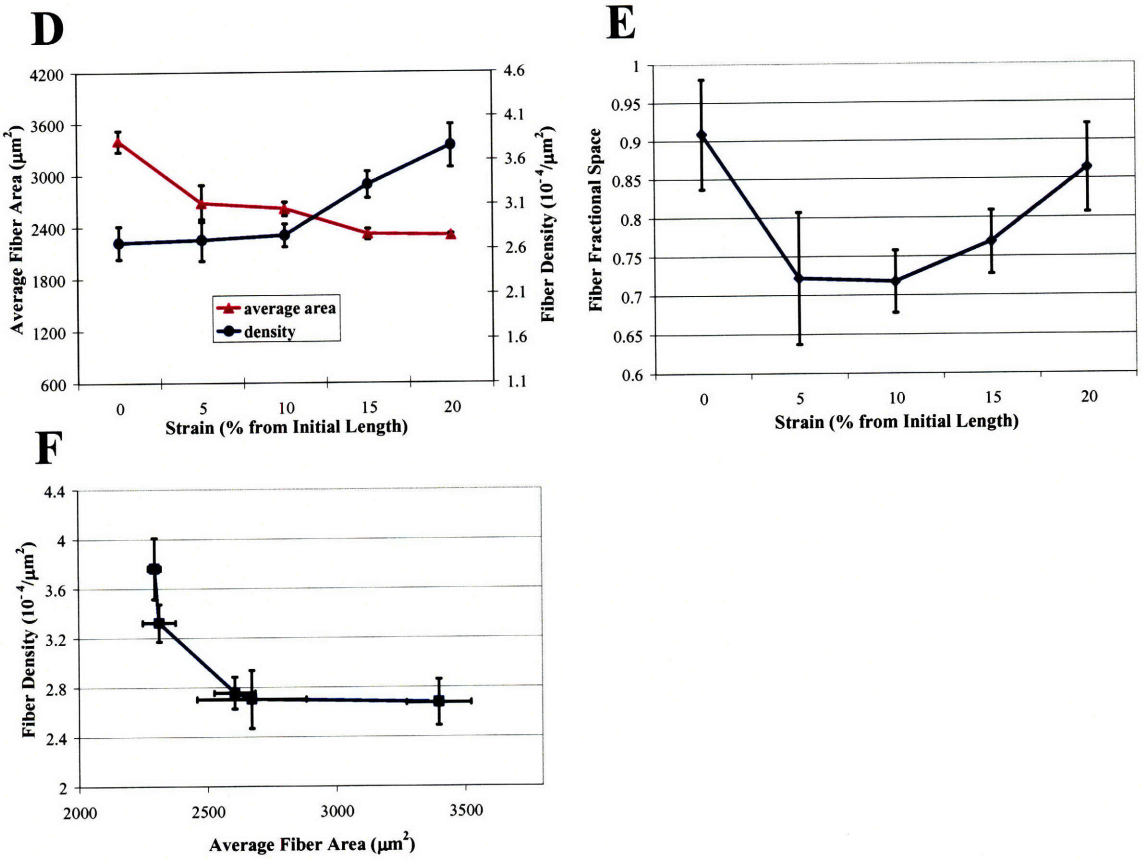

Figure 3.9 (*D-F*). Architectural parameters over 0%-20% strains. (*D*) Average cross-sectional area of a single myofiber and density of myofiber distribution change inversely with static strain. The average area decreases to an asymptotic value with increasing strain from 3397.6 ± 125.2 μm² at 0% strain to 2296.3 ± 24.4 μm² at 20%. Density increases from an asymptotic value of $2.67\times10^{-4} \pm 1.86\times10^{-5}$ μm^{-2} at 0% strain to $3.76\times10^{-4} \pm 2.46\times10^{-5}$ μm^{-2} at 20%. (*E*) Fractional space occupied by myofibers is calculated from the product of average area and density. Fractional space is the mathematical complement of porosity. (*F*) Change in porosity is demonstrated by the nonlinear relationship between fiber density and average fiber area.

3.4.3 Numerical Results

3.4.3.1 Static Strain

Drug transport under static strain was influenced by the combined effects of porosity and fiber arrangement (Figure 3.10). The theoretical upper bound of diffusivity, $D_{eff}/D_w = \varphi$, is along the myofiber axis [178]. Transport through the homogeneous fiber arrangement under 0% and 20% strains (Figure 3.9*A*) was accurately characterized as diffusion perpendicular to the axis of a homogeneous arrangement of myofibers (Figure

3.10, *Isotropic Medium,* lower limit of diffusivity) and the relationship, $D_{eff}/D_w = 0.58\varphi$. Fiber arrangement is also a significant parameter influencing transport [178]. Diffusion was greater across an inhomogeneous fiber arrangement with the presence of an enlarged channel aligned in the direction of transport (Figure 3.3*E*) than across a homogeneous fiber arrangement (Figure 3.3*B*) with uniformly widened interspaces even when both arrangements had identical average porosities. Transport through the inhomogeneous fiber arrangement produced by 5%, 10%, and 15% strains (Figure 3.9*A*) was accurately characterized by diffusion perpendicular to the axis of a myofiber arrangement with an enlarged channel aligned in the direction of transport (Figure 3.10, *Medium with Channel*) and the relationship, $D_{eff}/D_w = 1.044\varphi - 0.0442$, which had a slope that approximated the upper limit of diffusivity (diffusion along the myofiber axis). A slope approximating the upper bound likely reflects channel alignment in the direction of transport. These results demonstrate that in addition to average porosity, fiber area, and density, the arrangement and distribution of myofibers significantly impacts transport.

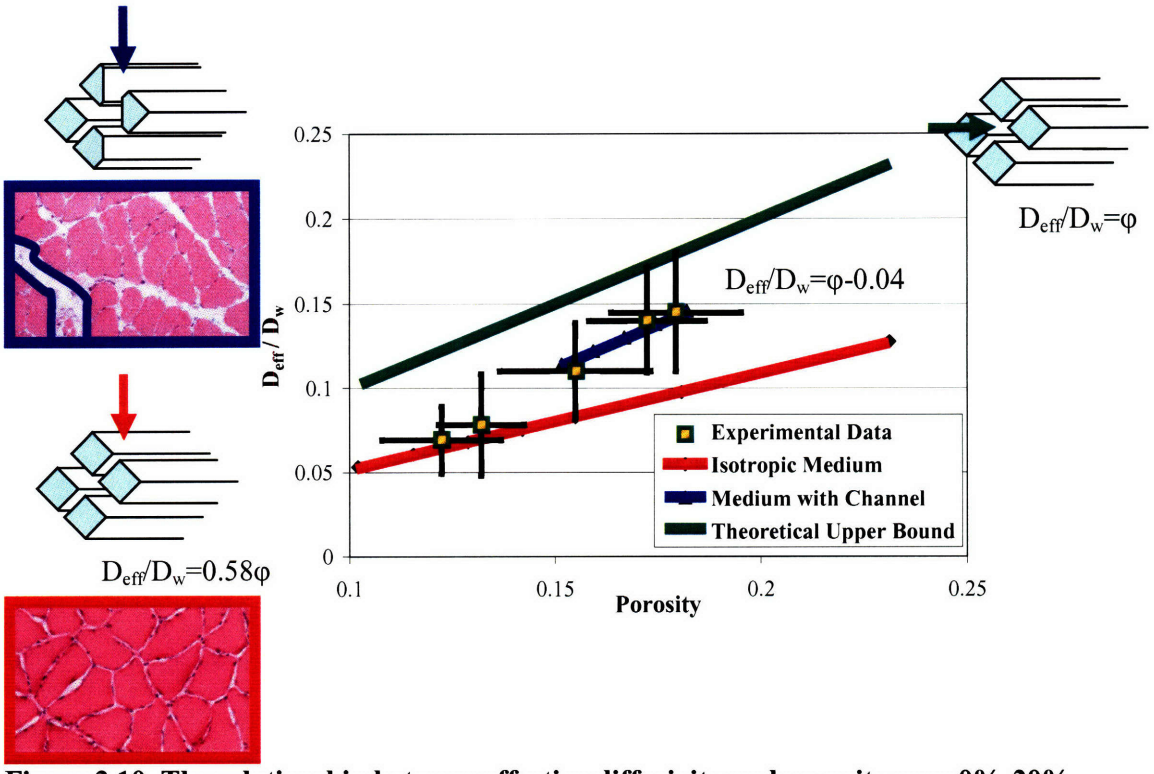

Figure 3.10 The relationship between effective diffusivity and porosity over 0%-20% strains. Numerical results were compared to experimental data in terms of D_{eff}/D_w versus porosity (φ) for the range of $0.1 \leq \varphi \leq 0.2$. The computational lower limit of drug diffusivity is transport through a porous medium represented by a homogeneous, repeating lattice of staggered diamonds (Figure 3.3*B*) in which the macroscopic direction of diffusion is across myofibers and perpendicular to their axis. The theoretical upper limit of drug diffusivity, $D_{eff}/D_w = \varphi$, represents diffusion in a unit cross-sectional area through straight, non-tortuous channels that run parallel to the myofiber axis and occupy a fraction φ of the unit area. The plot of *Medium with Channel* is the numerical result for diffusion across a diamond lattice with the addition of an enlarged interstitial channel running in the direction of effective drug diffusion (Figure 3.3*E*). General lattice interspacing was determined based on the local porosity measured in a fascicle in images of 5%, 10%, and 15% strain (0.087, 0.091, and 0.078, respectively). Computational channel widths for 5%, 10%, and 15% strain were calculated such that overall average porosity in the domain was 0.172, 0.179, and 0.155, respectively, to match histologic measurements. For a domain (Ω) size of 1x1 dimensionless values and diamond size of 0.34 x 0.34, channel widths were 0.099, 0.103, and 0.077 for 5%, 10%, and 15%, respectively. Thus, calculated channel sizes used in the numerical plot of *Medium with Channel* were 23%-30% of myofiber size, predicting widths of 11 μm-15 μm, which fall within the range of empirically measured channel widths.

3.4.3.2 Dynamic Strain

Dispersion resulting from cyclic structural oscillations in the radial direction likely explains the enhancement of radial drug penetration under dynamic loading. The presence of dispersion was computationally validated by the linear dependence of

penetration on frequency and number of loading cycles, independent of mean strain (Figure 3.11). Discrepancies between numerical and experimental results may be attributed to simplifying assumptions of model geometry, as a circular cylinder, and of the dynamics of mechanical behavior. Consideration of the

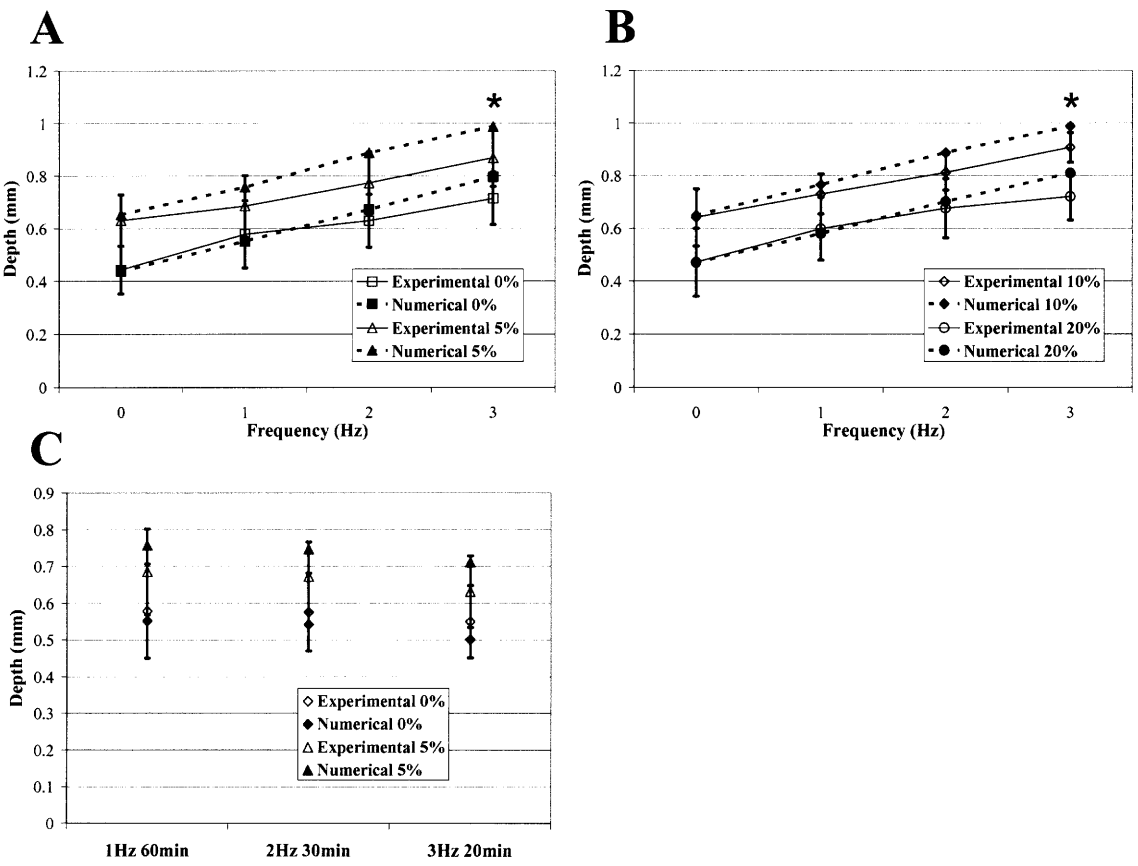

Figure 3.11. Dynamic loading. Dispersion increases drug penetration with linear dependence on the frequency of oscillation. (*A*) 0% and 5% mean strains. (*B*) 10% and 20% mean strains. (*) Numerical results lie within the confidence limits of experimental data. (*C*) Dispersive effects are dependent on the number of loading cycles, independent of the mean strain.

complex dampening effects of muscle viscoelasticity, which reduce the dispersive effects of structural deformations, during dynamic loading may more completely characterize muscle mechanics and mass transport. Interstitial fluid extrusion, which may initially

counteract drug penetration, can subsequently produce a wicking effect that draws drug into the tissue as a result of the transposition of interstitial and source fluid. These effects during dynamic loading may further compound the enhancement of drug penetration.

3.5 Discussion

Intramuscular drug transport is not simply a function of the physicochemical properties of the drug. Characteristic dynamic architecture, motion, and contraction in skeletal muscle targets significantly influence intramuscular pharmacokinetics. Before quantifying the transport of proteins or specifically binding drugs, it was necessary to analyze the pharmacokinetics of an inert tracer such as dextran. Using a mechanical loading system designed for *in vitro* drug transport studies in association with muscle biomechanics, we investigated the impact of controlled mechanical loading on dextran penetration in soleus muscle. A computational model of interstitial drug transport accurately elucidated the architectural and dispersive influences underlying the transport effects of static and dynamic strain.

3.5.1 Static Strain

Muscle lengths from 0% to 20% strain span the physiologic range of muscle function and extensibility [195]. Drug transport within this range reflects the pharmacokinetic environment dictated by physiologic architectural configurations and function. The exact correlation between effective diffusivity and porosity over static strain confirms the extracellular transport of soluble dextran [134-136, 196, 197] and

indicates that architectural changes like muscle stretch influence transport through impact on porosity.

Whereas previous studies have shown that passive stretch unilaterally increases glucose uptake [95], we have elucidated an architecturally defined optimal setpoint rendering maximal drug penetration at the physiologic configuration for peak muscle performance, optimal length L_o. Characteristic changes in fiber size, density, and organization suggest that strain-dependent porosity, which mediates this parabolic increase in transport, results from the asynchronous progression of conservation of myofiber volume and myofiber packing density with strain. Through conservation of volume, myofibers undergo continuous reduction in cross-sectional size with elongation. Upon initial stretch, this fiber thinning opens interstitial space, increasing porosity and transport. Interstitial enlargement is accompanied by space and myofiber redistribution along fascicular borders, likely corresponding with muscle volume changes known to occur during muscle activity [153]. Thus, increased tissue-averaged porosity results from not only homogeneous space enlargement, but also myofiber redistribution that can connect interstitial spaces and precipitate the formation of enlarged channels with low tortuosity. As demonstrated by our static model, these widened channels are likely aligned in the radial direction of drug penetration to greatly facilitate diffusion and render maximal penetration at L_o. With elongation past L_o, fiber density increases as the entire muscle bundle tightens and increasingly thin fibers compact together, resulting in contraction of interstitial space, recession of open channels, and reduction of tissue-averaged porosity and diffusion. These changes likely correspond to muscle volume decrease [153] and intramuscular and interstitial pressure increase [198] known to occur

with passive stretch beyond L_o. Through the structural changes depicted by the asymptotic profiles of fiber size and density, porosity is modulated predominantly by local effects such as fiber size at strains less than L_o, and by global effects such as fiber distribution at strains greater than L_o.

Correlation between transport, porosity, and the active force-length relationship, whereby all three increased 1.5-fold from baseline to a maximum at L_o, suggests the physiologic nexus ascribed to L_o, whose architectural configuration enables optimal interface between the tissue and its external environment. The profiles of fiber area and density over 0%-20% strain suggest that the architectural configurations within the physiologic range of muscle extensibility and function are defined by the passive material limits of myofibers and connective tissue. Fiber size asymptotes to a minimum by 20% strain, suggesting the extent of myofiber incompressible elasticity. Fiber density asymptotes to a minimum at the initial length, indicating the resting state of fiber aggregation and maximal mechanical compliance of the muscle bundle rendered by the connective collagen fascial framework. Between these physical limits, the profiles of both fiber size and distribution progress inversely with elongating strain and have a critical inflection point at L_o, where these parameters correlate maximal porosity and drug penetration with optimal mechanical performance. Perhaps maximal extracellular space is functionally related to optimal activity to increase vascular perfusion by reducing intramuscular pressure [152, 199] or to maximize the available volume surrounding fibers to enable maximal fiber swelling and thickening [107, 145] during contraction.

3.5.2 Dextran Molecular Weight

FITC-dextran is a neutrally charged [200, 201], highly branched, randomly coiled polysaccharide [202] with non-protein binding [135] properties. Size-dependent mobility of dextran in the interstitium captures the effect of steric interaction with architecture on transport. The continuous, dense network of collagen fibers forming the endomysium and perimysium sterically hinders soluble drug diffusion [97]. As this network provides support and force transmission between myofibers [100, 102], structural deformations associated with mechanical loading can modulate the screening effect on drug transport mediated by the network. The collagen fibers, which are randomly orientated in relaxed muscle, align circumferentially to myofibers with muscle shortening and axially with muscle elongation [103-105]. Because permeability is greater through a periodic, rather than a random, distribution of obstacles [154, 203], alignment of collagen fibers with strain increases interstitial permeability. These changes define mobility within the accessible volume to drug that is dictated by macro-scale tissue-averaged porosity. The extent of steric hindrance and interstitial mobility was demonstrated by the penetration of dextrans of various sizes. Results showed the transport effects of strain-dependent architecture were consistent across different physicochemical properties.

The architectural configuration at L_o defines an interstitial collagen and myofiber alignment that optimally reduces steric hindrance and enhances penetration. This transport effect likely varies, like L_o and its associated maximal force, among different muscles. Physical properties of the drug, namely molecular size, further dictate the ultimate effect on penetration presented by intramuscular fiber alignment. Diffusivity was observed to increase with decreasing dextran size. For lower molecular weight

molecules that penetrate farther in general, steric hindrance likely becomes negligible because the effective radius of such drugs is substantially smaller than the minimal barrier to diffusion posed by fiber alignment. Penetration of such small molecules would be the maximum achievable under the static, architecturally defined transport environment and could only be enhanced further by dynamic forces such as dispersion or convection induced by muscle activity. Whereas net penetration decreases with increasing dextran size, the relative enhancement of penetration at L_o increases. For 150kDa dextran, which has an 8.3 nm radius, penetration at L_o is significant compared to penetration at 0% strain. For this and larger sizes, penetration into muscle is minimal under static conditions and enhancement at L_o is therefore significant, enabling penetration of large molecules that otherwise would not have been able to enter the tissue. Molecules of even greater size may be altogether sterically excluded even at L_o and thus also derive no enhancement of penetration from the dynamics of muscle activity.

3.5.3 Cyclic Stretching

In the absence of a net external convective force driving bulk fluid flow into the muscle, and particularly as drug penetration proceeds against an increasing intramuscular pressure gradient during stretch [152], enhancement of penetration by oscillatory loading is unlikely the result of bulk convection. Dynamic loading may cyclically expose drug to strain-dependent architectural configurations with larger accessible volumes and result in a greater time-averaged porosity that increases penetration. However, this mechanism depends only on static architectural states, and average porosity over a single loading cycle remains the same regardless of loading frequency. Enhancement of transport that

readily superposes on the static strain transport profile suggests a dynamic process rather than further reduction of architectural exclusion. Thus, dispersion is likely a significant driving force because penetration was shown both experimentally and computationally to be enhanced linearly dependently on loading frequency and independently of mean strain.

Dispersion impacts the transport kinetics of soluble drug by increasing transport beyond molecular diffusion alone [155]. Axial strain translates into radial deformation due to conservation of volume and lateral force transmission by interstitial connective tissues [204, 205]. Cyclic displacement of myofibers compresses and expands extracellular space and imposes normal and shear forces on interstitial fluid, resulting in pulsatile agitation and movement of soluble drug in the absence of net bulk convective fluid flow. Such agitation can disperse or spread drug in a rate-dependent manner over a greater extracellular volume, thereby driving greater penetration.

3.5.4 Contractions

Unlike studies of contraction-induced substrate transport, which have shown that contraction increases glucose transport based on metabolic changes [94, 96], or that glucose [84, 90] or calcium [149] uptake scales unilaterally with frequency of contraction, we have elucidated a functionally-associated optimal setpoint rendering maximal drug penetration at 0.5 Hz isometric contractions at nominal length. Cyclic dynamics alone can increase penetration through dispersive effects that scale with frequency. However, decreasing penetration with contraction rates above 0.5 Hz suggests competing transport effects that predominate at higher frequencies. Contraction, which is functional tissue activity, imposes more complex transport effects than those

introduced by static or cyclic stretch of passive tissue that reflect the combined and interacting effects of architectural configuration and loading dynamics. We propose the bimodal trend in penetration with contraction rate results from time-dependent competition between dispersion and steric hindrance, whereby dispersion predominates below, and steric hindrance predominates above a critical contraction rate determined by the isometric muscle length.

Even under isometric conditions, contraction-associated myofiber thickening [206] occurs as a result of cytoplasmic volume displacement from the smaller end-regions of myofibers toward the middle [106]. Fiber thickening produces transverse forces and a squeezing effect that decreases porosity and increases interstitial fluid pressure [198, 199]. Fiber swelling resulting from interstitial water movement into the fibers [145] reduces interstitial space available for drug in the absence of vascular perfusion *in vitro* [146, 153]. These effects resist drug penetration. Fiber relaxation after contraction results in fiber thinning that re-opens interstitial space, restores porosity, and relieves interstitial fluid pressure. Cyclic transitions between the contracted and relaxed architectural states create dispersive effects that increase drug penetration. At contraction rates less than 0.5 Hz, muscle contracts infrequently and tissue architecture spends the majority of the duration of drug delivery in the relaxed state, which enables dispersive effects that do occur as a result of contraction to dominate. This in agreement with findings that low frequency isometric contractions (3 contractions/min) increase both inulin uptake and washout in papillary muscle [87]. At contraction rates greater than 0.5 Hz, muscle architecture spends an increasingly greater amount of time in the contracted state. More contractions occur over the duration of drug delivery, which exposes drug to

a greater temporal resistance to penetration and progressively swelling fibers. At these frequencies, the effects of increased temporal steric hindrance and elevated interstitial pressures outweigh the effects of dispersion, thereby precluding enhancement of drug penetration. At the extreme limit of complete tetani, elicited by 55 Hz electric pacing at room temperature [131], muscle architecture spends the entire extent of a given duration in the contracted state, thus eliminating cyclic transitions between structural states and associated dispersive effects altogether, and would likely reduce penetration to a depth even less than that occurring under static conditions in the relaxed state.

As static strain affects tissue porosity, it is likely that this contraction rate dependence of maximal penetration shifts with the isometric length of the muscle. This possibility is supported by the finding that the extent of contraction-associated muscle volume decreases varies with initial length of the muscle, becoming greater with greater initial lengths beyond L_o [153]. We predict that the optimal frequency may increase with isometric lengths that effect greater porosities.

3.5.5 Conceptual Paradigm

Mechanical loading and contractile function produce myofiber deformations, rearrangements, and extracellular pressure changes associated with interstitial space and fluid redistributions that can affect the intramuscular distribution of locally delivered drug. Histologic assessment of architecture and drug penetration findings that reflect structurally influenced steric interactions provided insights on strain-dependent architectural configuration. From these findings, we propose that myofiber cross-sectional area and packing density undergo an asynchronous progression of changes with

strain based on conservation of volume to render a spectrum of architectural configurations with muscle elongation spanning contraction through initial length to extreme tensile strain (Figure 3.12). Moderate passive stretch from initial length up to optimal length reduces myofiber thickness and opens or widens interstitial space to reach a maximal porosity at L_o that enables optimal drug transport. With extreme stretch past L_o, increasingly thin fibers compact together as the entire muscle bundle tightens, resulting in contraction of interstitial space that reduces drug transport. Muscle fiber swelling and thickening during isometric contraction can result in a squeezing effect that narrows interstitial space and increases interstitial fluid pressure, thus impeding drug penetration. Fiber relaxation and relief of contractile tone, which recreates muscle stretch

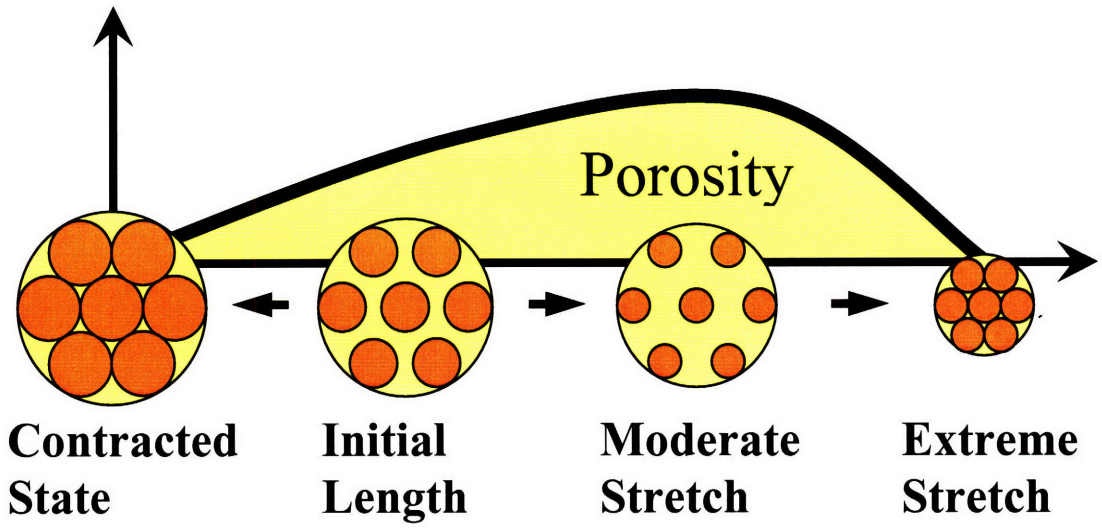

Figure 3.12. Conceptual paradigm of strain-dependent architecture. The spectrum of architectural configurations spanning contraction to extreme strain that is modulated by myofiber cross-sectional area and packing density. Porosity is maximized by moderate elongation to the architectural state at L_o.

and associated fiber thinning, results in an opening effect on interstitial space, increase in porosity, and relief of interstitial fluid pressure that reestablishes greater drug penetration.

Within this spectrum of architectural changes, the screening effect of mechanically influenced interstitial connective tissue can further modify drug mobility.

Structural configuration provides the foundation of architecture-induced changes in drug transport while enabling dynamic loading effects to be superposed either additively or competitively. Dynamic effects from cyclic tensile strain augment drug transport linearly dependently on loading frequency beyond the effects of architectural configuration imposed by static strain. Rhythmic contraction, however, enables a rate dependent maximal drug penetration, suggesting the transport effects of architectural configuration and cyclic transition between relaxed and contracted configurations may compete to modulate drug transport. Findings from cyclic strain experiments indicate the impact of dynamic loading on transport depends directly on the number of cycles of loading. Thus, it is likely that the rate dependent influences of contraction on drug penetration are related to competition between the total number of transitions between relaxed and contracted configurations, whose kinetics produce dispersive effects that accumulate with each set of transitions to enhance transport, and the duration of time the muscle spends in one configuration or the other, which determines time-averaged porosity over the duration of drug delivery. In this setting, as in cyclic tensile loading, transport effects of structural mechanics can be further compounded by fluid dynamics. Structural transition to a state or configuration that reduces interstitial space can produce fluid extrusion that resists drug entry. In contrast, transition to a configuration that reopens interstitial space can generate wicking or milking effects that draw bulk phase fluid and drug into the tissue. Likely with such fluid dynamics, as with structural mechanics, is the potential competition between interstitial fluid extrusion and influx that

may be time or rate dependent, and a consequent equilibrium setpoint at which these opposing effects balance to effect a pivotal degree of drug transport.

3.5.6 Perspectives

Our findings elucidate opportunities for diagnostic techniques and therapeutic windows for improved drug delivery to load-bearing tissues. Whereas static strain and isometric contraction enable adaptable physiologic mechanisms for modulating or maximizing drug transport, cyclic strain enables an easily scalable physical means for further increasing drug penetration. The consistent effect of strain-dependent steric hindrance across drugs of different physicochemical properties demonstrates a physiologic means for selective drug uptake. Strain to L_o could facilitate maximal penetration of low molecular weight drugs, or filter drugs delivered in mixed formulations to allow selective entry of drugs below a certain size at desired temporal windows. Insights on the pharmacokinetic role of fiber arrangement indicate the anisotropic nature of intramuscular drug transport with preference for the least tortuous pathway. The calculated upper limit for diffusion, which occurs parallel to the myofiber axis, suggests transport across fibers is the limiting direction in drug distribution. As axial drug transport outweighs radial penetration, focal application of drug along the muscle axis may possibly achieve delivery to the entire length of the muscle but come at the expense of reduced drug penetration into the tissue. Moderate strain towards L_o may precipitate the formation of widened interstitial channels aligned in the radial direction of drug penetration that reduce radial tortuosity, attenuate transport anisotropy, and enhance drug penetration. Dispersion presents a physically controlled mechanism by which drug

transport can be enhanced. It can be readily applied in combination with architectural control of tissue porosity to modulate drug penetration. These physiologic mechanisms engender physical therapies that stretch or stimulate muscle targets in controlled regimens as strategies for improving controlled drug delivery.

The relationship between drug uptake and target tissue functional architecture and activity presents new insights on the significance of biologic form and function. We hypothesize that maximal porosity occurs at the strain associated architectural configuration that dictates peak contractile performance because this, in fact, represents a true physiologic and evolutionary advantage rather than a coincidence of nature. One can readily envision how optimized transport is related to peak contractile performance by structural states in which energy conservation is maximized and muscle mechanics cycle most readily through relaxation and recovery after contraction. Greater porosity and reduced intramuscular and extravascular pressure at L_o may allow optimal muscle blood flow to sustain the necessary rate of metabolic substrate delivery and waste removal to meet the demands of peak contractile performance, thus optimizing functional efficiency. Reciprocally, peak contractile performance occurs at the structural configuration that facilitates optimal blood inflow to not only sustain the production of such peak function, but also to maximize venous outflow through the squeezing effect of peak muscle activity on intramuscular veins to match the rate of maximal blood inflow. The aim of such architectural design to maximize tissue function is also exemplified by biologic adaptation that centers the physiologic range of skeletal muscle extensibility and operation on L_o. Central placement of peak contractile performance within the physiologic range of function maximizes contractile effectiveness during locomotion and

postural stability. Correlation of maximal drug penetration with optimal muscle function reflects biologic design that harmonizes the reciprocal interaction between tissue and its physical environment. Just as optimal biologic responsiveness to pulsatile fluid flow in different cell types occurs at the inherent frequencies to which they are exposed in their physiologic environments [207], optimal intramuscular pharmacokinetics center within the range of physiologic tissue extensibility and operation at the length of maximal force generation and contractile efficiency, L_o. Architecturally and functionally dictated optimal pharmacokinetic conditions suggest the existence of potential therapeutic windows that correspond to unique setpoints in the physiologic operating range of all target tissues and organs.

3.5.7 Conclusions

Mechanically active and load-bearing tissues present an active pharmacokinetic environment in which permeability and drug transport are influenced by the interrelated effects of architectural configuration and functional dynamics. The dispersive effects of cyclic loading can be superposed on the structural dependence of tissue permeability to enhance drug penetration. The correlation of both L_o and an architecturally modulated optimal contractile rate with a respective maximal drug penetration elucidates the biologically resonant nature of skeletal muscle interaction with the physical environment. This biologic design not only introduces new strategies for controlled drug delivery, but also elucidates the pharmacokinetic impact of functional architecture in all target tissues.

TABLE OF SYMBOLS IN COMPUTATIONAL MODELS OF SKELETAL MUSCLE

Symbol	Definition	Units
α	normalized amplitude of radial deformation during cyclic stretch, $\Delta R/Rn$	
$c(r,t)$	concentration of the drug in the tissue	(g/mm^3)
$\langle c \rangle$	average concentration in the periodic unit	(g/mm^3)
$\chi(x,y)$	the small periodic component of the macroscopic drug concentration field	
δ_{ij}	Kronecker delta	
$D(\underline{X})$	diffusivity tensor of the drug in the extracellular space	(mm^2/s)
D_{eff}	effective diffusion coefficient of the drug in the tissue (in the direction $\underline{e}$)	(mm^2/s)
D_{int}	diffusion coefficient of the drug in the interstitial space	(mm^2/s)
D_w	free diffusion coefficient of the drug in water	(mm^2/s)
D_1	dimensionless reducing factor of D_w due to porosity and fiber arrangement	
D_2	dimensionless reducing factor of D_w due to interstitial characteristics	
$\underline{e}$	direction of macroscopic diffusion	
ε_{ax}	axial strain	
ε_{tr}	transverse strain	
Γ_1	symmetric and periodic boundaries of Ω	
Γ_2	boundaries of Ω at the fiber interface with the interstitial space	
κ	periodicity of myofibers on the microscopic level	
ΔL	change in length of the muscle	(mm)
Ln	length of the muscle at the mean strains defined by index n	(mm)
ν	Poisson ratio	
n	index of mean strains = 0, 5, 10, 20	
$\underline{n}$	outward unit normal vector at the solid boundaries, fiber surfaces, of Ω	
ω	radial frequency of pulsation of Ω_D	(rad/s)
$\Omega(x,y)$	computational domain for solving the homogenized equation of the static model	
$\Omega_D(r,\theta,t)$	computational domain for the dynamic model	
$\Omega_0(R,\Theta)$	reference domain used in the ALE formulation of the transport equation	
φ	tissue porosity; the ratio of the area or volume of interstitial space to the total area or volume, respectively, of the tissue	
P	periodic unit	
$r(t)$	radius of the muscle cross-section in Ω_D	(mm)
R	radius of the muscle cross-section in Ω_0	(mm)
ΔR	amplitude of radial deformation during cyclic stretch	(mm)
R_D	maximum or minimum radius of the muscle section during	(mm)

	cyclic stretching	
Rn	radius of the muscle at the mean strains defined by index n	(mm)
t	time	(s)
T	period of pulsation of Ω_D	(s)
T_f	simulation time (3600s)	(s)
V	initial volume of the muscle	(mm^3)
ΔV	change in volume of the muscle	(mm^3)
V_P	volume of the periodic unit	(mm^3)
$\underline{w}$	velocity vector of the moving domain Ω_D	(mm/s)
w_r	radial component of the velocity vector $\underline{w}$	(mm/s)
$\underline{X}=(X_1, X_2, X_3)$	Cartesian coordinate system used to describe the microscopic scale	
$\underline{x}= (x_1, x_2, x_3)$	Cartesian coordinate system used to describe the periodic unit $\Omega(x,y)$	

4. PHARMACOKINETICS IN CARDIAC MUSCLE: MULTIDIMENSIONAL ARCHITECTURE AND MECHANICAL LOADING

4.1 Abstract

Introduction: Dynamic tissue architecture, mechanics, and presentation of specific binding sites in contractile tissues can influence the pharmacokinetics of locally delivered agents. We investigated drug transport in the myocardium under controlled mechanical loads.

Methods and Results: Dextran (20 kDa) and fibroblast growth factor 2 (FGF2) solutions were delivered epicardially to *ex vivo* rat hearts in contracture-arrest with complete ventricular evacuation, and in diastolic arrest under static ventricular distension from 100 to 800 μL. Dextran and FGF2 penetration were maximal at the minimal equilibrium volume devoid of principal mural strain by either contractile tone or ventricular distension, and were reduced by both contracture and progressive left ventricular (LV) filling. Dextran penetration, tissue porosity, and active LV pressure correlated ($r \geq 0.98$) over both mural thickening (+37% principal radial strain) and thinning (-78%), and were all maximal in the absence of strain, demonstrating physiologic significance of the equilibrium dimensions and constitutive porosity of the heart, and their impact on function and pharmacokinetics. Effective diffusivity of non-specifically binding dextran exceeded that of FGF2 by more than 5.5-fold ($p<0.05$) at all volume states, demonstrating the effect of architectural strain on drug penetration was consistent across binding properties. Dextran penetration within *in vivo* beating hearts was enhanced above the maximum observed *ex vivo* at equilibrium volume under static

conditions alone. Drug penetration increased with increasing heart rate, LV pressure, contractility, and stroke volume in hearts whose inotropy was modulated by Esmolol, Ringer's lactate solution, or Dobutamine, demonstrating the dispersive effects of cyclic cardiac function.

Conclusions: Mechanical architecture and function underlie intramyocardial pharmacokinetics and act in concert to modulate drug transport across different binding properties. Therapeutic management of functional mechanics in myocardial targets may enable a physiologic mechanism for controlled drug delivery.

Keywords: Mechanical; Pharmacokinetics; Myocardium; Contraction; Binding

4.2 Introduction

Myocardial tissue presents a unique pharmacokinetic environment in which transport of locally delivered drugs can be influenced by not only physicochemical interactions, but also dynamic architectural configurations and mechanical function. The laminar architecture of the ventricular wall, composed of branching networks of interconnected myofibers layered in multiple transmural orientations [109] and defined by cleavage planes [111], presents a uniquely complex physical environment that can impact interstitial drug transport in a strain-dependent manner. Multi-dimensional dynamic effects such as intramuscular pressure [208], local myofiber deformations [209], shear of laminae [114, 210], and cross-fiber strains associated with mural thickening [115, 119] and thinning [114] during the coordinated wall mechanics of cyclic cardiac function can further alter transport kinetics. While local delivery strategies minimize systemic losses [163] and enable efficient administration of therapeutic agents to target

tissues [211], ultimate drug distribution and pharmacologic effect are determined by target tissue pharmacokinetics.

Strategies for controlled release of drugs to the myocardium must consider the transport effects of functional architecture and mechanical activity to optimize defined release kinetics [48] for therapeutic effectiveness. A quantitative understanding is critical for strategies like therapeutic angiogenesis to ischemic muscle, in which lesions are spatially focal [164], therapeutic windows are narrow [165], biologic half-lives of delivered proteins are short [50], and systemic side-effects of therapies are detrimental [174]. Knowledge of how specific binding of angiogenic therapies such as fibroblast growth factor 2 (FGF2) modulates drug transport in the context of mechanical loading is essential for delivery technologies to achieve accurately sustained and localized administration of pharmacologic doses to ischemic targets.

Whereas studies have investigated how myocardial stretch or contraction affects total uptake of L-arabinose [212] and amino acid [213, 214], they have elucidated primarily the influence of activity-dependent metabolism on substrate uptake. Few literature reports have focused on the pharmacokinetic impact of mechanical strain and *in vivo* cardiac dynamics on drug transport. Some have demonstrated atrial distension increases endocardial endothelial permeability [86] and atrial contraction and distension increase translocation of atrial natriuretic peptide and extracellular fluid [85]. Yet, there remain conflicting data on how myocardial contraction affects uptake of drugs like ouabain [215, 216], or how heart rate affects uptake of intravenously administered drugs [217, 218]. We applied a rigorous, quantitative framework to investigate the characteristic and synergistic impact of architecture and mechanics on intramyocardial

transport of locally delivered soluble macromolecules. Having previously demonstrated the pharmacokinetic impact of functional architecture in skeletal muscle, we systematically investigate the effects of mural strain, specific binding of heparin-binding FGF2, and dynamic mechanical loading intrinsic to cardiac function on drug transport.

4.3 Methods

4.3.1 Ventricular Distension

Experiments were conducted within the animal welfare regulations and guidelines of Massachusetts. Male Sprague-Dawley rats (380-400 g) were administered 1000 U of Heparin via intraperitoneal injection 5 min prior to euthanasia with inhaled CO_2. Thoracotomy was performed immediately after euthanasia, and 30 ml of Krebs-Henseleit-Butanedione Monoxime (KH-BDM) cardioplegia (118.1 mM NaCl, 20 mM KCl, 1.2 mM $CaCl_2$, 1.2 mM $MgSO_4$, 1.2 mM KH_2PO_4, 25 mM $NaHCO_3$, 11.1 mM Glucose, supplemented with 15 mM BDM at pH 7.4) oxygenated with 95% O_2-5% CO_2 at room temperature (RT) was retrogradely infused down the ascending aorta to perfuse the coronary vasculature and arrest the heart in diastole. The left atrium was excised and a fluid-filled balloon (Harvard Apparatus, Size 6 or 10) was inserted into the left ventricle (LV) via the mitral opening and inflated by syringe to 100 μL, 200 μL, 400 μL, or 800 μL to simulate distending mural strains produced by ventricular filling (Figure 4.1). Hearts for a 0 μL group were perfused with regular KH containing 5 mM KCl and no BDM and allowed to undergo contracture to complete LV emptying without the presence of a balloon. Hearts ($n = 6$) were excised and rinsed twice with their respective perfusate to remove epicardial blood. Hearts were immersed for 1 h in 15 ml of 1 mM neutrally

charged 20 kDa FITC-dextran in PBS that was oxygenated with 95% O_2-5% CO_2 and kept well-mixed by magnetic stir bar at RT.

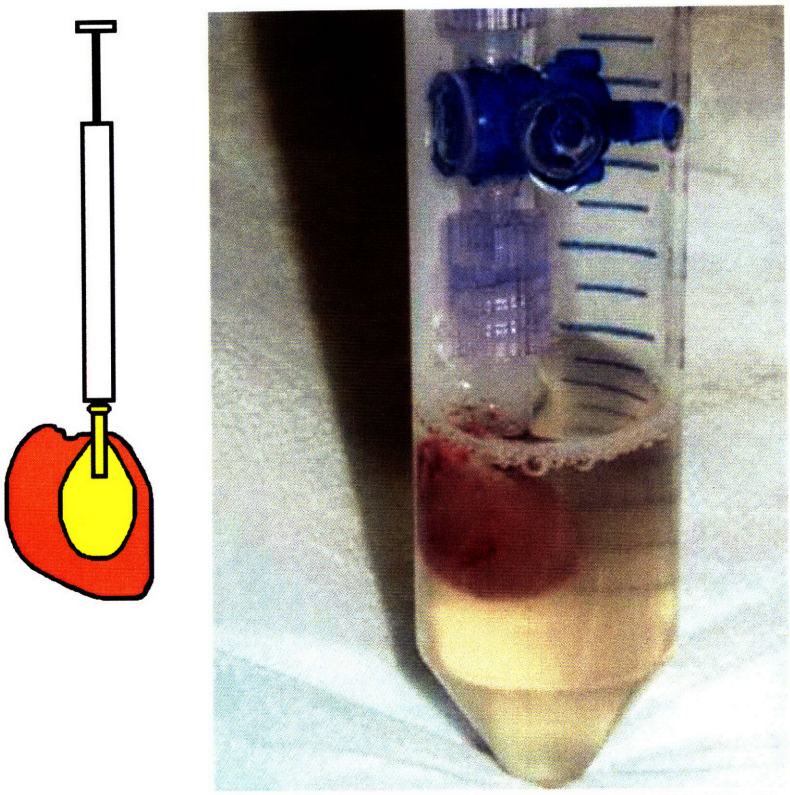

Figure 4.1. Ventricular distension. LVs were distended by a fluid-filled balloon to simulate chamber filling. Hearts were distended by incubated in drug source.

4.3.2 FGF

The LVs of diastolically arrested hearts (n = 6) were distended to 100 μL and 800 μL. 400 μL of 0.02 mM FGF2 conjugated to Alexa Fluor 488 in PBS was delivered to the myocardium for 1 h at RT from a drug releasing reservoir affixed to the epicardium of the anterior wall using a liquid tissue adhesive (Glustitch). The rest of the epicardium was kept moist by regularly dripping PBS.

4.3.3 Recombinant FGF2 Production

Recombinant human FGF2 (155 residue) was expressed from cDNA in *Escherichia coli* strain FICE-127 transformed by expression vector pFC80, which confers resistance to ampicillin and encodes FGF2 under the control of the tryptophan promoter (constructed by Dr. Antonella Isacchi, Amersham Pharmacia Biotech and Upjohn, Milan, Italy; donated by Dr. John Heath, School of Biochemistry, University of Birmingham, Edgbaston, Birmingham, UK). FICE-127 bacteria were inoculated into 100 ml of LB Medium (MP Biomedicals) containing 100 μg/ml of Ampicillin (Invitrogen) and incubated overnight at 37°C, shaking at 250 RPM. The inoculum was diluted 1:100 in antibiotics-free M9 Minimal Medium (Bioworld) containing 1 g/L of casamino acids (Becton Dickinson Diagnostic Systems) without tryptophan to induce protein production. Bacteria were incubated for 6 h at 37°C and 250 RPM. The broth was centrifuged at 8,000 RPM and 4°C for 10 min, supernatant was discarded, and pellets of cells were collected and stored overnight at -80°C. Frozen pellets were resuspended in GET buffer (50 mM Tris, 10 mM EDTA, 100 mM Glucose, pH 8.0) containing 1 mg/ml lysozyme and 1% Triton X-100, mixed for 5 min, and lysed by homogenization (Polytron; Kinematica AG, PT10/35 Drive) 3 times for 10 s each with 5 s resting periods on ice to prevent protein denaturation. The cell lysate was centrifuged at 9,000 RPM and 4°C for 10 min. Lysate supernatant was loaded into a Heparin-Sepharose affinity chromatography column (5 ml HiTrap Heparin HP, GE Healthcare) and allowed to bind for 1 h at 4°C. Using FPLC (Pharmacia Biotech), the column was washed with PBS and a linear gradient of NaCl concentration (0.15-2 M). Elution was collected at 1 ml fractions. FGF2 was present in fractions eluted with 1.5-1.8 M NaCl. FGF2 solution was

desalted, exchanged into PBS buffer, and concentrated by centrifugation using centrifugal filter devices with 9 kDa cut-off (ICON Protein Concentration, Pierce Biotechnology). Presence of FGF2 was confirmed by Western blot as a band of 18 kDa reacting to rabbit polyclonal anti-FGF2 antibody (Abcam). Bioactivity of FGF2 was confirmed by proliferation assay using bovine aortic endothelial cells. Final FGF2 concentration was determined by bicinchoninic acid assay (BCA, Pierce Biotechnology).

4.3.4 Fluorescent Labeling of FGF2

A 1 ml Heparin-Sepharose column was loaded with 1 ml FGF2 (5 mg/ml in PBS) and allowed to bind for 1 h at 4°C. The column was washed with 5 ml of 0.1 M sodium bicarbonate to change pH to 8.3 and loaded with 1 ml of 1 mg/ml Alexa Fluor 488 (AF488) succinimidyl ester (Molecular Probes). Binding reaction of AF488 to FGF2 was allowed for 10 min at RT. Using FPLC, the column was washed with PBS and a linear gradient of NaCl concentration (0.15-2 M). Elution was collected at 1 ml fractions. Labeled protein and fluorescence intensity in eluted fractions were verified by measuring absorbance at 280 nm and fluorescence emission (ThermoLabsystems Fluoroskan Ascent®FL, ex: 485 nm/ em: 538 nm). AF488-FGF2 fractions were exchanged into PBS buffer and concentrated by centrifugation. AF488-FGF2 concentration was determined by BCA.

4.3.5 Heart Rate and Contractility

Male Sprague-Dawley rats (380-400 g) were anesthetized with intraperitoneal injection of Pentobarbital (25 mg induction, 12.5 mg/h maintenance), intubated with a 14

gauge (2 mm diameter) endotracheal tube, and ventilated under positive pressure with O_2 (96 breaths/min, 1.3 ml tidal volume). The right jugular vein was cannulated with PE50 tubing. A 2-Fr Pressure-Volume catheter (Mikro-Tip® Ultra-Miniature PV Catheter, SPR-869, Millar Instruments) was introduced into the right carotid artery and advanced into the LV. Thoracotomy was performed with minimal bleeding by an incision from the diaphragm to the 3rd intercostal space just left of the sternum. The ribcage was held open by an Alm retractor, and the pericardial sac was resected to expose the beating heart. A drug releasing reservoir was affixed to the epicardium of the LV anterior wall with Glustitch. Rat temperature was monitored by rectal probe and maintained at 37°C by heat pad and lamp. After a 5 min stabilization period, proper PV catheter position in the LV was established by monitoring pressure-volume loops. 400 μL of 1 mM 20 kDa FITC-dextran in PBS was added to the reservoir and exposed to the epicardium for 1 h at RT. Pressure-volume loop behavior and hemodynamic parameters were monitored and recorded throughout drug delivery using an MPVS-300 system (Millar Instruments, PowerLab 8SP A/D Data Acquisition System, PVAN 3.6 Analysis). Heart rate and inotropy of hearts ($n = 4$) were modulated by intravenous (IV) infusion (1.2 ml/h) via the right jugular vein of Esmolol (300 μg/kg/min), Dobutamine (40 μg/kg/min), or Ringer's lactate solution.

4.3.6 Quantification and Microscopy

After drug delivery, hearts were rinsed twice in 15 ml of PBS and snap-frozen in -145°C Isopentane. 8 μm thickness cross-sections on the short-axis of the heart were cut using a Leica CM1850 cryotome. FITC-dextran or AF488-FGF2 in sections was imaged

using epifluorescence microscopy (Leica DMRA2, 50× magnification, Hamamatsu ORCA286, Metamorph 6.3, ex: 450-490 nm bandpass/ em: 515 nm longpass). An exposure rate was chosen that eliminated tissue autofluorescence and avoided intensity saturation of the system by the drug source. Images were analyzed using Matlab. A preliminary calibration confirmed the linear relationship between image fluorescence intensities and tissue drug concentrations for 3 orders of magnitude of source concentrations. This is in accordance with Beer's Law for very low source concentrations, $I=\varepsilon CQ$, in which I is fluorescence intensity, ε is the molar absorption coefficient, C the molar concentration, and Q the quantum yield [140]. Unidirectional drug penetration from the epicardial surface was quantified. Intramuscular penetration depth was defined as the perpendicular distance from the surface at which fluorescence intensity decreased to 5% of the surface intensity. Effective diffusivity, D_{eff}, associated with measured penetration depth was calculated based on the equation for diffusion in a semi-infinite solid, $D_{eff} = \frac{x^2}{4 \cdot t \cdot (erf^{-1}(0.95)^2)}$, where x is penetration depth, and t is the 3600 s duration of incubation. Effective diffusivity is used to describe the observed transport, which encompasses the impact of steric forces, potential specific and non-specific binding interactions within the tissue interstitium, and cellular internalization, in addition to the diffusive random thermal motion of solutes down concentration gradients.

4.3.7 Histology and Tissue Architecture

Hearts ($n = 4$) were contracture-arrested or diastolically arrested and immediately excised. Contracture-arrested hearts were allowed to undergo complete LV emptying without the presence of an intraventricular balloon. LVs of diastolically arrested hearts

were distended by an OCT-filled (Optimal Cutting Temperature Compound, Tissue-Tek) balloon to 100 μL, 200 μL, 400 μL, or 800 μL. Hearts were snap-frozen with balloons in place. 8 μm thickness cross-sections on the short-axis of the heart were cut and stained with Hematoxylin and Eosin. Light microscopy images (90× magnification) were processed using Matlab. Tissue porosity (ratio of extracellular space area between myofibers to total area) in LV regions comprised of axial cross-sections of myofibers was quantified. LV mural thickness was measured. Epicardial surface markers (1 x 0.5 x 0.05 mm) were placed onto the LV of contracture-arrested or diastolically arrested hearts ($n = 6$). The minimum equilibrium dimension of the LV was determined in diastolically arrested hearts as the volume at which balloon inflation first encounters LV resistance and produces mural strain. Circumferential and longitudinal surface strains relative to the minimum mural dimension were measured as contracture-arrested hearts underwent complete emptying and diastolically arrested hearts underwent distension to 100 μL, 200 μL, 400 μL, or 800 μL. Principal strains in the radial, circumferential, and longitudinal axes were calculated by the equation: $\varepsilon_{1\_Principal} = \varepsilon_1 - \upsilon\varepsilon_2 - \upsilon\varepsilon_3$, in which Poisson's ratio $\upsilon = 0.5$ for an incompressible material, and index 1 = radial, circumferential, or longitudinal axis while indices 2 and 3 were the two other axes. Total strain was determined by the amplitude of the three-dimensional strain vector:

$$\varepsilon_{total} = \sqrt{\varepsilon_1^2 + \varepsilon_2^2 + \varepsilon_3^2}\ .$$

4.3.8 LV Mechanical Properties

Hearts ($n = 5$) were immediately excised and the coronary arteries were retrogradely perfused with KH at 37°C and oxygenated with 95% O_2-5% CO_2 in a

Langendorff setup. A fluid-filled balloon connected to a pressure transducer (Kent Scientific) was inserted into the LV and used to measure intraventricular pressure. LVs were distended to 0 μL, 100 μL, 200 μL, 400 μL, or 800 μL and electrically stimulated to produce isovolumetric twitch contractions at 1 Hz. Biphasic electric stimulus (15 V, 50 ms pulse) was applied by 2 stainless steel electrodes contacting the base and apex of the LV. Stimulus was generated using a National Instruments DAQPAD-6062E data acquisition board controlled by LabView 7.0. Pressure was continually recorded during stimulation in the MPVS-300. Elastance of the balloon was subtracted from minimum pressures recorded at each LV volume to calculate the passive LV pressure-volume relationship. Active LV pressure developed was calculated by subtracting the minimum pressure from the maximum pressure during stimulated contractions.

4.3.9 Statistical Analysis

Results are presented as mean ± SD. Student's t-Test, Single Factor Analysis of Variance (ANOVA), and Two-Factor ANOVA with Replication were applied to determine statistical significance in empirical data. Propagation of uncertainty in normalized data was calculated using the formula, $\frac{\Delta_z}{z} = \sqrt{(\frac{\Delta_x}{x})^2 + (\frac{\Delta_y}{y})^2}$, where Δ_x, Δ_y, and Δ_z is the standard deviation of the numerator (x), denominator (y), and normalized value ($z = x/y$), respectively.

4.4 Results

4.4.1 LV Strain and Mechanical Properties

The minimum equilibrium dimension of the LV occurs at 100 μL, which is devoid of constitutive or residual strain. Smaller volumes can be observed only in contracture-arrested states. Contracture produces radial thickening with concomitant circumferential and longitudinal mural shortening (Figure 4.2). LV distension produces exponential radial thinning with concomitant circumferential and longitudinal extension. While circumferential extension reaches an upper limit with moderate LV filling, longitudinal extension continues with greater filling in agreement with cardiac mechanics that favor longitudinal dimension changes [116]. The Frank-Starling relationship,

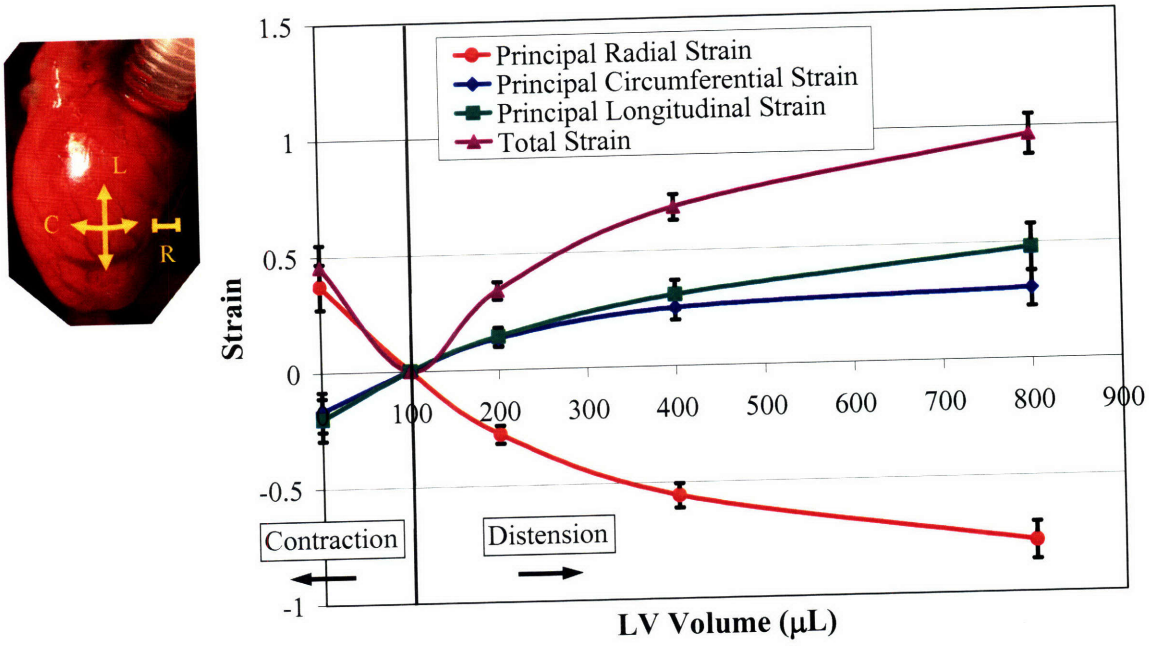

Figure 4.2. Principal radial, circumferential, longitudinal, and total mural strains associated with LV contraction and distension. Strains were measured relative to chamber dimensions at 100 μL, the equilibrium volume devoid of intrinsic mural strain (0% total strain). Contracture to full LV evacuation (0 μL) produces mural thickening (37 ± 10% radially) and shortening (-17 ± 9% circumferentially, -20 ± 9% longitudinally). LV filling produces exponential mural thinning (to -78 ± 8% at 800 μL) and extension (to 30 ± 8% circumferentially, 48 ± 10% longitudinally at 800 μL).

expressed in reference to tissue strain, correlates development of peak contractile force with the absence of strain (Figure 4.3). Thus, optimal overlap of myosin and actin contractile myofilaments occurs at equilibrium volume. Isovolumetric active

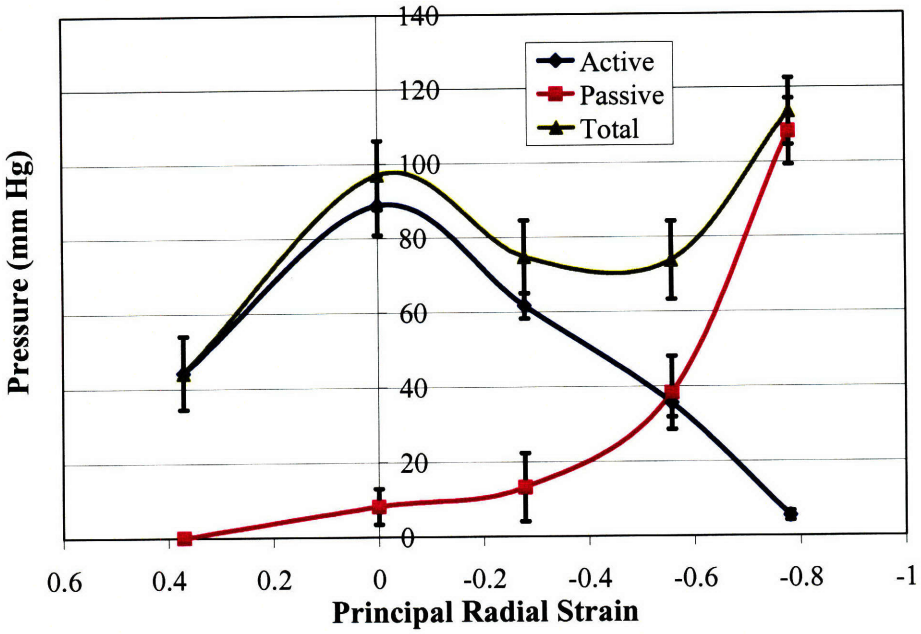

Figure 4.3. Total, active, and passive pressure-volume relationships of the LV plotted against principal radial strains associated with each intraventricular volume. Isovolumetric active pressure increases from 44.22 ± 9.82 mmHg at complete LV evacuation (37% mural thickening), to a maximum of 88.83 ± 8.02 mmHg in the absence of constitutive mural strain, and decreases thereafter with further chamber filling to 5.42 ± 1.26 mmHg at 78% mural thinning. Active pressures in both the increasing and decreasing halves of the profile are statistically significantly different (T-test, $p<0.05$).

pressure at complete LV evacuation increases by twofold to a maximum in the absence of mural strain and decreases thereafter with further chamber filling. The classic exponential curve characterizing the passive extensibility of muscle is observed.

4.4.2 Transport with LV Distension

Ventricular diffusion of dextran in contractured and diastolically arrested hearts is influenced by volume-modulated mural strain (Figure 4.4*B*). Drug penetration is bimodally related to total mural strain, peaking in the absence of strain at the equilibrium volume (Figure 4.4*C*). Maximal penetration is reduced by the presence of strain introduced by either contracture or LV filling, decreasing linearly with increasing distension. Drug penetration correlates with the Frank-Starling relationship ($r = 0.98$, Figure 4.3), suggesting architectural state and its functional correlate are significant indicators of the pharmacokinetic environment in contractile tissues. Maximal drug penetration correlates with peak contractile efficiency.

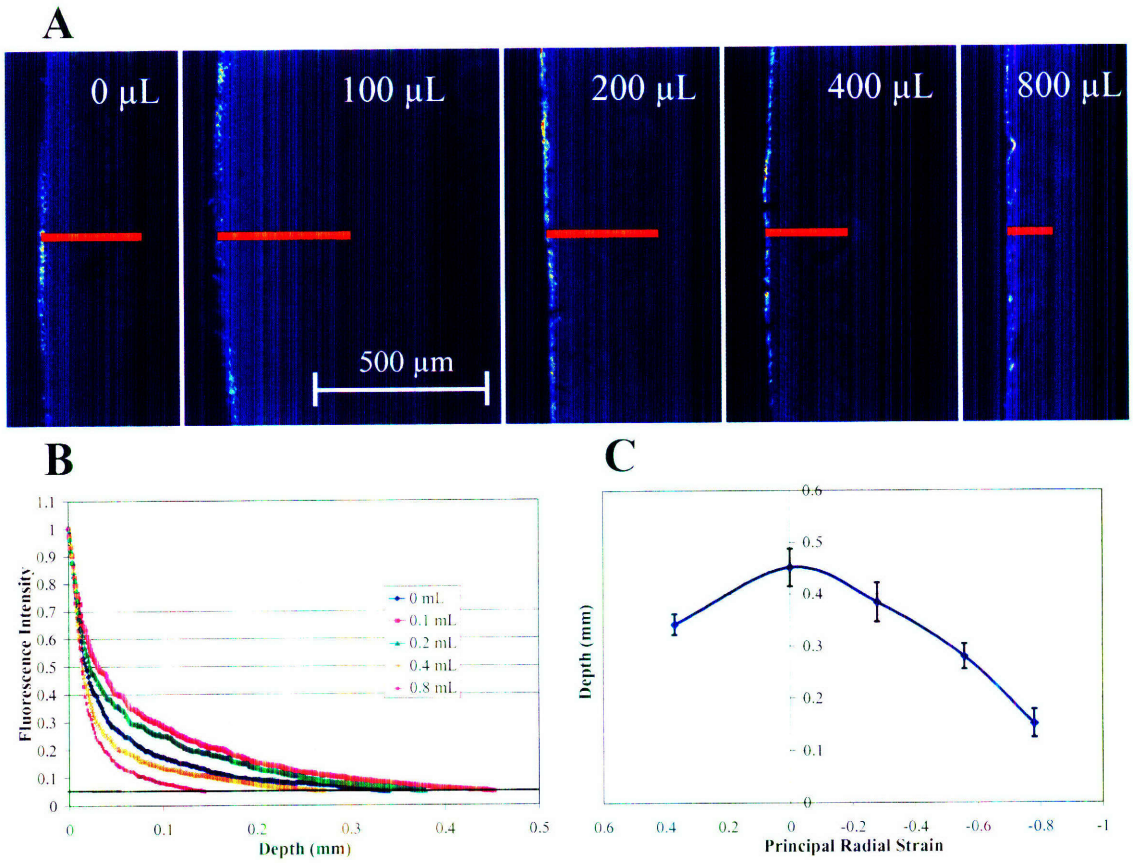

Figure 4.4. LV mural transport of dextran versus static intraventricular volume. (*A*) Fluorescent images of dextran penetration. (*B*) Fluorescent profiles of epicardial dextran penetration demonstrate diffusion (determined by fit to error function) modulated by static LV distension. (*C*) Drug penetration is maximal (0.45 ± 0.04 mm) in the absence of tissue strain and is reduced by contracture (0.34 ± 0.02 mm at complete LV evacuation) and diastolic filling, decreasing linearly with LV distension (-0.38 mm/compressive radial strain to 0.15 ± 0.03 mm at extreme distension). Penetration depths in the increasing and decreasing halves of the profile are statistically significantly different (T-test, $p<0.05$).

4.4.3 FGF

Two-Factor ANOVA reveals that penetration is significantly influenced by ventricular distension (D_{eff} at 100 µL exceeds that at 800 µL by 8.9- and 9.1-fold for dextran and FGF2, respectively, $p<0.05$) and drug binding (D_{eff} of 20 kDa dextran exceeds that of FGF2 by 5.5- and 5.7-fold at 100 µL and 800 µL, respectively, $p<0.05$) (Figure 4.5). While specific binding significantly reduces macromolecular diffusion,

mural strain consistently influenced drug penetration across different physicochemical and binding properties.

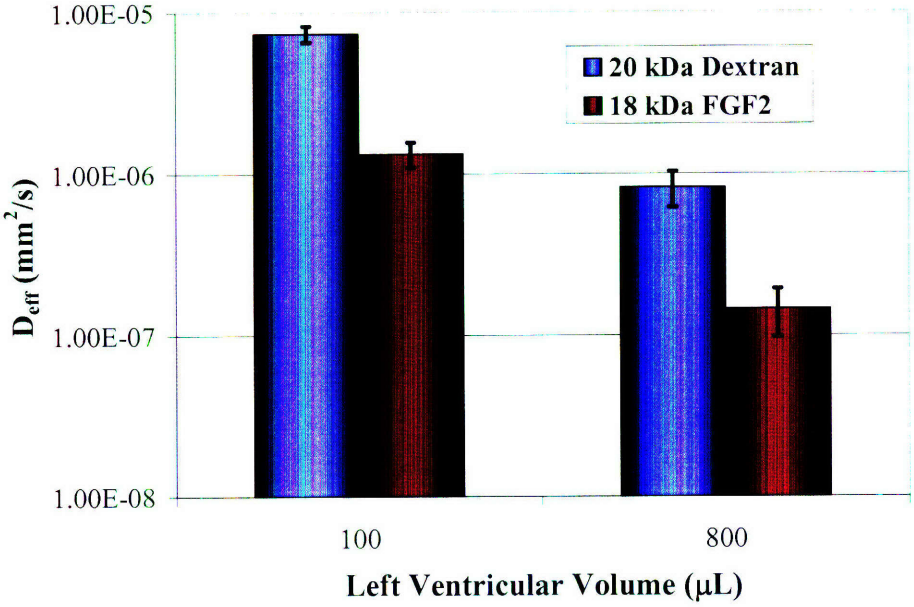

Figure 4.5. Pharmacokinetic impact of ventricular distension in the presence of drug binding. Effective diffusivity of 20 kDa dextran is greater than that of FGF2 at both 100 µL and 800 µL. D_{eff} at 100 µL and 800 µL is $7.36\text{x}10^{-6} \pm 8.46\text{x}10^{-7}$ mm^2/s and $8.28\text{x}10^{-7} \pm 2.07\text{x}10^{-7}$ mm^2/s, respectively, for dextran and $1.33\text{x}10^{-6} \pm 2.33\text{x}10^{-7}$ mm^2/s and $1.46\text{x}10^{-7} \pm 4.78\text{x}10^{-8}$ mm^2/s, respectively, for FGF2.

4.4.4 LV Architecture

Myofiber arrangement (Figure 4.6*A*) is isotropic and densely packed in the presence of significant total tissue strain (contracture, 400 µl, and 800 µl). This homogeneous distribution is interrupted by enlargement of intercellular channels and separation of myofiber bundles at cleavage planes when total strain is relieved (equilibrium volume and 200 µl). Fiber rearrangement by channels, which cleave muscle bundles in orientations that correlate with fascicular borders, not only increases porosity,

but is also an independent parameter that significantly impacts drug transport, as we have shown previously.

Tissue porosity, used as a measure of interstitial space, is maximal (0.27 ± 0.07) in the absence of strain (Figure 4.6*B*). This porosity is in agreement with an inulin distribution space, which characterizes the volume of extracellular space, of 26.4% found previously in rat myocardium [219]. Porosity is reduced by the presence of strain introduced by either contracture or LV filling, decreasing linearly with increasing distension. That the porosity profile correlates with the isometric active pressure ($r = 0.99$) and dextran penetration ($r = 0.98$) profiles (Figure 4.6*C*) suggests tissue porosity, which is the architectural correlate of functional state, is a direct determinant of drug transport in contractile tissues. There is significant correspondence of architectural state with both muscle function and pharmacokinetics.

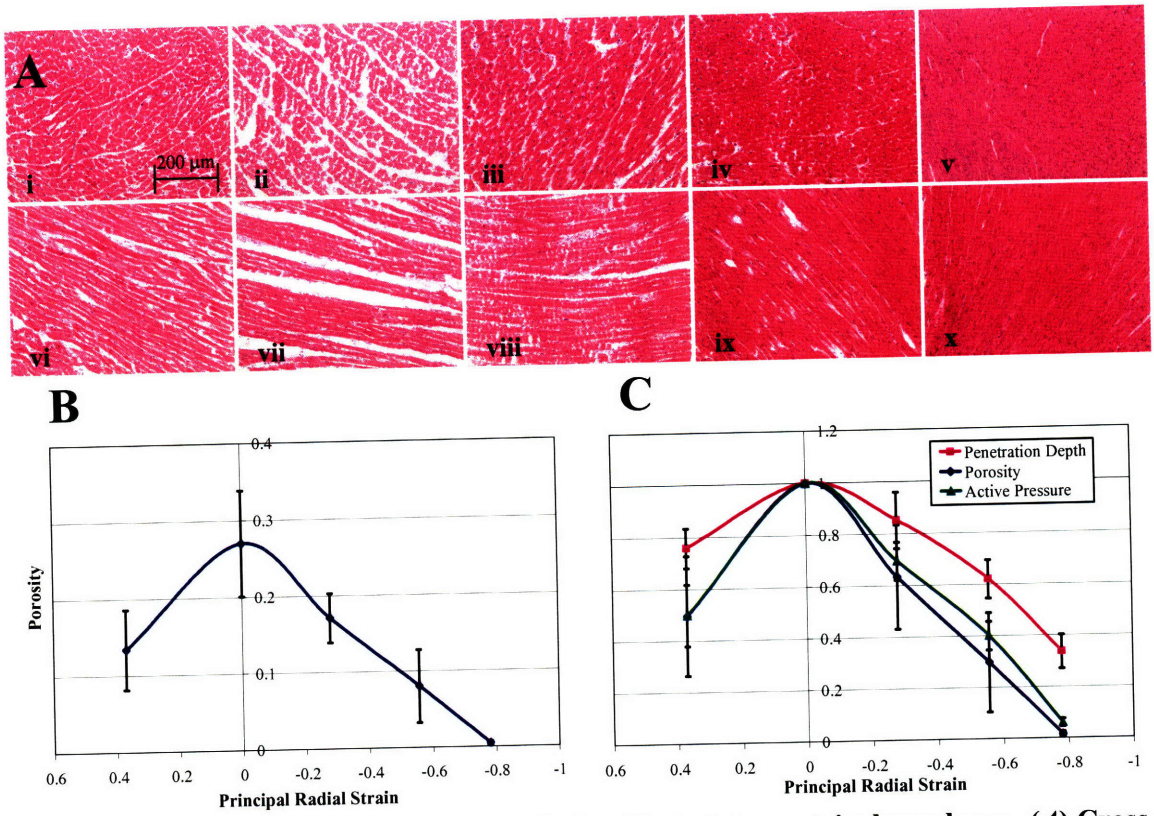

Figure 4.6. Architectural parameters in relationship to intraventricular volume. (*A*) Cross-fiber (*i-v*) and along-fiber (*vi-x*) regions in short-axis cross-sections of Hematoxylin and Eosin stained LV undergoing (*i, vi*) contracture, or distension to (*ii, vii*) 100 μL, (*iii, viii*) 200 μL, (*iv, ix*) 400 μL, or (*v, x*) 800 μL. Myofibers are pink and extracellular space is white. (*B*) Porosity is maximal (0.27 ± 0.07) in the absence of strain and is reduced by contracture (0.13 ± 0.05) and diastolic filling, decreasing linearly with LV distension (-0.34 /compressive radial strain to 0.004 ± 0.002 at extreme filling). Porosity values in both the increasing and decreasing halves of the profile are statistically significantly different (T-test, $p<0.05$). (*C*) Normalized drug penetration, porosity, and active pressure profiles correlate positively (r = 0.98, penetration/porosity; r = 0.98, penetration/pressure; r = 0.99, porosity/pressure). Peak drug penetration, porosity, and pressure occur at the equilibrium volume (0% strain).

4.4.5 Heart Rate and Contractility

The kinetics of contraction were modulated with IV administration of an antagonist (Esmolol) and agonist (Dobutamine) of β_1-adrenergic receptors in the heart, which respectively decreases and increases heart rate, contractility (dP/dt), and peak systolic LV pressure (Figure 4.7). The physiologic range of intraventricular volumes through the cardiac cycle demonstrates increasing end-diastolic volume and stroke volume and decreasing end-systolic volume with increasing adrenergic activity. End-diastolic volumes in hearts do not exceed the equilibrium volume even with increased adrenergic stimulation.

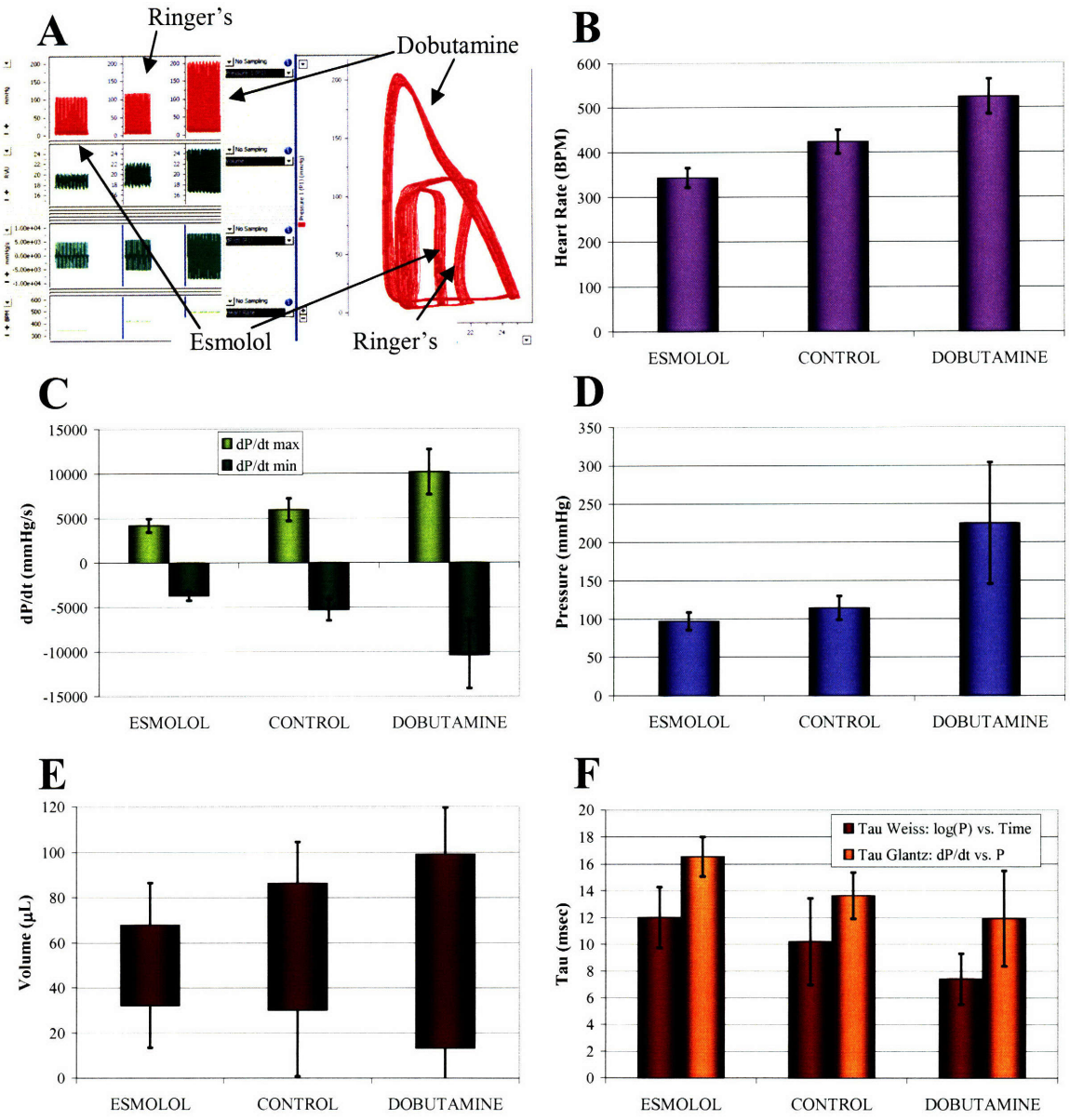

Figure 4.7. Inotropic modulation of cardiac performance. (*A*) Hemodynamic measurements and pressure-volume loops in the MPVS-300 showing cardiac function under pharmacologic effects of Esmolol, Ringer's lactate, and Dobutamine. (*B*) Heart rate (343.4 ± 21.5 BPM, 423.6 ± 26.4 BPM, 524.1 ± 39.2 BPM), (*C*) contractility (4207.7 ± 744.7 mmHg/s, 5956.2 ± 1248.0 mmHg/s, 10,176.9 ± 2507.9 mmHg/s), and (*D*) LV pressure (97.2 ± 11.4 mmHg, 114.6 ± 15.2 mmHg, 225.0 ± 79.2 mmHg) increase with increasing adrenergic activity (Esmolol, Ringer's lactate, and Dobutamine, respectively). (*E*) End-diastolic volume (67.9 ± 33.2 µL, 86.4 ± 36.7 µL, 99.2 ± 41.0 µL) and stroke volume (35.7 ± 18.7 µL, 56.4 ± 18.0 µL, 85.9 ± 20.2 µL) increase while end-systolic volume (32.1 ± 18.6 µL, 30.1 ± 29.2 µL, and 13.3 ± 30.4 µL) decreases with increasing adrenergic activity. (*F*) Relaxation time constants calculated from the regression of log(pressure) vs. time (τ_{weiss} = 12.0 ± 2.3 ms, 10.2 ± 3.2 ms, 7.4 ± 1.9 ms) and dP/dt vs. pressure (τ_{glantz} = 16.6 ± 1.4 ms, 13.6 ± 1.7 ms, 11.9 ± 3.6 ms) decrease with increasing adrenergic activity. All hemodynamic parameters occurring with each level of adrenergic activity are statistically significantly distinct (T-test, $p<0.05$).

Multi-dimensional mechanical loading inherent to cyclic cardiac function enhances drug penetration above that mediated by mural strain alone (Figure 4.8). Dextran penetration increases linearly with inotropic stimulation and heart rate ($r = 1$), contractility (dP/dt, $r = 0.99$), LV peak pressure ($r = 0.95$), diastolic volume ($r = 0.98$), and stroke volume ($r = 1$) and correlates negatively with relaxation time constants ($r = -0.98$) (Figure 4.7). Even with positive inotropic intervention, end-diastolic volumes are all less than the equilibrium volume, 100 μL, demonstrating a physiologic range of LV volumes bounded by a minimum equivalent to contracture to full LV emptying and a maximum equivalent to the equilibrium volume. This volume range not only confirms physiologic operation occurs on the ascending portion of the Frank-Starling curve [220], but also reveals through anatomic correlation that it occurs on the ascending and descending portions of the tissue porosity and total strain curves, respectively, which significantly influence the pharmacokinetic environment.

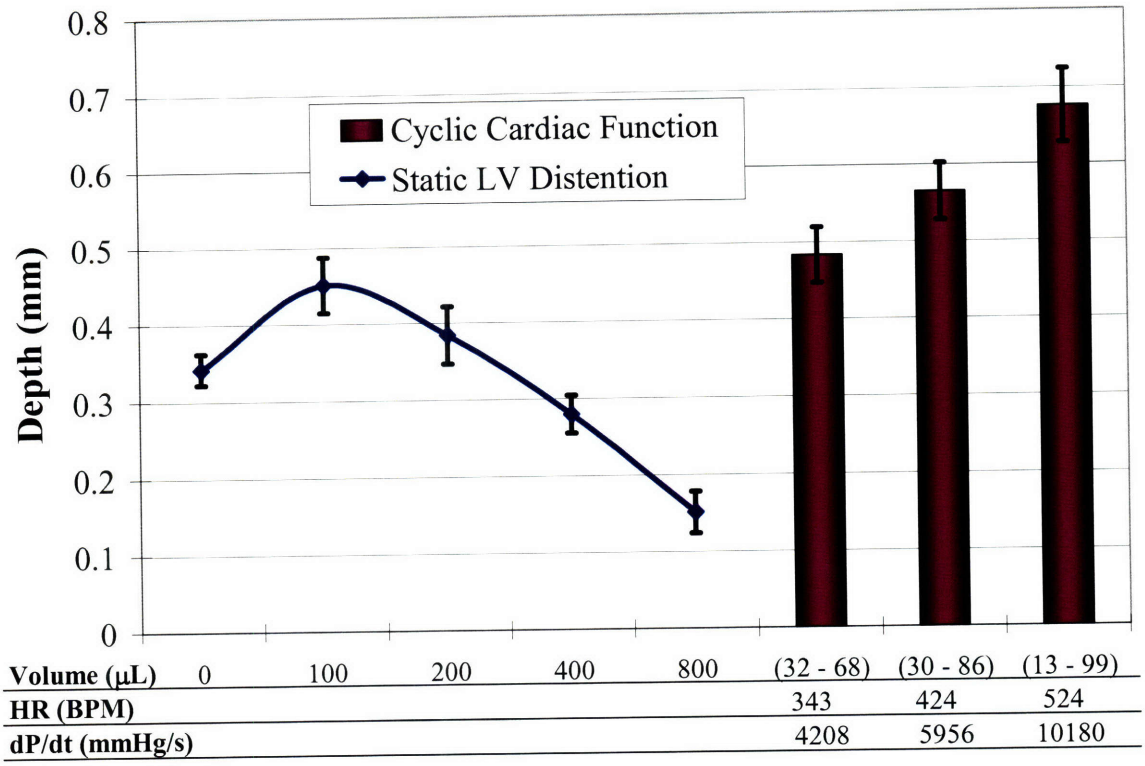

Volume (μL)	0	100	200	400	800	(32 - 68)	(30 - 86)	(13 - 99)
HR (BPM)						343	424	524
dP/dt (mmHg/s)						4208	5956	10180

Figure 4.8 Mural drug penetration under myocardial function. Cyclic cardiac function enhances dextran penetration above the maximum occurring at static equilibrium volume. Penetration increases significantly (T-test, $p<0.05$) with increasing adrenergic activity to 0.48 ± 0.04 mm with Esmolol (32.1-67.9 μl volume range, 343.4 ± 21.5 BPM, 4207.7 ± 744.7 mmHg/s), 0.57 ± 0.04 mm with Ringer's lactate (30.1-86.4 μl, 423.6 ± 26.4 BPM, 5956.2 ± 1248.0 mmHg/s), and 0.68 ± 0.05 mm with Dobutamine (13.3-99.2 μl, 524.1 ± 39.2 BPM, 10176.9 ± 2507.9 mmHg/s).

4.5 Discussion

Intramyocardial pharmacokinetics is greatly influenced by characteristic dynamic architecture, motion, and mechanical function in cardiac tissue. Within this paradigm, drug transport is further modulated by binding interactions dictated by specific pharmacology. Using both *ex vivo* and *in vivo* heart preparations, we compared transport of an inert tracer to a specifically binding protein to investigate the impact of controlled mechanical loading and specific binding on drug penetration in cardiac muscle.

4.5.1 Ventricular Distension

Drug transport investigated over the range of principal radial strains from 37% thickening (0 μL) to -78% thinning (800 μL) reflects the pharmacokinetic environment spanning physiologic LV architectural configurations and functional states throughout the cardiac cycle. Contracture to complete LV emptying (0 μL) represents architecture under extreme contraction while LV filling to the highest balloon volumes in relaxed hearts represents architecture under excessive distension. Within this range, 100 μL characterizes an equilibrium volume associated with mural architecture devoid of either contractile tone or ventricular distension and therefore total strain. This equilibrium configuration reflects the resting state of myofiber aggregation and maximal mechanical compliance of the ventricular wall rendered by the connective collagen fascial framework [112]. While myocardial distension has been shown to increase transport of atrial natriuretic peptide by enlarging the extracellular space [85], we have elucidated an architecturally defined optimal setpoint whereby maximal drug penetration corresponds with myocardial architecture absent of residual strain and primed for peak contractile efficiency. We previously showed that uniaxial strain in parallel-fibered soleus skeletal muscle influenced drug penetration through characteristic strain-dependent changes in myofiber cross-sectional area, fiber packing density, and tissue porosity that rendered maximal drug penetration at the physiologic configuration for peak muscle performance, L_o. Similarly, the bimodal pharmacokinetic environment in the myocardium likely results from characteristic strain-dependent changes in fiber arrangement [210], tissue porosity [221], and intramuscular pressure [208] associated with ventricular contraction and filling on either side of the equilibrium configuration that reduce drug penetration.

Myocardial tissue is formed of tightly knit bundles of elongated, multi-nucleated myofibers joined in an interdigitating manner to create a three-dimensional, branching network. This arrangement comprises a contiguous muscular strip that is wrapped helically to form the ventricular chambers and produces three major concentric layers, each with a different orientation, in the cardiac wall [109]. Within this global structural motif, myofibers are organized transmurally into distinct layers, or laminae, separated by connective membranes of collagen fibers in interposing demarcations known as cleavage planes [111]. While differences in myofiber arrangement and thus loading dynamics exist between regions such as the apex and mid-ventricle, local myofiber structure and mechanics are generally consistent. Through volume conservation, myofibers undergo thinning with elongation. With progressive mural stretch, fiber density increases and mural thickness decreases as increasingly thin fibers compact together and mural laminae slide relative to each other [114]. These rearrangements result in contraction of interstitial space, recession of cleavage plane interspaces, reduction of tissue-averaged porosity, and increase of intramuscular and interstitial pressure [208]. Such increases in interstitial steric hindrance reduce drug penetration during passive LV distension from the equilibrium volume. Similarly, contraction-associated fiber and cross-fiber shortening and myofiber thickening [209] produce transverse forces, mural thickening, and a squeezing effect that decrease extracellular space [221] and increase interstitial fluid pressure [222]. These effects during systolic contraction likewise increase interstitial steric hindrance and resistance to drug penetration. Therefore, both contraction and distension relative to the equilibrium configuration introduce total mural strain that compresses interstitial space and reduces interstitial permeability.

Correlation between drug penetration and tissue porosity indicates mechanically mediated architectural changes influence transport through impact on porosity. Correlation between transport, porosity, and the Frank-Starling relationship, whereby all three reach a maximum in the absence of total mural strain, suggests the physiologic nexus ascribed to the equilibrium volume, whose architectural configuration enables optimal interface between tissue and external environment. The functional range of LV volumes in beating hearts, even with inotropic stimulation, reached capacities no greater than the equilibrium volume during diastolic filling. A physiologic range of LV volumes within the decreasing half of the total strain profile does not simply agree with previous findings [223] that mural tone persists during physiologic diastolic filling, but reveals that physiologic diastolic distension reduces rather than augments constitutive material strain of the chamber until equilibrium volume is reached. A physiologic range of LV volumes within the increasing half of the porosity, active pressure, and transport profiles also suggests that physiologic cardiac function dictates a mural transport environment that enables drug penetration to vary proportionally with LV distension and contractile efficiency. Within this range, penetration is reduced during systolic contraction and maximized during diastolic filling, suggesting physiologic architectural states that functionally reduce intramuscular pressure [224] and increase tissue porosity [221] to favor coronary perfusion during diastole [220] consequently also enable a transport environment that enhances interstitial drug transport. While equilibrium dimensions and associated contractile performance will vary among different individuals, such biologic design suggests that distended hearts within the physiologic volume range may be more

receptive to drug uptake and engenders clinical therapeutic strategies that manipulate LV volumetric state to modulate mural permeability to drug.

4.5.2 FGF

Therapeutic effectiveness of FGF depends on its specific binding interactions with extracellular receptors [225], which can also influence drug pharmacokinetics. FGF binds specifically with high affinity to cell-surface tyrosine kinase FGF receptors and with lower affinity to more abundant cell-surface, basement- and extracellular-membrane co-receptors such as heparan sulfate proteoglycans (HSPG), $\alpha_V\beta_3$ integrins, and collagen types I and IV [58, 59, 226]. Thus, the fibrous, force-transmitting, connective tissue network in the myocardium, which is composed of collagen types I and III and increases in density near the epicardial and endocardial surfaces [112], can not only modulate interstitial drug mobility through strain-influenced steric hindrance and screening, but also contribute to sequestering soluble FGF from the interstitial space dictated by macro-scale tissue-averaged porosity.

While 18 kDa FGF2 and 20 kDa dextran share similar molecular weights, they differ in physiochemical and binding properties. FGF2 is a positively charged, globular protein [227] with specific binding properties, while FITC-dextran is a neutrally charged [200, 201], highly branched, randomly coiled polysaccharide [202] with non-protein binding [135] properties and is used in studies to capture the effect of steric interaction alone on transport. Because of its physicochemical properties, FGF2 has a hydrodynamic radius of 1.5 nm [227], which is two-fold less than the 3.2 nm [183] radius of 20 kDa dextran. Based on size alone, a smaller hydrodynamic radius would have enabled FGF2

to penetrate farther than 20 kDa dextran as suggested by our earlier finding of greater penetration for smaller dextrans in skeletal muscle. However, the specific binding properties of FGF2 reduced its effective diffusivity nearly 6-fold relative to that of non-specifically binding dextran of greater hydrodynamic size, demonstrating the spatially localizing effect of binding interactions with the target environment.

Receptor interaction has been shown to protect FGF from proteolytic degradation and denaturation, thereby stabilizing its local levels and increasing its biologic activity and half-life in tissues [63]. Local retention of FGF can create a spatially distributed storage reservoir, which allows growth factors to reach higher local concentrations and enables sustained local release of accumulated drug [66, 67]. However, binding interactions also serve to retard growth factor diffusion [227], which can reduce therapeutic efficacy by restricting subsequent availability of the growth factor to downstream targets [62] or lead to local toxicity by causing suprapharmacologic accumulation. Expectedly, the ability of specific binding to dynamically modulate growth factor bioavailability [62] and radius of diffusion and action [68] depends on the spatial distribution and concentration of receptors. Our results demonstrate the consistency of the pharmacokinetic impact of architectural configuration across physicochemical and binding properties such that extreme radial thinning to -78% resulted in a similar relative reduction of diffusivity for both specifically binding FGF2 and inert dextran. Within this paradigm of strain-dependent structural modulation of drug mobility, mechanical strain and architectural configuration may likely also impact the spatial presentation and pharmacokinetic distribution of tissue binding sites to the extent that these sites are mechanically influenced architectural elements. In addition to

extracellular receptors and HSPGs, the connective tissue network, which serves to anchor myofibers, support vascular tissues, and enable force transmission [112], presents a network of collagen binding sites whose spatial distribution is functionally influenced by mechanical loading. Circumferential stretch of the LV during filling, which compacts myofibers and contracts interstitial space, can concentrate cell-surface and extracellular binding sites as well as collagen fibers, which are known to straighten and align from coiled configurations in their interstitial networks during ventricular stretch [114], especially in mid-ventricular and epicardial regions. Increased density and spatial presentation of binding sites with distension enable more efficient FGF retention by tissue and reduce mural drug penetration.

The ability of the binding environment to be modulated mechanically has significant consequence on growth factor pharmacokinetics and biological activity. Growth factor pharmacodynamics may be further dictated by the characteristics of mechanically modulated sustained release from tissue reservoirs subsequent to initial exogenous delivery. These dynamics can uniquely impact drug efficacy in the proximity of ischemic lesions, which experience heterogeneous gradients in mechanical loading and strain resulting from regional contractile dysfunction and wall motion abnormalities [228, 229], as well as increased expression of receptors and HSPGs [69, 230]. Thus, the ischemic heart can present both a disrupted loading and complicated binding environment compared to the globally coordinated environment of the healthy heart that requires further investigation.

4.5.3 Heart Rate and Contractility

Mural architectural dynamics introduced through cyclic systolic contraction and diastolic relaxation during cardiac function enhanced drug penetration beyond that occurring with static LV distension to the same intraventricular volumes. Cardiac beating can cyclically expose drug to strain-dependent architectural configurations associated with diastolic filling up to the equilibrium volume that have larger accessible volumes and result in a greater time-averaged porosity that increases penetration. However, a greater time-averaged porosity enhances penetration only within the range established by static LV distension and independently of loading frequency. Enhancement of penetration above the maximum associated with static distension to the equilibrium volume suggests a dynamic process resulting from the kinetics of cyclic cardiac strain rather than further reduction of steric exclusion.

In the absence of an external convective force driving bulk fluid flow into the epicardium, and particularly as penetration proceeds against an increasing intramuscular pressure gradient during contraction [231] along with an overall transmural pressure gradient [222], enhanced penetration during cardiac beating is unlikely the result of bulk convection. Dispersive effects introduced by cyclic architectural transitions are likely the predominant driving force because enhanced penetration scaled linearly dependently with heart rate and contractility, and linearly inversely with relaxation time constants.

Dispersive effects may arise from the combination of various mural architectural processes that occur during cyclic cardiac function. Locally, systolic contraction leads to myofiber shortening and thickening, increased interstitial pressure, and reduced porosity, while diastolic relaxation results in fiber thinning that re-opens interstitial spaces, restores

porosity, and relieves interstitial fluid pressure. Globally, coordinated systolic contraction of helically oriented LV myofibers produces ventricular contraction favoring longitudinal over circumferential chamber shortening. Myocardial contraction in this manner results in an overall torsion of the ventricular chamber accompanied by shear of mural laminar sheets and reorientation of LV myofibers by ~20° in the transition from diastole to systole at any transmural position [210]. The processes that create ventricular ejection of blood during contraction and are modulated by stroke volume and contractility result in circumferential compression, especially in the inner half of the ventricular wall, and mural thickening [115-117, 119]. Torsion and significant mural thickening followed by torsional recoil and mural thinning during diastolic relaxation generate non-axial cyclic strains across myofibers in the ventricular wall. These strains introduce a distinct dimension of transport forces oriented along the direction of transmural drug penetration that modulates dispersive effects.

Dispersion impacts the transport kinetics of soluble drug by increasing transport beyond molecular diffusion alone [155]. Cyclic displacement of myofibers and compression and expansion of interstitial space and fluid result in pulsatile agitation of soluble drug in the absence of bulk fluid flow. Such agitation can disperse or spread drug in a frequency-dependent manner over a greater interstitial volume, thereby driving greater penetration. Thus, cardiac beating influences transport through the combined effects of active muscle function and architectural configuration. Dispersive enhancement of drug penetration agrees with findings that isometric contractions increase both inulin volumetric uptake and washout in papillary muscle [87], and electric pacing accelerates the washout of interstitial norepinephrine [232] and extracellular markers [89]

from the myocardium. This physiologic mechanism engenders potential therapeutic strategies leveraging administration of cardioactive agents or interventions concomitant with local administration of primary therapies to improve controlled drug delivery.

4.5.4 Conceptual Paradigm

As in skeletal muscle, strain-dependent structural configuration enables optimal porosity and associated maximal drug penetration at the physiologically defined state for peak contractile performance. Histologic assessment of architecture and drug penetration findings that reflect structurally influenced steric interactions provided insights on strain-dependent architectural configuration. These findings elucidate the similarity in strain-dependent local changes in myofiber cross-sectional area and packing density between skeletal and cardiac muscle. LV distension from the equilibrium volume results in circumferential stretch and radial compaction of muscle fibers, which progressively reduce porosity and narrow interstitial space as occurs analogously under extreme stretch from optimal length in skeletal muscle (Figure 4.9). LV contraction from the equilibrium volume results in circumferential shortening and radial thickening, which produce a squeezing effect that narrows interstitial space and increases interstitial fluid pressure as occurs analogously with contraction from optimal length in skeletal muscle. Ultimately, in either uniaxially structured and loaded skeletal muscle or multidimensionally structured and loaded cardiac muscle, structural configuration underscores drug transport while enabling dynamic loading effects to be superposed.

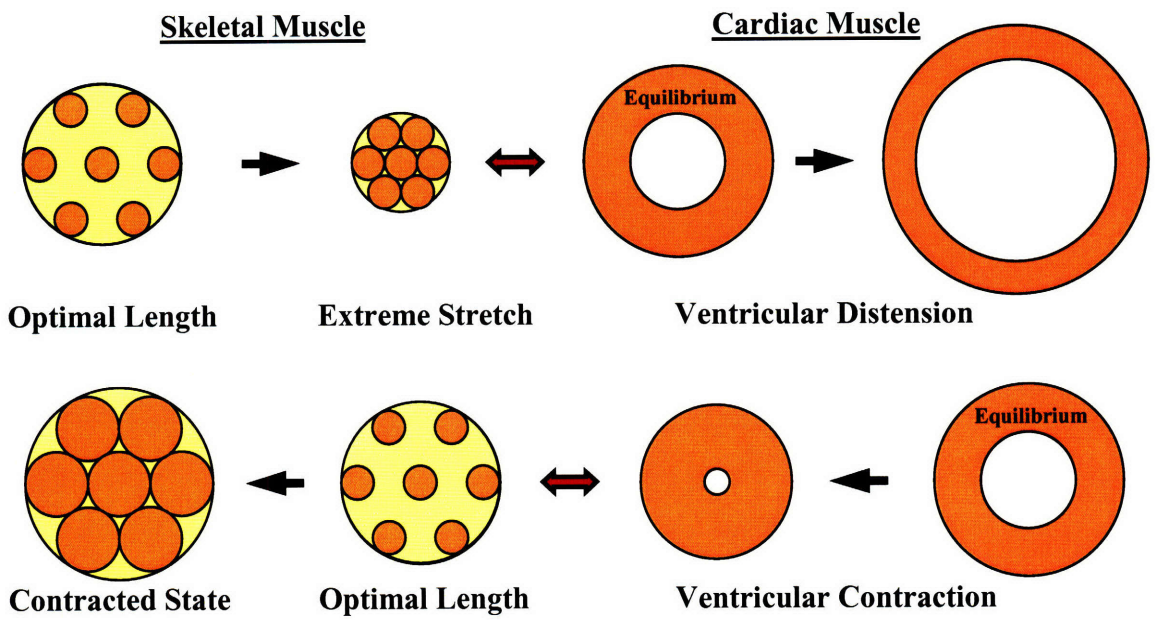

Figure 4.9. Architectural configurations under ventricular distension and contraction. Local changes in myofiber cross-sectional area and packing density during ventricular distension and contraction are analogous to changes occurring in skeletal muscle under extreme elongation and contraction, respectively.

4.5.5 Perspectives

Our findings elucidate opportunities to meet therapeutic windows and potential strategies to improve local drug delivery to the myocardium. Ventricular distension enables an adaptable physiologic mechanism for modulating or maximizing drug transport. Cyclic cardiac contraction *in vivo* enables a scalable physical means, which readily superposes on the structural dependence of tissue permeability, for further increasing drug penetration. Strain-dependent steric hindrance by functional architecture demonstrates a physiologic means for selective drug uptake based on the physicochemical and binding properties of the drug. Modulation of growth factor local distribution by ventricular distension could facilitate optimal deposition and retention of drug in strategies like therapeutic angiogenesis such that they meet the spatial and temporal therapeutic windows demanded by complex regenerative biologic processes and

thus achieve desired pharmacologic results. The presence of residual contractile tone during physiologic diastole reveals an LV volumetric range between end-diastolic volume and equilibrium volume that can be recruited by ventricular filling, which reduces mural strain in this range, to enhance drug penetration. Such recruitment could be mediated by therapeutic modulation of the volume status of the heart in the setting of intrapericardial controlled drug release. The pharmacokinetic impact of ventricular distension could be harnessed in the cardiac surgical setting during cardiopulmonary bypass and requisite diastolic cardiac arrest such that static ventricular filling could be employed to enhance local epicardial drug uptake. Moreover, the capacity of dynamic effects from cardiac beating to enhance drug penetration engenders both peri-operative and ancillary therapies that pharmacologically manage cardiac inotropy and chronotropy as strategies for controlled drug uptake.

While contraction dynamics augment drug mobility, tissue structural configuration is intimately linked to transport. As not only porosity, but also myofiber arrangement influences transport, the pharmacokinetic impact of functional cardiac architecture can be significantly dictated by its physiologic and pathophysiologic state. Drug penetration occurring in the setting of normal cardiac architecture comprised of organized and aligned myofibers may be potentially altered in the setting of a heart conditioned for athletic performance. Transport in this setting may be inhibited by myocyte hypertrophy that constricts interstitial space but enhanced by improved diastolic function [233] that enables a time-averaged porosity closer to equilibrium volume. In contrast, transport may be altogether significantly reduced in pathologic states such as hypertrophic obstructive cardiomyopathy, which exhibits not only myocyte hypertrophy,

but also considerable regional myocyte disarray, architectural disorganization, interstitial fibrosis, and ischemic scarring [234] that disrupt normal myofiber arrangement. Drug transport may be hindered especially as a result of the irregular and random versus aligned pattern of interstitial obstacles [154, 203] presented by myofiber disarray found also in conditions like dilated cardiomyopathy, alcoholic cardiomyopathy [235], hypertension, coronary heart disease, and cor pulmonale [236]. Furthermore, interstitial drug mobility may be considerably reduced in the setting of cardiac fibrosis that develops with hypertension, age, long-term athletic activity, myocardial ischemia [237], hemochromatosis, restrictive cardiomyopathy, aortic stenosis, viral myocarditis, and radiation and drug effects [238]. Other unique pathologic structural states that may dramatically hinder drug penetration include hyperthyroidism, which exhibits nonspecific hypertrophy that may constrict interstitial space; hypothyroidism, which exhibits myofiber swelling accompanied by interstitial mucopolysaccharide-rich edema fluid that may alter interstitial space and viscosity; cardiac amyloidosis, which exhibits interstitial amyloid deposits around myofibers [239] that may impede drug diffusion; and muscular dystrophy, which exhibits a cardiomyopathy comprised of myofiber size variation, myocyte degeneration and fatty replacement, necrosis, and interstitial fibrosis [240] that may variably reduce both drug mobility and accessible space. Architectural changes in each of these states may underlie the pharmacokinetic environment upon which altered contraction dynamics associated with such altered architecture, such as diastolic stiffness and abnormal contractile tone associated with interstitial cardiac fibrosis [241], may further impact drug transport.

The relationship between drug uptake and target tissue functional architecture and contraction presents new insights on the significance of biologic form and function. A physiologic volumetric range less than equilibrium volume, falling on the ascending half of the Frank-Starling and porosity relationships and descending half of the total mural strain relationship with LV volume, suggests reduction of residual mural strain opens interstitial space and increases porosity during diastolic filling. Diastolic filling that reflects relief of mural contractile tone rather than imposition of distensile strain up to equilibrium volume reveals a physiologic mechanism that uses internal restoring forces or elastic recoil to generate negative chamber pressures in early diastole that facilitate ventricular filling through a process of diastolic suction [242]. This mechanism may reflect biologic adaptation that relies on the passive mechanical properties of the ventricle to conserve energy during filling with the overall aim of maximizing cardiac functional efficiency. This adaptive measure for maximizing operational efficiency based solely on tissue structure spans not only diastolic, but also systolic function. Progressive LV filling is associated with increased porosity corresponding to diminished mural strain that by consequence renders a structural environment better suited for drug uptake. We hypothesize that maximal porosity occurs at the minimum-strain associated architectural configuration – equilibrium volume – which dictates peak contractile performance, because of the design of physiologic form based on its interrelationship with function. Greater porosity and reduced intramuscular pressure towards equilibrium volume may allow optimal coronary blood flow in diastole [243] to sustain the necessary rate of metabolic substrate delivery and waste removal to meet the demands of peak contractile performance, thus optimizing functional efficiency. Reciprocally, peak contractile

performance occurs in the structural configuration that facilitates optimal blood flow to sustain the production of such peak function. The aim of such structural design to maximize functional efficiency may also explain the adaptive advantage of having a greater relative duration of diastole during the cardiac cycle [244], which enables a greater duration for coronary perfusion and consequently drug uptake as well.

We subscribe to the concept that biologic adaptation centers the physiologic range of skeletal muscle extensibility and operation on peak contractile performance at optimal length to maximize contractile effectiveness during locomotion and postural stability. In contrast, biologic adaptation grants the greatest evolutionary advantage to an organ as vital to survival as the heart by setting its physiologic range of contractile performance on the ascending half of the Frank-Starling curve to render an intrinsic robustness to fluctuating volume status, maximizing the capacity of the heart to maintain circulatory homeostasis. As a consequence, we hypothesize the biologic significance of operating on the ascending portion of the porosity curve, which peaks with contractile performance at equilibrium volume, is to provide a structurally mediated functional reserve in coronary blood flow rate that is robust to the energetic and metabolic demands of dynamic contractile performance. Correlation of maximal drug penetration with optimal muscle function through constitutive tissue porosity reflects biologic design that harmonizes the reciprocal interaction between tissue and its physical environment. Architecturally and functionally dictated optimal pharmacokinetic conditions suggest the existence of potential therapeutic windows that correspond to unique setpoints in the physiologic operating range of all target tissues and organs.

4.5.6 Conclusions

Cardiac tissue presents an active pharmacokinetic environment in which drug transport is influenced by the interrelated effects of architectural configuration and functional mechanics. Architectural configuration, dictated by contractile tone and intraventricular volume, enables maximal drug penetration in the equilibrium state devoid of intrinsic material strain from either contractile tone or ventricular distension. Mural configuration impacts drug permeability across different drug physicochemical and binding properties. The dispersive effects of cyclic cardiac function enhance drug penetration above architecturally defined transport. Correlation of maximal drug penetration, tissue porosity, and LV functional efficiency elucidates the resonant nature of cardiac muscle interaction with the physical environment. Such biologic design and mechanisms not only elucidate the pharmacokinetic impact of functional cardiac architecture, but also introduce new strategies for controlled drug delivery.

5. CONCLUSIONS

Muscle tissue presents an exclusive transport environment in which dynamic, mechanically active architecture may present a predominant influence on the pharmacokinetics of locally delivered agents. The work described in this thesis used a systematic approach to elucidate the mechanistic underpinnings and physiologic significance of the impact of architectural configuration and its interaction with motion and mechanical loading on intramuscular drug transport. Findings from this work have elucidated a quantitative understanding of not only the pharmacokinetic role of muscle mechanics such as structural strain, cyclic tension, and rhythmic contraction, but also the integral function of tissue structural design in mediating both mechanical activity and the pharmacokinetic environment within skeletal and cardiac physiologic paradigms.

The work in this thesis endeavored to develop a quantitative schema with which to consider the mechanically influenced pharmacokinetic environment of skeletal and cardiac muscle. Insights derived from this work have significant impact on not only current knowledge of intramuscular pharmacokinetics, but also on understanding of biologic design in general and the potential pharmacokinetic significance of functional architecture in all target tissues. These insights further yield important implications for drug transport investigations, which should now duly consider the pharmacokinetic impact of the physiologic operational domain of its targeted tissues. Ultimately, we hope the fundamental findings from this work on how mechanical forces govern drug transport will contribute to the rational design, development, optimization, and clinical application of clinical drug delivery strategies to dynamic tissue targets such as skeletal and cardiac muscle.

6. FUTURE WORK

The work in this thesis highlighted the relevant mechanical issues involved in local intramuscular pharmacokinetics. The interactions between physicochemical and binding properties of delivered drug, structural properties of targeted tissues, and mechanical forces that these tissues sustain were quantitatively examined in the context of local drug delivery. Findings on the pharmacokinetic influence of functional architecture may ultimately provide insight on how drug transport associated with physiologic mechanical loading paradigms subserves transport in structural and mechanical dysfunction in the setting of muscular pathology and prompt the informed investigation of such processes.

As local pharmacologic approaches for treating coronary heart disease and peripheral arterial disease become realized and assessed in clinical trials, a detailed understanding of local pharmacokinetics in targeted tissues becomes important. In the clinical setting, tissue architecture and functional mechanics can undergo dramatic changes in pathologic states such as ischemic injury. Thus, intramuscular pharmacokinetics in the setting of ischemic dysfunction must be understood and further investigated. Currently, no investigations have elucidated the impact of spatially disrupted architecture and loading during ischemic pathology, which exhibits mechanical strain gradients across ischemic border zones. Further pharmacokinetics investigations using our experimental approach intend to determine the unique effects of heterogeneously disrupted cardiac tissue structure and mechanical loading on intramyocardial drug penetration and distribution. Ultimately, this work may provide a better understanding of the clinically relevant transport environment of ischemic muscle.

Pharmacokinetics in Ischemic Myocardium

The purpose of therapeutic angiogenesis in the heart is to restore blood supply and normal performance to a poorly functioning ischemic myocardium. Thus, patients with ischemic heart diseases with salvageable lesions such as hibernating myocardium or acute coronary occlusions may likely benefit from therapeutic angiogenesis. However, there exists no clear understanding of how to maximize myocardial distribution and retention of angiogenic growth factors, or how to target specific sites of reversible ischemia or ischemic "border zones." Therefore, the local transport forces predominating in ischemic myocardium need to be understood.

A heart with ischemic tissue can present a very heterogeneous and disordered mechanical loading environment for drug transport. In particular, there may be a region of dysfunctionally contracting ischemic tissue adjacent to regions of normally contracting healthy tissue. In these cases, the ischemic region may introduce variable degrees of ventricular regional wall motion and thickening abnormalities that may occur with stress and can be either reversible or progressive. As a result, the ischemic heart can present a dramatically different and even more complicated mechanical loading environment compared to the coordinated loading environment found in a healthy heart wall. And since the goal of therapeutic angiogenesis is to deliver drugs to ischemic tissues, it is vitally important to gain a clear understanding of the local transport forces exerted on a drug by such a pathological tissue environment. This understanding may help to improve drug delivery strategies for CAD because the wall motion heterogeneities experienced in a heart with an ischemic lesion may substantially affect drug pharmacokinetics in, as of yet, unanticipated ways. More importantly, the local motion heterogeneities surrounding

a lesion, which stem from its very presence, may present the most significant local transport forces for a drug that targets that lesion.

In myocardial ischemia, temporally disordered and spatially nonhomogeneous dysfunction of both the ischemic and non-ischemic ventricular tissues occurs throughout the contractile cycle. Within seconds of the sudden onset of severe myocardial ischemia resulting from acute coronary occlusion, contractile function of the heart becomes impaired. Systolic function in the ischemic segment, as detected by echocardiography, can exhibit hypokinesia (depressed contractile function) or akinesia (absence of contractile shortening) during ejection. After a prolonged period, there is left ventricular dysfunction, or myocardial stunning. If the coronary obstruction is subtotal, the contractile activity of the ischemic, yet viable, segment may remain akinetic. This results in chronically ischemic or hibernating myocardium.

However, if there is complete coronary obstruction leading to transmural ischemia, the impaired contractile shortening in the ischemic zone may progressively worsen to dyskinesia within the first 30 minutes after the acute onset. In dyskinesia, the injured tissue becomes compliant, displays greater local in-plane stretching and radial thinning during diastolic filling, and bulges paradoxically during isovolumetric systolic contraction. This is then followed by rapid recoiling of the stretched wall during isovolumetric relaxation. As a result, total systolic function is depressed, and global performance is altered. The adjacent non-ischemic myocardium compensates with hyperkinetic contractility, which incorporates increased fiber lengths and augmented shortening of normal segments, in order to sustain global ventricular function. The dyskinesia also impairs ventricular relaxation, which decreases peak filling rate and

increases preload on the non-ischemic heart muscle. This leads to increased wall strain and dilation [228, 245, 246]. As a result, these global effects may alter the distribution and transport of a drug to the ischemic lesion.

Moreover, segmental dyskinesia results in hypokinesia at the transitional margin between the central ischemic segment and the non-ischemic myocardium. This creates a functional border zone where contraction is reduced despite normal perfusion to the local tissue. In this zone, tethering between perfused and under-perfused myocardium affects the mechanics of both the inner and outer ventricular layers during systole. In the subepicardium and midwall, end-systolic wall thickening, normal strain between mural layers, and longitudinal shortening are decreased, while circumferential shear is increased. In the subendocardium, systolic fiber stretch and end-systolic shear between sheets are increased. Likewise, tethering at the border zone also affects the strains experienced in diastole, during which there are increased lengthening and thinning strains in response to the increased filling pressures and decreased peak filling rate [229]. Consequently, such characteristics of mechanical loading and strain in the ischemic border zone can have a significant impact on the local pharmacokinetics of drugs targeted to the ischemic segment.

Therefore, the heterogeneous and dramatically disrupted loading patterns caused by an ischemic lesion can introduce distinct effects on drug transport. Some of these enter simply as an escalation of physiological loading. For instance, hyperkinesia acts to increase the degree of redistribution of interstitial space, wall strain, or buildup of intramuscular pressure that is normally associated with physiologic contraction of the ventricular wall. Other effects modulate physiological function. Hypokinesia and

akinesia diminish the normal level of contraction while increasing the level of wall strain in the ischemic zone. And, still other effects introduce an altogether rearranged loading environment. For example, the ischemic border zone alters the strain patterns between the subepicardium and subendocardium and generates potential strain gradients between the ischemic and non-ischemic zones. The altered effect may influence the nature of drug uptake at the border zone. Thus, it is important to determine the local effect on transport caused by the juxtaposition of a zone with disrupted loading next to one with physiologic loading. The relevant questions then are how will focal dysfunction of mechanical loading patterns in the heart affect drug transport, and how will the border zone between functional zones mediate drug uptake. Perhaps, impairment of interstitial convection in akinetic regions may reduce drug transport into these regions. Or, focal drug concentration gradients of drug may develop at the border zone between functionally loaded and dysfunctionally loaded regions as a result of differential transport forces. Elucidating these effects would enable us to build upon the present comparison of transport in uniaxial and multiaxial loading environments to achieve a more complete characterization of how mechanical loading conditions affect drug transport. Also, this would enable us to synthesize a quantitative approach that not only extrapolates the transport role that uniaxial loading plays in multiaxial loading, but also defines how transport associated with both loading paradigms underlies the transport in a disrupted loading environment such as ischemic myocardium. Ultimately, this framework would give us a better understanding of the relevant transport environment experienced by growth factors targeted to ischemic lesions in the clinical setting.

- *Specific Aim:*

Regional ischemia results in local dysfunction of the mechanical loading pattern in the ventricular wall. This dysfunction leads to locally irregular convective forces and interstitial space variations that may modulate the transport of drug to the ischemic region. Thus, this study seeks to determine how penetration and local distribution of epicardially delivered drug is influenced by **regional wall motion abnormalities** resulting from acute ischemia. This will provide a better understanding of the transport environment resulting from a steep gradient of mechanical loading between functional and dysfunctional muscle.

- *Methods:*

Pharmacokinetic Effects of Mechanical Loading and Coronary Blood Flow in Cardiac Muscle

The pharmacokinetic impact of mechanical loading was compared to that of coronary flow by investigating epicardial drug penetration into the LV of *in vivo* beating rat hearts, control *in situ* hearts that were not beating but were receiving coronary perfusion, and control *in situ* hearts that were not beating and not receiving coronary perfusion.

Male Sprague-Dawley rats (600-800 g) were anesthetized by an induction dose of 80 mg/kg Ketamine and 10 mg/kg Xylazine via intraperitoneal injection, and maintenance doses of 40 mg/kg Ketamine and 5 mg/kg Xylazine every 20 min.

For the beating heart experiment group, the rat was intubated with a 2.0 mm endotracheal tube for positive pressure ventilation with O_2 at a rate of 72 breaths/min and tidal volume of 2.7 ml. Thoracotomy was performed with minimal bleeding by a midline

incision from the xiphoid process to just inferior of the suprasternal notch. The ribcage was held open by an Alm retractor, and the pericardial sac was resected to expose the beating heart. The left carotid artery was cannulated with PE50 tubing connected to a blood pressure transducer and base amplifier (Blood Pressure XDCR and XDCR Base Amplifier, Kent Scientific). Pressure signals were acquired using a National Instruments DAQPAD-6015 data acquisition board and recorded with LabView 7.0. Heart rate averaging 180 BPM and blood pressure between 90-120 mmHg were recorded throughout the surgical procedure and duration of drug delivery.

For the *in situ* non-beating heart control groups, rats were euthanized by Ketamine and Xylazine via intraperitoneal injection. Thoracotomy was performed and the pericardial sac was resected to expose the passive heart. For hearts receiving coronary perfusion, the superior vena cava and pulmonary artery were ligated, the aorta was cannulated, and the coronary vasculature was retrogradely perfused by bovine serum (Gibco) maintained at a constant pressure head of 100 mmHg and a temperature of 37°C by heat exchanger. Outflow from the inferior vena cava was collected. For hearts receiving no coronary perfusion, the aorta was cannulated and the coronary vasculature was retrogradely flushed with bovine serum. Immediately after coronary blood was cleared from the vasculature, coronary outflow was stopped by clamping both the right atria and pulmonary artery to allow the coronary vasculature to remain open but without the presence of perfusion flow.

In all groups, the rat was laid in a prostrate position on an elevated platform with a rectangular opening for access to the thoracic cavity. The heart was allowed to hang

through the opening and sit in a reservoir containing 961 Da Evans Blue dye (1% w/v in PBS) for 1 h. This position did not alter heart rate or blood pressure in beating hearts.

A cylindrical plug of LV myocardium was harvested from each group using an 8 mm-diameter biopsy punch (Miltex Instrument Company). Tissue samples were snap-frozen in -145°C Isopentane. 8 μm cross-sections were cut on a radial plane from tissue plugs using a cryostat (Leica CM1850). Evans Blue dye in tissue sections was imaged using epifluorescence microscopy (Leica DMRA2, 50× magnification, Hamamatsu ORCA 286, Metamorph 6.3, ex: 560 nm / em: 645 nm bandpass). Unidirectional drug penetration at the epicardial surface of the cross-section was quantified in Matlab. Intramuscular penetration depth was defined as the perpendicular distance from the surface at which fluorescence intensity decreased to 5% of the surface intensity.

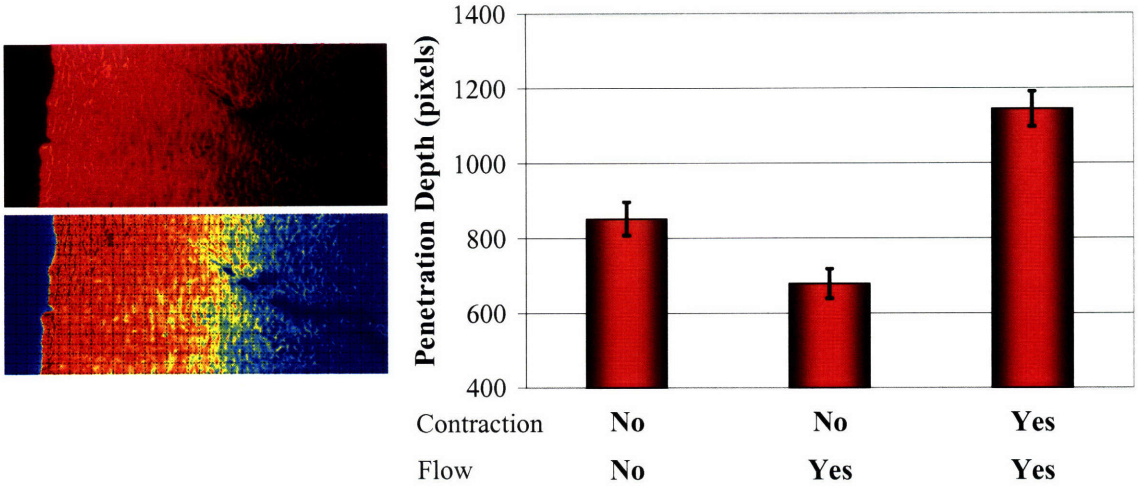

Figure 6.1. Effects of cardiac beating and coronary flow on penetration of Evans Blue into the LV. Penetration at baseline ("no" contraction, "no" flow) is reduced by the presence of coronary flow ("no" contraction, "yes" flow), suggesting drug is possibly convected away from myocardial tissue via coronary perfusion. Penetration is enhanced by contractile beating at 144 BPM ("yes" contraction, "yes" flow), suggesting dynamic mechanical loading resulting from myocardial contraction and distension during the cardiac cycle increases drug transport. Because *in vivo* cardiac beating naturally includes physiologic coronary flow, the pharmacokinetic impact of contractile function to enhance drug penetration appears to outweigh that of coronary flow to remove drug from the tissue.

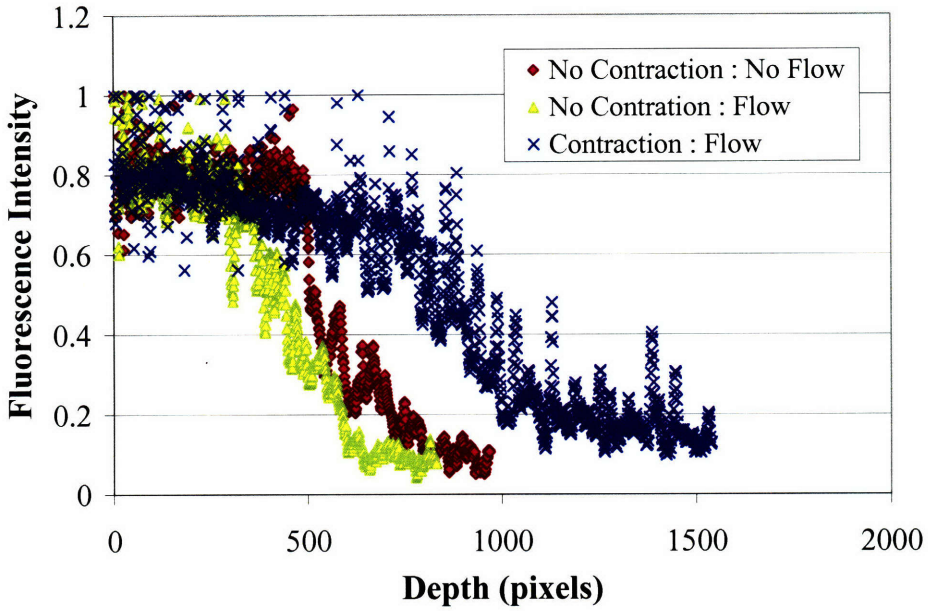

Figure 6.2. LV drug penetration profiles (*A*) in the absence of either contraction or coronary perfusion (No Contraction : No Flow), (*B*) in the presence of coronary perfusion without contractile function (No Contraction : Flow), and (*C*) in the presence of both contractile function and coronary flow (Contraction : Flow). In both groups *A* and *B*, drug concentration experiences a sharp drop in concentration, while in group *C*, the effect of mechanical loading appears to dampen this sudden drop, resulting in a greater spread of penetrating drug into the tissue.

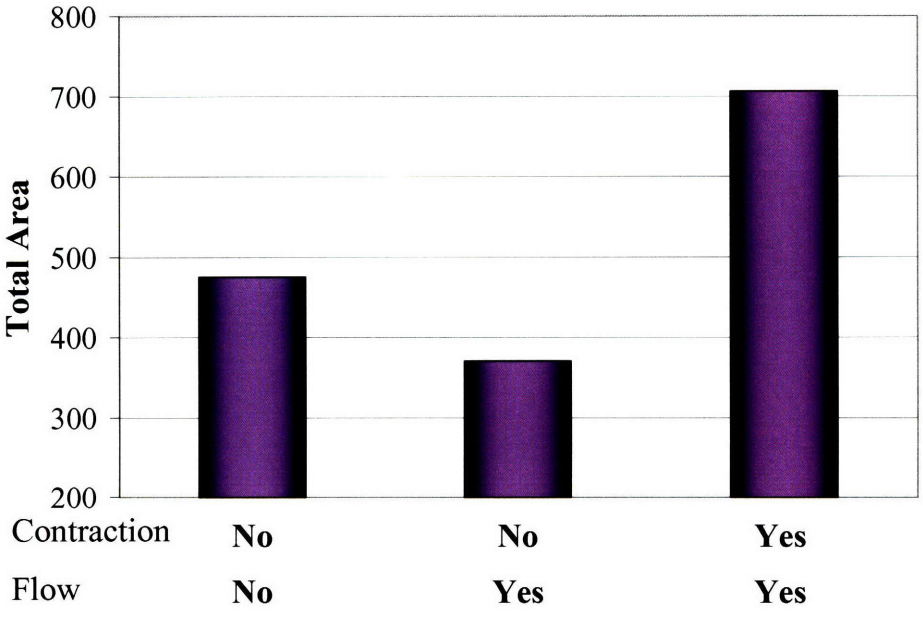

Figure 6.3. Total drug deposition, calculated from the area under the drug penetration profile, for each group corresponds with drug penetration depth.

Coronary Ligation

A surgical technique for creating acute myocardial ischemia in the LV of rat heart will be used. The distal left anterior descending (LAD) coronary artery will be ligated to induce local ischemia and disrupt regional wall motion and mechanics (Figure 6.4).

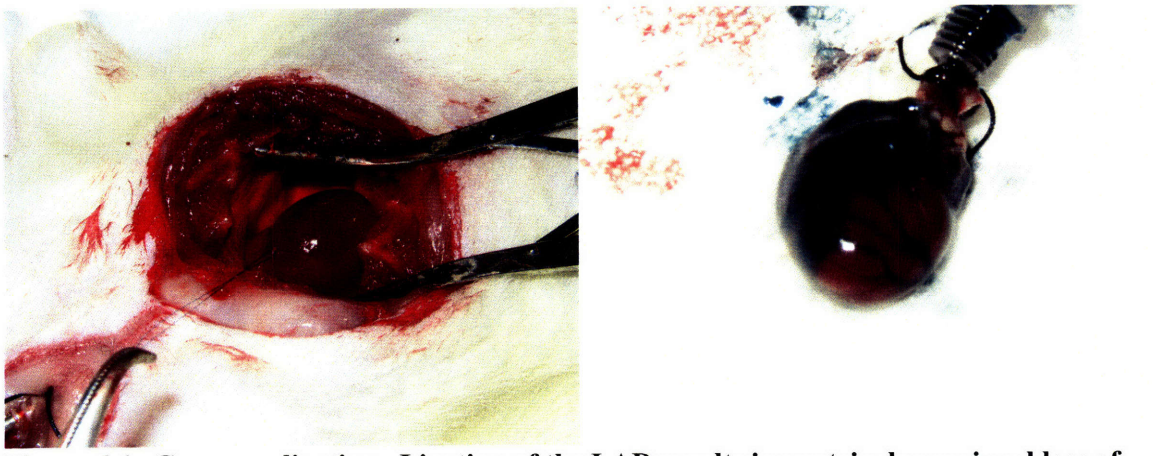

Figure 6.4. Coronary ligation. Ligation of the LAD results in ventricular regional loss of perfusion and regional wall motion abnormalities.

Echocardiography

Echocardiography using a SONOS 5500 (Agilent) Ultrasound system will be performed to assess left ventricular chamber size and wall thickness changes on the ventricular short-axis during diastole and systole (Figure 6.5). Regional wall motion abnormalities that results from acute ischemia will be characterized.

Diastole **Systole**

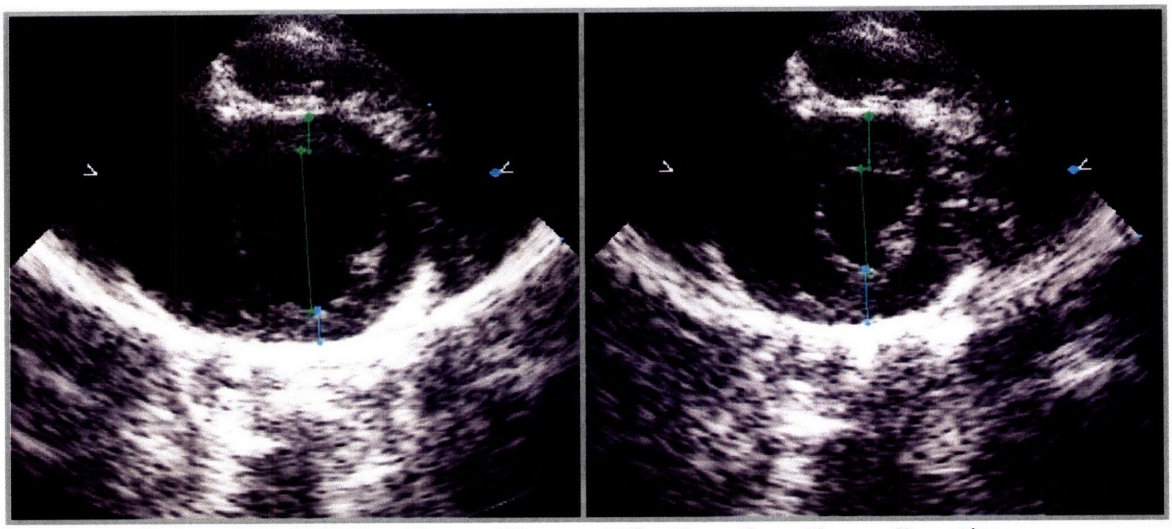

Figure 6.5. Echocardiographic quantification of cardiac wall motion.

These experiments will correlate the uptake and distribution of 20 kDa FITC-dextran with the presence of regional wall thickening abnormalities associated with the onset of acute ischemia. Delivery of FITC-dextran will be performed as described for previous myocardial experiments, with the additional step of coronary ligation. Drug distribution will be visualized by epifluorescence microscopy in short-axis cross-sections of the ventricular chamber in order to quantify distribution in both the radial and circumferential directions. Regional ischemia will be histologically quantified in short-axis cross-sections by tetrazolium stain and correlated to both echocardiographic assessment of wall motion and fluorescent assessment of drug distribution. Special interest will be directed toward drug deposition around the ischemic border zone.

7. REFERENCES

1. *Heart Disease and Stroke Statistics: 2008 Update.* 2008, American Heart Association: Dallas, TX 75231.
2. Ness, J., et al., *Prevalence of symptomatic peripheral arterial disease, modifiable risk factors, and appropriate use of drugs in the treatment of peripheral arterial disease in older persons seen in a university general medicine clinic.* J Gerontol A Biol Sci Med Sci, 2005. **60**(2): p. 255-7.
3. Criqui, M.H., et al., *Mortality over a period of 10 years in patients with peripheral arterial disease.* N Engl J Med, 1992. **326**(6): p. 381-6.
4. Shamoun, F., N. Sural, and G. Abela, *Peripheral artery disease: therapeutic advances.* Expert Rev Cardiovasc Ther, 2008. **6**(4): p. 539-53.
5. Levy, P.J., *Epidemiology and pathophysiology of peripheral arterial disease.* Clin Cornerstone, 2002. **4**(5): p. 1-15.
6. Mukherjee, D., et al., *Direct myocardial revascularization and angiogenesis--how many patients might be eligible?* Am J Cardiol, 1999. **84**(5): p. 598-600, A8.
7. Hughes, G.C. and B.H. Annex, *Angiogenic therapy for coronary artery and peripheral arterial disease.* Expert Rev Cardiovasc Ther, 2005. **3**(3): p. 521-35.
8. Kornowski, R., *Collateral formation and clinical variables in obstructive coronary artery disease: the influence of hypercholesterolemia and diabetes mellitus.* Coron Artery Dis, 2003. **14**(1): p. 61-4.
9. Svet-Moldavsky, G.J. and K.L. Chimishkyan, *Tumour angiogenesis factor for revascularisation in ischaemia and myocardial infarction.* Lancet, 1977. **1**(8017): p. 913.
10. Carmeliet, P., *Angiogenesis in health and disease.* Nat Med, 2003. **9**(6): p. 653-60.
11. Simons, M., *Integrative signaling in angiogenesis.* Mol Cell Biochem, 2004. **264**(1-2): p. 99-102.
12. Pepper, M.S., et al., *Potent synergism between vascular endothelial growth factor and basic fibroblast growth factor in the induction of angiogenesis in vitro.* Biochem Biophys Res Commun, 1992. **189**(2): p. 824-31.
13. Folkman, J. and C. Haudenschild, *Angiogenesis in vitro.* Nature, 1980. **288**(5791): p. 551-6.
14. Montesano, R., et al., *Basic fibroblast growth factor induces angiogenesis in vitro.* Proc Natl Acad Sci U S A, 1986. **83**(19): p. 7297-301.
15. Schumacher, B., et al., *The stimulation of neo-angiogenesis in the ischemic heart by the human growth factor FGF.* J Cardiovasc Surg (Torino), 1998. **39**(4): p. 445-53.
16. Akimoto, T. and M.R. Hammerman, *Fibroblast growth factor 2 promotes microvessel formation from mouse embryonic aorta.* Am J Physiol Cell Physiol, 2003. **284**(2): p. C371-7.
17. Bikfalvi, A., et al., *Biological roles of fibroblast growth factor-2.* Endocr Rev, 1997. **18**(1): p. 26-45.
18. Harada, K., et al., *Vascular endothelial growth factor administration in chronic myocardial ischemia.* Am J Physiol, 1996. **270**(5 Pt 2): p. H1791-802.

19. Walder, C.E., et al., *Vascular endothelial growth factor augments muscle blood flow and function in a rabbit model of chronic hindlimb ischemia.* J Cardiovasc Pharmacol, 1996. **27**(1): p. 91-8.
20. Hopkins, S.P., et al., *Controlled delivery of vascular endothelial growth factor promotes neovascularization and maintains limb function in a rabbit model of ischemia.* J Vasc Surg, 1998. **27**(5): p. 886-94; discussion 895.
21. Lopez, J.J., et al., *VEGF administration in chronic myocardial ischemia in pigs.* Cardiovasc Res, 1998. **40**(2): p. 272-81.
22. Chleboun, J.O., et al., *bFGF enhances the development of the collateral circulation after acute arterial occlusion.* Biochem Biophys Res Commun, 1992. **185**(2): p. 510-6.
23. Unger, E.F., et al., *Basic fibroblast growth factor enhances myocardial collateral flow in a canine model.* Am J Physiol, 1994. **266**(4 Pt 2): p. H1588-95.
24. Lazarous, D.F., et al., *Effects of chronic systemic administration of basic fibroblast growth factor on collateral development in the canine heart.* Circulation, 1995. **91**(1): p. 145-53.
25. Yang, H.T., et al., *Basic fibroblast growth factor increases collateral blood flow in rats with femoral arterial ligation.* Circ Res, 1996. **79**(1): p. 62-9.
26. Lopez, J.J., et al., *Basic fibroblast growth factor in a porcine model of chronic myocardial ischemia: a comparison of angiographic, echocardiographic and coronary flow parameters.* J Pharmacol Exp Ther, 1997. **282**(1): p. 385-90.
27. Watanabe, E., et al., *Effect of basic fibroblast growth factor on angiogenesis in the infarcted porcine heart.* Basic Res Cardiol, 1998. **93**(1): p. 30-7.
28. Rajanayagam, M.A., et al., *Intracoronary basic fibroblast growth factor enhances myocardial collateral perfusion in dogs.* J Am Coll Cardiol, 2000. **35**(2): p. 519-26.
29. von Degenfeld, G., et al., *Selective pressure-regulated retroinfusion of fibroblast growth factor-2 into the coronary vein enhances regional myocardial blood flow and function in pigs with chronic myocardial ischemia.* J Am Coll Cardiol, 2003. **42**(6): p. 1120-8.
30. Schumacher, B., et al., *Induction of neoangiogenesis in ischemic myocardium by human growth factors: first clinical results of a new treatment of coronary heart disease.* Circulation, 1998. **97**(7): p. 645-50.
31. Laham, R.J., et al., *Local perivascular delivery of basic fibroblast growth factor in patients undergoing coronary bypass surgery: results of a phase I randomized, double-blind, placebo-controlled trial.* Circulation, 1999. **100**(18): p. 1865-71.
32. Ruel, M., et al., *Long-term effects of surgical angiogenic therapy with fibroblast growth factor 2 protein.* J Thorac Cardiovasc Surg, 2002. **124**(1): p. 28-34.
33. Hendel, R.C., et al., *Effect of intracoronary recombinant human vascular endothelial growth factor on myocardial perfusion: evidence for a dose-dependent effect.* Circulation, 2000. **101**(2): p. 118-21.
34. Laham, R.J., et al., *Intracoronary basic fibroblast growth factor (FGF-2) in patients with severe ischemic heart disease: results of a phase I open-label dose escalation study.* J Am Coll Cardiol, 2000. **36**(7): p. 2132-9.
35. Pecher, P. and B.A. Schumacher, *Angiogenesis in ischemic human myocardium: clinical results after 3 years.* Ann Thorac Surg, 2000. **69**(5): p. 1414-9.

36. Udelson, J.E., et al., *Therapeutic angiogenesis with recombinant fibroblast growth factor-2 improves stress and rest myocardial perfusion abnormalities in patients with severe symptomatic chronic coronary artery disease.* Circulation, 2000. **102**(14): p. 1605-10.
37. Unger, E.F., et al., *Effects of a single intracoronary injection of basic fibroblast growth factor in stable angina pectoris.* Am J Cardiol, 2000. **85**(12): p. 1414-9.
38. Henry, T.D., et al., *Intracoronary administration of recombinant human vascular endothelial growth factor to patients with coronary artery disease.* Am Heart J, 2001. **142**(5): p. 872-80.
39. Simons, M., et al., *Pharmacological treatment of coronary artery disease with recombinant fibroblast growth factor-2: double-blind, randomized, controlled clinical trial.* Circulation, 2002. **105**(7): p. 788-93.
40. Lederman, R.J., et al., *Therapeutic angiogenesis with recombinant fibroblast growth factor-2 for intermittent claudication (the TRAFFIC study): a randomised trial.* Lancet, 2002. **359**(9323): p. 2053-8.
41. Rajagopalan, S., et al., *Regional angiogenesis with vascular endothelial growth factor in peripheral arterial disease: a phase II randomized, double-blind, controlled study of adenoviral delivery of vascular endothelial growth factor 121 in patients with disabling intermittent claudication.* Circulation, 2003. **108**(16): p. 1933-8.
42. Isner, J.M., et al., *Treatment of thromboangiitis obliterans (Buerger's disease) by intramuscular gene transfer of vascular endothelial growth factor: preliminary clinical results.* J Vasc Surg, 1998. **28**(6): p. 964-73; discussion 73-5.
43. Baumgartner, I., et al., *Constitutive expression of phVEGF165 after intramuscular gene transfer promotes collateral vessel development in patients with critical limb ischemia.* Circulation, 1998. **97**(12): p. 1114-23.
44. Shyu, K.G., et al., *Intramuscular vascular endothelial growth factor gene therapy in patients with chronic critical leg ischemia.* American Journal of Medicine, 2003. **114**(2): p. 85-92.
45. Cooper, L.T., Jr., et al., *Proteinuria in a placebo-controlled study of basic fibroblast growth factor for intermittent claudication.* Vasc Med, 2001. **6**(4): p. 235-9.
46. Lazarous, D.F., et al., *Pharmacodynamics of basic fibroblast growth factor: route of administration determines myocardial and systemic distribution.* Cardiovasc Res, 1997. **36**(1): p. 78-85.
47. Laham, R.J., et al., *Therapeutic Angiogenesis Using Basic Fibroblast Growth Factor and Vascular Endothelial Growth Factor Using Various Delivery Strategies.* Curr Interv Cardiol Rep, 1999. **1**(3): p. 228-233.
48. Nakajima, H., et al., *Therapeutic angiogenesis by the controlled release of basic fibroblast growth factor for ischemic limb and heart injury: toward safety and minimal invasiveness.* Journal of Artificial Organs, 2004. **7**(2): p. 58-61.
49. Davda, J. and V. Labhasetwar, *An update on angiogenesis therapy.* Crit Rev Eukaryot Gene Expr, 2001. **11**(1-3): p. 1-21.
50. Lopez, J.J., et al., *Angiogenic potential of perivascularly delivered aFGF in a porcine model of chronic myocardial ischemia.* Am J Physiol, 1998. **274**(3 Pt 2): p. H930-6.

51. Zisch, A.H., M.P. Lutolf, and J.A. Hubbell, *Biopolymeric delivery matrices for angiogenic growth factors.* Cardiovascular Pathology, 2003. **12**(6): p. 295-310.
52. Laham, R.J., M. Rezaee, and L. Garcia, *Tissue and Myocardial Distribution of Intracoronary, Intravenous, Intrapericardial, and Intramyocardial 125I-labeled basic fibroblast growth factor (bFGF) favor intramyocardial delivery.* Journal of the American College of Cardiology, 2000. **35**: p. 10A. Abstract.
53. Laham, R.J., et al., *Intrapericardial administration of basic fibroblast growth factor: myocardial and tissue distribution and comparison with intracoronary and intravenous administration.* Catheter Cardiovasc Interv, 2003. **58**(3): p. 375-81.
54. Celletti, F.L., et al., *Vascular endothelial growth factor enhances atherosclerotic plaque progression.* Nature Medicine, 2001. **7**(4): p. 425-9.
55. Nabel, E.G., et al., *Recombinant fibroblast growth factor-1 promotes intimal hyperplasia and angiogenesis in arteries in vivo.* Nature, 1993. **362**(6423): p. 844-6.
56. Gonzalez, A.M., et al., *Distribution of basic fibroblast growth factor in the 18-day rat fetus: localization in the basement membranes of diverse tissues.* J Cell Biol, 1990. **110**(3): p. 753-65.
57. Vlodavsky, I., et al., *Endothelial cell-derived basic fibroblast growth factor: synthesis and deposition into subendothelial extracellular matrix.* Proc Natl Acad Sci U S A, 1987. **84**(8): p. 2292-6.
58. Kanematsu, A., et al., *Type I collagen can function as a reservoir of basic fibroblast growth factor.* J Control Release, 2004. **99**(2): p. 281-92.
59. Presta, M., et al., *Fibroblast growth factor/fibroblast growth factor receptor system in angiogenesis.* Cytokine Growth Factor Rev, 2005. **16**(2): p. 159-78.
60. Coughlin, S.R., et al., *Acidic and basic fibroblast growth factors stimulate tyrosine kinase activity in vivo.* J Biol Chem, 1988. **263**(2): p. 988-93.
61. Moscatelli, D., *High and low affinity binding sites for basic fibroblast growth factor on cultured cells: absence of a role for low affinity binding in the stimulation of plasminogen activator production by bovine capillary endothelial cells.* J Cell Physiol, 1987. **131**(1): p. 123-30.
62. Colin, S., et al., *In vivo involvement of heparan sulfate proteoglycan in the bioavailability, internalization, and catabolism of exogenous basic fibroblast growth factor.* Mol Pharmacol, 1999. **55**(1): p. 74-82.
63. Damon, D.H., et al., *Heparin potentiates the action of acidic fibroblast growth factor by prolonging its biological half-life.* J Cell Physiol, 1989. **138**(2): p. 221-6.
64. Mueller, S.N., et al., *Stabilization by heparin of acidic fibroblast growth factor mitogenicity for human endothelial cells in vitro.* J Cell Physiol, 1989. **140**(3): p. 439-48.
65. Schonherr, E. and H.J. Hausser, *Extracellular matrix and cytokines: a functional unit.* Dev Immunol, 2000. **7**(2-4): p. 89-101.
66. Bashkin, P., et al., *Basic fibroblast growth factor binds to subendothelial extracellular matrix and is released by heparitinase and heparin-like molecules.* Biochemistry, 1989. **28**(4): p. 1737-43.

67. Saksela, O., et al., *Endothelial cell-derived heparan sulfate binds basic fibroblast growth factor and protects it from proteolytic degradation.* J Cell Biol, 1988. **107**(2): p. 743-51.
68. Flaumenhaft, R., D. Moscatelli, and D.B. Rifkin, *Heparin and heparan sulfate increase the radius of diffusion and action of basic fibroblast growth factor.* J Cell Biol, 1990. **111**(4): p. 1651-9.
69. Sellke, F.W., et al., *Enhanced microvascular relaxations to VEGF and bFGF in chronically ischemic porcine myocardium.* Am J Physiol, 1996. **271**(2 Pt 2): p. H713-20.
70. Ray, P.S., et al., *Early effects of hypoxia/reoxygenation on VEGF, ang-1, ang-2 and their receptors in the rat myocardium: implications for myocardial angiogenesis.* Mol Cell Biochem, 2000. **213**(1-2): p. 145-53.
71. Xu, X., et al., *Expression of vascular endothelial growth factor and its receptors is increased, but microvascular relaxation is impaired in patients after acute myocardial ischemia.* J Thorac Cardiovasc Surg, 2001. **121**(4): p. 735-42.
72. Li, J., et al., *Macrophage-dependent regulation of syndecan gene expression.* Circ Res, 1997. **81**(5): p. 785-96.
73. Nakahama, M., et al., *Expression of perlecan proteoglycan in the infarct zone of mouse myocardial infarction.* J Mol Cell Cardiol, 2000. **32**(6): p. 1087-100.
74. Li, J., et al., *VEGF, flk-1, and flt-1 expression in a rat myocardial infarction model of angiogenesis.* Am J Physiol, 1996. **270**(5 Pt 2): p. H1803-11.
75. Rissanen, T.T., et al., *Expression of vascular endothelial growth factor and vascular endothelial growth factor receptor-2 (KDR/Flk-1) in ischemic skeletal muscle and its regeneration.* Am J Pathol, 2002. **160**(4): p. 1393-403.
76. Meyer, G., R. Merval, and A. Tedgui, *Effects of pressure-induced stretch and convection on low-density lipoprotein and albumin uptake in the rabbit aortic wall.* Circ Res, 1996. **79**(3): p. 532-40.
77. Han, S., et al., *Changes in ADC caused by tensile loading of rabbit achilles tendon: evidence for water transport.* Journal of Magnetic Resonance, 2000. **144**(2): p. 217-27.
78. Quinn, T.M., V. Morel, and J.J. Meister, *Static compression of articular cartilage can reduce solute diffusivity and partitioning: implications for the chondrocyte biological response.* Journal of Biomechanics, 2001. **34**(11): p. 1463-9.
79. Quinn, T.M., et al., *Preservation and analysis of nonequilibrium solute concentration distributions within mechanically compressed cartilage explants.* J Biochem Biophys Methods, 2002. **52**(2): p. 83-95.
80. Burstein, D., et al., *Diffusion of small solutes in cartilage as measured by nuclear magnetic resonance (NMR) spectroscopy and imaging.* J Orthop Res, 1993. **11**(4): p. 465-78.
81. Bonassar, L.J., et al., *Mechanical and physicochemical regulation of the action of insulin-like growth factor-I on articular cartilage.* Arch Biochem Biophys, 2000. **379**(1): p. 57-63.
82. Papadopoulos, S., K.D. Jurgens, and G. Gros, *Protein diffusion in living skeletal muscle fibers: dependence on protein size, fiber type, and contraction.* Biophysical Journal, 2000. **79**(4): p. 2084-94.

83. Constable, S.H., et al., *Muscle glucose transport: interactions of in vitro contractions, insulin, and exercise.* Journal of Applied Physiology, 1988. **64**(6): p. 2329-32.
84. Holloszy, J.O. and H.T. Narahara, *Studies of tissue permeability. X. Changes in permeability to 3-methylglucose associated with contraction of isolated frog muscle.* Journal of Biological Chemistry, 1965. **240**(9): p. 3493-500.
85. Cho, K.W., et al., *Mechanical control of extracellular space in rabbit atria: an intimate modulator of the translocation of extracellular fluid and released atrial natriuretic peptide.* Exp Physiol, 2002. **87**(2): p. 185-94.
86. Page, E., J. Upshaw-Earley, and G. Goings, *Permeability of rat atrial endocardium, epicardium, and myocardium to large molecules. Stretch-dependent effects.* Circ Res, 1992. **71**(1): p. 159-73.
87. Cappelli, V., et al., *Inulin uptake and washout in contracting and quiescent rat papillary muscle.* Arch. Int. Physiol. Biochim., 1982. **90**(4): p. 231-6.
88. Zechner, C., F. Beyersdorf, and T. Doenst, *The role of calcium in the regulation of glucose uptake in isolated working rat heart.* Mol Cell Biochem, 2002. **232**(1-2): p. 75-80.
89. Young, D.A., *Factors controlling the washout of the interstitial space of the isolated, perfused rat heart.* J Physiol, 1968. **196**(3): p. 747-59.
90. Aslesen, R., et al., *Glucose uptake and metabolic stress in rat muscles stimulated electrically with different protocols.* Journal of Applied Physiology, 2001. **91**(3): p. 1237-44.
91. Gissel, H. and T. Clausen, *Excitation-induced Ca(2+) influx in rat soleus and EDL muscle: mechanisms and effects on cellular integrity.* American Journal of Physiology: Regulatory, Integrative and Comparative Physiology, 2000. **279**(3): p. R917-R924.
92. Abraham, K.A. and R.L. Terjung, *Phosphate uptake in rat skeletal muscle is reduced during isometric contractions.* Journal of Applied Physiology, 2004. **97**(1): p. 57-62.
93. Abel, E.D., *Glucose transport in the heart.* Front Biosci, 2004. **9**: p. 201-15.
94. Ihlemann, J., T. Ploug, and H. Galbo, *Effect of force development on contraction induced glucose transport in fast twitch rat muscle.* Acta Physiologica Scandinavica, 2001. **171**(4): p. 439-44.
95. Ihlemann, J., et al., *Effect of tension on contraction-induced glucose transport in rat skeletal muscle.* American Journal of Physiology: Endocrinology and Metabolism, 1999. **277**(2 Pt 1): p. E208-E214.
96. Ihlemann, J., et al., *Effect of stimulation frequency on contraction-induced glucose transport in rat skeletal muscle.* American Journal of Physiology: Endocrinology and Metabolism, 2000. **279**(4): p. E862-E867.
97. Nara, E., et al., *Contribution of interstitial diffusion in drug absorption from perfused rabbit muscle: effect of hyaluronidase on absorption.* Chemical & Pharmaceutical Bulletin, 1992. **40**(3): p. 737-40.
98. Segal, S.S., T.P. White, and J.A. Faulkner, *Architecture, composition, and contractile properties of rat soleus muscle grafts.* Am J Physiol, 1986. **250**(3 Pt 1): p. C474-9.

99. McComas, A.J., *Skeletal Muscle: Form and Function*. 1996, Champaign, IL: Human Kinetics.
100. Borg, T.K. and J.B. Caulfield, *Morphology of connective tissue in skeletal muscle.* Tissue Cell, 1980. **12**(1): p. 197-207.
101. DiMario, J., et al., *Fibroblast growth factor in the extracellular matrix of dystrophic (mdx) mouse muscle.* Science, 1989. **244**(4905): p. 688-90.
102. Jarvinen, T.A., et al., *Organization and distribution of intramuscular connective tissue in normal and immobilized skeletal muscles. An immunohistochemical, polarization and scanning electron microscopic study.* Journal of Muscle Research and Cell Motility, 2002. **23**(3): p. 245-54.
103. Purslow, P.P., *Strain-induced reorientation of an intramuscular connective tissue network: implications for passive muscle elasticity.* Journal of Biomechanics, 1989. **22**(1): p. 21-31.
104. Purslow, P.P. and J.A. Trotter, *The morphology and mechanical properties of endomysium in series-fibred muscles: variations with muscle length.* Journal of Muscle Research and Cell Motility, 1994. **15**(3): p. 299-308.
105. Williams, P.E. and G. Goldspink, *Connective tissue changes in immobilised muscle.* Journal of Anatomy, 1984. **138 (Pt 2)**: p. 343-50.
106. Willems, M.E. and P.A. Huijing, *Mechanical and geometrical properties of the rat semimembranosus lateralis muscle during isometric contractions.* Journal of Biomechanics, 1994. **27**(9): p. 1109-18.
107. Trombitas, K., et al., *Contraction-induced movements of water in single fibres of frog skeletal muscle.* Journal of Muscle Research and Cell Motility, 1993. **14**(6): p. 573-84.
108. Canale, E.D., et al., *Cardiac Muscle*. 1986, New York: Springer-Verlag.
109. Brecher, G.A. and P.M. Galletti, *Functional Anatomy of Cardiac Pumping*, in *Handbook of Physiology, Section II, Circulation, Volume II*, W.F. Hamilton and P. Dow, Editors. 1963, American Physiological Society: Baltimore, MD.
110. Hunter, P., M. Nash, and G. Sands, *Computational Electromechanics of the Heart*, in *Computational Biology of the Heart*, A.V. Panfilov and A.V. Holden, Editors. 1997, Wiley & Sons: U.K.
111. Young, A.A., et al., *Extended confocal microscopy of myocardial laminae and collagen network.* J Microsc, 1998. **192 (Pt 2)**: p. 139-50.
112. Caulfield, J.B. and T.K. Borg, *The collagen network of the heart.* Lab Invest, 1979. **40**(3): p. 364-72.
113. MacKenna, D.A., J.H. Omens, and J.W. Covell, *Left ventricular perimysial collagen fibers uncoil rather than stretch during diastolic filling.* Basic Res Cardiol, 1996. **91**(2): p. 111-22.
114. Factor, S.M., et al., *The effects of acutely increased ventricular cavity pressure on intrinsic myocardial connective tissue.* J Am Coll Cardiol, 1988. **12**(6): p. 1582-9.
115. Waldman, L.K., et al., *Relation between transmural deformation and local myofiber direction in canine left ventricle.* Circ Res, 1988. **63**(3): p. 550-62.
116. Ashikaga, H., et al., *Transmural left ventricular mechanics underlying torsional recoil during relaxation.* Am J Physiol Heart Circ Physiol, 2004. **286**(2): p. H640-7.

117. Tischler, M. and J. Niggel, *Left ventricular systolic torsion and exercise in normal hearts.* J Am Soc Echocardiogr, 2003. **16**(6): p. 670-4.
118. Takayama, Y., K.D. Costa, and J.W. Covell, *Contribution of laminar myofiber architecture to load-dependent changes in mechanics of LV myocardium.* Am J Physiol Heart Circ Physiol, 2002. **282**(4): p. H1510-20.
119. Harrington, K.B., et al., *Direct measurement of transmural laminar architecture in the anterolateral wall of the ovine left ventricle: new implications for wall thickening mechanics.* Am J Physiol Heart Circ Physiol, 2005. **288**(3): p. H1324-30.
120. Sinusas, A.J., et al., *Quantification of 3-D regional myocardial deformation: shape-based analysis of magnetic resonance images.* Am J Physiol Heart Circ Physiol, 2001. **281**(2): p. H698-714.
121. Cheng, A., et al., *Transmural cardiac strains in the lateral wall of the ovine left ventricle.* Am J Physiol Heart Circ Physiol, 2005. **288**(4): p. H1546-56.
122. Sreter, F.A., *Distribution of water, sodium, and potassium in resting and stimulated mammalian muscle.* Canadian Journal of Biochemistry and Physiology, 1963. **41**: p. 1035-45.
123. Huang, C.Y. and W.Y. Gu, *Effects of tension-compression nonlinearity on solute transport in charged hydrated fibrous tissues under dynamic unconfined compression.* Journal of Biomechanical Engineering, 2007. **129**(3): p. 423-9.
124. Helmer, K.G., et al., *Water movement in tendon in response to a repeated static tensile load using one-dimensional magnetic resonance imaging.* Journal of Biomechanical Engineering, 2006. **128**(5): p. 733-41.
125. Fry, D.L., R.W. Mahley, and S.Y. Oh, *Effect of arterial stretch on transmural albumin and Evan's blue dye transport.* American Journal of Physiology: Heart and Circulatory Physiology, 1981. **240**(4): p. H645-H649.
126. Epstein, S.E., et al., *Therapeutic interventions for enhancing collateral development by administration of growth factors: basic principles, early results and potential hazards.* Cardiovascular Research, 2001. **49**(3): p. 532-42.
127. Ettema, G.J., *Mechanical behaviour of rat skeletal muscle during fatiguing stretch-shortening cycles.* Experimental Physiology, 1997. **82**(1): p. 107-19.
128. Ettema, G.J., J.T. Goh, and M.R. Forwood, *A new method to measure elastic properties of plastic-viscoelastic connective tissue.* Medical Engineering and Physics, 1998. **20**(4): p. 308-14.
129. Loeffler, L., 3rd and K. Sagawa, *A one-dimensional viscoelastic model of cat heart muscle studied by small length perturbations during isometric contraction.* Circulation Research, 1975. **36**(4): p. 498-512.
130. Templeton, G.H., et al., *Dynamic stiffness of papillary muscle during contraction and relaxation.* American Journal of Physiology, 1973. **224**(3): p. 692-8.
131. Segal, S.S. and J.A. Faulkner, *Temperature-dependent physiological stability of rat skeletal muscle in vitro.* American Journal of Physiology: Cell Physiology, 1985. **248**(3 Pt 1): p. C265-C270.
132. Petrofsky, J.S. and A.R. Lind, *The influence of temperature on the isometric characteristics of fast and slow muscle in the cat.* Pflügers Archiv: European Journal of Physiology, 1981. **389**(2): p. 149-54.

133. Blomstrand, E., L. Larsson, and L. Edstrom, *Contractile properties, fatiguability and glycolytic metabolism in fast- and slow-twitch rat skeletal muscles of various temperatures.* Acta Physiologica Scandinavica, 1985. **125**(2): p. 235-43.
134. Osman, F.H., J.L. Munson, and D.M. Paton, *Estimation of extracellular space in rabbit detrusor muscle.* Comp Biochem Physiol A, 1971. **40**(1): p. 45-54.
135. Rutili, G. and K.E. Arfors, *Fluorescein-labelled dextran measurement in interstitial fluid in studies of macromolecular permeability.* Microvascular Research, 1976. **12**(2): p. 221-30.
136. Elmquist, S., et al., *Dextrans as markers for endocytosis in innervated and denervated skeletal muscle.* Muscle Nerve, 1992. **15**(8): p. 876-84.
137. Lovich, M.A. and E.R. Edelman, *Tissue average binding and equilibrium distribution: an example with heparin in arterial tissues.* Biophysical Journal, 1996. **70**(3): p. 1553-9.
138. Mehvar, R., *Dextrans for targeted and sustained delivery of therapeutic and imaging agents.* Journal of Controlled Release, 2000. **69**(1): p. 1-25.
139. Schroder, U., K.E. Arfors, and O. Tangen, *Stability of fluorescein labeled dextrans in vivo and in vitro.* Microvascular Research, 1976. **11**(1): p. 57-66.
140. Pringsheim, P., *Fluorescence and Phosphorescence.* 1963, New York: Interscience Publishers, Inc. p. 347.
141. Ryall, J.G., et al., *Beta 2-agonist fenoterol has greater effects on contractile function of rat skeletal muscles than clenbuterol.* American Journal of Physiology: Regulatory, Integrative and Comparative Physiology, 2002. **283**(6): p. R1386-R1394.
142. Rankin, L.L., et al., *Coexistence of twitch potentiation and tetanic force decline in rat hindlimb muscle.* Journal of Applied Physiology, 1988. **65**(6): p. 2687-95.
143. Cappelli, V., et al., *Tritiated water (HTO) and inulin spaces in isolated skeletal and cardiac muscles: influence of contractile activity.* Experientia, 1981. **37**(8): p. 849-50.
144. Creese, R., J.L. D'Silva, and S.E. Hashish, *Inulin space and fibre size of stimulated rat muscle.* Journal of Physiology, 1955. **127**(3): p. 525-32.
145. Ward, D.S., M.T. Hamilton, and P.D. Watson, *Measurement of tissue volume during non-steady state high-intensity muscle contraction.* American Journal of Physiology: Regulatory, Integrative and Comparative Physiology, 1996. **271**(6 Pt 2): p. R1682-R1690.
146. Baker, C.H. and D.L. Davis, *Isolated skeletal muscle blood flow and volume changes during contractile activity.* Blood Vessels, 1974. **11**(1-2): p. 32-44.
147. Sreter, F.A., *Cell Water, Sodium, And Potassium In Stimulated Red And White Mammalian Muscles.* American Journal of Physiology, 1963. **205**: p. 1295-1298.
148. McDermott, J.C. and A. Bonen, *Lactate transport in rat sarcolemmal vesicles and intact skeletal muscle, and after muscle contraction.* Acta Physiologica Scandinavica, 1994. **151**(1): p. 17-28.
149. Gissel, H. and T. Clausen, *Excitation-induced Ca2+ uptake in rat skeletal muscle.* American Journal of Physiology: Regulatory, Integrative and Comparative Physiology, 1999. **276**(2 Pt 2): p. R331-R339.
150. Armstrong, R.B., et al., *Elevations in rat soleus muscle [Ca2+] with passive stretch.* Journal of Applied Physiology, 1993. **74**(6): p. 2990-7.

151. Hawkins, D. and M. Bey, *Muscle and tendon force-length properties and their interactions in vivo.* Journal of Biomechanics, 1997. **30**(1): p. 63-70.
152. Wisnes, A. and A. Kirkebo, *Regional distribution of blood flow in calf muscles of rat during passive stretch and sustained contraction.* Acta Physiologica Scandinavica, 1976. **96**(2): p. 256-66.
153. Baskin, R.J. and P.J. Paolini, *Muscle volume changes.* Journal of General Physiology, 1966. **49**(3): p. 387-404.
154. Gauthier, M.G. and G.W. Slater, *Exactly solvable Ogston model of gel electrophoresis. IX. Generalizing the lattic model to treat high field intensities.* Journal of Chemical Physics, 2002. **117**(14): p. 6745-6756.
155. McCarthy, M.J., D.S. Soong, and E.R. Edelman, *Control of Drug Release From Polymer Matrices Impregnated with Magnetic Beads - A Proposed Mechanism and Model for Enhanced Release.* Journal of Controlled Release, 1984. **1**: p. 143-147.
156. Zuurbier, C.J. and P.A. Huijing, *Changes in geometry of actively shortening unipennate rat gastrocnemius muscle.* Journal of Morphology, 1993. **218**(2): p. 167-80.
157. van Donkelaar, C.C., et al., *Skeletal muscle transverse strain during isometric contraction at different lengths.* Journal of Biomechanics, 1999. **32**(8): p. 755-62.
158. Saltzman, W.M. and W.L. Olbricht, *Building drug delivery into tissue engineering.* Nat Rev Drug Discov, 2002. **1**(3): p. 177-86.
159. Gu, F., B. Amsden, and R. Neufeld, *Sustained delivery of vascular endothelial growth factor with alginate beads.* J Control Release, 2004. **96**(3): p. 463-72.
160. Guan, J., J.J. Stankus, and W.R. Wagner, *Biodegradable elastomeric scaffolds with basic fibroblast growth factor release.* Journal of Controlled Release, 2007. **120**(1-2): p. 70-8.
161. Tabata, Y., et al., *Controlled release of vascular endothelial growth factor by use of collagen hydrogels.* Journal of Biomaterials Science, Polymer Edition, 2000. **11**(9): p. 915-30.
162. Richardson, T.P., et al., *Polymeric system for dual growth factor delivery.* Nature Biotechnology, 2001. **19**(11): p. 1029-34.
163. Hosaka, A., et al., *Gelatin hydrogel microspheres enable pinpoint delivery of basic fibroblast growth factor for the development of functional collateral vessels.* Circulation, 2004. **110**(21): p. 3322-8.
164. Boodhwani, M., et al., *The future of therapeutic myocardial angiogenesis.* Shock, 2006. **26**(4): p. 332-41.
165. Freedman, S.B. and J.M. Isner, *Therapeutic angiogenesis for coronary artery disease.* Annals of Internal Medicine, 2002. **136**(1): p. 54-71.
166. Fannon, M., K.E. Forsten, and M.A. Nugent, *Potentiation and inhibition of bFGF binding by heparin: a model for regulation of cellular response.* Biochemistry, 2000. **39**(6): p. 1434-45.
167. Kang, S.S., et al., *Selective stimulation of endothelial cell proliferation with inhibition of smooth muscle cell proliferation by fibroblast growth factor-1 plus heparin delivered from fibrin glue suspensions.* Surgery, 1995. **118**(2): p. 280-6; discussion 286-7.

168. Carmeliet, P., *Mechanisms of angiogenesis and arteriogenesis.* Nature Medicine, 2000. **6**(4): p. 389-95.
169. Peirce, S.M. and T.C. Skalak, *Microvascular remodeling: a complex continuum spanning angiogenesis to arteriogenesis.* Microcirculation, 2003. **10**(1): p. 99-111.
170. Lu, H., et al., *Combinatorial protein therapy of angiogenic and arteriogenic factors remarkably improves collaterogenesis and cardiac function in pigs.* Proc Natl Acad Sci U S A, 2007. **104**(29): p. 12140-5.
171. Zakrzewska, M., et al., *Highly stable mutants of human fibroblast growth factor-1 exhibit prolonged biological action.* Journal of Molecular Biology, 2005. **352**(4): p. 860-75.
172. Takeshita, S., et al., *Therapeutic angiogenesis. A single intraarterial bolus of vascular endothelial growth factor augments revascularization in a rabbit ischemic hind limb model.* J Clin Invest, 1994. **93**(2): p. 662-70.
173. Masuoka, K., et al., *The interaction of chitosan with fibroblast growth factor-2 and its protection from inactivation.* Biomaterials, 2005. **26**(16): p. 3277-84.
174. Epstein, S.E., et al., *Angiogenesis therapy: amidst the hype, the neglected potential for serious side effects.* Circulation, 2001. **104**(1): p. 115-9.
175. Carpenter, A.E., et al., *CellProfiler: image analysis software for identifying and quantifying cell phenotypes.* Genome Biol, 2006. **7**(10): p. R100.
176. Gilbert, D.L. and S.W. Kim, *Macromolecular release from collagen monolithic devices.* Journal of Biomedical Materials Research, 1990. **24**(9): p. 1221-39.
177. Khaled, A.-R.A. and K. Vafai, *The role of porous media in modeling flow and heat transfer in biological tissues.* International Journal of Heat and Mass Transfer, 2003. **46**(26): p. 4989-5003.
178. El-Kareh, A.W., S.L. Braunstein, and T.W. Secomb, *Effect of cell arrangement and interstitial volume fraction on the diffusivity of monoclonal antibodies in tissue.* Biophysical Journal, 1993. **64**(5): p. 1638-46.
179. Nicholson, C. and J.M. Phillips, *Ion diffusion modified by tortuosity and volume fraction in the extracellular microenvironment of the rat cerebellum.* Journal of Physiology, 1981. **321**: p. 225-57.
180. Chen, K.C. and C. Nicholson, *Changes in brain cell shape create residual extracellular space volume and explain tortuosity behavior during osmotic challenge.* Proceedings of the National Academy of Sciences of the United States of America, 2000. **97**(15): p. 8306-11.
181. Nicholson, C., *Diffusion and related transport mechanisms in brain tissue.* Reports on Progress in Physics, 2001. **64**(7): p. 815-884.
182. Blum, J.J., et al., *Effect of cytoskeletal geometry on intracellular diffusion.* Biophysical Journal, 1989. **56**(5): p. 995-1005.
183. Nugent, L.J. and R.K. Jain, *Plasma pharmacokinetics and interstitial diffusion of macromolecules in a capillary bed.* Am J Physiol, 1984. **246**(1 Pt 2): p. H129-37.
184. Bensoussan, A., J.L. Lions, and G. Papanicolaou, *Asymptotic Analysis for Periodic Structures*. 1978, New York: North Holland Science Publishers.
185. H. Gordon Harris, J. and S.L. Goren, *Axial diffusion in a cylinder with pulsed flow.* Chemical Engineering Science, 1967. **22**: p. 1571-1576.

186. Thomas, A.M. and R. Narayanan, *Physics of oscillatory flow and its effect on the mass transfer and separation of species.* Physics of Fluids, 2001. **13**(4): p. 859-866.
187. Azer, K., *Taylor diffusion in time-dependent flow.* International Journal of Heat and Mass Transfer, 2005. **48**(13): p. 2735-2740.
188. Fung, Y.C., *Biomechanics: Mechanical Properties of Living Tissues*. 2 ed. 1993, New York: Springer-Verlag.
189. Formaggia, L. and F. Nobile, *A stability analysis for the arbitrary lagrangian eulerian formuation with finite elements.* East-West Journal of Numerical Mathematics, 1999. **7**(2): p. 105-131.
190. Leypoldt, J.K. and L.W. Henderson, *Molecular charge influences transperitoneal macromolecule transport.* Kidney Int, 1993. **43**(4): p. 837-44.
191. Deen, W.M., *Analysis of Transport Phenomena*. Topics in Chemical Engineering: A Series of Textbooks and Monographs, ed. K.E. Gubbins. 1998, New York: Oxford University Press. p. 19.
192. Hill, D.K., *The organization of the inter-fibre space in the striated muscle of the toad, and the alignment of striations of neighbouring fibres.* Journal of Physiology, 1965. **179**(2): p. 368-84.
193. Kobayashi, N. and K. Yonemura, *The extracellular space in red and white muscles of the rat.* Japanese Journal of Physiology, 1967. **17**(6): p. 698-707.
194. Sreter, F.A. and G. Woo, *Cell Water, Sodium, And Potassium In Red And White Mammalian Muscles.* American Journal of Physiology, 1963. **205**: p. 1290-4.
195. Gajdosik, R.L., *Passive extensibility of skeletal muscle: review of the literature with clinical implications.* Clinical Biomechanics, 2001. **16**(2): p. 87-101.
196. Bozler, E., *Determination of extracellular space in amphibian muscle.* Journal of General Physiology, 1967. **50**(5): p. 1459-65.
197. Neville, M.C. and R.T. Mathias, *The extracellular compartments of frog skeletal muscle.* Journal of Physiology, 1979. **288**: p. 45-70.
198. Davis, J., K.R. Kaufman, and R.L. Lieber, *Correlation between active and passive isometric force and intramuscular pressure in the isolated rabbit tibialis anterior muscle.* Journal of Biomechanics, 2003. **36**(4): p. 505-12.
199. Sejersted, O.M. and A.R. Hargens, *Intramuscular Pressures For Monitoring Different Tasks and Muscle Conditions*, in *Fatigue*, S.C. Gandevia, Editor. 1995, Plenum Press: New York. p. 339-350.
200. Mulherkar, P. and R.v. Reis, *Flex test: a fluorescent dextran test for UF membrane characterization.* Journal of Membrane Science, 2004. **236**(1-2): p. 171-182.
201. Sahagun, G., S.A. Moore, and M.N. Hart, *Permeability of neutral vs. anionic dextrans in cultured brain microvascular endothelium.* Am J Physiol, 1990. **259**(1 Pt 2): p. H162-6.
202. Tanford, C., *Physical Chemistry of Macromolecules*. 1961, New York: John Wiley and Sons, Inc.
203. Han, J. and J. Herzfeld, *Macromolecular diffusion in crowded solutions.* Biophys J, 1993. **65**(3): p. 1155-61.

204. Huijing, P.A., *Muscle as a collagen fiber reinforced composite: a review of force transmission in muscle and whole limb.* Journal of Biomechanics, 1999. **32**(4): p. 329-45.
205. Passerieux, E., et al., *Physical continuity of the perimysium from myofibers to tendons: involvement in lateral force transmission in skeletal muscle.* Journal of Structural Biology, 2007. **159**(1): p. 19-28.
206. Neering, I.R., et al., *Nonuniform volume changes during muscle contraction.* Biophysical Journal, 1991. **59**(4): p. 926-33.
207. Balcells, M., et al., *Cells in fluidic environments are sensitive to flow frequency.* Journal of Cellular Physiology, 2005. **204**(1): p. 329-35.
208. Yin, F.C. and H. Yamada, *The effects of left ventricular stretch versus cavity pressure on intramyocardial pressure.* Cardiovasc Res, 1997. **34**(2): p. 299-305.
209. Rademakers, F.E., et al., *Relation of regional cross-fiber shortening to wall thickening in the intact heart. Three-dimensional strain analysis by NMR tagging.* Circulation, 1994. **89**(3): p. 1174-82.
210. Chen, J., et al., *Regional ventricular wall thickening reflects changes in cardiac fiber and sheet structure during contraction: quantification with diffusion tensor MRI.* Am J Physiol Heart Circ Physiol, 2005. **289**(5): p. H1898-907.
211. Iwakura, A., et al., *Intramyocardial sustained delivery of basic fibroblast growth factor improves angiogenesis and ventricular function in a rat infarct model.* Heart Vessels, 2003. **18**(2): p. 93-9.
212. Elbrink, J. and I. Bihler, *The effect of stimulating frequency and of ouabain on the intracellular penetration of L-arabinose in rabbit ventricular muscle, in vitro.* Life Sci II, 1973. **12**(2): p. 79-87.
213. Peterson, M.B. and M. Lesch, *Protein synthesis and amino acid transport in the isolated rabbit right ventricular papillary muscle. Effect of isometric tension development.* Circ Res, 1972. **31**(3): p. 317-27.
214. Lesch, M., R. Gorlin, and E.H. Sonnenblick, *Myocardial amino acid transport in the isolated rabbit right ventricular papillary muscle. General characteristics and effects of passive stretch.* Circ Res, 1970. **27**(3): p. 445-60.
215. Rosen, M.R. and H. Gelband, *Effects of ouabain on canine Purkinje fibers in situ or perfused with blood.* J Pharmacol Exp Ther, 1973. **186**(2): p. 366-72.
216. Lullmann, H., T. Peters, and U. Ravens, *Studies on the kinetics of (3H)-ouabain uptake and exchange in the isolated papillary muscle of the guinea-pig.* Br J Pharmacol, 1975. **53**(1): p. 99-107.
217. Huang, Y.F., et al., *Tachycardia alone fails to change the myocardial pharmacokinetics and dynamics of lidocaine, thiopental, and verapamil after intravenous bolus administration in sheep.* J Pharm Sci, 1998. **87**(7): p. 854-8.
218. Lloyd, B.L. and R.R. Taylor, *Influence of myocardial mechanical activity and coronary blood flow on myocardial digoxin uptake.* Cardiovasc Res, 1976. **10**(4): p. 487-93.
219. Cieslar, J., M.T. Huang, and G.P. Dobson, *Tissue spaces in rat heart, liver, and skeletal muscle in vivo.* Am J Physiol, 1998. **275**(5 Pt 2): p. R1530-6.
220. Berne, R.M. and M.N. Levy, eds. *Physiology.* 4th ed. 1998, Mosby, Inc.: Philadelphia, PA. 361.

221. Poole-Wilson, P.A., P.D. Bourdillon, and D.P. Harding, *Influence of contractile state on the size of the extracellular space in isolated ventricular myocardium.* Basic Res Cardiol, 1979. **74**(6): p. 604-10.
222. Rabbany, S.Y., J.Y. Kresh, and A. Noordergraaf, *Intramyocardial pressure: interaction of myocardial fluid pressure and fiber stress.* Am J Physiol, 1989. **257**(2 Pt 2): p. H357-64.
223. Stein, P.D., et al., *Comparison of the distribution of intramyocardial pressure across the canine left ventricular wall in the beating heart during diastole and in the arrested heart. Evidence of epicardial muscle tone during diastole.* Circ Res, 1980. **47**(2): p. 258-67.
224. Stein, P.D., H.N. Sabbah, and M. Marzilli, *Intramyocardial pressure and coronary extravascular resistance.* J Biomech Eng, 1985. **107**(1): p. 46-50.
225. Dinbergs, I.D., L. Brown, and E.R. Edelman, *Cellular response to transforming growth factor-beta1 and basic fibroblast growth factor depends on release kinetics and extracellular matrix interactions.* J Biol Chem, 1996. **271**(47): p. 29822-9.
226. Liu, L., et al., *Adult cardiomyocytes express functional high-affinity receptors for basic fibroblast growth factor.* Am J Physiol, 1995. **268**(5 Pt 2): p. H1927-38.
227. Dowd, C.J., C.L. Cooney, and M.A. Nugent, *Heparan sulfate mediates bFGF transport through basement membrane by diffusion with rapid reversible binding.* J Biol Chem, 1999. **274**(8): p. 5236-44.
228. Gallagher, K.P., et al., *The distribution of functional impairment across the lateral border of acutely ischemic myocardium.* Circ Res, 1986. **58**(4): p. 570-83.
229. Rodriguez, F., et al., *Alterations in transmural strains adjacent to ischemic myocardium during acute midcircumflex occlusion.* J Thorac Cardiovasc Surg, 2005. **129**(4): p. 791-803.
230. Finsen, A.V., et al., *Increased syndecan expression following myocardial infarction indicates a role in cardiac remodeling.* Physiol Genomics, 2004. **16**(3): p. 301-8.
231. Kresh, J.Y., M.A. Cobanoglu, and S.K. Brockman, *The intramyocardial pressure: a parameter of heart contractility.* J Heart Transplant, 1985. **4**(2): p. 241-6.
232. Henning, R.J., et al., *Increased heart rate accelerates norepinephrine washout from normal myocardium.* Am J Physiol, 1987. **253**(6 Pt 2): p. H1581-5.
233. Fagard, R., *Athlete's heart.* Heart, 2003. **89**(12): p. 1455-61.
234. Hughes, S.E., *The pathology of hypertrophic cardiomyopathy.* Histopathology, 2004. **44**(5): p. 412-27.
235. Roberts, W.C. and V.J. Ferrans, *Pathologic anatomy of the cardiomyopathies. Idiopathic dilated and hypertrophic types, infiltrative types, and endomyocardial disease with and without eosinophilia.* Hum Pathol, 1975. **6**(3): p. 287-342.
236. van der Bel-Kahn, J., *Muscle fiber disarray in common heart diseases.* Am J Cardiol, 1977. **40**(3): p. 355-64.
237. Sun, Y. and K.T. Weber, *Infarct scar: a dynamic tissue.* Cardiovasc Res, 2000. **46**(2): p. 250-6.
238. Lakhan, S.E. and L. Harle, *Cardiac fibrosis in the elderly, normotensive athlete: case report and review of the literature.* Diagn Pathol, 2008. **3**: p. 12.

239. Schoen, F.J., *The Heart*, in *Robbins Pathologic Basis of Disease*, R.S. Cotran, V. Kumar, and T. Collins, Editors. 1999, W.B. Saunders Company: New York, NY. p. 586-587.
240. Perloff, J.K., A.C. de Leon, Jr., and D. O'Doherty, *The cardiomyopathy of progressive muscular dystrophy.* Circulation, 1966. **33**(4): p. 625-48.
241. Burlew, B.S. and K.T. Weber, *Connective tissue and the heart. Functional significance and regulatory mechanisms.* Cardiol Clin, 2000. **18**(3): p. 435-42.
242. Nikolic, S., et al., *Passive properties of canine left ventricle: diastolic stiffness and restoring forces.* Circ Res, 1988. **62**(6): p. 1210-22.
243. Duncker, D.J. and R.J. Bache, *Regulation of coronary blood flow during exercise.* Physiol Rev, 2008. **88**(3): p. 1009-86.
244. Plehn, G., et al., *Loss of diastolic time as a mechanism of exercise-induced diastolic dysfunction in dilated cardiomyopathy.* Am Heart J, 2008. **155**(6): p. 1013-9.
245. Braunwald, E. and M.A. Pfeffer, *Ventricular enlargement and remodeling following acute myocardial infarction: mechanisms and management.* Am J Cardiol, 1991. **68**(14): p. 1D-6D.
246. Holmes, J.W., T.K. Borg, and J.W. Covell, *Structure and mechanics of healing myocardial infarcts.* Annu Rev Biomed Eng, 2005. **7**: p. 223-53.
247. Zilberman, M. and M. Sofer, *A mathematical model for predicting controlled release of bioactive agents from composite fiber structures.* J Biomed Mater Res A, 2007. **80**(3): p. 679-86.

8. ACKNOWLEDGMENTS

Sources of Funding

These studies were supported in part by graduate fellowships from the Department of Defense, the Whitaker Foundation for Biomedical Engineering, and the Harvard-MIT Division of Health Sciences and Technology Medical Engineering and Medical Physics Program to Peter I. Wu, the "Progetto Roberto Rocca" MIT-Politecnico di Milano collaboration to Sara Minisini, the Department of Anesthesiology and Pain Medicine at Caritas St. Elizabeth's Medical Center, Brighton, MA, and a research grant from the National Institutes of Health (NIH/NIGMS R01/HL049039) to Elazer R. Edelman.

Chapter 2

Thank you to Gerry Wentworth and Mark Belanger from the M.I.T. Laboratory of Manufacturing and Productivity for providing technical advice and assistance on the manufacturing process of the mechanical loading system. Thank you to Martin J. Kushmerick, M.D., Ph.D. from the University of Washington Physiology and Biophysics Department for providing expertise and insight on experimental techniques related to muscle physiology. Thank you to Kha N. Le for discussions on the conceptual design of the mechanical loading system and setup of drug transport experiments.

Chapter 3

Thank you to Sara Minisini for providing mathematical expertise and producing the mathematical analyses and computational models that were used to characterize drug transport in skeletal muscle. Thank you to Abraham Wei for providing assistance on surgical, experimental, and histologic work.

Chapter 4

Thank you to Mark A. Lovich, M.D., Ph.D. for providing expertise on anesthesiology and cardiovascular pharmacology, as well as supplying the MPVS 300 data acquisition system. Thank you to Robert P. Marini D.V.M., D.A.C.L.A.M. from the M.I.T. Division of Comparative Medicine for serving as a resource on surgical protocol and techniques. Thank you to Michael J. Raher from the Massachusetts General Hospital Department of Anesthesia and Critical Care for serving as a technical resource on hemodynamic monitoring of small rodents in the surgical setting. Thank you to Abraham Wei for providing assistance on growth factor production and surgical, experimental, and histologic work. Thank you to Philip Seifert, Leslie Arnold, Gilan Hashemi, and Gee Wong for technical assistance in histology.

APPENDIX A: MATLAB SOURCE CODE TO SIMULATE RESTING MUSCLE RESPONSES TO LENGTH PERTURBATIONS

Simulation of Step Response

```
clear
clc

%____Parameter Values for Inertial Mass, Muscle Stiffnesses, and Damping
Coefficients___
%____In SI Units, Newton, Kg, Meter, Seconds_____

%_____Amplitude of length perturbation_____
A=.002; %m

k0=10*9.806658*20;  %N/m          conversion from g/mm to N/m multiplied by
k1=3*9.80665*20;  %N/m         cross-sectional area of 20 mm^2
k2=2.5*9.80665*20;  %N/m
c1=.1625*9.80665*20;  %N.s/m
c2=6*9.80665*20;  %N.s/m

%______Time-Domain
Equations_____
t=linspace(0,10,100);

first=A*k0;
second=A*k1*exp(-t/(c1/k1));
third=A*k2*exp(-t/(c2/k2));

fp=first+second+third;

max(fp)
plot(t,fp)
title('Passive Tension Response of Muscle to Step Displacement of 0.002m')
xlabel('Time (sec)')
ylabel('Force (N)')
```

Simulation of Frequency Response

```
clear
clc

%____Parameter Values for Inertial Mass, Muscle Stiffnesses, and Damping
Coefficients___
%____In SI Units, Newton, Kg, Meter,
Seconds_____

%____Total Mass Estimate of muscle and loading assembly components
m=0.2;          %kg

%____Model
Parameters_____
k0=10*9.806658*20;  %N/m          conversion from g/mm to N/m multiplied by
k1=3*9.80665*20;  %N/m                    cross-sectional area of 20 mm^2
k2=2.5*9.80665*20;  %N/m
c1=.1625*9.80665*20;  %N.s/m
c2=6*9.80665*20;  %N.s/m

%_____
___
%____State Space
Model_____
A=[0 (-1/m) (-1/m) (-1/m); k1 (-k1/c1) 0 0; k2 0 (-k2/c2) 0; k0 0 0 0 ];
B=[(1/m); 0;0;0];
C=[1 0 0 0];
D=[0];
sys=ss(A,B,C,D);

%_____
___
%____Vm/Fin Transfer
Function_____
sys2=tf(sys);

%____Creation of the Fin/Xm Transfer
Function_____
den=[5 94.39 38.46 0];
num=[1 18.88 1.521e004 2.316e005 7.544e004 0];

%____Maximum
Estimate_____
%Transfer function
% 5 s^3 + 94.39 s^2 + 38.46 s
```

```
%-------------------------------------------------------
%s^4 + 18.88 s^3 + 1.521e004 s^2 + 2.316e005 s + 7.544e004

%____Bode Plot of Displacement Input and Force
Output_____________________________
w=logspace(0,1.3,1000);
bode(num,den,w)
[MAG,PHASE,W] = BODE(num,den,w);

%_____________________________________________________________________
___
%Multiply the Force by a 20% displacement for a 10mm length of muscle
%or a 2mm length perturbation
```

APPENDIX B: LOADING SYSTEM COMPONENT DESIGNS

Fibula Mounting Block (all units are in inches)

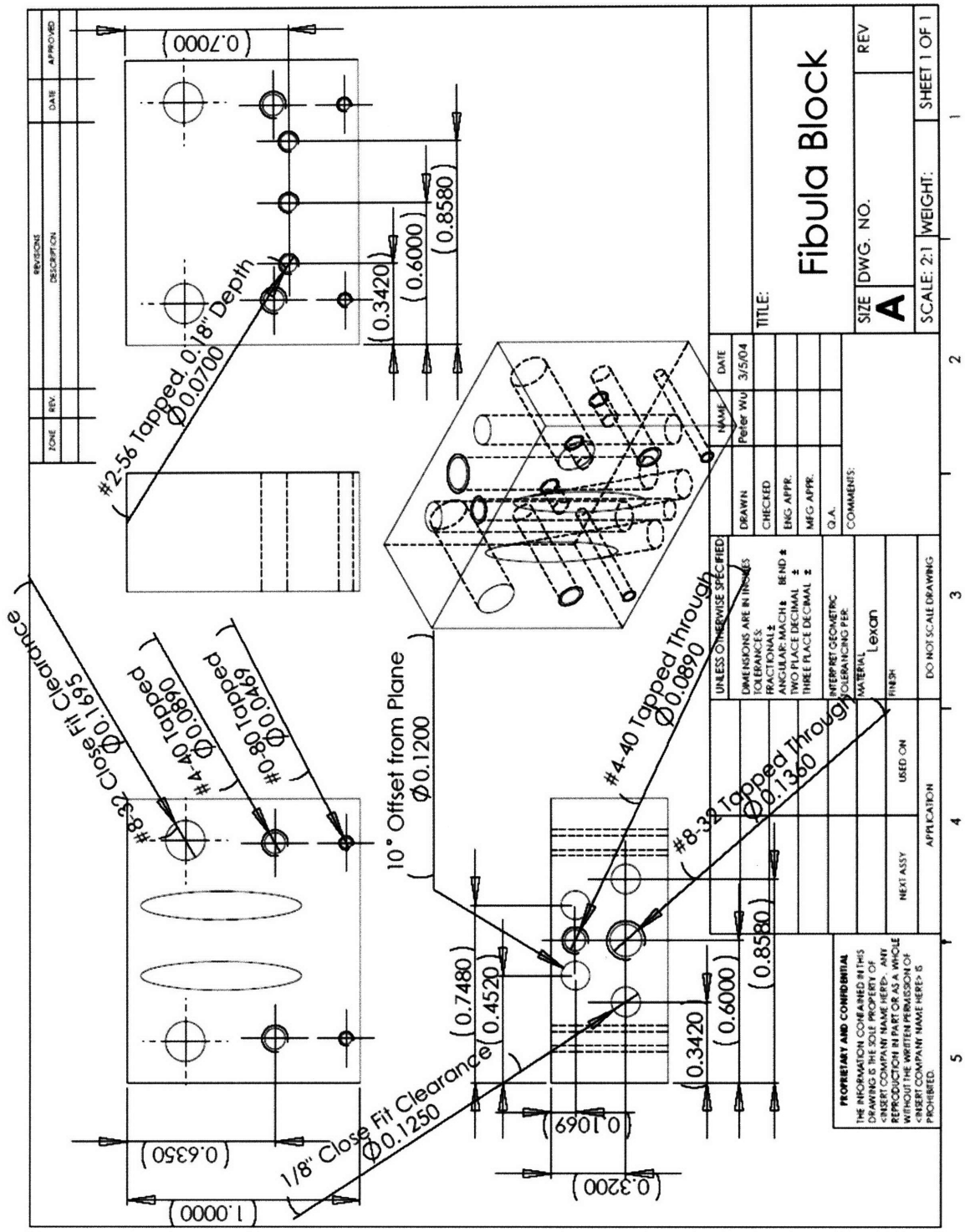

Calcaneus Mounting Block

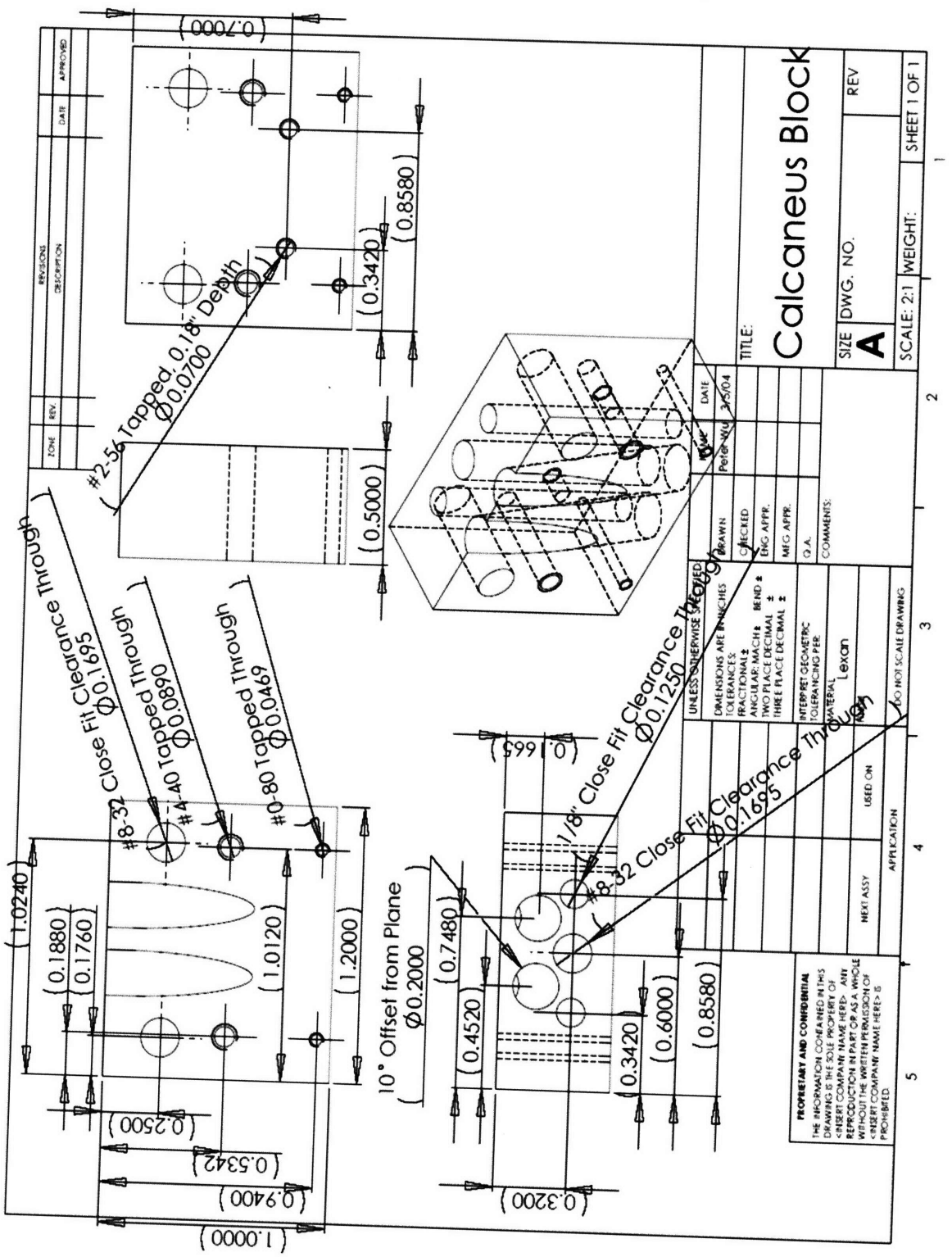

Bone Clamp

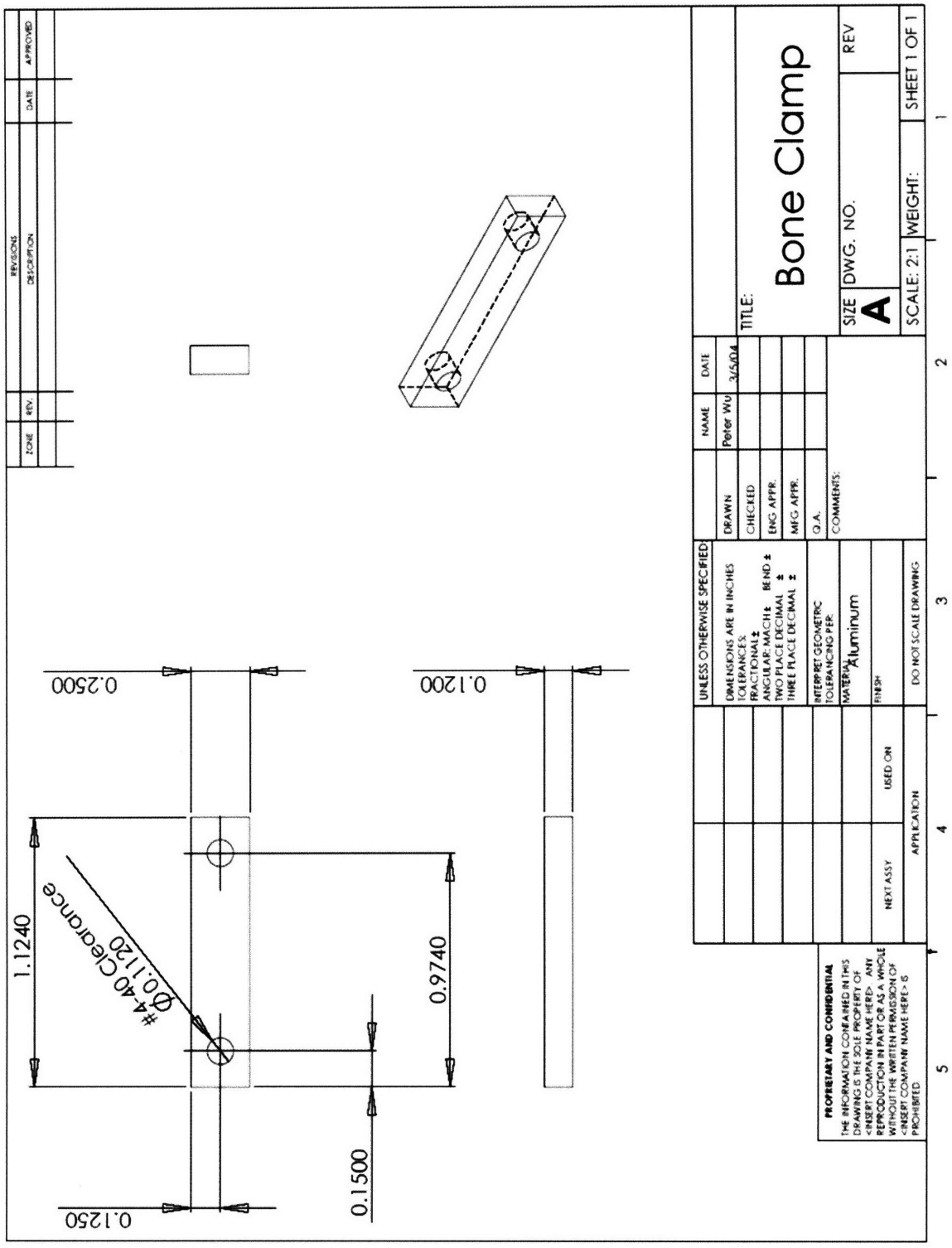
Bone Clamp
0.2500
0.1200
1.1240
#4-40 Clearance
Ø0.1120
0.9740
0.1500
0.1250
Aluminum
SCALE: 2:1
WEIGHT:
SHEET 1 OF 1
DWG. NO.
A
REV
DRAWN
Peter Wu
3/5/04
CHECKED
DWG APPR.
MFG APPR.
Q.A.
COMMENTS:
TITLE:
PROPRIETARY AND CONFIDENTIAL
THE INFORMATION CONTAINED IN THIS DRAWING IS THE SOLE PROPERTY OF <INSERT COMPANY NAME HERE>. ANY REPRODUCTION IN PART OR AS A WHOLE WITHOUT THE WRITTEN PERMISSION OF <INSERT COMPANY NAME HERE> IS PROHIBITED.
DO NOT SCALE DRAWING

Connecting Block

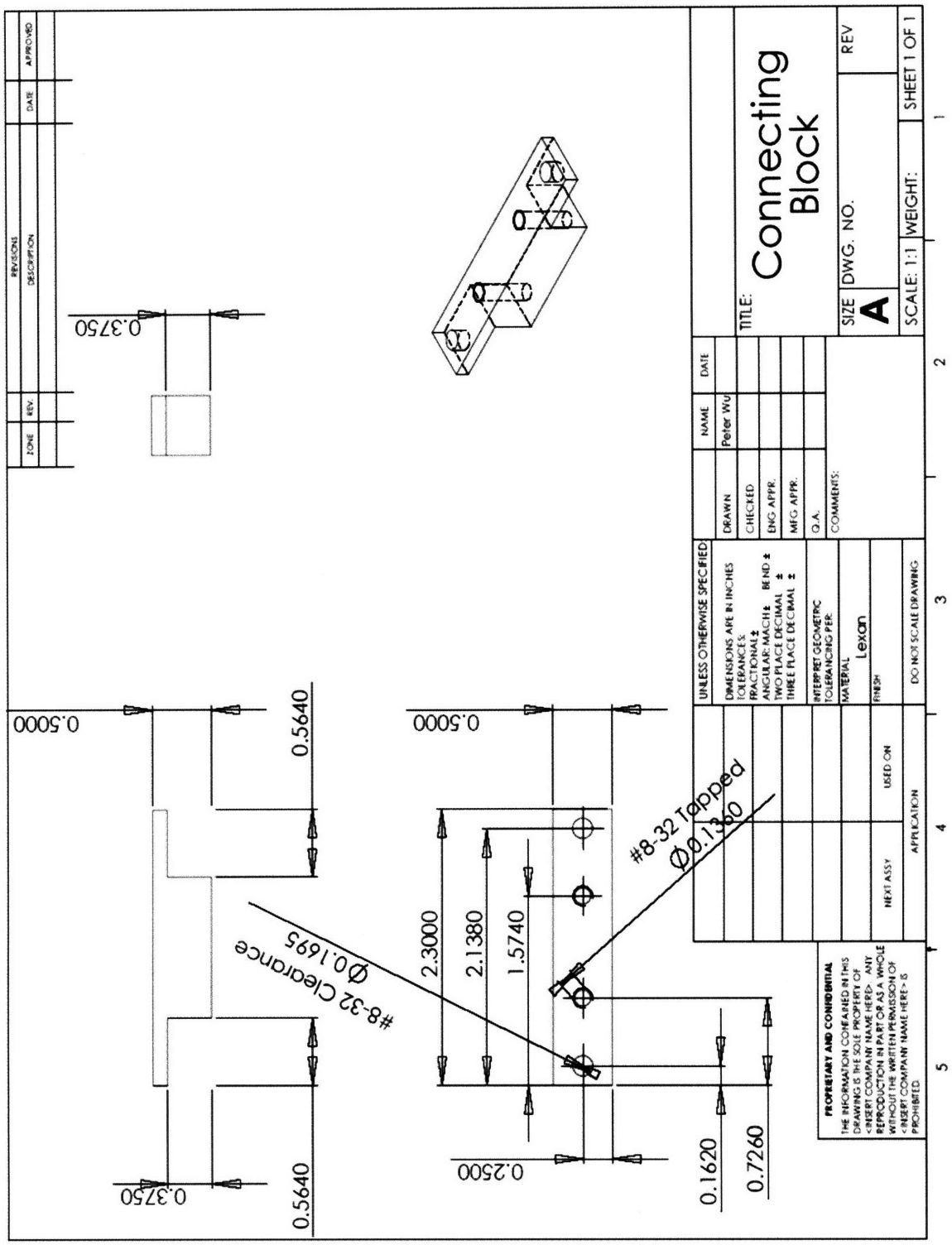

Sliding Block – Motor

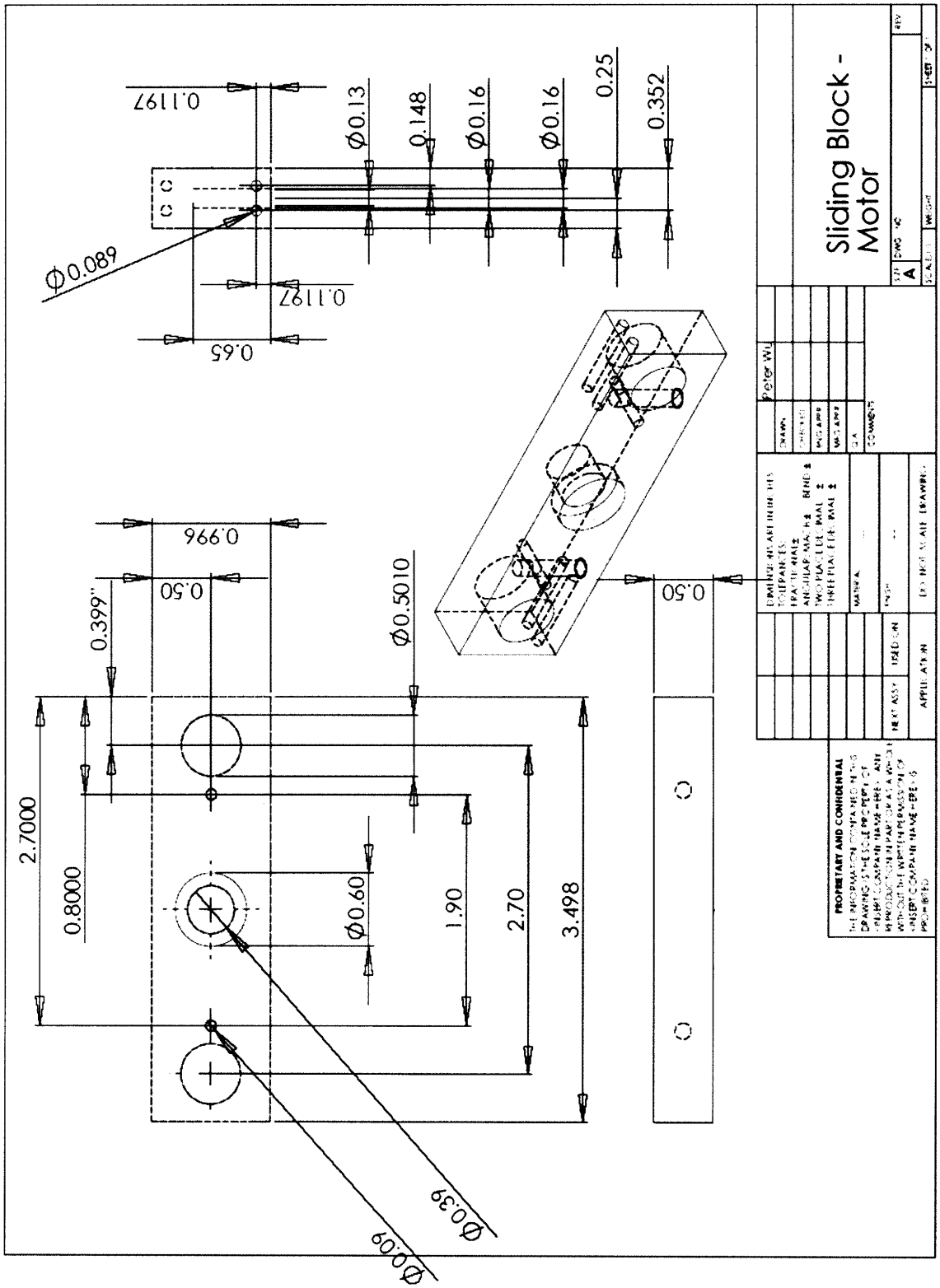

Sliding Block – Load Cell

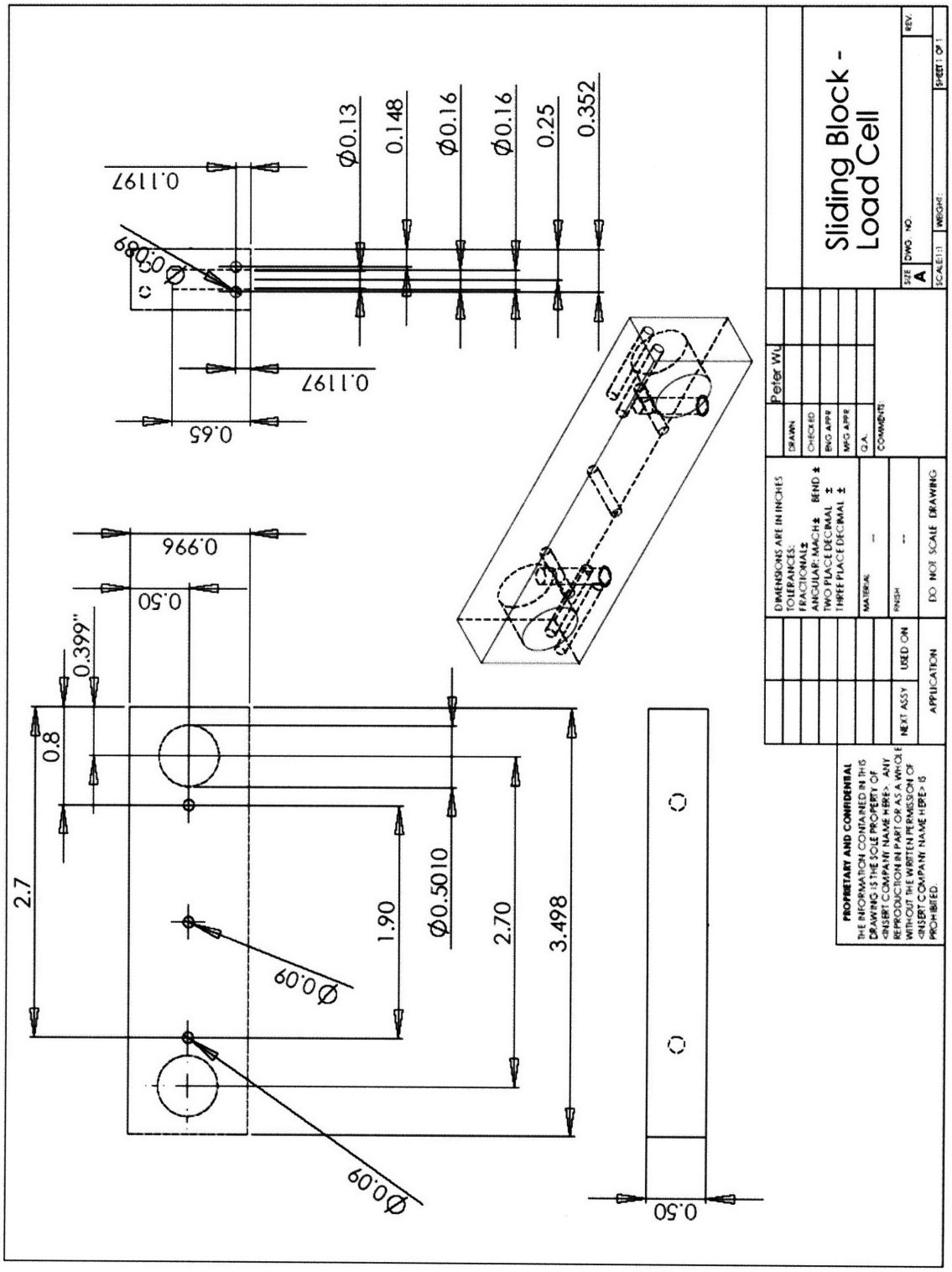

Rack

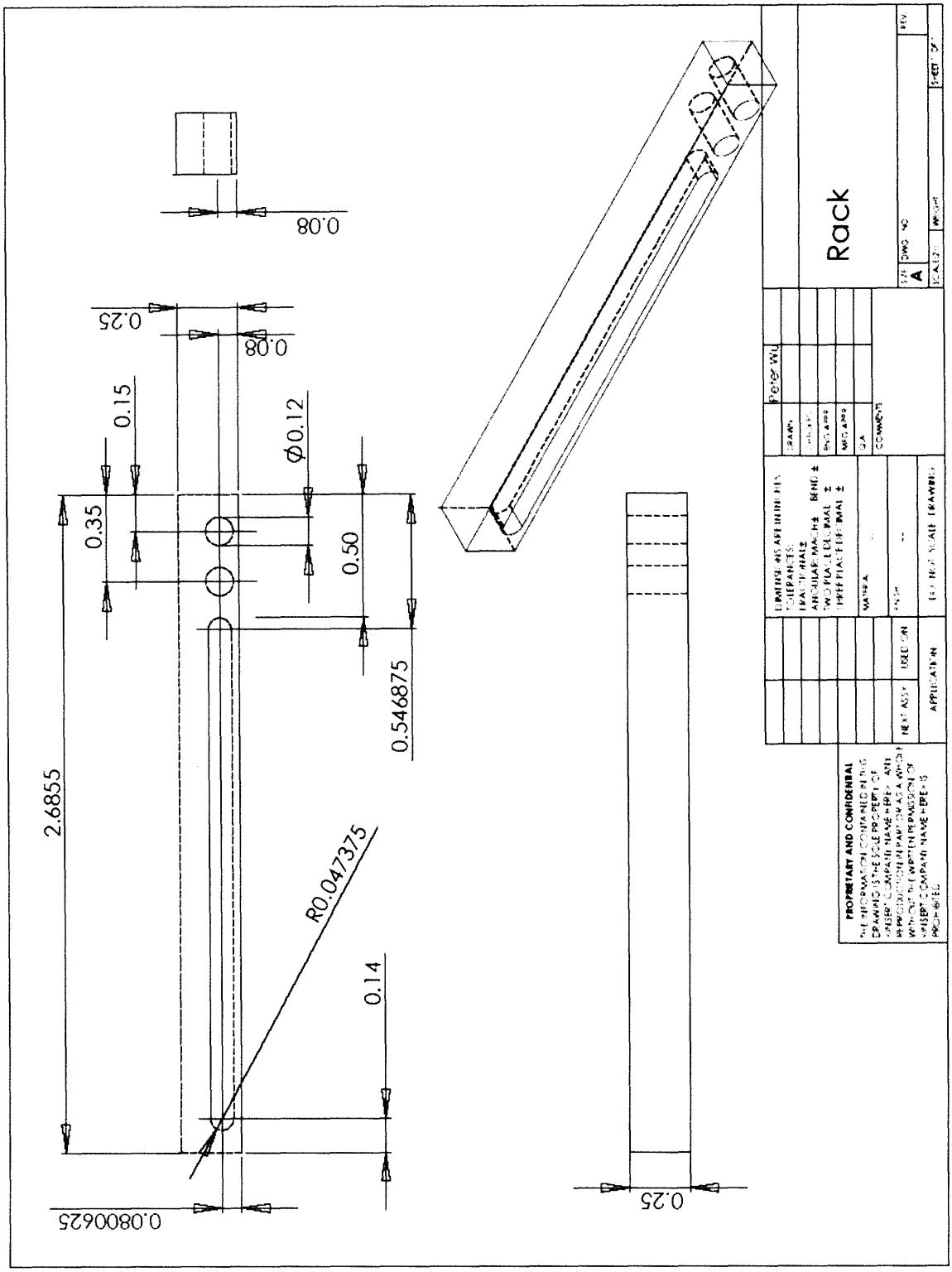
Rack
Peter Wu
0.08
0.25
0.08
0.15
Φ0.12
0.35
0.50
0.546875
2.6855
R0.047375
0.14
0.080625
0.25

Pinion Shaft

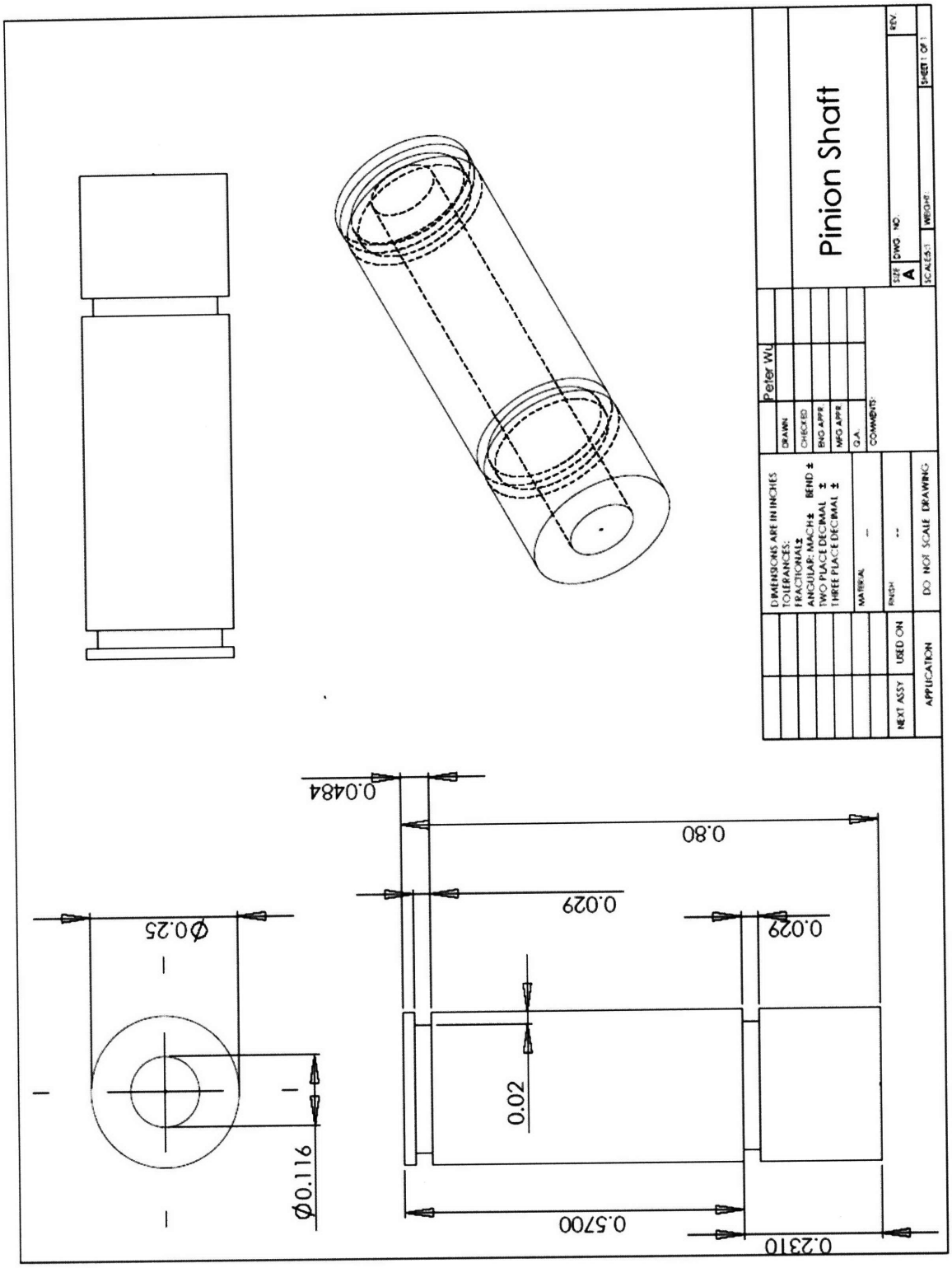

Pinion Strut

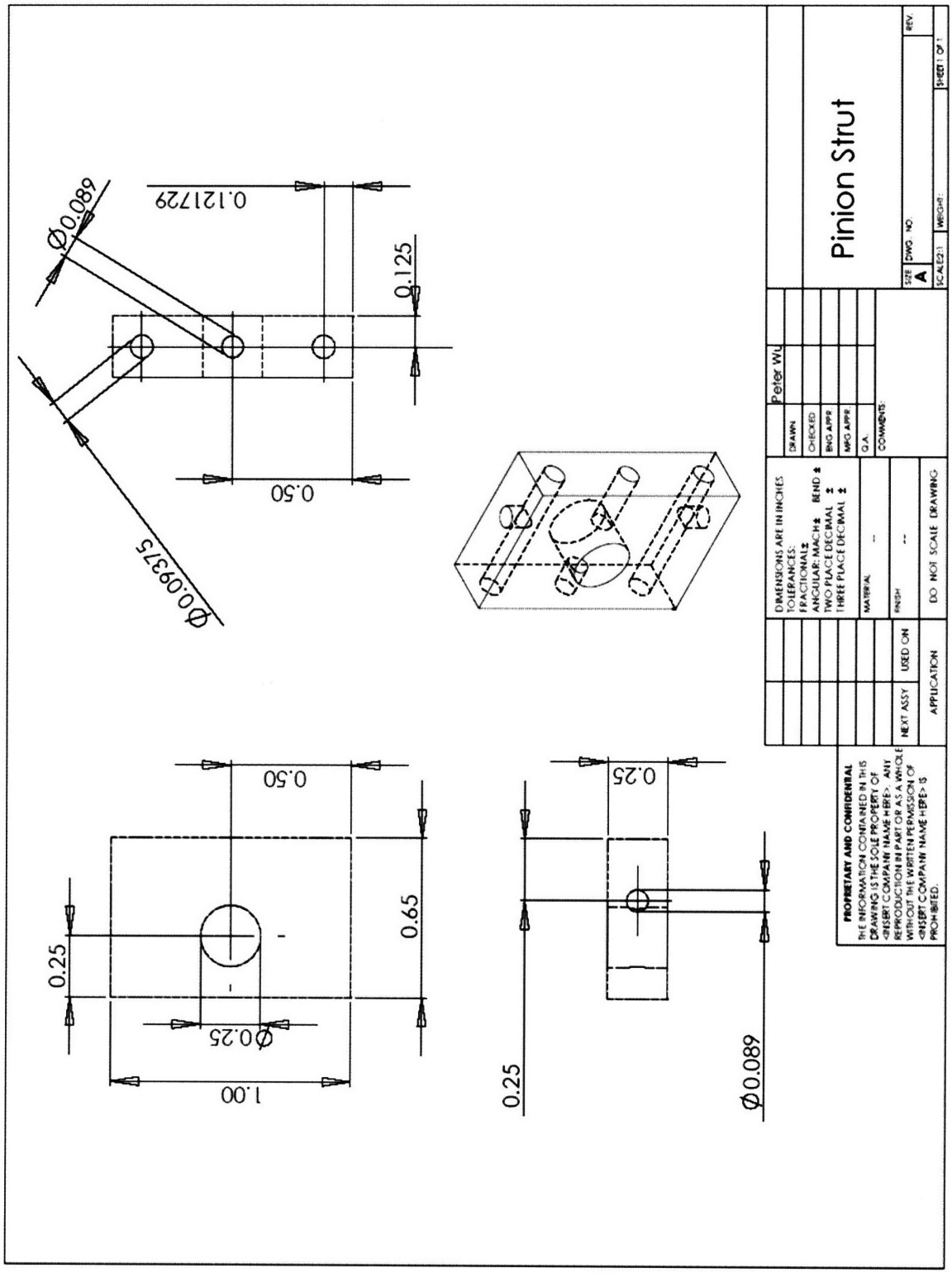

Guide-Rail – Dynamic Assembly

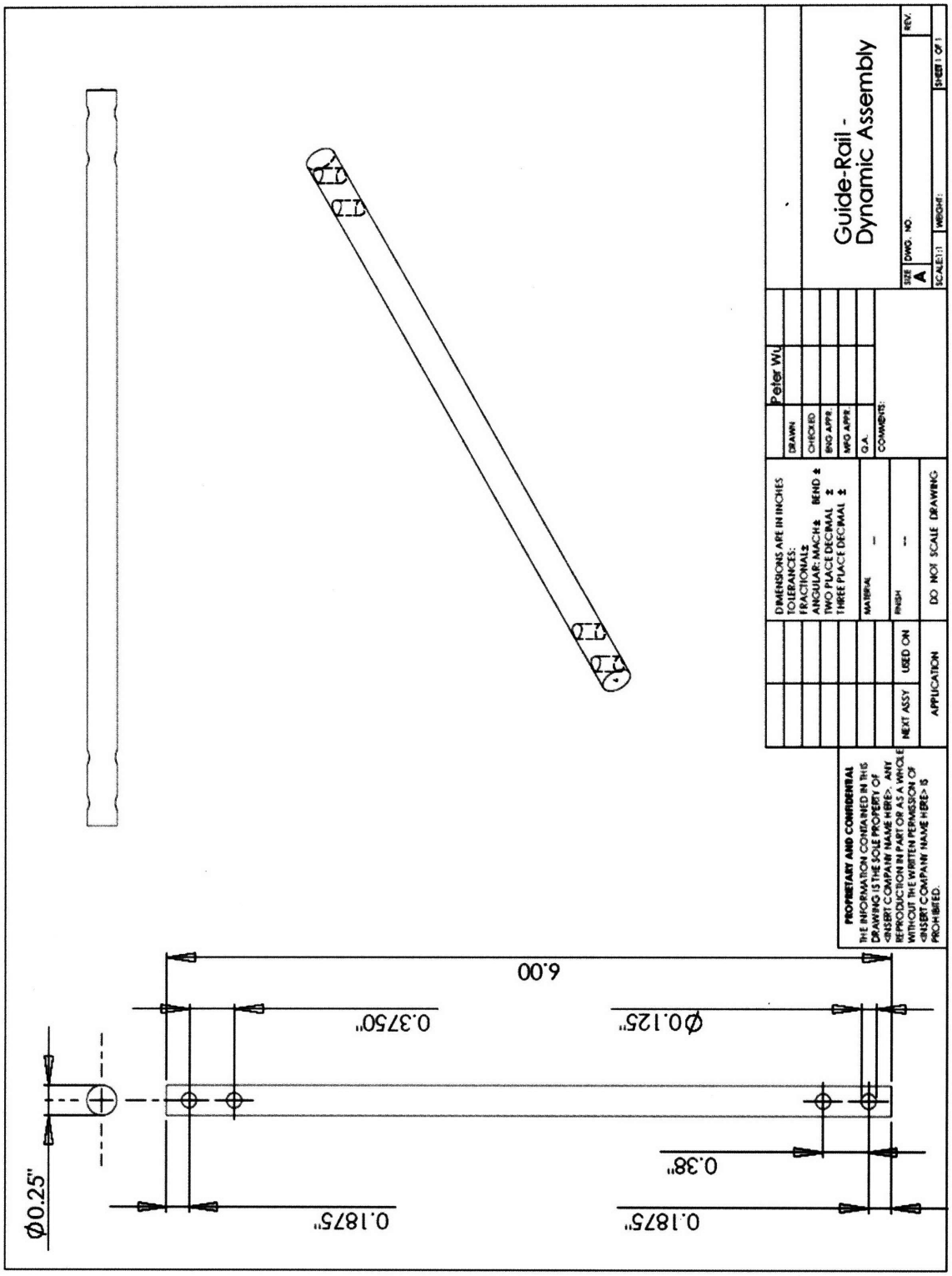

Support Bracket – Motor

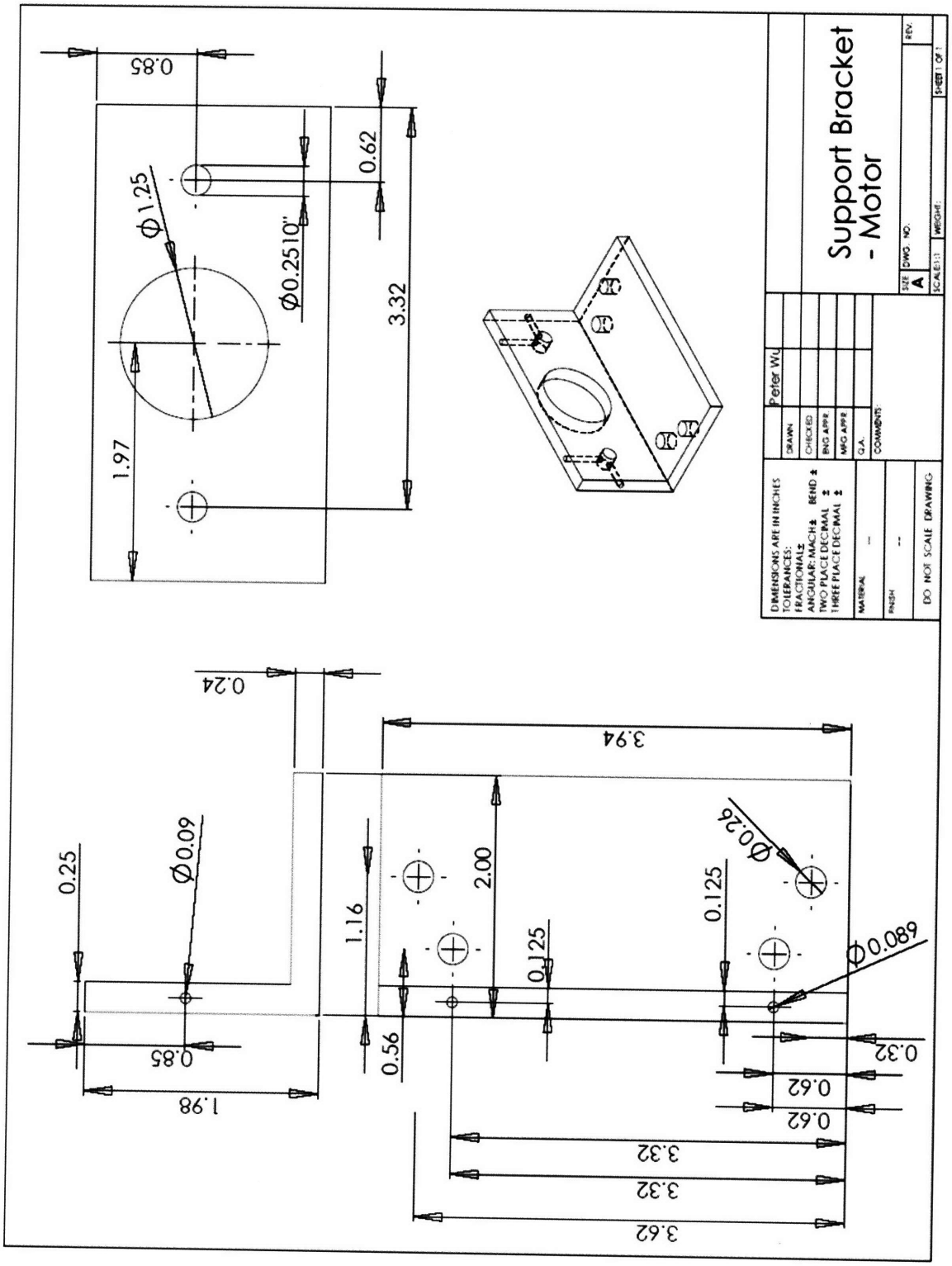

Support Bracket – Load Cell

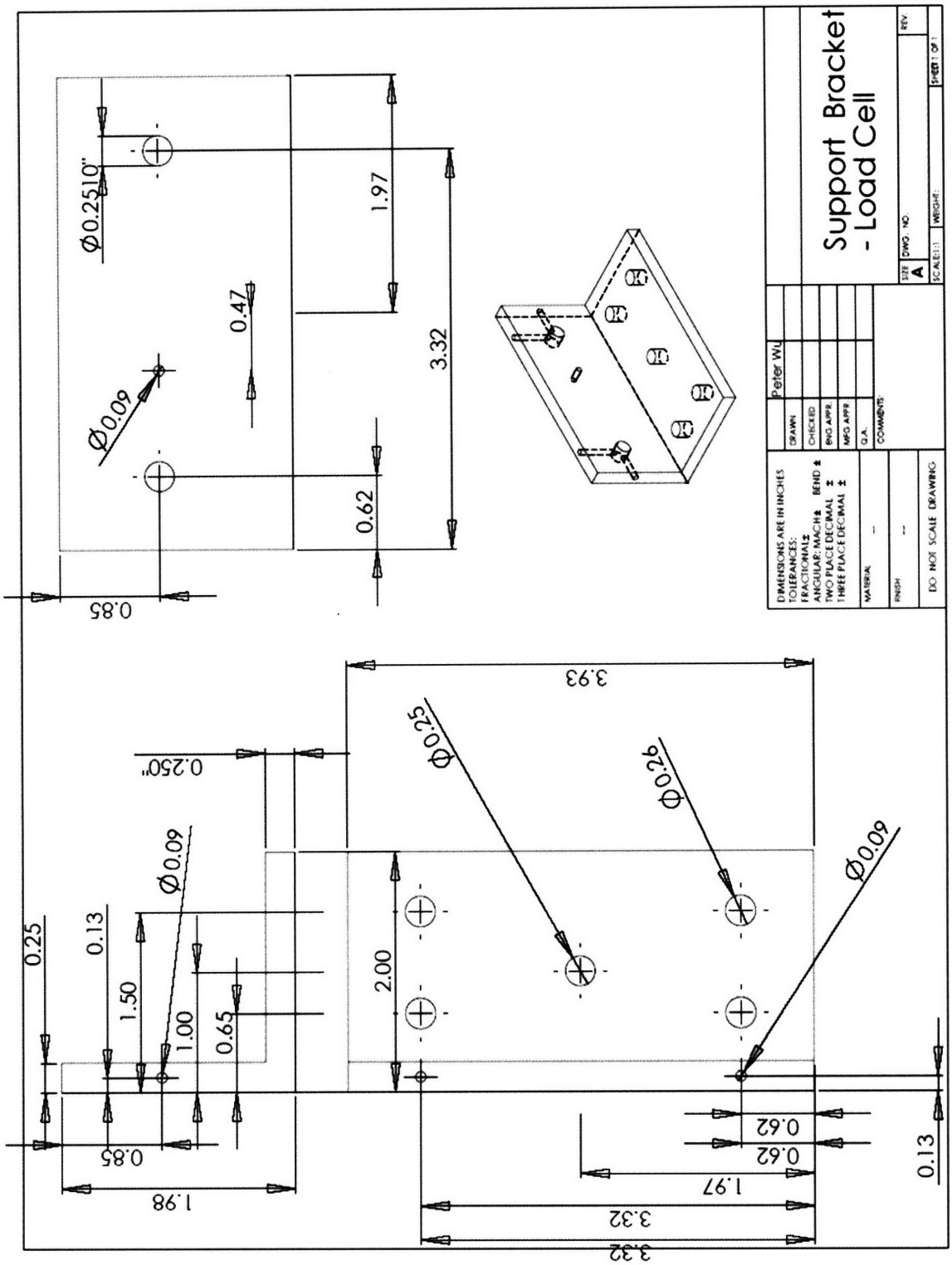

Platform Base - Motor

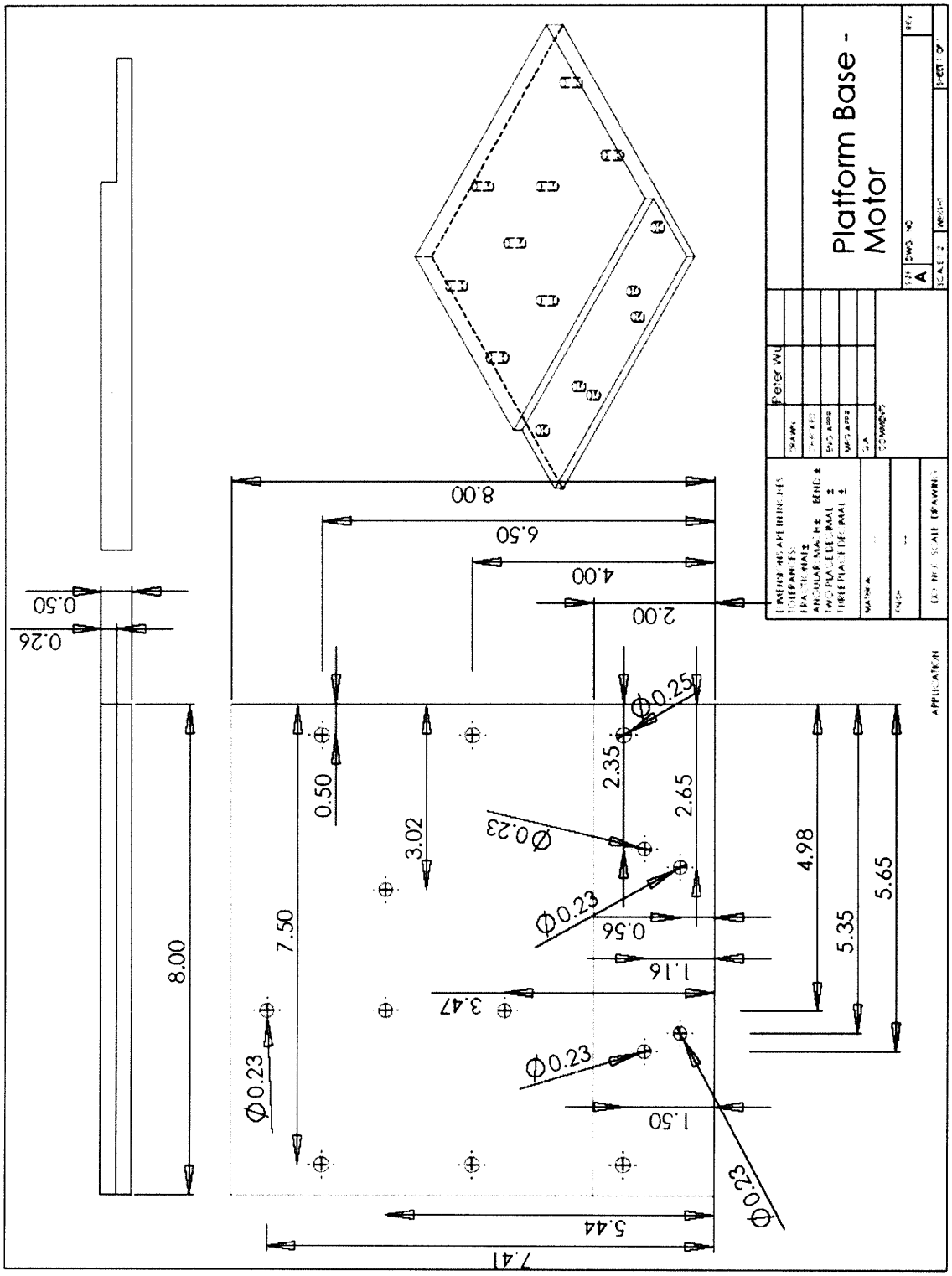

Platform Base

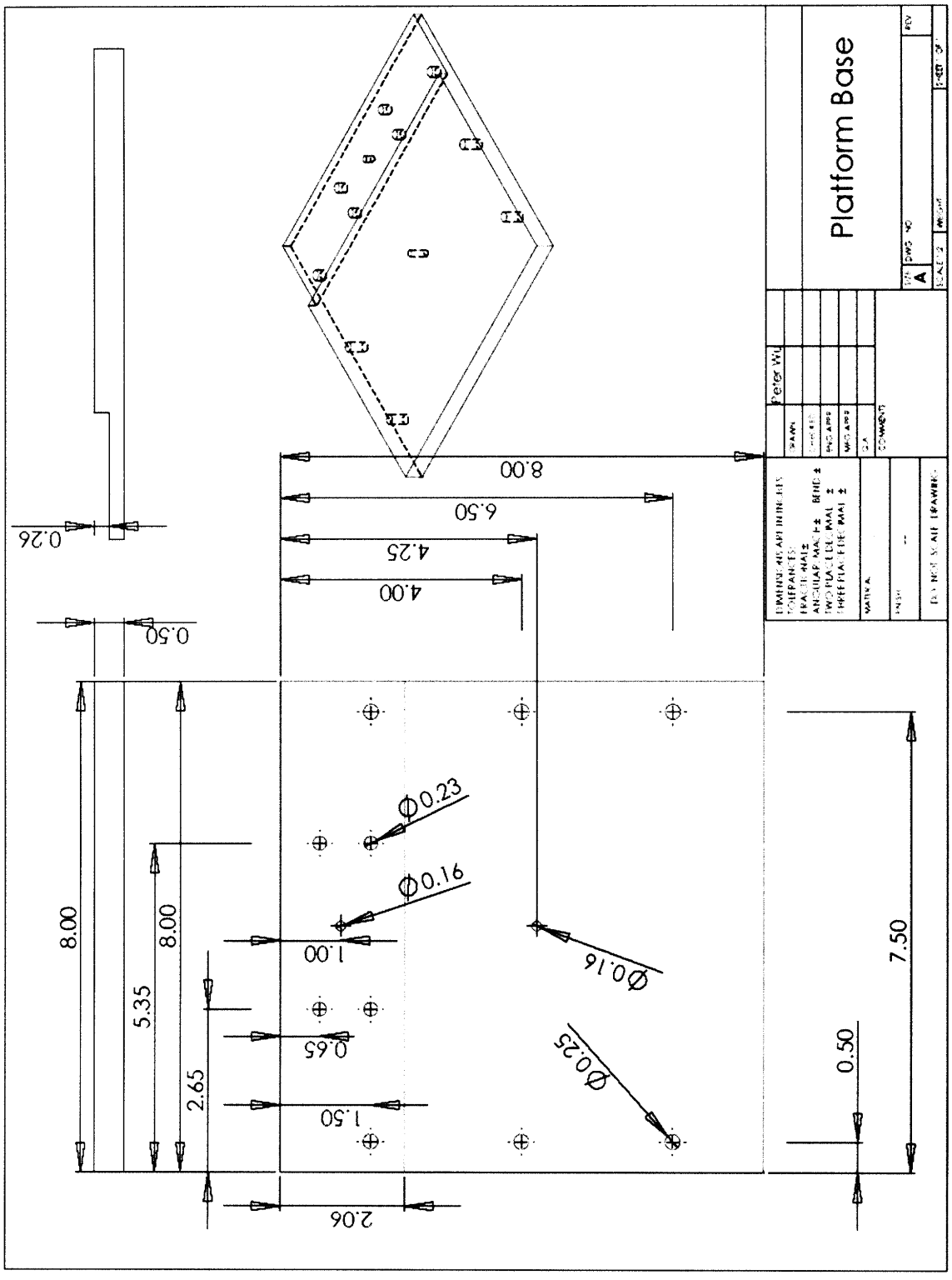

Platform Brace

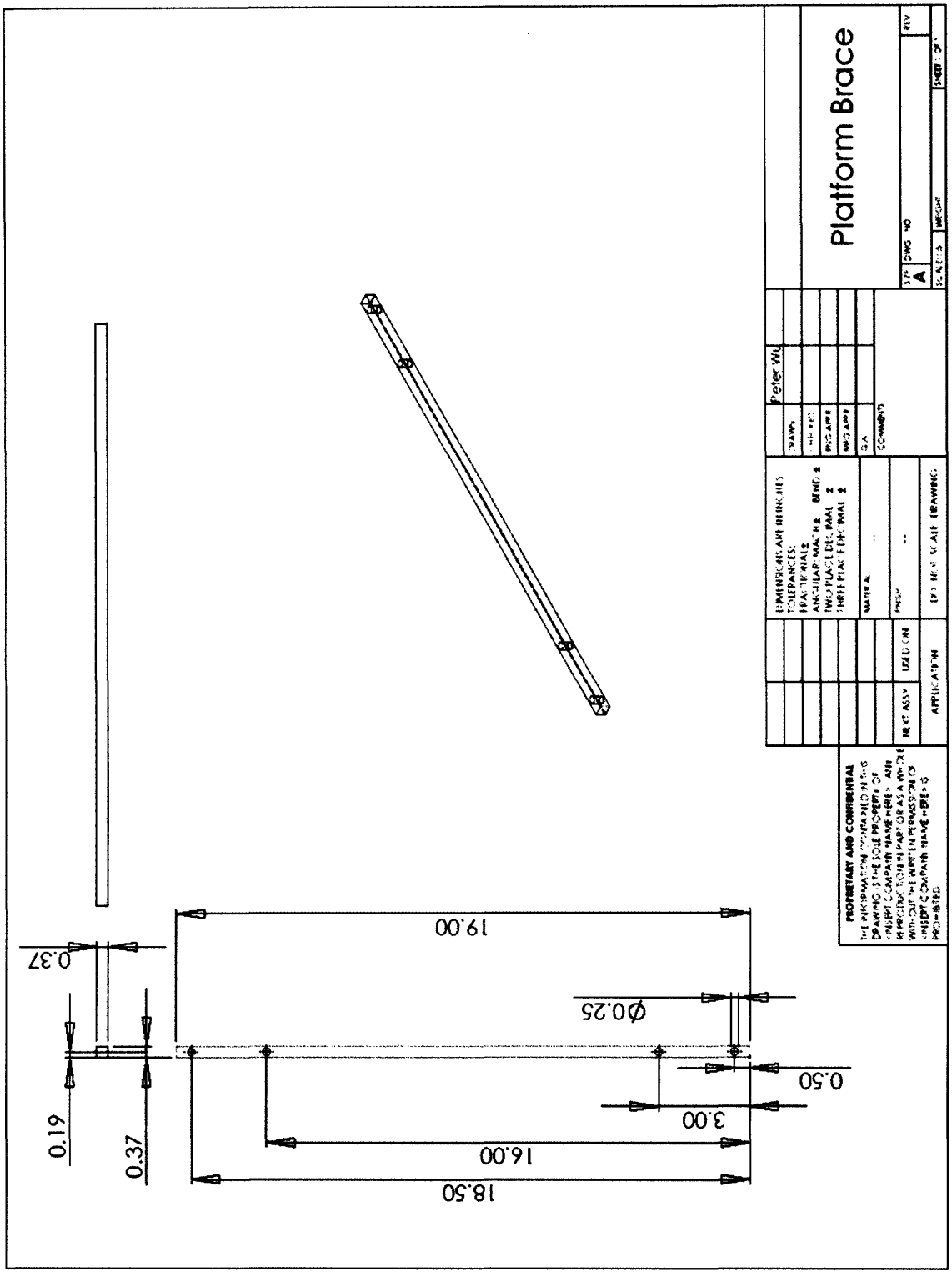

Axial Ballast on Dynamic Loading System

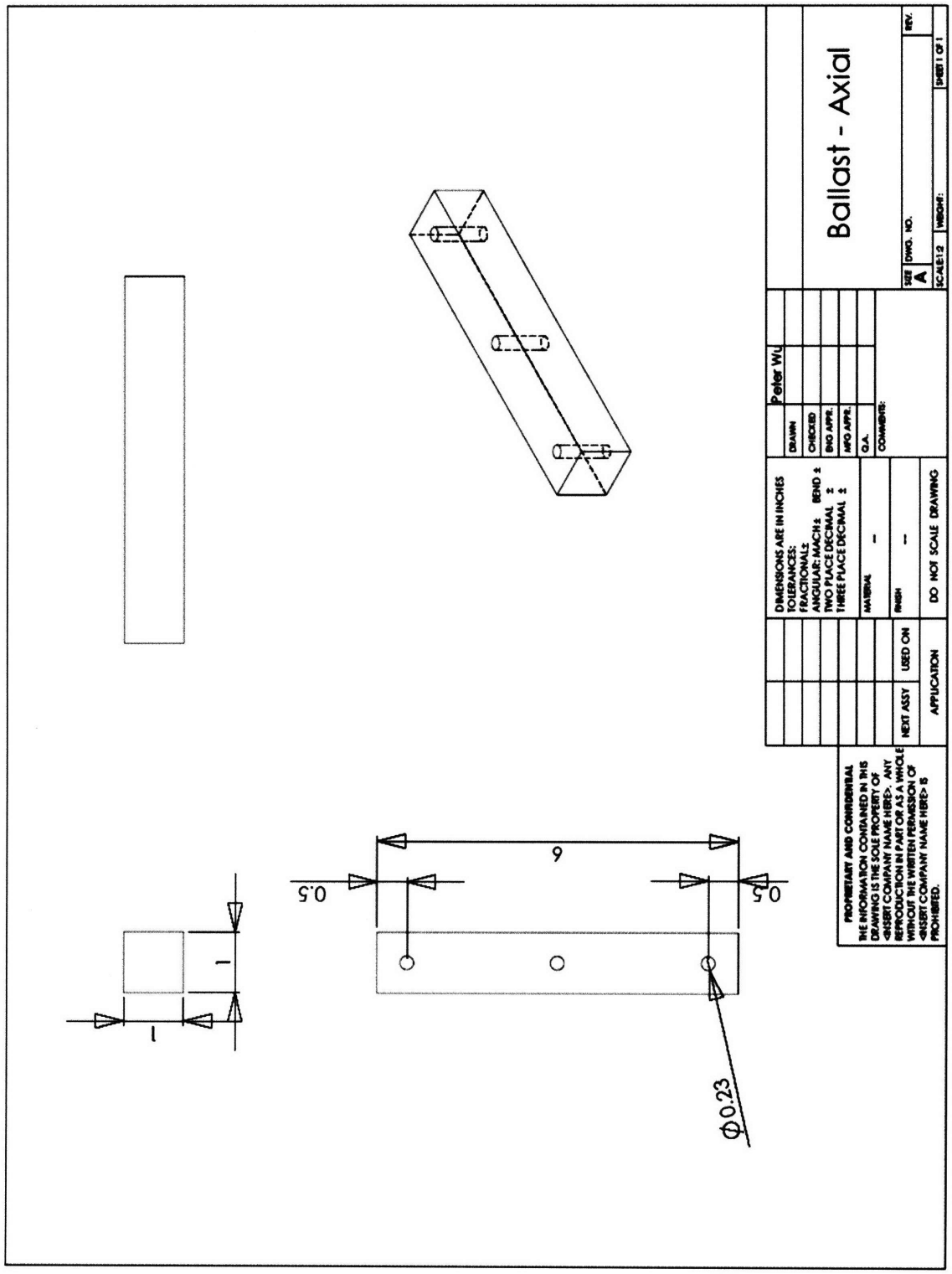

Perpendicular Ballast on Dynamic Loading System

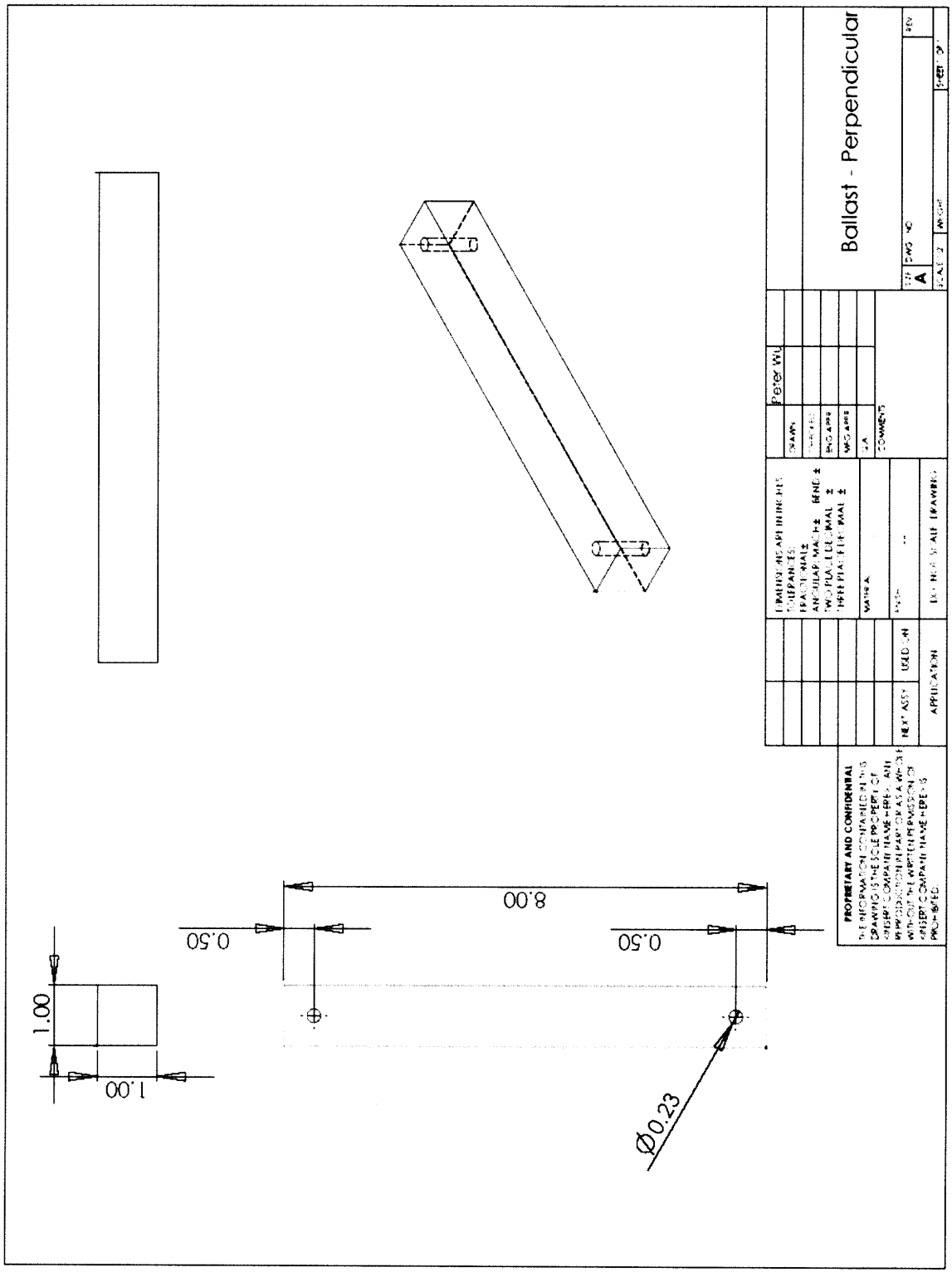

Leg

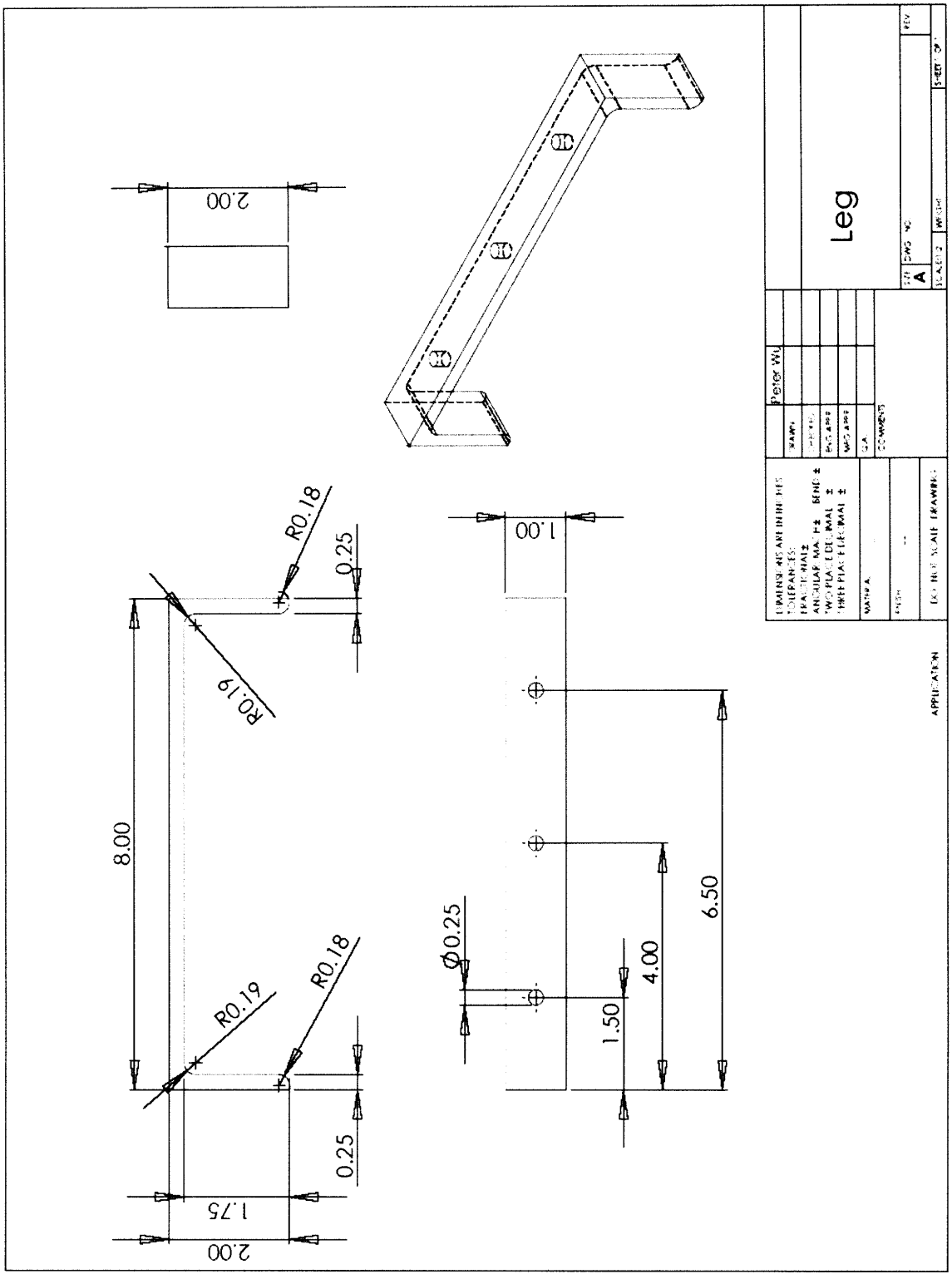
Leg
Peter Wu
A
2.00
R0.18
0.25
R0.19
8.00
R0.19
R0.18
0.25
1.75
2.00
1.00
Ø0.25
1.50
4.00
6.50

APPENDIX C: MOTOR SPECIFICATIONS

Linmot® Linear Motor Specifications

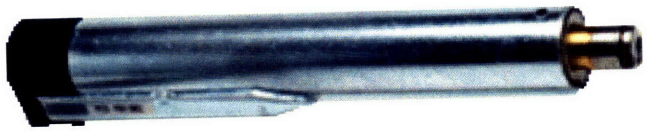

Linear Motor	*LinMot® P01-37x240/60x260*
Servo Controller	*E100-MT*
Power Supply	48VDC, 150W
Peak Force, Fp	120N (27lbf)
Continuous Force, Fc	55N (12.4lbf)
Limit Force, Fb	72N (16.2lbf)
Force Constant, cF	40N/A (9lbf/A)
Maximum Stroke, s	260mm (10.2in)
Shortened Stroke, SS	60mm (2.4in)
Zero Position, ZP	75mm (3in)
Max. Acceleration, a	144m/s^2 (5700in/s^2)
Max. Velocity, v	1.3m/s (51in/s)
Position Repeatability	± 0.1mm (± 0.004in)
Linearity	± 0.3%
Slider Mass, mS	829g (1.83lb)
Slider Length, lS	395mm (15.6in)

Stroke / Force - Diagram

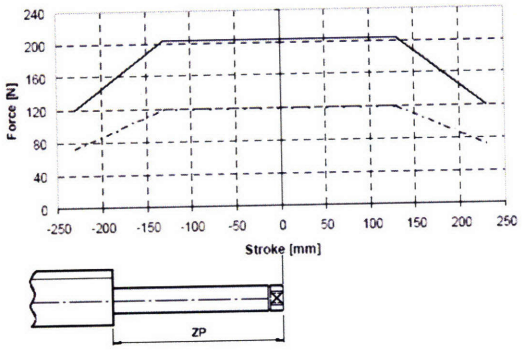

Servo Controller:

—— Series 1000
supply voltage 72 V DC
phase current 5.0 A

- — - Series 100
supply voltage 48 V DC
phase current 3.0 A

Controller Settings: CFG1ST.CFG

User Name: user
Password: savior

System — Info — Hardware — **Device**

Type: E200-MT/V2A
Serial No High: 2322
Serial No Low: 133

Memory

Flash Type: 514
EEPROM Type: 3075
RAM Type: 257

Software

Release: R1.3.8
Monitor: LinMon/V1.6.11
Base: LinBase/V1.3.40
Application: MT/V1.3.11/T02
Tree Type: 3
Tree Version: 4

Info — Error Handling — **Error Mask (all selected)**

DCLV Power Too Low
DCLV Power Too High
DCLV Signal Too Low
DCLV Signal Too High
Electronic Fault

Warn Mask (all selected)

DCLV Power Too Low
DCLV Power Too High
DCLV Signal Too Low
DCLV Signal Too High
Electronic Fault

Msg Mask (none selected)

DCLV Power Too Low
DCLV Power Too High
DCLV Signal Too Low
DCLV Signal Too High
Electronic Fault
Drive Type Mismatch
Curve Error
Slider Missing
Init Failed
Drive Following Error
Drive Too Hot Calculated
Drive Too Hot Sensor
In Position

Logging Mask (all selected except italics)

DCLV Power Too Low
DCLV Power Too High
DCLV Signal Too Low
DCLV Signal Too High
Electronic Fault
Drive Type Mismatch

Curve Error
Slider Missing
Init Failed
Drive Following Error
Drive Too Hot Calculated (Default selected)
Drive Too Hot Sensor

DCLV Monitoring

Power Low Warn: 21.123V
Power High Warn: 50.859V
Power Low Error: 18.252V
Power High Error: 53.73V
Signal Low Warn: 21.123V
Signal High Wanr: 50.859V
Signal Low Error: 18.252V
Signal High Error: 53.73V

Startup Mode (selected, except italics)

Auto Start (default selected)
Init Together

IO Configuration (all selected except italics)

Run Input
Init Input
Freeze Input
Emerg Stop Input
Analog/Trig Drive A
Analog/ Trig Drive B
Error Output
Warn Output

Pos Error Output
Msg Output

Command Interface

AT
MT
ASCII RS232
ASCII RS485
Application

Time

Hours: 5h
Seconds: 2986s

Drives | Drive A | **Type**

No Drive
LinMot P0x-23
LinMot P0x-37
LinMot P0x-37F
Stepper
Magnet
Sin/Cos Position Sensor

Initialization | **Init Mode**

Actual Position
Auto Move Out
Auto Move In (Default selected)
Trig Move Out
Trig Move In

Init Switches

Init Once (Default selected)

Init Config (Defaults in Parentheses)

Init Speed: 24.414 mm/s (Doesn't matter) (48.828mm/s)
Home Position: 0 mm (0 mm)
Check Init Position: 0 mm (39.997 mm) depends on strain
Initial Position 0 mm (19.999 mm)

Set Value Generation

Run Mode

Serial
Analog (Default selected)
Continuous Curve
Trigger Curve
Two Point

Set Value Configuration

Minimal Position: -9.999 mm	(-629.959 mm)
Maximal Position: 9.999 mm	(629.959 mm)
Curve Number: 1	(1)
Curve Position Offset: 0 mm	(0 mm)
Curve Amplitude: 100%	(100%)
Curve Speed: 100%	(100%)

Filter Parameter (Doesn't matter when motion profile is being run)

Max Speed: 4.687 m/s	(0.781 m/s)
Max Acceleration: 366.211 m/s^2	(30.518 m/s^2)

Position Monitoring

Pos Range Min: -9.999 mm	(-9.999 mm)
Pos Range Max: 9.999 mm	(9.999 mm)
In Position -: 0.098 mm	(0.996 mm) Active in on interfaces modes MT, ASCII, PROFIBUS
In Position +: 0.098 mm	(0.996 mm)
Following Error –: 0.391 mm	(2.5 mm)
Following Error +: 0.391 mm	(2.5 mm)

Control Switches

Current 3A

Control Parameters (Default) [Tuned]

Maximal Current: 2.995 A	(2.995 A)	
Current Offset: 0A	(0 A)	[-0.047 A]
P: 3.5A/mm	(0.999 A/mm)	[3 A/mm]
D: 4.005 A*s/m	(3.99 A*s/mm)	[6 A*s/m]
I: 1.005 A/(mm*s)	(0 A/(mm*s))	[3.016 A/(mm*s)]
FF Friction: 0.164A	(0 A)	[0.023 A]
FF Acceleration 4 mA/(m/s^2)	(0 mA/(m/s^2))	[38 mA/(m/s^2)] based on 720g load w/o slider
FF Deceleration 4 mA/(m/s^2)	(0 mA/(m/s^2))	[38 mA/(m/s^2)] based on 720g load w/o slider

Error Handling

Error Mask (all selected except italics)

Drive Type Mismatch
Curve Error
Slider Missing
Init Failed
Drive Following Error
Drive Too Hot Calculated (Default selected)

Drive Too Hot Sensor

Warn Mask (all selected except italics)

Slider Missing
Drive Init Not Done
Drive Following Error
Pos Range Indicator
Drive Hot Calculated (Default Selected)
Drive Hot Sensor
In Position

Emergency Stop

Emergency Stop Mode

Off (Default selected)
Freeze
Goto Position

Emergency Configuration

Max Acceleration: 30.518m/s^2

Advanced

Commutation

Sine (Default)
Trapezoid
Block

Master / Booster

Master
Booster Parallel
Booster Reverse

Gantry Slave parallel

Position Sensor

Internal Sensor 20μm
Internal Sensor 40μm
External 20 μm
External 10 μm
External 5 μm
External 2.5 μm
External 1.25 μm
AB Enc 1 1X
AB Enc 1 2X
AB Enc 1 4X
AB Enc 2 1X
AB Enc 2 2X
AB Enc 2 4X

Load Mass is 238.42g (includes the rack and pinion, with 4 Lexan pieces, bearings, and bolts)
Round up to 250g

Tuning Tool

Motor Data	
Motor Type:	P01-37x240/60x260
Application Data	
Load Mass [g]:	720g
Add:	Slider Mass
Dry Friction [N]:	0.95N (Estimate)
External Force [N]:	2N (External constant force like Mag Spring, Rounded for 3mm * 500N/m spring constant = 1.5N)
Angle [deg]:	0 deg
Current Offset [A]:	-0.049A
FF Friction [A]:	0.023
FF Acceleration:	37.966 mA/(m/s^2)
FF Deceleration:	37.966 mA/(m/s^2)

Matlab Source Code for Generating Strain Profiles for Linear Motor

```
%____Generate a Curve for the Linmot_Median Strain 5%
%____Enter the Frequency (Hz) and the Length of the Muscle (mm) and the Desired
%____Strain (Decimal)_____
clear
clc
%____n Points in time

        %____Frequency (Hz)
frequency=1;

%____1000 milliseconds divided by 5ms intervals (200 points / sec) divided by the
%____frequency = NUMBER OF POINTS / PERIOD (or oscillation)
%____Frequency 3 Hz, One period is 333.333ms, with 5ms points = 67 points
n=round(1000/5/frequency)

%____0 --> n counting by ones in each oscillation = N POINTS (3Hz = 67 points)
interval=linspace(0,n,n+1);

%____0 to 1 in n number of points
t=(interval/n);

%____Sinusoidal Curve (mm)

        %____Length of Muscle (mm)
A=26;

        %____Strain
s=0.05;

curve=A*(s/4)*sin(2*pi*t);
%____One complete cycle or oscillation with amplitude 1/4 of the desired strain
%____Set Muscle at Amplitude Strain first, then start motor
%____Single Step Conversion for Linmot (mm --> singlesteps)

ss=(1024/20)*curve;

%____Round
values=round(ss')

%____Specify in Linmot the time (ms) in which you want the curve to run
time=1/frequency*1000
%____time of 1/frequency (or period) -- (3Hz = 1/3s or 333.333ms)
%____Erase the last point in the generated values as this is a redundancy in
%____the oscillation
```

APPENDIX E: THEORETICAL BACKGROUND ON HOMOGENIZATION THEORY

Transport through a complex medium composed of smaller elements can be represented on multiple scales. For muscle tissues, micro-scale corresponds to the cellular or myofiber level while macro-scale corresponds to the tissue or muscle bundle level. On the cellular level, free diffusion is influenced by boundary conditions defined by cell geometry. On the tissue level, transport occurs across a continuous medium. Diffusion of drug through muscle can be studied using a multi-scale approach [178] starting with:

$$\frac{\partial c}{\partial t} = \nabla \cdot (D(\underline{X}) \nabla c) \qquad \text{(E1)}$$

where $\underline{X}=(X_1, X_2, X_3)$ denotes the three-dimensional coordinate system on the cellular length scale L_c. The diffusivity tensor $D(\underline{X})$, which D_{int} defines on the cellular level, is a continuous function of the position $\underline{X}$. $D(\underline{X}) = 0$ inside muscle fibers where no diffusion occurs.

Homogenization was used to derive macro-scale behaviors in the tissue based on micro-scale phenomena. This technique accounts for spatial variations in drug concentration on the cellular level to characterize drug concentration profiles on the tissue level (Figure E.1).

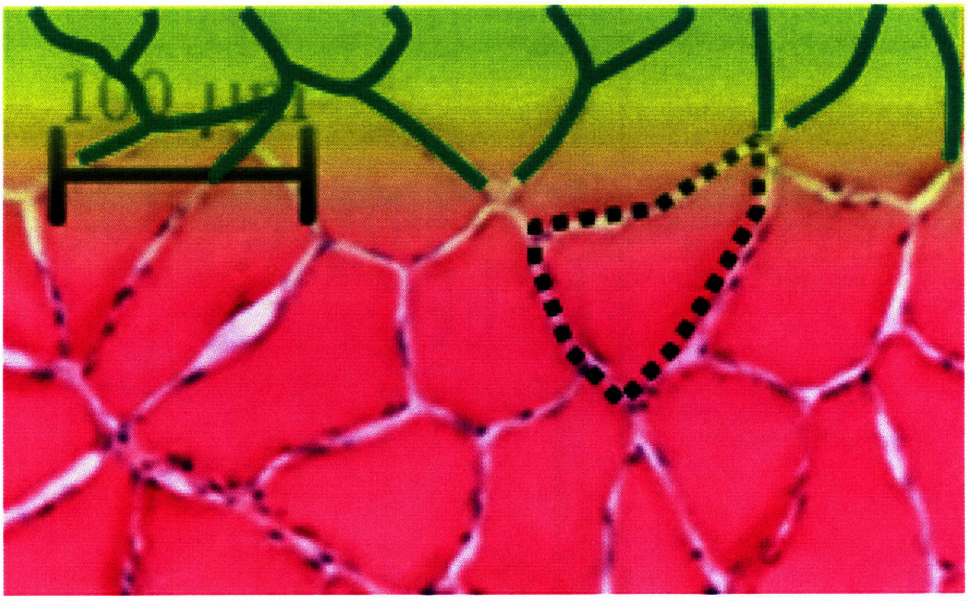

Figure E.1. Homogenization theory accounts for drug concentration on the cellular level in interstitial spaces (*green lines*) to characterize concentration gradients on the tissue level (*green shade*). A myofiber is outlined in *black*.

As fibers in the muscle can be considered repeating elements, a representative volume describing a periodic distribution of fiber elements that compose the macro-scale tissue was introduced. In our model, muscle fibers are represented by white diamond elements arranged in a staggered periodically repeating array, and diffusion occurs in the pink interstitial space between them (Figure 3.3*B*). As the axial length of our muscle sample is significantly greater than its radial cross-sectional area, the representative volume can be defined by a two dimensional configuration and solved on a reduced computational domain Ω (Figure 3.3*B*, *inset*), which is a periodic or repeating unit that sufficiently characterizes the symmetrical aspects of the problem. This idealized configuration was used to derive continuous behaviors on the tissue length scale (L_t), e.g. muscle diameter, by averaging or "homogenizing," variations on the cellular length scale (L_c), e.g. myofiber diameter. The homogenized version of Equation E1 [178, 184] on the tissue level has the form:

$$\frac{\partial\langle c\rangle}{\partial t} = D_{eff}^{ij}\frac{\partial^2\langle c\rangle}{\partial x_i \partial x_j} \tag{E2}$$

where $\underline{x} = (x_1, x_2, x_3)$ denotes the three-dimensional coordinate system on the tissue length scale L_t, D_{eff} is the macroscopic diffusion coefficient, $\langle c\rangle$ is average concentration, and $i,j = (1,2,3)$. Homogenization takes place for $X = x/\kappa$ in the theoretical limit as $\kappa \rightarrow 0$, where $\kappa = L_c/L_t$ is a small parameter representing the periodicity of repeating elements.

Macro-scale concentration, $\langle c\rangle$, was represented in Ω as the sum of a linear function of position, $\underline{e}$, reflecting the assumption of steady state diffusion, and a function $\chi(x,y)$ on the micro-scale that is periodic with period L_c. For the canonically defined concentration gradient, $\nabla\langle c\rangle = -1$, with unit amplitude :

$$\nabla\langle c\rangle = -\underline{e} + \nabla\chi \tag{E3}$$

where $\underline{e}$ is a unit vector defining the direction of macro-scale transport (Figure 3.3*B*) and χ is the small periodic component of the macroscopic concentration field used in the periodic domain Ω to represent perturbations to diffusion posed by the myofiber elements. χ is bounded by conditions Γ_1, at interstitial borders of Ω, and Γ_2, on myofiber surfaces (Figure 3.3*C*). Components of Γ_1 are conditions of symmetry that represents zero net flux ($\underline{n}\cdot\nabla\chi = 0$) at interstitial boundaries parallel to $\underline{e}$, and of periodicity that represents unconstrained flux ($\chi = 0$) at interstitial boundaries perpendicular to $\underline{e}$ [180]. Γ_2 is a boundary condition of myofiber impermeability defined by the non-homogeneous Neumann condition:

$$\underline{n}\cdot\nabla\chi = \underline{n}\cdot\underline{e} \tag{E4}$$

which is equivalent to $\nabla\langle c\rangle = 0$ according to Equation E3.

χ satisfies the Laplacian equation:

$$\nabla^2\chi = 0 \tag{E5}$$

in Ω [184] under boundary conditions Γ_1 and Γ_2. The solution of χ is used in an integral summation of micro-scale flux to calculate space averaged macro-scale effective diffusivity. Total flux in the direction of $\underline{e}$ is calculated using Equation E3 by:

$$D_{eff}\nabla cA = D_{int}\int_{\Omega}\underline{e}\cdot(-\underline{e}+\nabla\chi)\,d\Omega \tag{E6}$$

where D_{eff} is macro-scale effective diffusivity, D_{int} is micro-scale diffusivity in the interstitium, and A is the area of domain Ω. Macro-scale effective diffusivity is then calculated by reformulating Equation E6 according to the following general form [178, 184]:

$$D_{eff}^{ij} = \frac{1}{V_P}\int_{P}\left(D(\underline{X})\delta_{ij} - D(\underline{X})\frac{\partial\chi^j}{\partial X_i}\right)d\underline{X} \tag{E7}$$

where V_p is the volume of the periodic unit P, which is in our case is Ω, and δ_{ij} is the Kronecker delta. From Equation E6, effective diffusivity in the direction of $\underline{e}$ is:

$$D_{eff} = \frac{D_{int}}{A}\int_{\Omega}(1-\underline{e}\cdot\nabla\chi)\,d\Omega \tag{E8}$$

D_2 in Equation 1 accounts for the effects of interstitial fluid viscosity and possible hydrodynamic interactions of the drug with muscle fibers due to the relative size of the drug. Because drug size is substantially smaller than pore size, D_2 is independent of tissue porosity. Also, it is assumed that *in vitro* incubated muscle samples are infiltrated by saline media and that the interstitial fluid has the physical characteristics of water. Thus, $D_{int} = D_w$, the free diffusivity of the drug in water, which is $1.026\text{x}10^{-4}$ mm^2/s for 20 kDa dextran [183]. With these assumptions, $D_2 = 1$, and Equation E8 becomes:

$$D_1 = \frac{D_{eff}}{D_w} = \frac{1}{A}\int_{\Omega}(1 - \underline{e}\cdot\nabla\chi)\, d\Omega \qquad \text{(E9)}$$

Here, D_1 accounts for the effects of porosity and fiber geometry and arrangement on effective diffusivity. D_1 is generally recognized as:

$$D_1 = \frac{D_{eff}}{D_w} = \frac{\varphi}{\lambda} \qquad \text{(E10)}$$

where φ is porosity, which describes the volume fraction of tissue accessible to diffusing drug, and λ is the geometric tortuosity factor (Figure E.2), which is the ratio of the actual length of the transport path to the linear length or thickness of the tissue [247]. Tortuosity is a parameter that accounts for the transport effects of fiber geometry and arrangement to describe the average hindrance to transport in a complex medium relative to that in an obstacle-free medium.

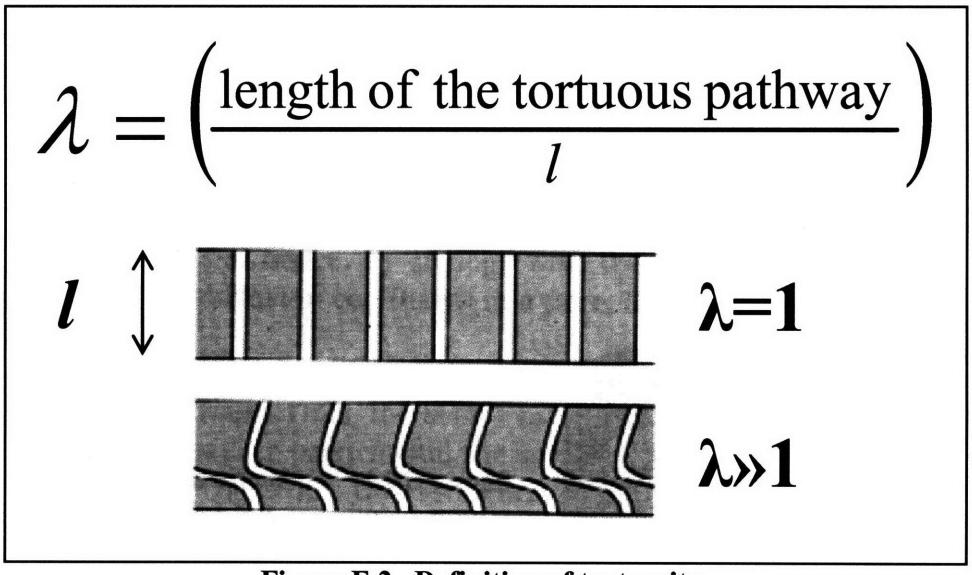

Figure E.2. Definition of tortuosity.

Matlab Source Code of the Static Model used in COMSOL Multiphysics®

```
% COMSOL Multiphysics Model M-file
% Generated by COMSOL 3.2b (COMSOL 3.2.0.304, $Date: 2006/04/04 14:56:13 $)

flclear fem

% COMSOL version
clear vrsn
vrsn.name = 'COMSOL 3.2';
vrsn.ext = 'b';
vrsn.major = 0;
vrsn.build = 304;
vrsn.rcs = '$Name:  $';
vrsn.date = '$Date: 2006/04/04 14:56:13 $';
fem.version = vrsn;

% Geometry
g1=square2('2.2','base','center','pos',{'2','2'},'rot','45');
g11=square2('2','base','center','pos',{'2','2'},'rot','45');
garr=geomarrayr(g11,3,3,3,3);
[g12,g13,g14,g15,g16,g17,g18,g19,g20]=deal(garr{:});
g21=square2('2','base','center','pos',{'7/2','7/2'},'rot','45');
garr=geomarrayr(g21,3,3,2,2);
[g22,g23,g24,g25]=deal(garr{:});
g26=square2('6','base','corner','pos',{'2','2'},'rot','0');
g27=rect2('1.5','6','base','corner','pos',{'(5+8)/2','(5+8)/2'},'rot','0');
g28=rect2('1.5','6','base','corner','pos',{'(5+8)/2','2'},'rot','0');
g29=rect2('1.5','6','base','corner','pos',{'5','2'},'rot','0');
clear s
s.objs={g11,g13,g14,g15,g16,g17,g18,g19,g20,g21,g23,g24,g25,g26,g29};
s.name={'SQ1','SQ2','SQ3','SQ4','SQ5','SQ6','SQ7','SQ8','SQ9','SQ10', ...
 'SQ11','SQ12','SQ13','SQ14','R1'};
s.tags={'g11','g13','g14','g15','g16','g17','g18','g19','g20','g21', ...
 'g23','g24','g25','g26','g29'};

fem.draw=struct('s',s);

% (Default values are not included)

% Application mode 1
clear appl
appl.mode.class = 'Poisson';
appl.sshape = 2;
appl.assignsuffix = '_poeq';
clear pnt
```

```
pnt.weak = {};
pnt.dweak = {};
pnt.constr = {};
pnt.name = {};
pnt.ind = [];
appl.pnt = pnt;
clear bnd
bnd.type = {};
bnd.r = {};
bnd.h = {};
bnd.weak = {};
bnd.dweak = {};
bnd.constr = {};
bnd.g = {};
bnd.q = {};
bnd.name = {};
bnd.ind = [];
appl.bnd = bnd;
clear equ
equ.gporder = {};
equ.init = {};
equ.c = {};
equ.f = {};
equ.weak = {};
equ.dweak = {};
equ.usage = {};
equ.constr = {};
equ.cporder = {};
equ.name = {};
equ.ind = [];
appl.equ = equ;
fem.appl{1} = appl;
fem.sdim = {'x','y'};
fem.frame = {'ref'};
fem.border = 1;
fem.units = 'SI';

% Multiphysics
fem=multiphysics(fem);
```

APPENDIX F: CALCULATIONS FOR AMPLITUDE OF RADIAL OSCILLATION IN DYNAMIC MODEL

An elastic material satisfies the law:

$$\frac{\Delta V}{V} = \frac{\Delta L}{L}(1-2\nu) \tag{F1}$$

where ΔV is the change in total volume, ν is the Poisson ratio, and ΔL is the change in axial length. The Poisson ratio is defined as the ratio between the transverse, ε_{tr}, and axial strain, ε_{ax}:

$$\nu = -\frac{\varepsilon_{tr}}{\varepsilon_{ax}} = -\frac{\frac{\Delta R}{R}}{\frac{\Delta L}{L}} \tag{F2}$$

For an incompressible material, whose Poisson ratio is 0.5, volume is conserved during deformation, and no volume change occurs with axial strain according to Equation F1.

For a cylindrical sample of nominal radius R0 and length L0:

$$\Delta V = \pi R^2 L - \pi R0^2 L0 = 0 \tag{F3}$$

where R and L are the radius and the length, respectively, of the sample after deformation. R is determined by:

$$R = R0\sqrt{\frac{L0}{L}} \tag{F4}$$

The length and radius at each mean strain are:

$$\begin{aligned} Ln &= L0 + n\%L0 \\ Rn &= R0\sqrt{\frac{1}{1+n\%}} \end{aligned} \tag{F5}$$

where L0 and R0 are the nominal length and radius, respectively, of the muscle, and n = 0, 5, 10, and 20, corresponding to the value of axial strain (Figure F.1).

For cyclic strains, the maximum and minimum values for length and radial deformations are:

$$L_D = Ln \pm 0.025 * L0$$
$$R_D = Rn\sqrt{\frac{Ln}{Ln \pm 0.025 * L0}} \quad \text{(F6)}$$

where n = 0, 5, 10, and 20. The absolute value of the amplitude of radial deformation during cyclic strain is:

$$\Delta R = |Rn - R_D| \quad \text{(F7)}$$

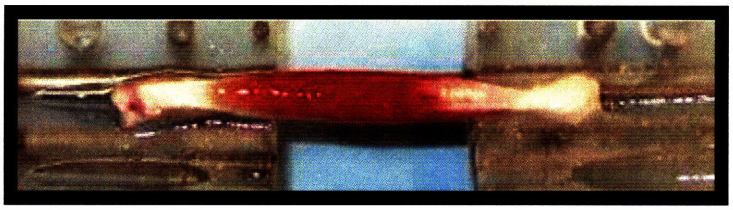

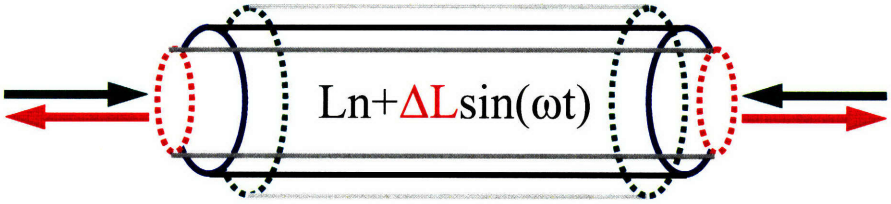

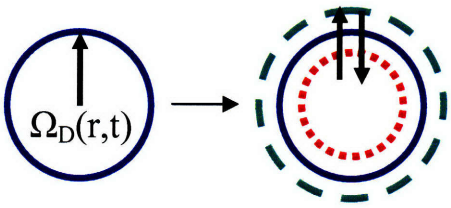

$$R(t) = Rn + \Delta R\sin(\omega t)$$

$$\Delta L = 0.7 \text{ mm} \rightarrow \Delta R = 12 \text{ μm}$$

Figure F.1. Model of skeletal muscle dimensions. A picture of soleus skeletal muscle mounted for linear tensile loading and a schematic of muscle mechanics as modeled by an incompressible circular cylinder that relates length changes to radius changes by Poisson's ratio.

APPENDIX G: THEORETICAL BACKGROUND ON DYNAMIC MODEL – ARBITRARY LAGRANGIAN EULERIAN FORMULATION

During cyclic strain, the boundary of the radial section moves according to the sinusoidal law:

$$r(t) = Rn\,(1 + \alpha \sin(\omega t)) \tag{G1}$$

where α is the radial strain amplitude relative to the mean radius, Rn:

$$\alpha = \frac{\Delta R}{Rn} \tag{G2}$$

r(t) is the radial coordinate in the moving domain, $\Omega_D(r,\theta,t) = \{0 \le r(t) \le Rn\,(1 + \alpha \sin(\omega t)),\ 0 < \theta \le 2\pi\}$. And, R is the radial coordinate in the reference domain, $\Omega_0(R,\Theta) = \{0 \le R \le Rn,\ 0 < \Theta \le 2\pi\}$.

The transport equation is:

$$\frac{\partial c}{\partial t} - D_{static,\,Rn}\,\nabla^2 c = 0 \qquad \text{in } \Omega_D(t) \tag{G3}$$

which can be formulated on Eulerian coordinates such that:

$$\left.\frac{\partial c}{\partial t}\right|_{\Omega_0} - D_{static,\,Rn}\,\nabla^2 c - \underline{w}\cdot\nabla c = 0 \qquad \text{in } \Omega_D(t) \tag{G4}$$

where $\underline{w}$ is the oscillatory velocity of the domain $\Omega_D(t)$.

Using cylindrical coordinates (r,θ) and considering the axial symmetry of the problem in θ, Equation G4 can be written as:

$$\left.\frac{\partial c}{\partial t}\right|_{\Omega_0} - D_{static,\,Rn}\,\nabla^2 c - w_r\frac{\partial c}{\partial r} = 0 \qquad \text{in } \Omega_D(t) \tag{G5}$$

where w_r is the radial component of $\underline{w}$, and reformulated in the reference domain Ω_0 with the boundary conditions as follows:

$$\begin{cases} \dfrac{\partial c}{\partial t} - \dfrac{D_{static,Rn}}{(1+\alpha\sin(\omega t))^2}\nabla^2 c - \dfrac{R\omega\alpha\cos(\omega t)}{1+\alpha\sin(\omega t)}\dfrac{\partial c}{\partial R} = 0 & in\ \Omega_0 \\ c(t) = c_0 & R = R_0, t > 0 \\ c = 0 & 0 \le R < R_0, t = 0 \end{cases} \tag{G6}$$

Concentration at the final time is computed by averaging over the final period as follows:

$$c(R, T_f) = \frac{\int_{T1}^{T2} c(R,t)\, dt}{T2 - T1} \tag{G7}$$

where $T_1 = T_f - (T/2)$, $T_2 = T_f + (T/2)$, T is the period of a cycle, and R is the radial coordinate used to describe the domain Ω_0.

APPENDIX H: MATLAB SOURCE CODE FOR IMAGE PROCESSING

Image Montaging – Horizontal

```
clear
clc

%____Load Image File_____________________________________________
load c10wt

%____Define Images to be Joined_____________________________________
leftimage=c10wdv;
rightimage=c10wev;

%____X = 480 Rows, Y = 640 Columns_____________________________
% ____Least Squares Matrix Comparison_____________________________

diff=[ ];
startright=1
endright=70
for k=startright:endright,  %____K is the index for the columns in the rightimage
   diff(k)= sum(sum((leftimage(:,260:360)-rightimage(:,k:(k+100))).^2));
end
ly=259;

[minimum ry]=min(diff(startright:endright));
figure(3); plot(diff)
diff
minimum
ly
ry=ry+startright-1
newimage=[leftimage(:,1:ly) rightimage(:,ry:640)];

%___V-Intensity Value Scale_____________________________________
V=[0 1];
figure(4); imagesc(newimage); CAXIS(V); colorbar
%figure(5); newimage=[leftimage(:,1:ly) rightimage(:,ry:640)]; imagesc(newimage)

%____Preliminary Pictures_____________________________________
c10wabcdev=[c10wav(:,1:529) c10wbv(:,14:520) c10wcv(:,76:499) c10wdv(:,50:259)
c10wev(:,11:640)];
c10wabcde=[c10wa(:,1:529,:) c10wb(:,14:520,:) c10wc(:,76:499,:) c10wd(:,50:259,:)
c10we(:,11:640,:)];
figure(6); imagesc(c10wabcdev); CAXIS(V); colorbar
```

```
figure(7); imagesc(c10wabcde)
save c10wabcdepics c10wabcde c10wabcdev

%____Joined Images_____________________________________________
%figure(1); imagesc(c10wav); CAXIS(V); pixval; figure(2); imagesc(c10wbv);
CAXIS(V); pixval;
%figure(1); imagesc(c10wbv); CAXIS(V); pixval; figure(2); imagesc(c10wcv);
CAXIS(V); pixval;
%figure(1); imagesc(c10wcv); CAXIS(V); pixval; figure(2); imagesc(c10wdv);
CAXIS(V); pixval;
%figure(1); imagesc(c10wdv); CAXIS(V); pixval; figure(2); imagesc(c10wev);
CAXIS(V); pixval;
```

Image Montaging – Vertical

```
clear
clc

%____Load Image File_____________________________________________
load c10wt
V=[0 1];

%____Define Images to be Joined_____________________________________
topimage=c10tbv;
bottomimage=c10tcv;

%____X = 480 Rows, Y = 640 Columns_____________________________________
% ____Least Squares Matrix Comparison_____________________________________

diff=[ ];
startbottom=200;
endbottom=250;
for k=startbottom:endbottom,  %____K is the index for the rows in the bottomimage
   diff(k)= sum(sum((topimage(450:479,:)-bottomimage(k:(k+29),:)).^2));
end
tx=449;

[minimum bx]=min(diff(startbottom:endbottom));
figure(3); plot(diff)
%diff
minimum
tx
bx=bx+startbottom-1
```

```
newimage=[topimage(1:tx,:); bottomimage(bx:480,:)];

%___V-Intensity Value Scale_____________________________________________
V=[0 1];
figure(4); imagesc(newimage); CAXIS(V); colorbar
%figure(5); newimage=[topimage(1:tx,:); bottomimage(bx:480,:)]; imagesc(newimage)

%____Final Picture _____________________________________________________
c10tabcv=[c10tav(1:299,:); c10tbv(14:449,:); c10tcv(217:480,:)];%; c3tdv(22:480,:)];
c10tabc=[c10ta(1:299,:,:); c10tb(14:449,:,:); c10tc(217:480,:,:)];%; c3td(22:480,:,:)];
figure(6); imagesc(c10tabcv); CAXIS(V); colorbar
figure(7); imagesc(c10tabc)
save c10tabcpics c10tabcv c10tabc

%____Preliminary Pictures _____________________________________________
%figure(1); imagesc(c10tav); CAXIS(V); pixval; figure(2); imagesc(c10tbv); CAXIS(V);
pixval;
%figure(1); imagesc(c10tbv); CAXIS(V); pixval; figure(2); imagesc(c10tcv); CAXIS(V);
pixval;
%figure(1); imagesc(c4tcv); CAXIS(V); pixval; figure(2); imagesc(c4tdv); CAXIS(V);
pixval;
```

Measurement of Drug Penetration

```
figure(1); imagesc(c10tabcv); pixval; grid minor
v=[.844153 .042208];
figure(2); imcontour(c10tabcv,v,'b'); grid minor

figure(1); imagesc(c10wabcdev); pixval; grid minor
v=[.844153 .042208];
figure(2); imcontour(c10wabcdev,v,'b'); grid minor
```